Published by Empress Catherine II
Saint Petersburg Mining University

SINCE 1907

E-ISSN 2541-9404
ISSN 2411-3336

JOURNAL OF MINING INSTITUTE

ZAPISKI GORNOGO INSTITUTA

SCIENTIFIC JOURNAL

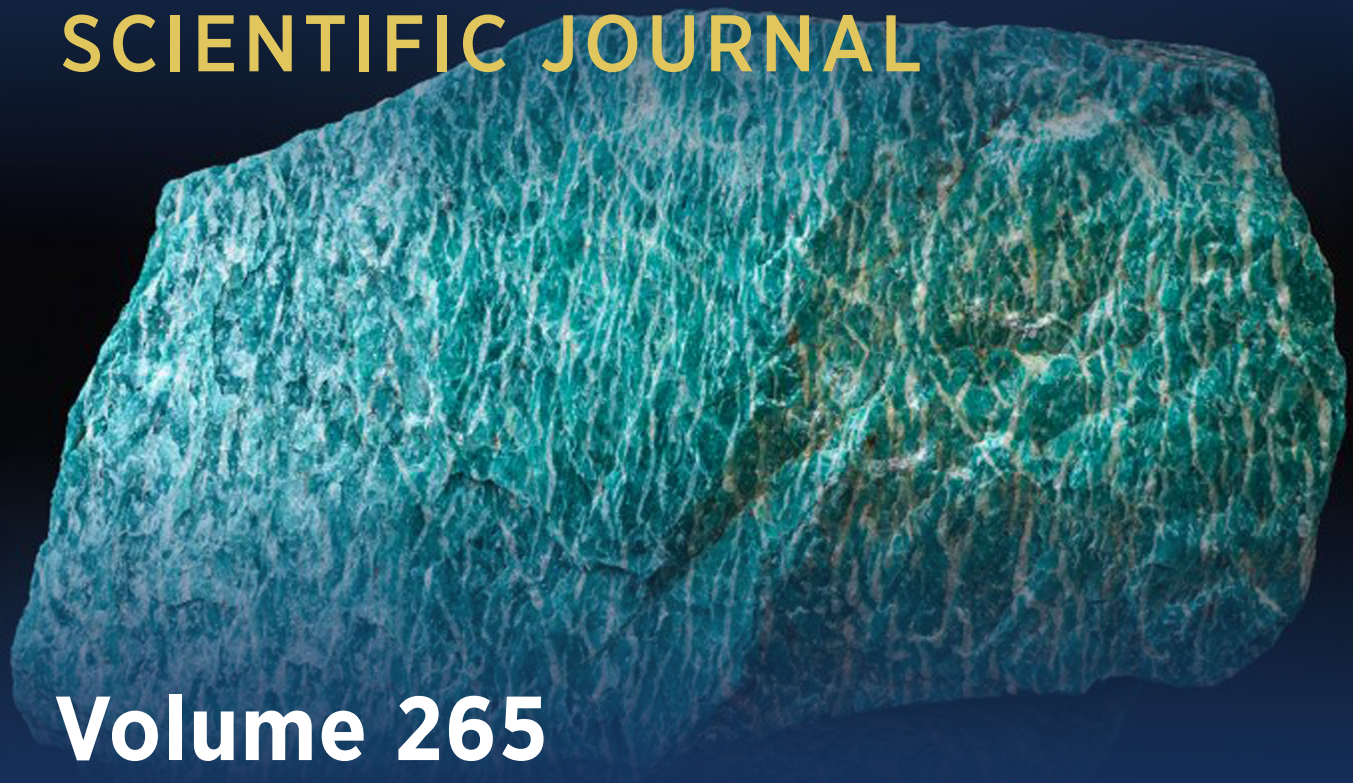

Volume 265
№ 1 • 2024

INDEXING IN
SCOPUS (Q1)
WEB OF SCIENCE (ESCI)

WWW.PMI.SPMI.RU

Journal of Mining Institute

Empress Catherine II Saint Petersburg Mining University

The International Competence Center for Mining Engineering Education under the auspices of UNESCO

The scientific periodical “Journal of Mining Institute” is published since 1907 by Empress Catherine II Saint Petersburg Mining University – the first higher technical educational institution in Russia, founded in 1773 by the decree of Catherine II as the embodiment of the ideas of Peter I and M.V. Lomonosov on the training of engineers for the development of mining business.

The International Competence Center for Mining Engineering Education under the auspices of UNESCO operates on the basis of Empress Catherine II Saint Petersburg Mining University and contributes to active interaction of the Journal with the international scientific community.

The purpose of the Journal is to create an information space in which Russian and foreign scientists can present results of their theoretical and empirical research on the problems of the mining sector.

Published articles cover the issues of geology, geotechnical engineering and engineering geology, mining and petroleum engineering, mineral processing, energy, geoecology and life safety, economics of raw materials industries.

The Journal is indexed by Scopus (Q1), Web of Science Core Collection (ESCI), DOAJ Seal, RSCI, GeoRef, Google Scholar, RSCI. It is included in the White list of the Ministry of Education and Science of the Russian Federation.

The Journal is published six times a year. The average first decision time is one month.

Articles are published free of charge. Translation is provided by the author.

The cover shows an exhibit of the Mining Museum – microcline (amazonite). Punched from a large crystal of bright green color, it has a perthite pattern – a natural fusion of green microcline with white albite. It is believed that the best amazonite in the world in terms of beauty and richness of color is found on the Keivy hill, Kola Peninsula.

The Mining Museum is the world’s third largest natural-science exposition, it contains more than 230 thousand exhibits, including precious metals and stones, unique collections of minerals, ores, rocks, paleontological remains, meteorites, a collection of models and prototypes of mining equipment, pieces of stone-cutting and jewelry art.

JOURNAL OF MINING INSTITUTE

ZAPISKI GORNOGO INSTITUTA

PEER-REVIEWED SCIENTIFIC JOURNAL

Published since 1907

ISSN 2411-3336
e-ISSN 2541-9404

Volume 265

ST. PETERSBURG • 2024

Journal founder: Empress Catherine II Saint Petersburg Mining University

Sections

• Geology • Geotechnical Engineering and Engineering Geology • Economic Geology • Energy

Registration Certificate PI No. FS77-70453 dated 20.07.2017

PH License No. 06517 dated 09.01.02

Editorial staff: Head of the Editorial Center V.L.Lebedev; Editors: E.S.Dribinskaya, M.G.Khachirova, L.V.Nabieva
Computer Design: N.N.Sedykh, V.I.Kashirina, E.A.Golovinskaya

Passed for printing 29.02.2024. Format 60 × 84/8. Academic Publishing Division 40.
Circulation: 300 copies. Order 83. Printed by RIC of Empress Catherine II Saint Petersburg Mining University. Free sale price.

Mailing address of the Journal Founder and the Editorial Board
21st Linia V.O., No. 2, St. Petersburg, Russia, 199106
Phone: +7 (812) 328-8416; Fax +7 (812) 327-7359;
E-mail: pmi@spmi.ru Journal website: pmi.spmi.ru

CONTENTS

Geology

Geotechnical Engineering and Engineering Geology

Energy

ISSN 2411-3336; e-ISSN 2541-9404

JOURNAL OF MINING INSTITUTE
Zapiski Gornogo instituta
Journal homepage: pmi.spmi.ru

Research article

Origin of carbonate-silicate rocks of the Porya Guba (the Lapland-Kolvitsa Granulite Belt) revealed by stable isotope analysis ($\delta^{18}O$, $\delta^{13}C$)

Dmitrii P. KRYLOV ✉, **Ekaterina V. KLIMOVA**
Institute of Precambrian Geology and Geochronology RAS, Saint Petersburg, Russia

How to cite this article: Krylov D.P., Klimova E.V. Origin of carbonate-silicate rocks of the Porya Guba (the Lapland-Kolvitsa Granulite Belt) revealed by stable isotope analysis ($\delta^{18}O$, $\delta^{13}C$). Journal of Mining Institute. 2024. Vol. 265, p. 3-15. EDN GISHQG

Abstract. Carbonate-silicate rocks of unclear origin have been observed in granulites of the Porya Guba of the Lapland-Kolvitsa Belt within the Fennoscandinavian Shield. The present work aims to reconstruct possible protoliths and conditions of metamorphic transformation of these rocks based on oxygen and carbon isotopic ratios combined with phase equilibria modeling. Isotope analysis and lithochemical reconstructions suggest that carbonate-silicate rocks of the Porya Guba represent metamorphosed sediments (possibly marls) with the isotopic composition corresponding to the Precambrian diagenetically transformed carbonates ($\delta^{18}O \approx 17.9$ ‰, SMOW and $\delta^{13}C \approx -3.4$ ‰, PDB). The chemical composition varies depending on the balance among the carbonate, clay, and clastic components. Significant changes of the isotopic composition during metamorphism are caused by decomposition reactions of primary carbonates (dolomite, siderite, and ankerite) producing CO_2 followed by degassing. These reactions are accompanied by $\delta^{18}O$ and $\delta^{13}C$ decrease of calcite in isotopic equilibrium with CO_2 down to 15 ‰ (SMOW) and –6 ‰ (PDB), respectively. The isotopic composition is buffered by local reactions within individual rock varieties, thus excluding any pronounced influence of magmatic and/or metasomatic processes.

Keywords: carbonate-silicate rocks; stable isotopes; metamorphism; inorganic carbon cycle; isotope fractionation; Rayleigh distillation

Acknowledgment. The work was financed by Russian Science Foundation, grant N 22-27-00275, https://rscf.ru/en/project/22-27-00275/.

Received: 07.02.2023 ***Accepted: 20.06.2023*** ***Online: 06.09.2023*** ***Published: 29.02.2024***

Introduction. The carbonate-silicate geochemical cycle (the inorganic carbon cycle [1]) includes the processes of weathering, sedimentation (with silicate to carbonate transformations), metamorphism and volcanic activity (with conversion of carbonates to silicates). Over an interval of several million years or more, this cycle controls the balance of CO_2 during interactions of the atmosphere, hydrosphere, crust, and mantle of the Earth and largely determines global climate changes [2-4]. Carbonate-silicate rocks in metamorphic complexes (hereafter, for brevity, the obsolete term calciphyres is used) represent a sequence of phase transformations in the cycle stages associated with formation of the carbonate substrate, metamorphism, degassing, and the release of significant amounts of CO_2 into the atmosphere [5-7]. Phase reactions in the carbonate-silicate cycle are accompanied by isotopic reactions, and the ratios of stable isotopes ($^{18}O/^{16}O$,$^{13}C/^{12}C$), as well as "unconventional" isotopes of magnesium, calcium silicon and titanium can serve as the most important geochemical tracers [8-10] and provide an opportunity to estimate the influence of different reservoirs on the composition of gases, temperatures of processes, as well as CO_2/H_2O balance in the atmosphere, hydrosphere and gases of deep origins. Nevertheless, stable isotope data have been mostly limited to sedimentary carbonate rocks of low metamorphic degrees; the sources

of matter and conditions of calciphyre transformations within highly metamorphosed (granulite) terranes have been less studied [11, 12].

Ancient granulite terranes which are widely developed within the shields and in the crystalline basement of platforms provide important evidence on the composition and degree of transformation of the continental crust formed during early stages of the Earth history [13-15]. The Lapland-Kolvitsa Granulite Belt is a part of the Fennoscandinavian Shield, which in recent years provides a scientific testing ground for various geological models and concepts [16-18]. The Paleoproterozoic events that led to the formation of rock associations of the Lapland-Kolvitsa Belt have also been widely manifested in the adjacent tectonic structures, for example in the rocks of the Belomorian Mobile Belt [19-21].

Within the Lapland-Kolvitsa Granulite Belt among other formations, rare outcrops of calciphyres have been observed, so far with unclear origin. A general description, sporadic measurements of the chemical composition [22-24] and carbon isotope ratios [25] suggest a sedimentary precursor and possible biogenic component of some rocks of the belt, but the alternation of calciphyres with presumably metaintrusive rocks makes their assignment to metasediments doubtful. The aim of the present work is to study oxygen and carbon isotopic compositions accomplished by the phase equilibria modeling of the Porya Guba calciphyres, and to reconstruct possible protolith origins and metamorphic conditions. The results of the isotopic measurements are supplemented by new data on chemical and phase compositions of the rocks.

Methods. *The isotope composition measurements*. Standard procedures [26, 27] were used to extract CO_2 from carbonates (100 % H_3PO_4) and O_2 from silicates (the fluorination followed by the conversion to CO_2). The extraction yield (at least 98 %) was controlled by measuring the gas volume, the completeness of the conversion was checked by measuring the residual oxygen pressure. CO_2 isotope ratios were determined on the SIRA-9 mass spectrometer (VG-Isogas). The entire extraction and measurement cycle for each sample was repeated at least twice. In addition, the oxygen isotopic composition of the in-lab CO_2 standard was determined every 4-5 experiments. Calcite samples calibrated relative to the NBS-18 standard were used to control the carbonate determinations. The accepted acid fractionation factor of calcite (T = 25 °C) is 1.01049 [28]. Samples of quartz and potassium feldspar calibrated relative to NBS-28 were used to control the results of the silicate measurements. Isotopic data are given according to the conventional δ-notation relative to V-SMOW (for oxygen) and PDB (for carbon) standards: $\delta = [R_{sam}/R_{std} - 1]1000$, where R_{sam}/R_{std} is the ratio of heavy and light isotopes in the sample and the standard. The average error of the values $\delta^{18}O$ is 0.07 ‰, $\delta^{13}C$ 0.05 ‰ (1σ). Sample preparation and measurement of oxygen isotope composition were performed at the Institute of Petrology and Mineralogy (Bonn).

The fractionation of isotopes between phases A and B is quantified by the value $\alpha_{AB} = R_A/R_B = (\delta_A + 1000)/(\delta_B + 1000)$. The value α_{AB} can be obtained using so-called "β-factors", so that provided isotopic equilibrium $10^3 \ln\alpha_{AB}(T) = 1000\ln\beta_A(T) - 1000\ln\beta_B(T)$. Temperatures of the isotopic equilibrium are determined by the measured isotopic ratios of phases given the temperature dependences of the β-factors. For the purposes of the present work, $\beta(T)$ dependences in the form of the cubic polynomials determined on the basis of isotopic frequency shifts [29] have been adopted.

Calculation of phase equilibria. Phase equilibria were modeled for the system SiO_2-TiO_2-Al_2O_3-FeO-MgO-CaO-Na_2O-K_2O-H_2O-CO_2 (STAFMCNK-H_2O-CO_2) using the Perple_X (version 6.9, http://www.perplex.ethz.ch/) [30, 31] and GeoPS [32] software. For the fluid (H_2O-CO_2), the equation of state and thermodynamic database ([33], modified in 2004) have been adopted. The calculations account for the phases present in the rocks, their possible precursors and transformation products. The results of X-ray fluorescence spectrometry (Philips PW-1480 device) with an analytical error less than 3 % were taken as the input data to calculate the phase equilibria (pseudosections).

Journal of Mining Institute. 2024. Vol. 265. P. 3-15

Compositions of individual phases were determined on the JEOL JXA-8230 device (IGGD RAS) at 15 kV accelerating voltage, 20 nA electron probe current, and 10 μm beam diameter. Calcite CO_2 content was quantified after drying the sample (for 1 h at $T = 105$ °C) using value of the gas extracted during reaction with 10 % hydrochloric acid solution. Termination of the carbonate decomposition was recorded by the cessation of the gas release.

Geological background and rock composition. The metacarbonate rocks had been distinguished as part of the lower sequence of the Kolvitsa granulite zone (Ploskotundrovskaya series [22]), and are also noted at the southeastern end of the Lapland block (Salny and Tuadash tundras). The rocks are mostly observed in the Porya Guba area of the Kandalaksha Bay of the White Sea on the Medvezhy Island and the western coast of the Porya Guba, where outcrops of calciphyres are traced for 10-15 km along the strike (NW-SE). This paper presents data on the rocks from the Medvezhy Island and the Tamarkina Luda Island (West of the Porya Guba, Fig.1). Within the outcrop on the Medvezhy Island, calciphyres form interlayers (extending up to several tens of meters) with a thickness from few centimeters to 50-60 cm, alternating with mafic schists (two-pyroxene, garnet-two-pyroxene, amphibole-diopside, actinolite, scapolite-bearing, etc.), acidic granulites, and variably migmatized gneisses. In places, the schists and gneisses contain sulfide mineralization. The rocks of the interbedded calciphyres and mafic schists are characterized by boudinage and delamination structures due to the different resistance of carbonates and silicates.

Metamorphic age of the rocks from the granulite complex are estimated from 1925 Ma (the beginning of metamorphism) to 1870 Ma (its termination) [34]. The protolith formation refers to the Early Proterozoic, although there is evidence of the pre-Proterozoic (the Late Archean?) age [35].

The calciphyres are presented by medium to large-grained, gray, banded rocks, usually of granoblastic (heterogranoblastic) texture. According to the mineral composition, two main groups can be distinguished within the calciphyre layers:

• Calciphyres, dominated by calcite, monoclinic pyroxene (diopside), garnet (up to 13 vol.%), quartz (0.1-0.5 mm, 5-15 %), sometimes plagioclase (0.01-1.5 mm). Calcite occurs as large polysynthetic grains up to 2-3 mm. Large colorless segregations of diopside (0.3-2 mm, reaching 30 % of the rock volume) have been replaced by tremolite and phlogopite. Garnet poikiloblasts (up to 1 cm) are dominated by the grossular-andradite series, with a small content of pyrope and almandine. However, in rocks with the significant plagioclase content (reaching 10-15 vol.%) garnet (sometimes relic, up to 5-7 vol.%) is dominated by almandine with pyrope. Magnesite, dolomite, sometimes olivine (forsterite), titanite or ilmenite, and apatite are present as accessories (< 5 %). For the sake of brevity, this variety will be referred to as the diopside calciphyres (*di*-calciphyres).

• Calciphyres dominated by forsterite, calcite with a small amount of monoclinic pyroxene. Within some rocks idioblastic (up to a few mm) calcite segregations are found. Olivine grains (0.3-0.5 mm) are replaced by serpentine (0.2-0.3 mm). Other secondary hydroxyl-bearing minerals are also present: mainly mica, chlorite, epidote, and amphibole (actinolite-tremolite, up to 0.5 mm). It should be noted that, despite the significant MgO content in the olivine-bearing varieties of the studied calciphyres, dolomite is usually found as relics. Apatite, titanite, ilmenite, and spinel (hercinite) are observed as accessories. This variety of the carbonate-silicate rocks is further referred to as the olivine calciphyres (*ol*-calciphyres).

In addition to the mineral composition, the two calciphyre varieties differ also by the content of the major oxides (Table 1). The olivine calciphyres have significantly higher MgO/(MgO + CaO) ratio (about 0.4) if compared with the calciphyres of the first group (less than 0.1). FeO and MnO contents of the *ol*-calciphyres are slightly lower than in the *di*-calciphyres, higher alkaline contents are noted in the olivine-bearing varieties. Differences in the concentrations of other components (including CO_2, SiO_2, Al_2O_3) are insignificant.

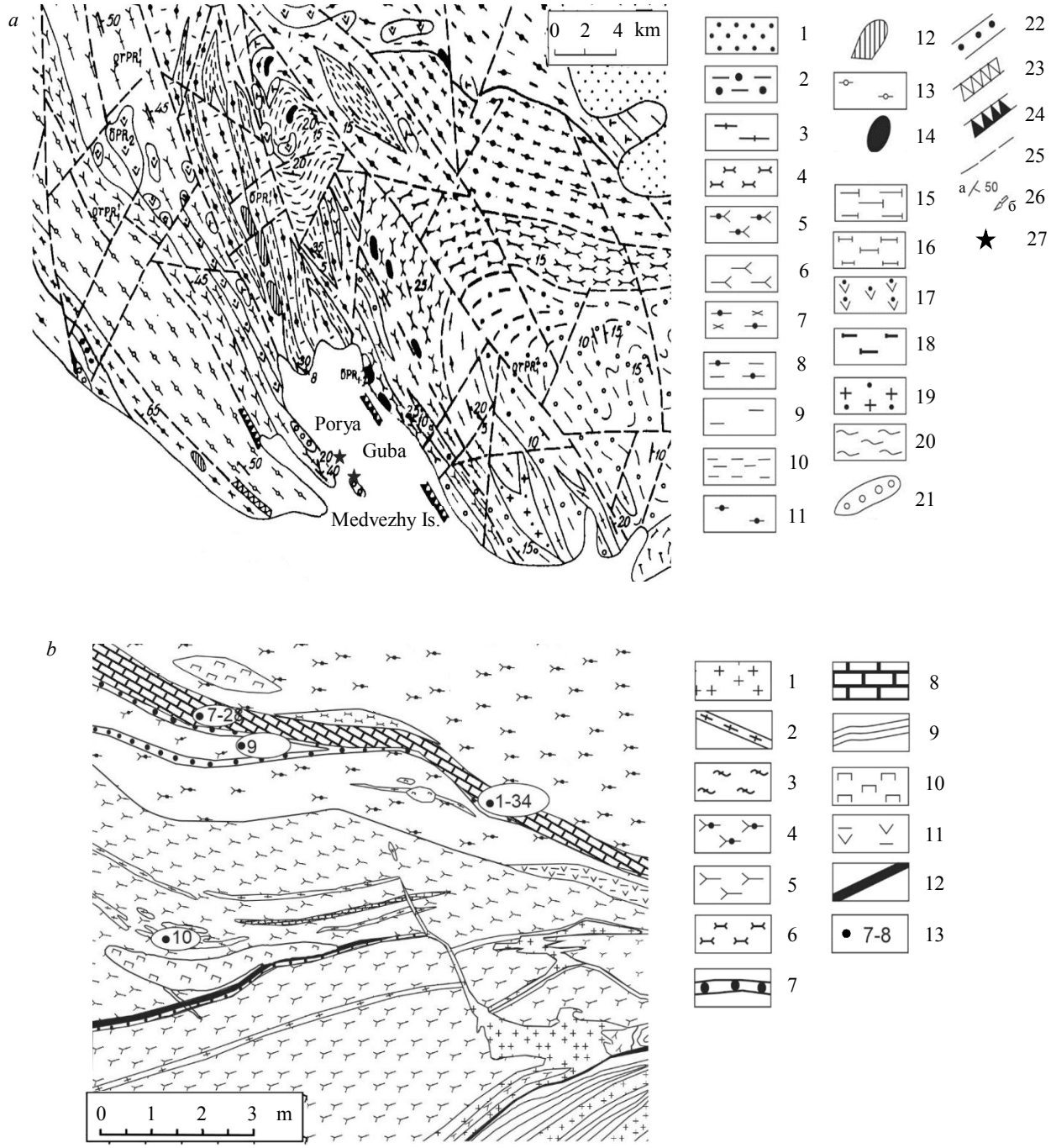

Fig.1. Geological map of the Porya Guba area (*a*) and sketch of the detailed area on the Medvezhy Island (*b*) modified after [22]:

a – Porya Guba: 1 – Quaternary sediments; 2-7 – supracrustal formations: 2 – sillimanite-granite-biotite gneisses, 3 – acidic granulites, 4 – plagioclase-orthopyroxene crystalline schists, 5 – two-pyroxene mafic schists, 6 – plagioclase-granite-pyroxene mafic schists, 7 – garnet-amphibolites; 8, 9 – gneiss complex of the granulite framing: 8 – biotite-amphibole gneisses, 9 – gneisses (unclassified); 10, 11 – diaphtorites over granulites: 10 – garnet-bearing gneisses with relict pyroxenes, 11 – garnet-pyroxene amphibolites; 12-19 – magmatic rocks: 12 – druzites (13 – plagioclasites, metagabbro-anorthosites, 14 – norites and pyroxenites, 15 – enderbites, 16 – charnockites, 17 – hornblende peridotites, 18 – unclassified ultrabasites, 19 – alkaline gneissic-granites); 20-24 – other rocks: 20 – migmatites, 21 – calciphyres, 22 – conglomerates, 23 – eruptive breccia, 24 – tectonic breccia with sulfide cement; 25 – tectonic discontinuaties; 26 – structural attitudes (a – schistocity, b – linearity); 27 – sampling sites (the Medvezhy Island and the Tamarkina Luda Island);

b – the Medvezhy Island locality: 1 – pegmatites; 2 – acidic granulites; 3 – charnockite-migmatites; 4 – amphibole-diopside plagioclase mafic schists with garnet; 5 – garnet-two-pyroxene plagioclase mafic schists; 6 – plagioclase-hyperstene mafic schists; 7 – quartzites; 8 – calciphyres; 9 – biotite gneisses with sillimanite; 10 – clinopyroxenites; 11 – actinolite schists; 12 – gabbro-diabases; 13 – sampling spots (Table 1)

Journal of Mining Institute. 2024. Vol. 265. P. 3-15

Table 1

The whole-rock composition of the calciphyres and spatially related Porya Guba mafic schists

Rock	*di*-calciphyres			*ol*-calciphyres			Mafic schists		
	Sample number								
	7	28	13	8	1	3	12	9	10
SiO_2	29.97	20.36	19.97	33.07	19.15	22.05	31.36	57.53	52.61
TiO_2	0.27	0.07	0.17	0.13	0.20	0.61	0.47	0.76	0.67
Al_2O_3	4.04	2.69	0.10	2.55	1.45	1.55	2.20	13.41	9.66
FeO	5.77	4.40	3.77	2.91	2.56	2.89	1.71	7.66	10.56
MnO	0.39	0.23	0.38	0.18	0.33	0.63	0.76	0.09	0.15
MgO	2.55	1.87	1.69	18.52	19.52	17.61	16.62	6.87	11.32
CaO	36.87	42.33	43.25	25.38	28.87	29.11	25.55	5.94	10.12
Na_2O	0.25	0.15	0.27	0.31	0.67	1.11	1.29	3.94	2.29
K_2O	0.10	0.62	0.05	0.10	0.59	0.99	0.57	1.62	0.93
P_2O_5	0.18	0.09	0.20	0.05	0.04	0.05	0.33	0.05	0.07
CO_2	19.60	25.77	28.00	16.79	20.63	20.02	17.54	–	–
LOI	–	0.29	–	0.97	4.70	3.82	0.44	2.12	1.59
Total	99.99	98.87	97.85	100.96	98.71	100.44	98.84	99.99	99.97
MgO/(MgO + CaO)	0.06	0.04	0.04	0.42	0.40	0.38	0.39	0.54	0.53

Notes: sample 13 – the Tamarkina Luda Island, others – the Medvezhy Island; LOI – loss on ignition (105 °C).

Oxygen and carbon isotopes. Measured isotopic ratios of calcite ($\delta^{18}O$ and $\delta^{13}C$ relative to SMOW and PDB, respectively) and silicates ($\delta^{18}O$) are given in Table 2. The $\delta^{18}O$ value of calcite in the calciphyres vary from 15.0 до 17.8 ‰ (the mean value at 16.44±0.92 ‰) with $\delta^{13}C$ varying from –3.6 to –6.2 ‰ (the mean at –4.90±0.89 ‰), suggesting the sedimentary nature of the rocks. At the same time, average $\delta^{18}O$ of calcite from the diopside calciphyres is 17.05 (±0.61) ‰, whereas average $\delta^{18}O$ of calcite in the olivine-bearing varieties is lower, 15.68 (±0.59) ‰. Average $\delta^{13}C$ values of calcite are –4.35 (±0.65) and –5.58 (±0.67) ‰, respectively. Calcite $\delta^{18}O$ and $\delta^{13}C$ increase following the increase of the calcite content in the rock (which is expressed for example, as a linear dependence of $\delta^{18}O_{cal} \approx 0.15CO_2 + 13.02$ wt.%, $R^2 = 0.7$). In the limit of the pure calcite rock ($CO_2 = 44$ wt.%), $\delta^{18}O_{cal}$, according to this relationship, is estimated at 19.6 ‰, which corresponds to the isotopic composition of the Precambrian diaphtorised carbonate sediments [36, 37]. Another noted pattern – the relationship $\delta^{18}O$ and $\delta^{13}C$ of calcite – may reflect metamorphic degassing of the rocks. Representative isotopic analyses of the calciphyres taken from the Tamarkina Luda Island for comparison follow the same pattern.

Temperature dependences of the stable isotope fractionations are determined based on the β-factors (the reduced partition function ratios):

$$\ln\beta = \frac{1}{N_q}\sum_{\{q\}}\left[\frac{1}{N}\sum_{i=1}^{3N_{at}}\ln\left(\frac{\nu^*_{q,i}}{\nu_{q,i}}\frac{\sinh(h\nu_{q,i}/2kT)}{\sinh(h\nu^*_{q,i}/2kT)}\right)\right],$$

where $\nu_{q,i}$ are the vibrational frequencies with the wave vector q and phonon branch index i from 1 to $3N_{at}$; N_{at} is the number of atoms in a unit cell; T temperature, K; h and k – the Planck and Boltzmann constants; N is the number of atoms undergoing isotopic substitution; N_q is the number of vectors q considered in the summation; the superscript * refers to the heavier isotope.

The β-factors (calcite, quartz, monoclinic pyroxene, olivine, and garnet) between 0 and 1500 °C are interpolated by the cubic polynomials against $x = 10^6/T^2 : 1000\ln\beta^{18}O = ax + bx^2 + cx^3$ [29]. The vibration frequencies of the isotopologues of the studied phases were determined by the frozen phonon method (CRYSTAL software: https://www.crystal.unito.it/) within the density functional theory (DFT).

Table 2

Isotopic composition of pure fraction separates

Sample number	Measured isotopic composition (δO^{18}_{SMOW}, δC^{13}_{PDB})						T, °C				F	$CO_2(i)$
	$\delta^{18}O_{cal}$	$\delta^{13}C_{cal}$	$\delta^{18}O_{qtz}$	$\delta^{18}O_{cpx}$	$\delta^{18}O_{ol}$	$\delta^{18}O_{oth}$	*qtz-cal*	*ol-cal*	*cpx-cal*	Others		
di-calciphyres												
7	16.50	–4.62	17.14	13.10	–	14.47_{grt}	990	–	620	$856_{grt\text{-}qtz}$	0.70	27.96
28	17.54	–4.20	18.07	–	–	–	1110	–	–	–	0.90	28.54
13	17.78	–3.57	19.85	16.45	–	16.32_{grt}	430	–	810	$701_{grt\text{-}qtz}$	0.96	29.25
21	16.41	–5.31	17.85	–	–	–	570	–	–	–	0.69	39.69
34	17.03	–4.05	17.65	–	–	–	1010	–	–	–	0.80	38.24
ol-calciphyres												
8	15.02	–6.06	–	–	12.04	–	–	520	–	–	0.49	34.35
1	16.31	–5.32	–	–	12.51	–	–	410	–	–	0.67	30.82
3	16.03	–4.76	–	–	14.75	–	–	990	–	–	0.63	32.02
Mafic schists												
12	15.37	–6.18	–	–	12.07	–	–	470	–	–	0.53	32.95
9	–	–	–	12.11	–	13.42_{pl}	–	–	–	$670_{pl\text{-}cpx}$	–	–
10	–	–	–	11.60	–	13.38_{pl}	–	–	–	$480_{pl\text{-}cpx}$	–	–
Coefficients of temperature dependence of the β-factors												
	$\beta^{18}O_{cal}$	–	$\beta^{18}O_{qtz}$	$\beta^{18}O_{cpx}$	$\beta^{18}O_{ol}$	$\beta^{18}O_{pl}$	–	–	–	–	–	$\beta^{18}O_{CO_2}$
a	11.6603	–	12.6764	10.0399	9.50807	11.478	–	–	–	–	–	15.1896
b	–0.3544	–	–0.3543	–0.205	–0.1654	–0.457	–	–	–	–	–	–0.7068
c	0.00908	–	0.00841	0.00401	0.0018	0.0077	–	–	–	–	–	0.0206

Notes: F – fraction of CO_2, remaining in calcite after degassing; $CO_2(i)$ – CO_2 content in a rock prior to degassing (see Table 1). For samples 21, 34 the measured CO_2 concentrations are 27.22 and 30.50, respectively.

The value of $\delta^{18}O$ within the silicate fraction of the calciphyres (quartz, pyroxene, olivine, garnet, Table 2) depends both on the isotopic composition of the carbonate fraction (the higher $\delta^{18}O_{cal}$, generally the higher $\delta^{18}O$ of each particular phase), and the $^{18}O/^{16}O$ fractionation between different phases depending on temperature. $\delta^{18}O$ variation of quartz in the *di*-calciphyres is 17.1-19.9 ‰, pyroxene 13.1-16.5 ‰. $\delta^{18}O$ values of olivine from the *ol*-calciphyres vary between 12.0 and 14.8 ‰. Generally, the decrease of $\delta^{18}O$ values occurs in the sequence quartz-calcite-(garnet-pyroxene). The lack of equilibrium between minerals is indicated by the large scatter of temperatures calculated from the distribution of isotopes between different phases of each particular sample (Table 2). For example, temperatures calculated using the quartz-calcite isotope geothermometer vary from 430 °C (sample 13) to 990 °C (sample 7) and 1110 °C (sample 34), calcite-clinopyroxene from 620 to 810 °C (on two samples).

Within rocks without carbonates, both at contacts with calciphyres and at some distance (5-10 m) the evolved $\delta^{18}O$ (reaching 11.6-13.5 ‰ for pyroxene and plagioclase) is also observed.

Revealing primary composition of metamorphic rocks. The oxygen and carbon isotopic ratios imply primary sedimentary nature of the Porya Guba calciphyres and possibly, of the entire rock sequence studied (NW coast of the Porya Guba). Hence, the phase compositions of primary sediments were reconstructed based on the rock chemistry. Using the Perple_X program (see the methods), the restored ("model") phase composition of rocks in the conditions of the sedimentation (25 °C, 1 bar) was calculated (Table 3).

Sediments chemically corresponding to the *di*-calciphyres contained 70-85 wt.% of the carbonate fraction dominated by calcite (reaching 78 %), with subordinate amounts of dolomite (up to 10 %) and ankerite (up to 15 %). The clastic component includes quartz (reaching 22 wt.%), while kaolin dominates in the clay fraction (up to 9 wt.%). The detrital component (rutile and titanite) content is estimated at 0.1-0.2 %. The primary composition of sediments transformed into the *ol*-calciphyres (mostly forsterite) was characterized by significant amount of dolomite within carbonate fraction (up to 62 wt.%) together with ankerite (up to 8 %), siderite (up to 4 %), and magnesite (less than 1 %). Calcite content did not exceed 35 wt.%.

Journal of Mining Institute. 2024. Vol. 265. P. 3-15

Table 3

Reconstructed composition of rocks in the conditions of sedimentation, wt.%

Rock	Sample number								
	di-calciphyres			*ol*-calciphyres				Mafic schists	
	7	28	13	8	1	3	12	9	10
Carbonate component									
Calcite	44.3	74.4	78.0	–	35.1	32.4	20.4	–	5.3
Dolomite	10.0	–	–	61.7	24.9	20.5	33.1	15.4	2.0
Siderite	–	–	–	3.5	–	–	–	9.7	–
Magnesite	–	–	–	0.4	–	–	–	4.3	–
Ankerite	14.9	–	5.5	–	7.2	7.9	4.6	–	3.3
Carbonate total	69.3	74.4	83.5	65.6	67.2	60.8	58.1	29.4	10.6
Clastic component									
Quartz	21.7	0.3	14.6	22.2	–	–	9.2	43.3	5.8
Rutile	0.2	–	0.2	0.1	–	0.6	0.4	0.6	–
Clinopyroxene	–	4.8	–	–	–	–	–	–	–
Titanite	–	0.2	–	–	–	–	–	–	1.5
Zeolites	–	18.3	–	–	–	–	–	–	–
Ilmenite	–	–	–	–	0.4	–	–	–	–
Clastic total	21.9	23.6	14.9	22.3	0.4	0.6	9.6	43.9	7.3
Clay fraction, amphibole, mica, other phyllosilicates									
Kaolinite	8.8	–	0.8	4.8	–	–	–	26.7	–
Talc	–	–	–	–	–	1.9	5.3	–	–
Glaucophane	–	–	–	–	–	3.3	10.8	–	26.7
Chlorite	–	2.0	0.8	–	–	–	–	–	2.9
Mica	–	–	–	7.4	–	2.1	–	–	7.3
Serpentine	–	–	–	–	20.3	10.3	–	–	–
Stylpnomelan	–	–	–	–	12.1	21.0	16.2	–	–
Chloritoid	–	–	–	–	–	–	–	–	10.2
Actinolite	–	–	–	–	–	–	–	–	35.0
Total fraction	8.8	2.0	1.6	12.1	32.4	38.6	32.3	26.7	82.1

Notes. Composition calculated from data in Table 1 at ambient conditions $T = 298.15$ °C, $P = 1$ bar (Werami module of the Perple_X software [30]). CO_2 content calculated from the measured composition accounting the degree of degassing F and given at Table 2; in the absence of the respective data, calculations were performed under conditions of the volatile saturation ($H_2O > 5$ %).

Sedimentary rocks currently represented by mafic schists, contained less than 30 wt.% carbonates (as reconstructed with CO_2 excess), and probably were dominated either by the clastic components (up to 43 % quartz, sample 9) or the clay components (sample 10). Oxygen isotopic variations of the sediments in interaction with seawater at 25 °C are estimated at 31.8±2.3 ‰ (probable oxygen isotopic composition prior to the sediments lithification).

Metamorphic phase equilibria of the calciphyres. Phase equilibrium diagrams with the stability fields of phase associations in *P-T* coordinates (pseudosections) were constructed accounting for chemical composition of representative samples of the diopside calciphyres from the Medvezhy and the Tamarkina Luda islands, the olivine calciphyres, and garnet-pyroxene plagioclase schists (see Table 1). The pseudosections constrain *P-T* conditions of phase transformations and in particular, probable temperatures of fluid component releases, which is essential when evaluating isotopic composition of rocks. Close spatial relations of the studied rocks imply similar *P-T* conditions of metamorphism, which should correspond to the intersection of the stability fields observed in different mineral associations of the samples. For clarity, the results of pseudosection modeling are presented without considering components presented in insignificant amounts (Fig.2).

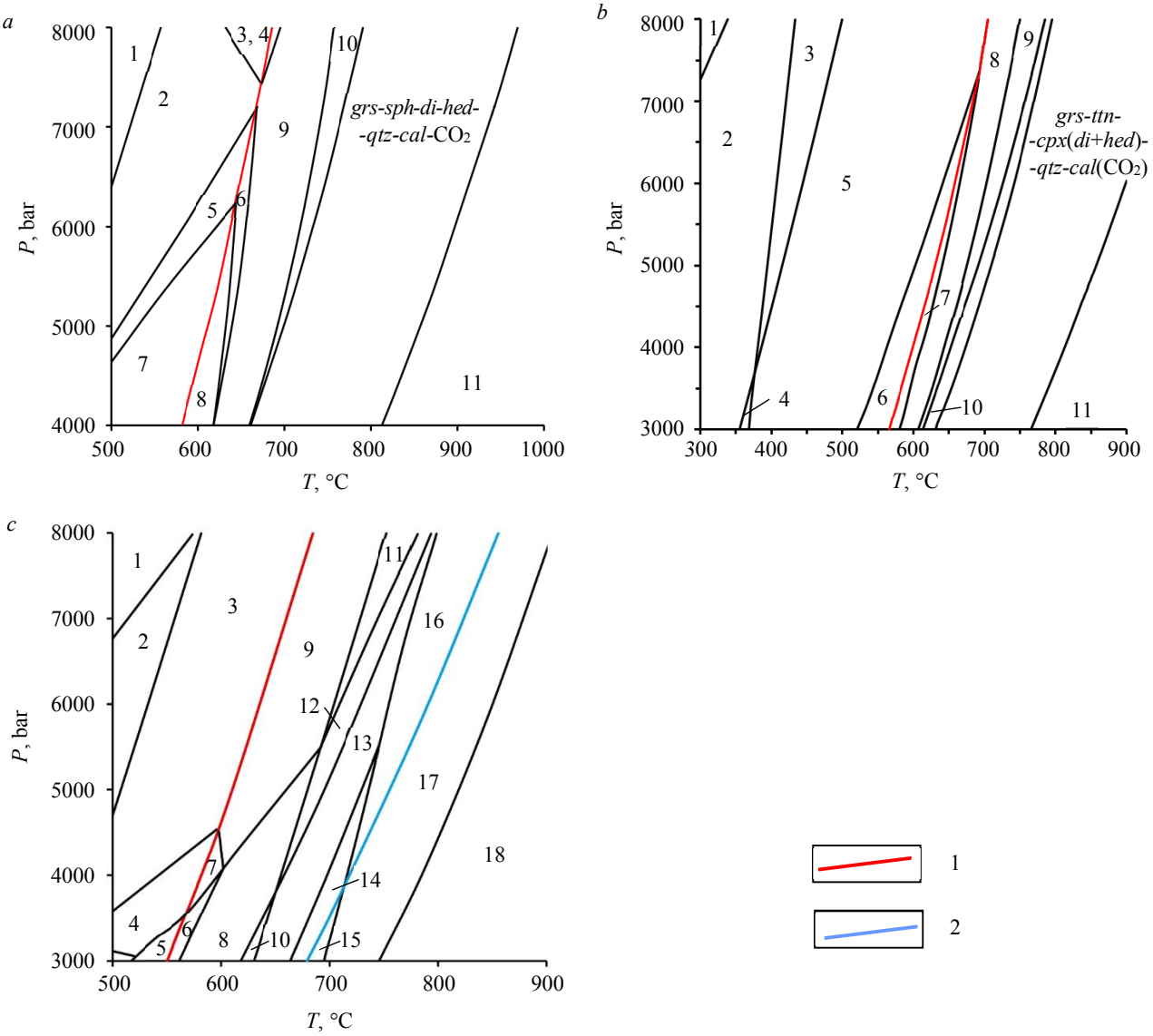

Fig.2. Phase *P-T*-diagrams (pseudosections) constructed from the analysis of the representative Porya Guba calciphyres:

a: sample 7. Anhydrous projection. Stable phases: 1 – *alm-grs-ttn-di-qtz-cal-dol*; 2 – *alm-ttn-di-qtz-hc-cal-dol*; 3 – *alm-ttn-di-qtz-spr-cal-dol*; 4 – *alm-ttn-di-qtz-spr-cal*-CO_2; 5 – *alm-di-qtz-ilm-hc-cal-dol*; 6 – *alm-di-qtz-ilm-hc-cal*-CO_2; 7 – *alm-crd-di-qtz-ilm-cal-dol*; 8 – *alm-crd-di-qtz-ilm-cal*-CO_2; 9 – *alm-ttn-di-qtz-hc-cal*-CO_2; 10 – *alm-grs-ttn-di-qtz-cal*-CO_2; 11 – *grs-ttn-di-hed-wo-cal*-CO_2;

b: sample 13. Anhydrous projection. Stable phases: 1 – *grs-ttn-di-hed-qtz-arg-ank*; 2 – *grs-ttn-di-hed-qtz-cal-ank*; 3 – *alm-ttn-di-hed-qtz-cal-ank*; 4 – *grs-ilm-di-hed-qtz-cal-ank*; 5 – *alm-ilm-di-hed-qtz-cal-ank*; 6 – *alm-ilm-di-fa-qtz-cal-ank*; 7 – *alm-ilm-di-fa-qtz-cal*-CO_2; 8 – *alm-ilm-di-hed-qtz-cal*-CO_2; 9 – *alm-ttn-di-hed-qtz-cal*-CO_2; 10 – *sil-ttn-di-hed-qtz-cal*-CO_2; 11 – *grs-ttn-di-hed-wo-cal*-CO_2;

c: sample 8. Projection including H_2O. Stable phases: 1 – *alm-ky-di-tr-qtz-ilm-mgs-dol*; 2 – *alm-an-di-tr-qtz-ilm-mgs-dol*; 3 – *alm-en-di-tr-an-qtz-ilm-dol*; 4 – *alm-en-di-act-an-qtz-ilm-dol*; 5 – *fa-en-di-an-qtz-ilm-dol-act*; 6 – *fa-en-di-an-ilm-dol*-CO_2-*act*; 7 – *alm-en-di-an-ilm-dol*-CO_2-*act*; 8 – *fa-en-di-tr-an-ilm-dol*-CO_2; 9 – *alm-en-di-tr-an-ilm-dol*-CO_2; 10 – *fo-fa-di-tr-an-ilm-dol*-CO_2; 11 – *alm-en-di-tr-ilm-hc-dol*-CO_2; 12 – *fa-en-di-tr-ilm-hc-dol*-CO_2; 13 – *fo-fa-di-tr-ilm-hc-dol*-CO_2; 14 – *fo-fa-di-clin-ilm-hc-dol*-CO_2; 15 – *fo-fa-di-clin-ilm-hc-cal*-CO_2; 16 – *fo-fa-di-ilm-hc-dol*-H_2O-CO_2; 17 (observed association) – *fo-fa-di-ilm-hc-cal*-H_2O-CO_2; 18 – *fo-fa-di-hc-usp-cal*-H_2O-CO_2

Phase abbreviations. Carbonates: *ank* – ankerite; *cal* – calcite; *dol* – dolomite; *mgs* – magnesite; *sid* – siderite; *arg* – aragonite. Silicates: *qtz* – quartz; *ol* – olivine (*fo* – forsterite, *fa* – fayalite); *cpx* – monoclinic pyroxene (*di* – diopside, *hed* – hedenbergite); *opx* – rhombic pyroxene (*en* – enstatite, *hyp* – hypersten); *grt* – garnet (*alm* – almandine, *grs* – grossular); *pl* – plagioclase (*an* – anorthite); *spr* – sapphirin; *crd* – cordierite; *sil* – sillimanite; *ky* – kyanite; *wo* – wollastonite; *amp* – amphibole (*act* – actinolite, *gl* – glaucophane, *hrn* – hornblende, *tr* – tremolite); mica (*bt* – biotite, *mu* – muscovite, *phl* – phlogopite); oxides: *spl* – spinel (*hc* – hercinite, *usp* – ulvospinel); *rt* – rutile; *ttn* – titanite; *ilm* – ilmenite

1 – lines of monovariant equilibria limiting the appearance of CO_2; 2 – lines limiting calcite appearance

Journal of Mining Institute. 2024. Vol. 265. P. 3-15

Decarbonatization reactions that accompany phase transformations of all the calciphyres studied deserve special attention to explain the change in the isotopic composition of rocks, because these reactions cause isotopic fractionation of both oxygen and carbon; the isotopic fractionation factors between CO_2 and solid phases are significant even at elevated temperatures; large volume increase associated with the formation of fluid components causes complete or partial removal of CO_2.

Considering the *di*-calciphyres, CO_2 release is caused by the decomposition reactions of dolomite or ankerite, which becomes unstable as temperature increases:

$$CaMg(CO_3)_2(dol) + SiO_2 = CaCO_3(cal) + MgSiO_3(cpx) + CO_2; \quad (1)$$

$$CaMg(CO_3)_2(dol) + 2SiO_2 = > CaMgSiO_3(cpx) + 2CO_2. \quad (2)$$

If carbonates with iron (ankerite, sample 13) prevail in the source rock at low temperatures, carbon dioxide is released for example, by the reaction

$$CaFe(CO_3)_2\ (sid) + SiO_2 = CaCO_3(cal) + FeSiO_3(cpx) + CO_2. \quad (3)$$

The source of silica can be quartz as well as other silicates including:

$$CaMg(CO_3)_2(dol) + Fe_3Al_2(SiO_4)_3(alm) =$$
$$= CaCO_3(cal) + 2FeSiO_3(cpx) + MgSiO_3(cpx) + FeAl_2O_4(spl) + CO_2; \quad (4)$$

$$3CaMg(CO_3)_2(dol) + CaMg(SiO_3)_2(di) = 4CaCO_3(cal) + 2Mg_2SiO_4(fo) + 2CO_2. \quad (5)$$

In the *di*-calciphyres of the Medvezhy Island (sample 7) at pressures below 6 kbar, the decarbonatization reactions start within the range of 580-630 °C (Fig.2, *a*, red lines). The simplified anhydrous projection of the system is shown for clarity. At higher pressures, the onset temperature of CO_2 release also rises (e.g., if $P = 8$ kbar, the onset of CO_2 release shifts to $T \approx 700$ °C). By the sequence of phase reactions, primary sediments (see Table 1) transform into the observed *grs-ttn-di-hed-qtz-cal* association which at 8 kbar is stable from 790 to 970 °C (at another pressure the stability field shifts by about 30 °C/kbar). At lower temperatures, hedenbergite is stable rather than almandine and at higher temperatures, wollastonite appears instead of quartz.

Association of the *di*-calciphyres from the Tamarkina Luda Island (sample 13) is *cal-cpx*(*di* + *hed*)-*-grt*(*grs*)-*qtz-ttn*. The onset of decarbonatization at a reduced pressure is possible from 560 °C ($P = 3$ kbar). At higher pressures, the temperature of CO_2 release increases to 705 °C ($P = 8$ kbar), with an estimated $\partial T/\partial P$ gradient of approximately 29 °C/kbar (Fig.2, *b*). Similar to the Medvezhy Island diopside calciphyres (sample 7), the stability field of the observed *grs-ttn-cpx-qtz-cal* association with increasing temperature is limited by the association with wollastonite instead of quartz. It is noteworthy that for these rocks, carbonates which are stable up to temperatures of approximately 570-650 °C consist of calcite and ankerite rather than dolomite (as in sample 7) and accordingly, decarbonatization is caused by the decomposition of ankerite by a reaction similar to (3).

The *ol*-calciphyres (sample 8, Fig.2, *c*). The observed *fo-fa-di-ilm-hc-cal* association remains in equilibrium with the fluid components ($H_2O + CO_2$) starting from 690 °C at 3 kbar or 860 °C at 8 kbar; the upper stability boundary is 750 to 905 °C, respectively. The lower-temperature association includes dolomite, relics of which are observed in thin sections; in the higher-temperature association *fo-fa-di-usp-hc-cal*-(H_2O-CO_2) ulvospinel is formed at the expense of ilmenite. It should be noted that, in contrast to diopside calciphyres, the beginning of decarbonatization (marked by red line in Fig.2, *c*) does not lead to the total breakdown of dolomite, and calcite becomes stable only from 680 °C (3 kbar) to 860 °C (8 kbar), which coincides with the lower temperature limit at which the observed association remains stable (Fig.2, *c*, blue line).

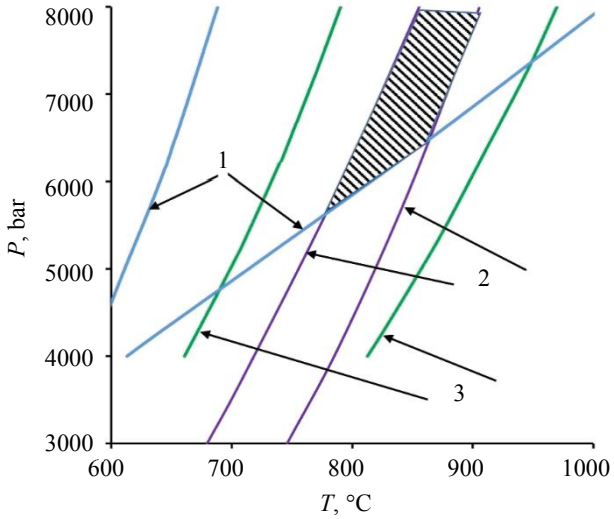

Fig.3. Stability fields of mineral associations of the calciphyres and mafic schists. The intersection area of all observed associations is shaded

1 – *grt-px*-schists; 2 – *ol*-calciphyres; 3 – *di*-calciphyres

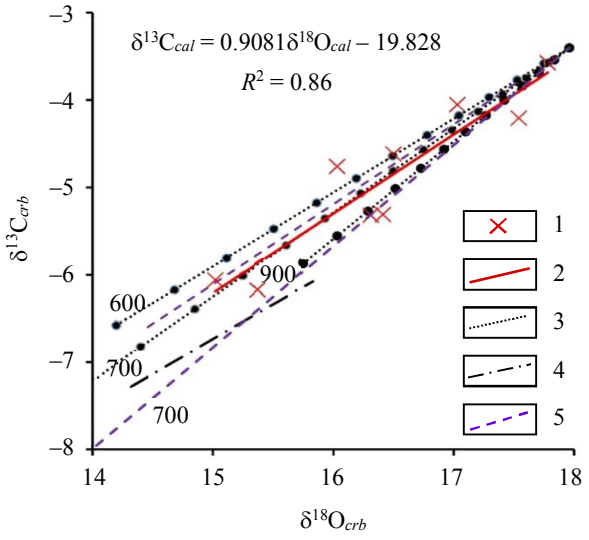

Fig.4. Isotopic ratios $^{18}O/^{16}O$ and $^{13}C/^{12}C$ of calcite from the Porya Guba calciphyres

1 – data points; 2 – linear array, plotted according to the results of isotopic analysis; 3 – calculated according to equation (6) for isotopic fractionations (the values of the oxygen fractionation factor $\alpha^{18/16}$ *cal*-CO_2 given T = 600, 700 and 900 °C are estimated at 1.00411, 1.00311 and 1.00242, respectively; $\alpha^{18/16}$ *dol*-CO_2 – 1.00303, 1.0025, 1.0018, respectively [29]; the carbon fractionation factor $\alpha^{13/12}$ *cal*-CO_2 at the given T are 1.0035, 1.0033, 1.0027; $\alpha^{13/12}$ *dol*-CO_2 – 1.00306, 1.0029, 1.00246 [29]); 4 – calculated provided isotopic equilibrium of CO_2 with carbonates and silicates at 600 °C; 5 – calculated provided isotopic equilibrium of CO_2 with dolomite at T = 500, 700 °C

All the observed mineral associations are stable within *PT*-conditions determined by the intersection of the equilibrium fields for different rocks (Fig.3). At the minimum possible pressures (5.5-6 kbar), the temperature limiting the stability of all associations is 740-870 °C. If the metamorphic pressure is higher, temperature estimates increase ($dT/dP \approx$ 30-40 °C/kbar), and at P = 8 kbar the temperature interval at which all the observed associations can coexist is 860-910 °C.

Discussion. *Evolution of the isotope composition during metamorphism.* A significant correlation between $\delta^{13}C$ and $\delta^{18}O$ values of calcite (R^2 = 0.86; Fig.3) is generally observed (within samples composing all varieties of the studied calciphyres). The reactions of CO_2 release characterizing metamorphic transformations of the calciphyre precursors are accompanied by fractionation of oxygen and carbon isotopes with the restite (solid phase residue after gas extraction) depletion in the heavy isotope (1000lnα between CO_2 and carbonates and (or) silicates is always greater than zero for the equilibrium oxygen isotope fractionation, and for temperature above ca. 150-200 °C for the carbon isotope fractionation also [29]). Provided constant volume, continuous removal of the released CO_2 from the system is likely, so that the change in the isotopic composition of the solid phases can be evaluated with equation of the Rayleigh's distillation, the latter expressed by the relation [38] for isotope fractionation:

$$\delta_r^f - \delta_r^i = 1000(F^{(\alpha-1)} - 1), \qquad (6)$$

where F stands for the mole fraction of an element remaining in the restite after gas extraction; δ expresses the isotopic ratio of an element (oxygen, carbon) in a solid; α is the isotopic fractionation factor between fluid and solid phases: $(^{18}O/^{16}O)$fluid/$(^{18}O/^{16}O)$restite; f and i denote values after gas release and before gas release, respectively.

The linear array expressing simultaneous changes of oxygen and carbon isotopic ratios agrees with the analytical dependence of $\delta^{13}C_{cal}$ and $\delta^{18}O_{cal}$ (Fig.4), provided that the isotopic equilibrium of CO_2 and the produced carbonate (calcite and (or) dolomite) was maintained during degassing, isotopic reactions of CO_2 with carbonates were hardly accompanied by isotopic reactions with silicates. The latter assumption can be justified by the disagreement of the calculated array considering isotopic equilibrium involving silicates with the analytical data (dashed line in Fig.4).

Journal of Mining Institute. 2024. Vol. 265. P. 3-15

In addition, the measured distribution of oxygen isotopes between calcite and silicates (see Table 2) significantly deviates from the equilibrium distribution. In the absence of the isotope equilibrium with silicates, values of F for oxygen and carbon coincide ($F_C = F_O$ [39]). The *cal*-CO_2 isotope fractionation in the latter case corresponds to 700 °C, which is wholly endorsed by the estimates of decarbonatization temperatures obtained from phase relations modeling (with the construction of P-T pseudosections).

The averaged dependence combines analytical data over all samples, including the diopside and olivine calciphyres. Some deviations of the analytical points can be caused by fluctuation of the fractionation values (variations of the decarbonatization temperature, changes of the composition of carbonates in equilibrium with CO_2 of the olivine calciphyres). In particular, however, the measured variations of $\delta^{18}O$ and $\delta^{13}C$ reflect the degree of distillation F of equation (6) provided the same isotopic composition of carbonate at the initial stage of distillation (F = 1, the beginning of CO_2 release) and similar degassing temperature (at T = 700 °C the values of $\delta^{18}O_{cal}$ = 17.96 and $\delta^{13}C_{cal}$ = –3.4 ‰ closely follow the analytical data).

Depleted $\delta^{18}O$ values of calcite from the *ol*-calciphyres relative to $\delta^{18}O$ of calcite from the *di*-calciphyres with a general trend $\delta^{18}O$ vs $\delta^{13}C$ can be interpreted as a result of larger degassing degree of the former. Thus, maximum values of $\delta^{18}O_{cal}$ = 17.78 and $\delta^{13}C_{cal}$ = –3.57 ‰ (sample 13) reflect initial stages of the distillation (F = 0.96), whereas minimum values of $\delta^{18}O_{cal}$ = 15.02 and $\delta^{13}C_{cal}$ = –6.06 ‰ (sample 8) correspond to more advanced distillation (F = 0.5). The results are consistent with the process of decarbonatization with decomposition of dolomite (or Fe-carbonate, sample 13) producing calcite (see Fig.2, *b*) due to a series of sequential reactions with removal of the released CO_2. Temperature of the degassing obtained from the isotopic analysis is supported by the phase modeling (T = 700 °C at $P \approx$ 8 kbar).

Close agreement of the analytical data in the $\delta^{13}C$ vs $\delta^{18}O$ diagram with the Rayleigh distillation model suggests that the isotopic composition of the removed CO_2 and the remaining carbonate was controlled by the equilibrium exchange between the remaining carbonate (calcite) after carbon dioxide extraction and the continuously removed gas. The process occurred without isotopic exchange with silicates. Isotopic composition of the produced CO_2 in equilibrium with calcite vary depending on the degree of degassing, from $\delta^{18}O$ = 21.9 and $\delta^{13}C$ = –1.0 ‰ ($F \approx 1$) up to 18.9 and –3.7 ‰ ($F \approx 0.5$), respectively. The integrated (batch) isotopic composition of the resulting CO_2 falls between these values and is determined by the material balance relations. In case of insignificant change of the fractionation during decarbonatization, the isotopic composition of all formed CO_2 is estimated at $\delta^{18}O$ =19.9 and $\delta^{13}C$ = –2.2 ‰ (F = 0.5).

Equilibrium of the released gas with calcite without silicates [40] does not restrict F by the so-called calc-silicate limit (F = 0.6 [38]), and the minimum values of the measured isotope ratios correspond to degassing degree at about 0.5 (the *ol*-calciphyres).

Conclusion. The results of oxygen and carbon isotope analysis indicate that the Porya Guba calciphyres and the intercalated mafic schists with the evolved $\delta^{18}O$ and $\delta^{13}C$ resulted from metamorphism of sedimentary rocks (limestones, marls, and graywackes). Lithochemical reconstructions suggest marly sediments as the precursors for the carbonate-silicate rocks, while chemical composition of the former varied depending on the ratio of clay, carbonate, and clastic components. Carbonates comprise 58-84 wt.% (in the sediment precursors of the calciphyres) and 10-30 wt.% (in the possible protoliths of the mafic schists). The isotopic composition of the sediments ($\delta^{18}O$ 17.9 ‰ SMOW and $\delta^{13}C$ –3.4 ‰ PDB) lies within the values typical for the Precambrian diagenetically transformed sedimentary carbonates [36, 37, 41] without any influence of both organic carbon [25] and carbon of the magmatic origin [42].

The most significant shifts in the isotopic composition during metamorphism of the rocks are due to the sequence of reactions producing CO_2 following decomposition of dolomite or other carbonates (siderite, ankerite), which become unstable when temperature rises to 700 °C

($P \approx 8$ kbar) and are replaced by magnesium/iron silicates (e.g., monoclinic pyroxene, garnet). The degassing was accompanied by the simultaneous reduction of the calcite $\delta^{18}O$ and $\delta^{13}C$ as a result of the isotopic fractionation (accompanied by the Rayleigh distillation) yielding values of 15.0 and –6.2 ‰, respectively (half of the initial CO_2 removed) and producing the linear relationship $\delta^{18}O$ vs $\delta^{13}C$. The isotopic composition of the carbon dioxide released (and possibly added to the atmosphere) is estimated at 20 ‰ (SMOW) and –2 ‰ (PDB).

The shift of the calcite isotopic composition thus reflects different degrees of degassing, which in turn, depends on the composition of the parent rocks. For example, the more dolomite prior to metamorphism contained in a sedimentary rock, the higher the degree of degassing. In the olivine calciphyres (MgO up to 20 wt.%), $\delta^{18}O$ and $\delta^{13}C$ are generally lower than in the diopside calciphyres. At the same time, variations in the isotopic composition of calcite of the interbedded rocks are consistent with the internal (local) control of the emitting fluid [40] and contradict the large-scale interaction with any external (deep or surface) reservoir. Among other things, our results are not consistent with the possibility of mixing (assimilation) of the studied carbonate rocks with magmatic rocks and/or metasomatic transformations during the skarn formation.

It can be noted that at metamorphic temperatures below 650-700 °C dolomite remains stable and the observed dolomite calciphyres of the Kolvitsa granulite zone [24], chemically similar to the olivine calciphyres considered in the present work, might be the “precursors” of olivine calciphyres at lower peak metamorphic temperatures.

REFERENCES

1. Berner R.A., Lasaga A.C., Garrels R.M. The carbonate-silicate geochemical cycle and its effect on atmospheric carbon dioxide over the past 100 million years. *American Journal of Science*. 1983. Vol. 283. Iss. 7, p. 641-683. DOI: 10.2475/ajs.283.7.641

2. Groppo C., Rolfo F., Castelli D., Connolly J.A.D. Metamorphic CO_2 production from calc-silicate rocks via garnet-forming reactions in the CFAS-H_2O-CO_2 system. *Contributions to Mineralogy and Petrology*. 2013. Vol. 166, p. 1655-1675. DOI: 10.1007/s00410-013-0947-5

3. Catling D.C., Kasting J.F. Atmospheric Evolution on Inhabited and Lifeless Worlds. Cambridge: Cambridge University Press, 2017, p. 579. DOI: 10.1017/9781139020558

4. Sorokhtin N.O., Nikiforov S.L., Kozlov N.Ye. Crust-mantle branch of the global carbon cycle and origin of deep-seated hydrocarbons. *Vestnik of MSTU*. 2018. Vol. 21. N 1, p. 61-79 (in Russian). DOI: 10.21443/1560-9278-2018-21-1-61-79

5. Brovarone A.V., Tumiati S., Piccoli F. et al. Fluid-mediated selective dissolution of subducting carbonaceous material: Implications for carbon recycling and fluid fluxes at forearc depths. *Chemical Geology*. 2020. Vol. 549. N 119682. DOI: 10.1016/j.chemgeo.2020.119682

6. Deep Carbon: Past to present / Ed. by Orcutt B.N., Daniel I., Dasgupta R. Cambridge: Cambridge University Press, 2020, p. 669. DOI: 10.1017/9781108677950

7. Stagno V. Carbon, carbides, carbonates and carbonatitic melts in the Earth’s interior. *Journal of the Geological Society*. 2019. Vol. 176. Iss. 2, p. 375-387. DOI: 10.1144/jgs2018-095

8. Skublov S.G., Rumyantseva N.A., Qiuli Li et al. Zircon xenocrysts from the Shaka Ridge record ancient continental crust: New U-Pb geochronological and oxygen isotopic data. *Journal of Earth Science*. 2022. Vol. 33. N 1, p. 5-16. DOI: 10.1007/s12583-021-1422-2

9. Levashova E.V., Skublov S.G., Oitseva. T.A. et al. First Age and Geochemical Data on Zircon from Riebeckite Granites of the Verkhnee Espe Rare Earth-Rare Metal Deposit, East Kazakhstan. *Geochemistry International*. 2022. Vol. 60. N 1, p. 3-18. DOI: 10.31857/S0016752522010083

10. Rumyantseva N.A., Skublov S.G., Vanshtein B.G. et al. Zircon from Gabbroids of the Shaka Ridge (South Atlantic): U-Pb Age, Oxygen Isotope Ratios and Trace Element Composition. *Proceedings of the Russian Mineralogical Society*. 2022. S. CLI. N 1, p. 44-73 (in Russian). DOI: 10.31857/S0869605522010099

11. Satish-Kumar M., Miyamoto T., Hermann J. et al. Pre-metamorphic carbon, oxygen and strontium isotope signature of high-grade marbles from the Lützow-Holm Complex, East Antarctica: apparent age constraints of carbonate deposition. *Geological Society, London, Special Publications*. 2008. Vol. 308. Iss. 1, p. 147-164. DOI: 10.1144/SP308.7

12. Thaworndumrongsakul P., Booth J., Nantasin P., Kim Y. Metamorphic Evolution of Calc-silicate Body Enclosed in Charnockitic Gneiss at West Ongul Island, Lützow-Holm Complex, East Antarctica. *IOP Conference Series: Earth and Environmental Science*. 2021. Vol. 837. N 012015. DOI: 10.1088/1755-1315/837/1/012015

13. Jacobs J., Mikhalsky E., Henjes-Kunst F. et al. Neoproterozoic geodynamic evolution of easternmost Kalahari: Constraints from U-Pb-Hf-O zircon, Sm-Nd isotope and geochemical data from the Schirmacher Oasis, East Antarctica. *Precambrian Research*. 2020. Vol. 342. N 105553. DOI: 10.1016/j.precamres.2019.105553

14. Gusev N.I., Sergeeva L.Yu., Larionov A.N., Skublov S.G. Relics of the eoarchean continental crust of the Anabar shield, Siberian craton. *Petrology*. 2020. Vol. 28. N 2, p. 115-138. DOI: 10.31857/S086959032002003X

15. Gusev N.I., Sergeeva L.Yu., Skublov S.G. Evidence of subduction of the paleoproterozoic oceanic crust in the Khapchan belt of the Anabar shield, Siberian craton. *Petrology.* 2021. Vol. 29. N 2, p. 115-135. DOI: 10.31857/S0869590321020047

16. Il'chenko V.L., Afanasieva E.N., Kaulina T.V. et al. Litsa Uranium ore occurrence (Arctic zone of the Fennoscandian Shield): new results of petrophysical and geochemical studies. *Journal of Mining Institute.* 2022. Vol. 255, p. 393-404. DOI: 10.31897/PMI.2022.44

17. Kudryashov N.M., Udoratina O.V., Kalinin A.A. et al. U-Pb (SHRIMP-RG) age of zircon from rare-metal (Li, Cs) pegmatites of the Okhmylk deposit of the Kolmozero-Voron'ya greenstone belt (northeast of the Fennoscandian shield). *Journal of Mining Institute.* 2022. Vol. 255, p. 448-454. DOI: 10.31897/PMI.2022.41

18. Smolkin V.F., Mokrushin A.V., Bayanova T.B. et al. Magma feeding paleochannel in the Monchegorsk ore region: geochemistry, isotope U-Pb and Sm-Ndanalysis (Kola region, Russia). *Journal of Mining Institute.* 2022. Vol. 255, p. 405-418. DOI: 10.31897/PMI.2022.48

19. Salimgaraeva L.I., Skublov S.G., Berezin A.V., Galankina O.L. Fahlbands of the Keret archipelago, White Sea: the composition of rocks and minerals, ore mineralization. *Journal of Mining Institute.* 2020. Vol. 245, p. 513-521. DOI: 10.31897/ PMI.2020.5.2

20. Melnik A.E., Skublov S.G., Rubatto D. et al. Garnet and zircon geochronology of the Paleoproterozoic Kuru-Vaara eclogites, northern Belomorian Province, Fennoscandian Shield. *Precambrian Research*. 2021. Vol. 353. N 106014. DOI: 10.1016/j.precamres.2020.106014

21. Skublov S.G., Berezin A.V., Salimgaraeva L.I. Eclogites of the Belomorian mobile belt: geological-petrological and isotope-geochemical age criteria. *Geochemistry International.* 2022. Vol. 60. N 7, p. 626-640. DOI: 10.31857/S0016702922070047

22. Kozlov N.E., Ivanov A.A., Nerovich L.I. The Lapland Granulite Belt: the primary nature and evolution. Apatity: KNTs AN SSSR, 1990, p. 168 (in Russian).

23. Vinogradov L.A., Bogdanova M.N., Efimov M.M. The Granulite Belt of the Kola Peninsula. Leningrad: Nauka, 1980, p. 208 (in Russian).

24. Safronov V.T., Rosen O.M. Metacarbonate Rocks (Calciphyres) of the Lapland-Kolvitsa Granulite Belt, Baltic Shield. *Lithology and Mineral Resources.* 2004. Vol. 39. N 5, p. 425-436.

25. Ivliev A.I. Geology of the Lapland granulite belt metamorphic terraines (Sal'nye Tundras, the Kola Peninsula): Avtoref. dis. … kand. geol.-mineral. nauk. Moscow: IMGRE, 1977, p. 23 (in Russian).

26. McCrea J.M. On the Isotopic Chemistry of Carbonates and a Paleotemperature Scale. *The Journal of Chemical Physics*. 1950. Vol. 18. N 6, p. 849-857. DOI: 10.1063/1.1747785

27. Clayton R.N., Mayeda T.K. The use of bromine pentafluoride in the extraction of oxygen from oxides and silicates for isotopic analysis. *Geochimica et Cosmochimica Acta.* 1963. Vol. 27. Iss. 1, p. 43-52. DOI: 10.1016/0016-7037(63)90071-1

28. Sang-Tae Kim, O'Neil J.R. Equilibrium and nonequilihrium oxygen isotope effects in synthetic carbonates. *Geochimica et Cosmochimica Acta*. 1997. Vol. 61. N 16, p. 3461-3475. DOI: 10.1016/s0016-7037(97)00169-5

29. Krylov D.P. Stable isotope fractionations involving Ca-Mg carbonates: evaluation of the β-factors by the "frozen phonon" method. *Geokhimiya*. 2022. Vol. 67. N 10, p. 942-960 (in Russian). DOI: 10.31857/S0016752522100065

30. Connoly J.A.D. Multivariable phase-diagrams – an algorithm based on generalized thermodynamics. *American Journal of Science*. 1990. Vol. 290. Iss. 6, p. 666-718. DOI: 10.2475/ajs.290.6.666

31. Connolly J.A.D. A Primer in Gibbs Energy Minimization for Geophysicists. *Petrology*. 2017. Vol. 25. N 5, p. 526-534. DOI: 10.1134/S0869591117050034

32. Hua Xiang, Connolly J.A.D. GeoPS: An interactive visual computing tool for thermodynamic modelling of phase equilibria. *Journal of Metamorphic Geology*. 2022. Vol. 40. Iss. 2, p. 243-255. DOI: 10.1111/jmg.12626

33. Holland T.J.B., Powell R. An internally consistent thermodynamic data set for phases of petrological interest. *Journal of Metamorphic Geology*. 1998. Vol. 16. N 3, p. 309-343. DOI: 10.1111/j.1525-1314.1998.00140.x

34. Bibikova E.V., Melnikov V.F., Avakyan K.Kh. The Lapland granulites: petrology, geochemistry, isotopic age. *Petrologiya*. 1993. Vol. 1. N 2, p. 215-234 (in Russian).

35. Mints M.V., Glaznev V.N., Konilov A.N. et al. The Lapland-Kolvitsa Granulite-Gneiss Belt. The Early Precambrian of the northeastern Baltic Shield: paleogeodynamics, crustal structure and evolution. Moscow: Nauchnyi Mir, 1996, p. 112-138 (in Russian).

36. Schidlowski M., Eichmann R., Junge C.E. Precambrian sedimentary carbonates: carbon and oxygen isotope geochemistry and implications for the terrestrial oxygen budget. *Precambrian Research.* 1975. Vol. 2. Iss. 1, p. 1-69. DOI: 10.1016/0301-9268(75)90018-2

37. Shields G., Veizer J. Precambrian marine carbonate isotope database: Version 1.1. *Geochemistry, Geophysics, Geosystems*. 2002. Vol. 3. N 6, p. 1-12. DOI: 10.1029/2001GC000266

38. Baumgartner L.P., Valley J.W. Stable Isotope Transport and Contact Metamorphic Fluid Flow. *Reviews in Mineralogy and Geochemistry*. 2001. Vol. 43. N 1, p. 415-467. DOI: 10.2138/gsrmg.43.1.415

39. Valley J.W. Stable isotope geochemistry of metamorphic rocks. Stable Isotopes in High Temperature Geological Processes. 1986, p. 445-490. DOI: 10.1515/9781501508936-018

40. Lattanzi P., Rye D.M., Rice J.M. Behavior of ^{13}C and ^{18}O in carbonates during contact metamorphism at Marysville, Montana: implications for isotope systematics in impure dolomitic limestones. *American Journal of Science*. 1980. Vol. 280, p. 890-906. DOI: 10.2475/ajs.280.9.890

41. Graf D.L. Geochemistry of Carbonate Sediments and Sedimentary Carbonate Rocks: Part IA-A. Isotopic Composition Chemical Analysis. Urbana: Illinois State Geological Survey, 1960, p. 42.

42. Hoefs J. Stable Isotope Geochemistry. Springer, 2015, p. 389. DOI: 10.1007/978-3-319-19716-6

***Authors*: Dmitrii P. Krylov**, *Doctor of Geological and Mineralogical Sciences, Leading Researcher, d.p.krylov@ipgg.ru, https://orcid.org/0000-0001-6654-8659* (*Institute of Precambrian Geology and Geochronology RAS, Saint Petersburg, Russia*), **Ekaterina V. Klimova,** *Junior Researcher, https://orcid.org/0000-0002-9771-9518* (*Institute of Precambrian Geology and Geochronology RAS, Saint Petersburg, Russia*).

The authors declare no conflict of interests.

ISSN 2411-3336; e-ISSN 2541-9404

JOURNAL OF MINING INSTITUTE

Zapiski Gornogo instituta

Journal homepage: pmi.spmi.ru

Research article

Trace elements in the silicate minerals of the Borodino Meteorite (H5)

Kristina G. SUKHANOVA
Institute of Precambrian Geology and Geochronology RAS, Saint Petersburg, Russia

How to cite this article: Sukhanova K.G. Trace elements in the silicate minerals of the Borodino Meteorite (H5). Journal of Mining Institute. 2024. Vol. 265, p. 16-33. EDN WHSYGT

Abstract. Major (EPMA) and trace (SIMS) element geochemistry in olivine, low-Ca pyroxene and mesostasis from porphyritic and barred chondrules, as well as the pyroxene-olivine aggregate and matrix of equilibrated ordinary Borodino chondrite (H5) is discussed. No differences in major element concentrations in the silicate minerals of the chondrules and matrix of the meteorite were found. The minerals of porphyritic olivine-pyroxene and barred chondrules display elevated trace element concentrations, indicating the rapid cooling of chondrule melt in a nebula, and are consistent with experimental data. The trace element composition of low-Ca pyroxene is dependent on the position of a pyroxene grain inside a chondrule (centre, rim, matrix) and the composition of mesostasis is controlled by the type of the object (porphyritic and barred chondrules, pyroxene-olivine aggregate). The depletion in trace elements of low-Ca pyroxene from the rims of chondrules in comparison with those from the centre and matrix of the meteorite was revealed. The chondrule rim is affected by interaction with surrounding gas in a nebula, possibly resulting in the exchange of moderately volatile trace elements in low-Ca pyroxene and depletion in these elements relative to pyroxene from the centre of the chondrule or matrix of the meteorite. The mesostasis of barred and porphyritic olivine-pyroxene chondrules contains more trace elements than that of porphyritic olivine chondrule and pyroxene-olivine aggregate, suggesting the rapid cooling of these objects or their high liability to thermal metamorphism, which results in the recrystallization of chondrule glass into plagioclase. However, no traces of the elevated effect of thermal metamorphism on the above objects have been revealed. The results obtained indicate no traces of the equilibration of the trace element composition of silicate minerals in equilibrated chondrites.

Keywords: ordinary chondrites; trace elements; olivine; pyroxene; mesostasis; ion probe

Acknowledgment. The study was carried out within the framework of the research topic of the IPGG RAS FMUW-2022-0005.

Received: 04.04.2023 ***Accepted: 20.06.2023*** ***Online: 09.10.2023*** ***Published: 29.02.2024***

Introduction. The Borodino Meteorite is one of few meteorites with a unique history. The history of its finding and living on the Earth is unusual. The meteorite fell at night on the eve of the Borodino Battle, on September 5, 1812, near the village of Gorky [1]. The stone was picked up by a Russian soldier who was on duty. The soldier gave the stone to Major Christian Ivanovich Dieterichs. Major Dieterichs was wounded on the battle field. After resigning, he lived in his estate in Kurlandia (modern Latvia) [2]. The Major's family kept the meteorite for 80 years, in 1890, Gerke, manager of the son of Major Dieterichs, donated a large piece of meteorite (320 g) to the Mining Institute museum. However, a small piece was owned by Y.I.Simashko, an entomologist, a writer and a publisher. Simashko described the meteorite's history in a letter to the British Museum of Natural History [3].

The Borodino Meteorite is an equilibrated ordinary chondrite, the most common type of meteorites known on Earth [4]. Chondrites consist of silicate spherules (chondrules), less than one millimeter in size, which occur in a weightless nebula of melt drops consisting of olivine, low-Ca pyroxene and mesostasis. Structurally, chondrules are subdivided into a porphyritic type composed of olivine and/or pyroxene phenocrysts and a nonporphyritic type (barred, radiated-structured, cryptocrystalline, etc.).

Journal of Mining Institute. 2024. Vol. 265. P. 16-33

A variety of chondrule structures suggests a variety of the cooling conditions of the melt. Experiments have shown that porphyritic chondrules are formed from slowly cooling melt (1-500 °C/h), which was heated below liquidus temperature (1400-1700 °C) and preserved an abundance of relict grains. The crystallization of barred chondrules requires the heating of the melt at temperatures slightly above liquidus temperature followed by rapid cooling (500-3000 °C/h). Radial chondrules suggest that melt was subjected to high temperatures and then cooled instantaneously (1000-3000 °C/h) [5].

The sample taken from the Borodino Meteorite mainly contains olivine and olivine-pyroxene porphyritic chondrules. Barred and cryptocrystalline chondrules are scarce.

The porphyritic chondrules of unaltered ordinary chondrites (UOC) occasionally display isolated MgO-enriched refractory olivine grains, differing in the isotopic composition of oxygen from chondrule olivine [6, 7], and MgO-richer olivine grain cores overgrown with MgO-poorer forsterite rims [8]. The presence of relict olivine grains in porphyritic chondrules suggests that they were produced by the melting of precursor minerals, such as refractory inclusions (e,g, calcium-aluminium and amoeba-like olivine inclusions) [9], the fine-grained material of chondrite matrix and fragments of previous generations of chondrules, fragments of planetesimals [10], H_2O ice [11], "relict" olivine and dust clusters [12].

Chondrules from ordinary chondrites occur among single grains of silicate minerals, troilite, kamacite-taenite, chromite and other minerals, making up meteorite matrix. The Borodino Meteorite matrix consists of coarse well-defined grains of minerals commonly occurring in the matrix of chondrites. The chondrule-matrix boundaries are well defined. No veinlets or melting pockets have been revealed.

Most of ordinary chondrites show traces of thermal metamorphism, which took place on fairly big (over 50 km in diameter) parent bodies. Thermal metamorphism resulted in the homogenization (equilibration) of Fe-Mg in olivine and low-Ca pyroxene, the recrystallization of mesostasis into plagioclase, the formation of high-Ca pyroxene, apatite and chromite and the obliteration of chondrule-matrix boundaries [13]. The petrologic type (p.t.) of ordinary chondrite is identified from the petrographic characters and compositional variability of silicate minerals. UOC's are of three petrologic types. Their Fe and Mg concentrations in olivine and low-Ca pyroxene are most variable. The variability of Fe and Mg in the fourth to a sixth p.t. fades out gradually (ordinary equilibrated chondrites – EOC), giving way to other signs of thermal metamorphism. The Borodino Meteorite (H5) is of a fifth p.t. and the high-Fe group (H) of EOC.

In spite of an abundance of EOC, which make up over 90 % of all meteorites found, they are poorly understood. Thermal metamorphism disturbed the original distribution of chemical elements and their isotopes in EOC minerals, they were not used for the study of chondrule formation and accretion. However, trace elements in silicate minerals are practically immobile on parental chondrite bodies affected by thermal metamorphism [14, 15]. Therefore, they are used for the study of early stages in the formation of the Solar System [16-18]. The study of the composition of refractory trace elements in olivine, pyroxene and the glass of UOC chondrules has revealed various types of porphyritic chondrule crystallization [19] making it possible to calculate their relative cooling rates [20-22]. The composition of moderately volatile trace elements usually indicates the interaction of a chondrule with surrounding gas in a protoplanetary disk [23].

Trace and rare-earth elements are widely used for the study of geochemical settings, in which genetically different minerals, such as zircon [24, 25], beryl [26, 27], olivine [28], etc., were formed.

Pioneer studies on the compositions of the silicate minerals of EOC showed heterogeneous trace element concentrations [29, 30] and oxygen isotope ratios [31] in the olivine and pyroxene of EOC. The trace element composition of silicate minerals from Borodino Meteorite chondrules will be

analyzed to assess the effect of thermal metamorphism on trace element concentrations and to reveal differences in the settings in which structurally different chondrules were formed.

Analytical methods. A sample of the Borodino chondrite (H5) was provided by the Mining Museum of Saint Petersburg Mining University. The chemical composition of minerals at the level of major elements was determined using the EPMA method at IGGD RAS on a Jeol JXA-8230 microprobe analyzer with five wave spectrometers. The meteorite substance was placed in a standard epoxy resin mould sprayed with carbon after polishing. Point measurements of mineral compositions were carried out at an accelerating voltage of 20 kV and a current of 20 nA for olivine and pyroxene and at 10 nA for mesostasis [32]. The focused beam was 3 μm in diameter. Natural minerals, pure oxides and metals were used as standards. ZAF algorithm was used for correcting the matrix effect. Kα1 lines were measured for all elements.

Trace and rare-earth element (REE) concentrations in minerals were identified using the secondary ion mass spectrometry (SIMS) method on a Cameca IMS-4f ion microprobe at the Yaroslavl Branch of K.A.Valiev Physico-Technological Institute, RAS, using the technique described in [33]. The preparation was sprayed with gold prior to measurements. Survey on a Cameca IMS-4f ion microprobe was done under the following conditions: a primary ion beam was $16O_2^-$, beam diameter was ~20 μm; ion current was 5-7 nA; and the accelerating voltage of the primary beam was 15 keV. The measurement error was no more than 10 % for impurities with concentrations over 1 ppm and 20 % for concentrations of less than 1 ppm. The trace element composition of rock-forming minerals was analyzed as close as possible to the analytical points of major elements using the EPMA method. REE distribution spectra in minerals were CI chondrite-normalized [34].

Results. Two porphyritic and one barred chondrules, as well as olivine-pyroxene aggregate, from the Borodino Meteorite were studied. The porphyritic chondrules display olivine composition for 14PO-4 and olivine-pyroxene composition for 14POP-1. Barred chondrule 14BOP-2 consists of thin parallel olivine and low-Ca pyroxene bars. The porphyritic chondrules measure about 0.5 mm and a barred chondrule is over 1 mm in size. No well-defined metallic and silicate rims of the chondrules were revealed, but coarse kamacite-taenite and troilite grains are occasionally encountered at the chondrule-matrix boundary.

Pyroxene-olivine aggregate 14APO-3 consists of coarse low-Ca pyroxene grains overgrowing fine olivine grains in the centre of the aggregate. Coarse kamacite-taenite grains and fine troilite grains occur along the aggregate boundaries. The contours of the aggregate resemble the rounded shape of the chondrules, suggesting the recrystallization and coarsening of chondrule minerals as a result of thermal metamorphism on the parent body. However, the complete absence of mesostasis in the aggregate is not typical of chondrules.

Chondrule 14POP-1 has a rounded shape, a porphyritic structure and a small size (0.5 mm). It consists of coarse olivine phenocrysts occurring in the centre of the chondrule and evenly distributed low-Ca pyroxene grains. Olivine also occurs as fine grains near the chondrule boundary. Mesostasis fills interstices between olivine and pyroxene, typically occurring in the centre of the chondrule. The matrix surrounding the chondrule consists of equigranular material composed of olivine and low-Ca pyroxene. Mesostasis is scarce.

Olivine in porphyritic chondrule 14POP-1 was identified as forsterite (Fo 81). It occurs as a coarse (200 μm lengthwise) idiomorphic grain in the centre and fine (50-100 μm) hypidiomorphic grains near chondrule rims (Fig.1). Major element concentrations are practically invariable. There is no difference in olivine composition between the chondrule and the matrix (Table 1). Trace element concentrations in olivine vary markedly: refractory Zr and Ti, as well as moderately volatile Ba, V, Ni, Cr and REE, vary by several orders of magnitude. The highest trace element concentrations are exhibited by olivine at the chondrule rim, where Zr, Hf, REE and Sr concentrations are more than twice as high as those of olivine in the centre of the chondrule and matrix of the meteorite.

Journal of Mining Institute. 2024. Vol. 265. P. 16-33

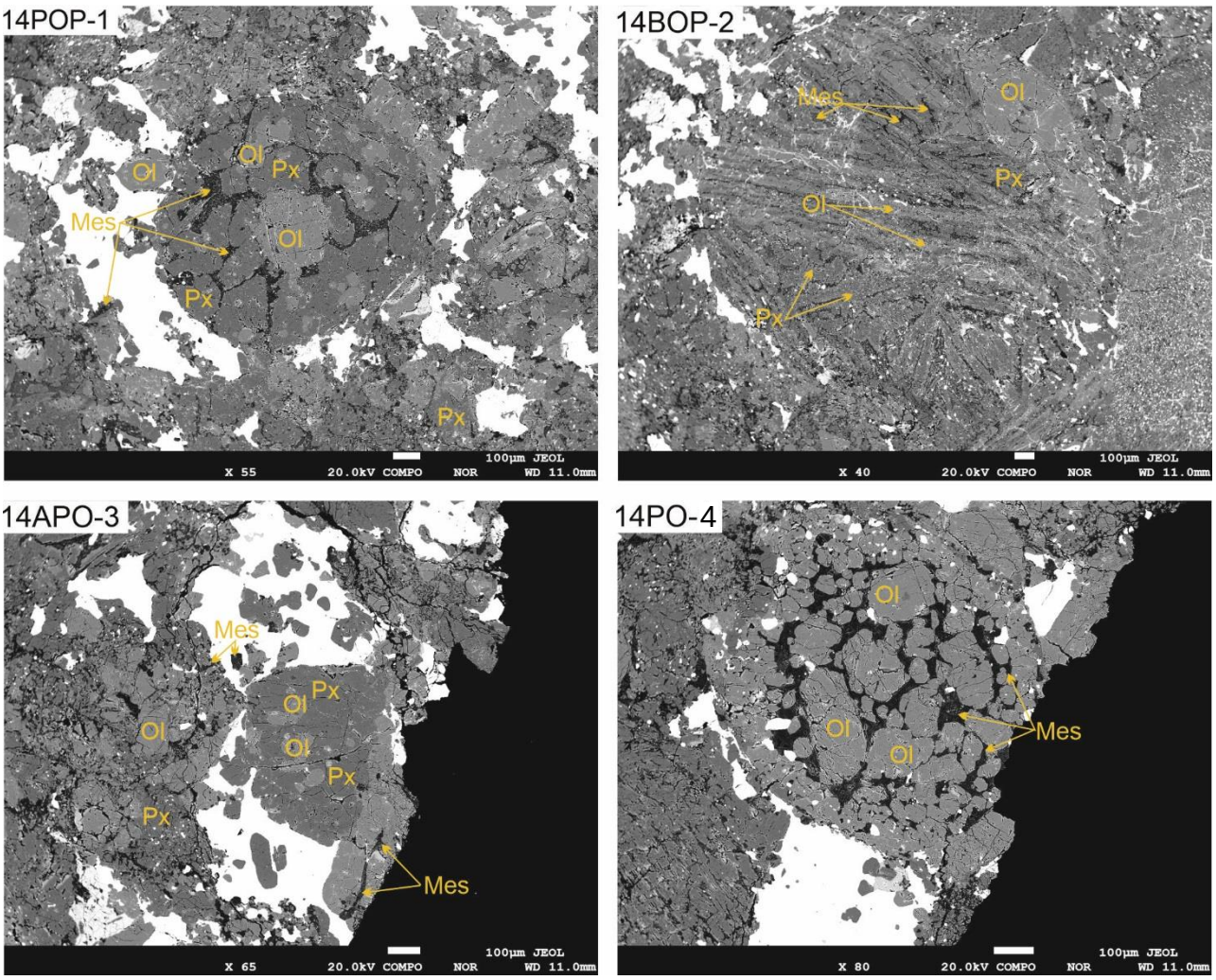

Fig.1. BSE images of chondrules of the Borodino Meteorite:
Ol – olivine, Px – low-Ca pyroxene, Mes – mesostasis

Table 1

Major (wt.%) and trace (ppm) element composition of silicate minerals from 14POP-1 chondrule of the Borodino Meteorite

Component	Ol			Px			Mes		
	Centre	Rim	Matrix	Centre	Rim	Matrix	Rim	Rim	Matrix
SiO_2	39.38	39.60	39.23	57.87	57.70	56.76	63.13	64.22	64.26
Al_2O_3	0.00	0.02	0.01	0.12	0.10	0.24	19.64	19.38	21.46
MgO	43.27	43.60	42.78	30.44	30.84	30.34	1.31	0.36	0.30
TiO_2	0.00	0.00	0.02	0.11	0.11	0.20	0.38	1.89	0.02
CaO	0.02	0.01	0.03	0.60	0.56	0.72	4.30	1.96	2.90
FeO	17.55	17.40	17.63	10.96	11.15	10.94	1.80	1.45	0.58
MnO	0.49	0.46	0.48	0.53	0.51	0.51	–	–	–
Cr_2O_3	0.02	0.02	0.02	0.11	0.08	0.31	–	–	–
NiO	0.00	0.01	0.00	0.00	0.01	0.02	–	–	–
Na_2O	–	–	–	–	–	–	9.75	10.07	9.78
K_2O	–	–	–	–	–	–	0.56	1.55	0.65
Total	100.74	101.11	100.19	100.73	101.04	100.05	100.86	100.87	99.95
Zr	1.06	5.28	2.05	21.4	2.05	8.01	61.7	61.8	112
Hf	b.d.l.	0.25	0.11	0.45	0.09	0.18	1.45	1.39	3.03
Ca	4299	3987	6230	5210	5524	5821	–	–	–
Y	0.03	0.08	0.08	0.36	0.18	0.31	1.61	2.09	1.30

End of Table 1

Component	Ol			Px			Mes		
	Centre	Rim	Matrix	Centre	Rim	Matrix	Rim	Rim	Matrix
Al	165	155	110	612	696	1181	–	–	–
Ti	80.8	104	326	894	732	1077	2009	1776	1454
Nb	0.40	0.09	0.19	0.33	0.17	0.41	1.63	1.05	2.02
La	0.01	0.26	0.12	1.15	0.04	0.27	2.81	2.99	3.12
Ce	0.02	0.60	0.20	2.38	0.11	0.50	4.60	3.79	5.76
Pr	b.d.l.	0.04	0.03	0.22	0.01	0.06	0.59	0.52	0.62
Nd	b.d.l.	0.24	0.13	0.89	0.06	0.27	2.12	2.26	2.35
Sm	b.d.l.	0.06	0.04	0.14	0.07	0.04	0.32	0.14	0.25
Eu	0.01	0.03	0.01	0.04	0.01	0.01	0.27	0.15	0.76
Gd	0.03	0.27	0.02	0.13	0.04	0.07	0.36	0.16	0.45
Tb	–	–	–	–	–	–	–	–	–
Dy	b.d.l.	b.d.l.	b.d.l.	0.07	b.d.l.	0.06	0.33	0.28	0.18
Ho	–	–	–	–	–	–	–	–	–
Er	b.d.l.	b.d.l.	b.d.l.	0.04	0.06	0.07	0.26	0.17	0.09
Yb	0.03	0.05	0.02	0.14	0.06	0.09	0.17	0.26	0.16
Lu	0.01	0.01	0.01	0.02	0.02	0.03	0.03	0.04	0.03
Sr	0.10	1.20	1.47	0.40	0.49	0.88	28.4	23.3	104
Ba	0.12	6.79	1.53	4.10	0.37	4.00	14.9	12.9	34.7
V	45.7	14.3	34.0	64.0	47.6	133	102	126	64.7
Ni	17.9	103	53.2	50.6	56.7	160	–	–	–
Cr	1939	316	1546	2733	1583	5921	3133	2881	1793
Rb	2.36	1.66	3.22	0.57	1.47	1.76	5.34	8.31	14.1
REE	0.12	1.56	0.57	5.21	0.48	1.49	11.8	10.8	13.8
LREE	0.05	1.23	0.53	4.82	0.30	1.16	10.7	9.86	12.9
HREE	0.07	0.33	0.04	0.39	0.18	0.33	1.14	0.91	0.90

Note. Dash – no element detected; b.d.l. – element content is below the detection limit.

Trace element distribution spectra for olivine are mildly differentiated (Fig.2, *a*). Trace element concentrations in olivine at the rim of chondrule 14POP-1 in the Borodino Meteorite practically reach chondrite values, which is not typical of olivine from ordinary chondrites. Olivine from chondrule 14POP-1 displays higher trace element concentrations than those in olivine from UOC, except for Al. Al concentration in olivine from the chondrule and the matrix is less by one order of magnitude than Al concentration in olivine from UOC.

Olivine from chondrule 14POP-1 is also richer in REE than olivine from UOC, although it typically displays the prevalence of heavy rare-earth elements (HREE) over light (LREE). Olivine from the matrix shows the prevalence of LREE.

Low-Ca pyroxene from chondrule 14POP-1 occurs as enstatite (En 81, Wo 1). It is evenly distributed over the chondrule area, occurring as fine (about 100 μm lengthwise) idiomorphic and hypidiomorphic grains. Major element concentrations vary slightly. Pyroxene from the chondrule does not differ in major element concentrations, but pyroxene from the matrix is twice as rich in Al and Ti as pyroxene from the chondrule.

Trace element concentrations in low-Ca pyroxene are relatively stable. Elevated Zr and Ce concentrations in pyroxene from the centre of the chondrule (21.4 and 2.38 ppm, respectively) and low REE concentrations (0.48 ppm) in the pyroxene of the chondrule rim were revealed.

Trace element distribution spectra for low-Ca pyroxene from chondrule 14POP-1 are poorly differentiated (Fig.2, *c*). They differ mainly in REE concentrations. For instance, pyroxene from the centre of the chondrule and the matrix typically displays the prevalence of LREE over HREE, but pyroxene from the chondrule rim exhibits elevated HREE concentrations relative to LREE. Pyroxene from the meteorite matrix displays a positive europium anomaly.

Pyroxene in chondrule 14POP-1 is richer in refractory trace elements and REE than low-Ca pyroxene from UOC, except for Al. Moderately volatile element concentrations in pyroxene from chondrules 14POP-1 and UOC are practically the same.

Journal of Mining Institute. 2024. Vol. 265. P. 16-33

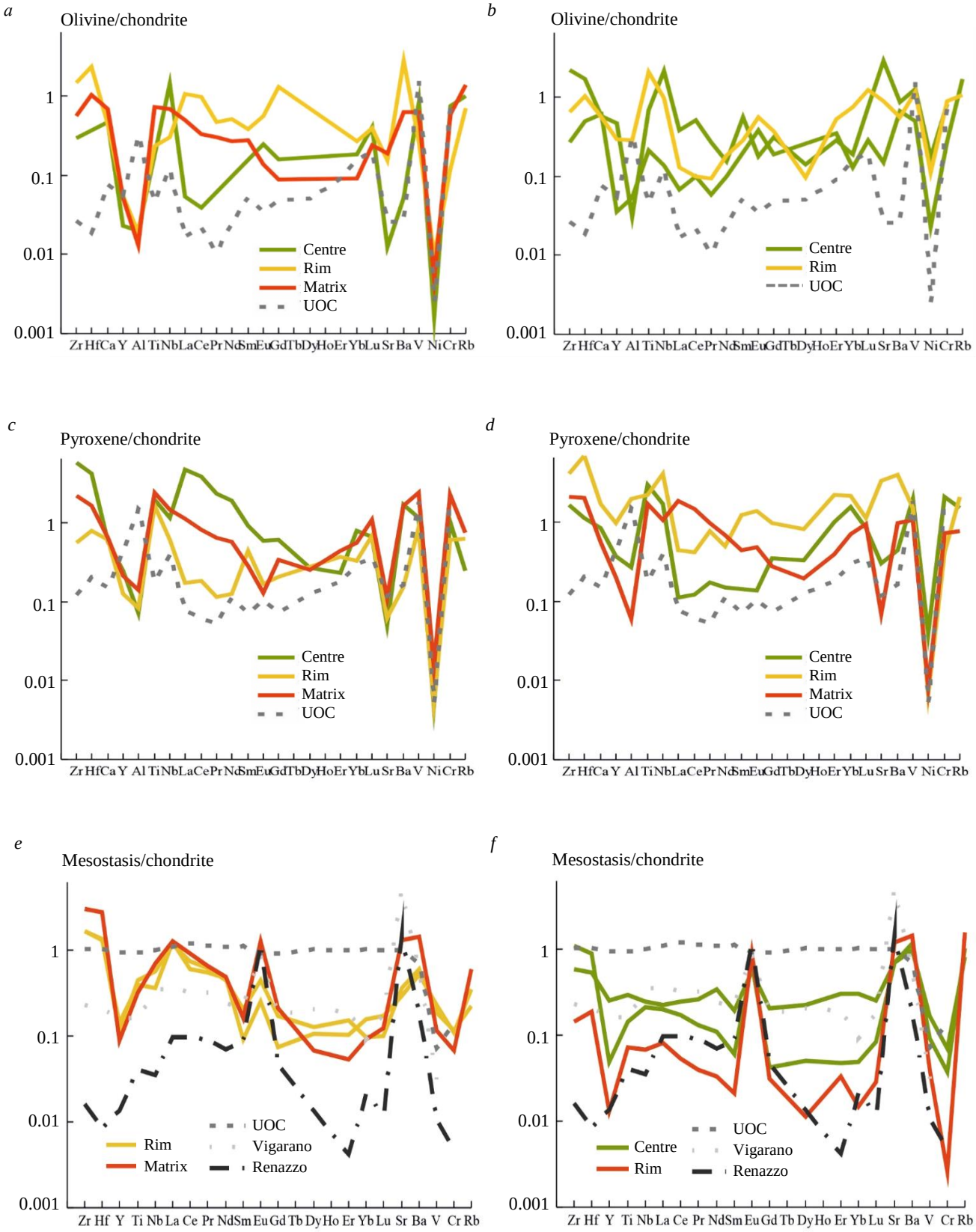

Fig.2. Spider diagrams for trace elements normalized to CI chondrite. Chondrule 14POP-1: olivine (*a*); low-Ca pyroxene (*c*) and mesostasis (*e*). Chondrule 14BOP-2: olivine (*b*); low-Ca pyroxene (*d*) and mesostasis (*f*). Data on the composition of UOC minerals are given according to [20, 21]

Mesostasis from chondrule 14POP-1 consists of highly recrystallized glass of albite (An 8 Or 8) and oligoclase (An 19 Or 3) composition. It fills large interstices between olivine and pyroxene, and is more abundant near the chondrule rim. The mesostasis contains acicular aggregates of high-Ca pyroxene and micron-sized chromite and troilite grains. Its slightly variable major element composition is due to the heterogeneity of the mesostasis. MgO 0.30-1.31 (wt.%) and TiO_2 concentrations (0.02-1.89 wt.%) are most variable.

Trace elements in the mesostasis of chondrule 14POP-1 vary slighly. Mesostasis from the meteorite matrix is slightly enriched in Zr and moderately volatile elements (Sr, Ba, V and Rb). Trace element concentrations in mesostasis from the chondrule remains unchanged in spite of its heterogeneity.

Trace element distribution spectra for mesostasis from chondrule 14POP-1 fully coincide with those for plagioclase from Vigarano coaly chondrule, but contain more Zr, Hf and LREE (Fig.2, *e*).

Barred chondrule 14BOP-2 consists of thin olivine and low-Ca pyroxene bars. Small interstices between them are filled with mesostasis. The chondrule is over 1 mm in size, has no metallic or silicate rims, is rounded in shape and the chondrule-matrix boundary is poorly-defined (see Fig.1).

Olivine in barred chondrule 14BOP-2 is present as forsterite (Fo 81). It occurs as thin highly elongated (from one chondrule rim to the other) inequidirectional skeletal crystals and is evenly distributed throughout the chondrule. Major element concentrations in olivine are practically invariable, except for FeO and MgO, which is typical of a meteorite of a fifth petrologic type (Table 2).

Trace elements in olivine from the chondrule also vary slightly. Olivine grains depleted in refractory elements (Y, Al, Ti, Nb) occur in the centre of the chondrule. Olivine from the chondrule rim is slightly different in trace element concentrations from that in the centre of the chondrule.

Trace element distribution spectra for olivine from the chondrule are poorly differentiated (Fig.2, *b*). No significant differences between olivine from the centre and rim of the chondrule were revealed. Olivine from chondrule 14BOP-2 contains higher trace and rare-earth element concentrations than olivine from UOC. Al concentration in olivine from the chondrule rim is similar to that in olivine from UOC, a feature not typical of olivine from other chondrules.

Low-Ca pyroxene from the chondrule is present as enstatite (En 81, Wo 1). Like olivine, it forms skeletal crystals elongated from one chondrule rim to the other. It mainly occurs in the centre of chondrules. Pyroxene occasionally has thin ore mineral (kamacite-taenite, chromite and troilite) streaks. Major element concentrations in low-Ca pyroxene from the chondrule and matrix of the meteorite are stable.

Trace elements in low-Ca pyroxene from the barred chondrule varies slightly, depending on the position of pyroxene in the chondrule. Pyroxene from the centre of the chondrule is depleted in LREE and contains low refractory trace element (Zr, Al, Ca) concentrations. Pyroxene from the chondrule rim is richer in refractory and rare-earth elements than pyroxene from the centre and matrix of the meteorite. Low-Ca pyroxene from the matrix has low Al and HREE concentrations.

Trace element distribution spectra for low-Ca pyroxene from chondrule 14BOP-2 are poorly differentiated, and trace element concentrations are close to chondrite values (Fig.2, *d*). HREE's typically prevail over LREE's in pyroxene from the chondrule, but pyroxene from the matrix displays an inverse trend.

Low-Ca pyroxene from the barred chondrule is richer in refractory and rare-earth elements than low-Ca pyroxene from UOC, although pyroxene from the chondrule is poor in Al than pyroxene from UOC.

Mesostasis fills micron-sized interstices between olivine and pyroxene bars. The aggregates are no more than 50 μm in size. The mesostasis on BSE-images generally looks homogeneous, although it often occurs with fine ore mineral grains. In chondrule 14BOP-2, mesostasis is present as poorly recrystallized glass of oligoclase composition (An 11 Or 5). In the matrix, its composition may vary to anorthoclase (An 7 Or 13). The minor element composition of the mesostasis is invariable, except for FeO and MgO.

Journal of Mining Institute. 2024. Vol. 265. P. 16-33

Table 2

Major (wt.%) and trace (ppm) element composition of silicate minerals from 14BOP-2 chondrule of the Borodino Meteorite

Component	Ol			Px			Mes		
	Centre	Centre	Rim	Centre	Rim	Matrix	Centre	Centre	Matrix
SiO_2	39.82	39.16	39.59	57.65	57.23	57.45	64.79	63.68	63.37
Al_2O_3	0.01	0.01	0.00	0.16	0.16	0.12	20.97	19.84	20.22
MgO	42.71	42.18	43.57	30.42	30.77	30.78	0.07	0.32	1.08
TiO_2	0.00	0.00	0.01	0.14	0.16	0.10	0.00	0.06	0.04
CaO	0.02	0.05	0.02	0.68	0.70	0.72	2.46	2.42	2.50
FeO	17.93	18.37	17.21	11.04	11.26	11.06	0.89	2.26	1.32
MnO	0.47	0.47	0.50	0.51	0.48	0.47	–	–	–
Cr_2O_3	0.00	0.06	0.00	0.21	0.15	0.14	–	–	–
NiO	0.01	0.18	0.00	0.01	0.02	0.04	–	–	–
Na_2O	–	–	–	–	–	–	10.36	9.90	8.94
K_2O	–	–	–	–	–	–	0.81	1.04	1.10
Total	100.97	100.47	100.90	100.83	100.93	100.87	100.33	99.51	98.57
Zr	0.96	8.10	2.36	5.93	15.0	7.49	21.6	40.2	5.18
Hf	0.05	0.18	0.11	0.12	0.74	0.22	0.58	0.97	0.20
Ca	5626	5320	5035	7713	15349	5080	–	–	–
Y	0.05	0.68	0.43	0.54	1.44	0.29	3.69	0.72	0.19
Al	452	257	2417	2239	16514	509	–	–	–
Ti	94.7	308	939	1317	990	752	1326	642	328
Nb	0.04	0.60	0.27	0.49	1.18	0.30	0.71	0.60	0.20
La	0.02	0.09	0.03	0.03	0.11	0.45	0.55	0.48	0.20
Ce	0.06	0.32	0.06	0.08	0.26	0.90	1.56	1.09	0.33
Pr	0.01	0.03	0.01	0.02	0.07	0.09	0.25	0.12	0.04
Nd	0.05	0.07	0.09	0.07	0.24	0.33	1.62	0.52	0.16
Sm	b.d.l.	0.09	0.04	b.d.l.	0.19	0.07	0.30	0.09	0.03
Eu	0.02	0.01	0.03	0.01	0.08	0.03	0.32	0.40	0.52
Gd	0.04	0.06	0.08	0.07	0.20	0.06	0.43	0.09	0.06
Tb	–	–	–	–	–	–	–	–	–
Dy	b.d.l.	0.04	0.02	0.08	0.21	0.05	0.57	0.13	0.03
Ho	–	–	–	–	–	–	–	–	–
Er	0.06	0.05	0.09	0.17	0.37	0.07	0.51	0.08	0.06
Yb	0.02	0.03	0.13	0.26	0.36	0.12	0.52	0.08	0.02
Lu	0.01	0.02	0.03	0.02	0.03	0.02	0.06	0.02	0.01
Sr	1.18	22.2	6.90	2.35	26.4	0.55	55.5	56.0	93.7
Ba	1.59	2.09	1.35	1.07	9.62	2.39	24.1	28.2	35.4
V	27.5	70.2	63.9	109	81.9	57.5	91.7	50.5	21.8
Ni	248	1910	1200	424	73.3	90.2	–	–	–
Cr	727	2176	2326	5498	1097	1917	1851	991	68.5
Rb	3.98	b.d.l.	2.48	3.51	4.82	1.77	18.8	24.5	36.6
REE	0.28	0.80	0.61	0.81	2.11	2.18	6.70	3.12	1.46
LREE	0.15	0.60	0.27	0.20	0.95	1.86	4.60	2.71	1.28
HREE	0.13	0.20	0.35	0.61	1.16	0.32	2.10	0.40	0.18

Trace element concentrations vary considerably. For instance, mesostasis from the centre of the chondrule is richer in refractory trace elements than that from the meteorite matrix. There are also some differences between mesostasis grains in the centre of the chondrule. FeO-depleted mesostasis contains higher refractory and rare-earth concentrations than other central mesostasis grains.

The trace element distribution spectra are highly differentiated (Fig.2, *f*). Mesostasis from the matrix is poor in trace elements. The spectra clearly show the prevalence of LREE over HREE and a well-defined europium anomaly. Mesostasis from the matrix coincides largely with a trace element distribution spectrum for plagioclase from Renazzo coaly chondrite. However, it contains high refractory element (Zr, Hf and Ti) and low REE concentrations. Mesostasis from chondrule 14BOP-2 shows a trace element distribution spectrum similar to that for plagioclase from the Vigarano Meteorite, although it seems to decline towards the Renazzo spectrum, occupying an intermediate position.

Pyroxene-olivine aggregate 14APO-3 was formed as the isometric intergrowth of fine (250-300 μm) low-Ca crystals with hypidiomorphic olivine grains (50-100 μm) (see Fig.1) in its centre. Mesostasis from the aggregate is poorly-defined. It mainly occurs at the matrix-aggregate boundary. The aggregate could be interpreted as a highly metamorphosed chondrule with completely obliterated boundaries. However, it is hardly a chondrule, because its rims are not rounded and its internal structure is specific.

Olivine from the aggregate is present as forsterite (Fo 81). It occurs as several grains located mainly in the centre of the aggregate. The major element composition of olivine is stable.

Trace element concentrations in olivine from the aggregate are slightly variable (Table 3). Olivine from aggregate 14APO-3 tends to be slightly richer in trace elements than olivine from the matrix. However, no significant differences in trace element concentrations were revealed.

Table 3

Major (wt.%) and trace (ppm) element composition of silicate minerals from aggregate 14APO-3 chondrule of the Borodino Meteorite

Component	Ol			Px			Mes		
	Centre	Centre	Matrix	Rim	Rim	Matrix	Centre	Rim	Matrix
SiO_2	39.37	39.33	39.70	56.64	57.40	57.71	65.32	64.27	65.61
Al_2O_3	0.02	0.00	0.00	0.21	0.14	0.12	20.98	21.02	19.95
MgO	42.77	43.10	42.91	30.95	30.24	30.43	0.18	0.10	0.39
TiO_2	0.01	0.00	0.02	0.22	0.14	0.14	0.07	0.01	0.01
CaO	0.04	0.01	0.03	0.74	0.74	0.76	2.43	2.41	1.48
FeO	17.90	17.78	17.86	11.26	11.12	11.02	0.65	2.26	0.77
MnO	0.48	0.48	0.46	0.50	0.47	0.49	–	–	–
Cr_2O_3	0.03	0.02	0.01	0.22	0.17	0.13	–	–	–
NiO	0.01	0.02	0.00	0.02	0.00	0.00	–	–	–
Na_2O	–	–	–	–	–	–	10.15	10.15	9.25
K_2O	–	–	–	–	–	–	0.97	0.89	2.41
Total	100.61	100.72	100.98	100.75	100.42	100.80	100.74	101.11	99.86
Zr	0.33	1.25	0.48	0.88	0.41	2.13	2.30	7.43	9.20
Hf		0.09	0.06	0.05	0.14	0.10	b.d.l.	0.29	0.25
Ca	4538	4529	4189	5506	4657	5063	–	–	–
Y	0.02	0.10	0.06	0.29	0.23	0.31	0.15	0.30	0.59
Al	76.5	221	38.0	649	422	784	–	–	–
Ti	103	390	45.2	1028	701	1156	303	319	469
Nb	0.08	0.08	0.06	0.03	0.05	0.16	0.23	0.42	0.47
La	0.02	0.01	0.01	0.04	0.01	0.03	0.11	0.25	0.11
Ce	0.02	0.03	0.02	0.06	0.02	0.05	0.15	0.35	0.31
Pr	0.01	0.01	0.01	0.01	0.00	0.01	0.01	0.04	0.03
Nd	b.d.l.	0.05	b.d.l.	0.10	b.d.l.	0.06	0.06	0.21	0.09
Sm	0.05	b.d.l.	0.04	0.04	b.d.l.	0.05	b.d.l.	0.06	0.04
Eu	0.01	b.d.l.	b.d.l.	0.01	b.d.l.	0.02	0.49	0.59	0.41
Gd	0.02	0.02	b.d.l.	0.02	0.02	0.02	0.02	0.03	0.06
Tb	–	–	–	–	–	–	–	–	–
Dy	–	0.03	0.03	0.05	0.03	0.03	0.02	0.06	0.07
Ho	–	–	–	–	–	–	–	–	–
Er	b.d.l.	0.01	0.04	0.11	0.03	0.07	0.08	0.03	0.04
Yb	0.06	0.04	0.03	0.07	0.07	0.11	0.03	0.03	0.06
Lu	b.d.l.	b.d.l.	0.01	0.02	0.01	0.01	0.01	0.01	0.01
Sr	0.09	0.28	0.21	0.14	0.12	0.34	82.7	100	76.4
Ba	0.21	0.58	0.25	0.28	0.20	0.55	33.8	42.5	40.0
V	17.3	31.1	24.1	50.5	39.9	56.0	21.0	26.2	41.3
Ni	27.4	121	64.8	40.4	49.4	89.2	–	–	–
Cr	459	648	430	1080	962	1181	146	113	330
Rb	1.55	1.70	2.91	0.73	0.97	1.21	25.6	28.6	248
REE	0.20	0.21	0.20	0.53	0.20	0.47	0.98	1.67	1.23
LREE	0.11	0.10	0.09	0.26	0.03	0.22	0.82	1.50	0.99
HREE	0.09	0.10	0.11	0.27	0.17	0.25	0.16	0.17	0.24

Journal of Mining Institute. 2024. Vol. 265. P. 16-33

The trace element distribution spectrum for the aggregate is slightly fractionated. Trace element concentrations in olivine are below chondrite values (Fig.3, *a*). Olivine from aggregate 14APO-3 is richer in refractory and rare-earth elements than olivine from UOC, except for Al.

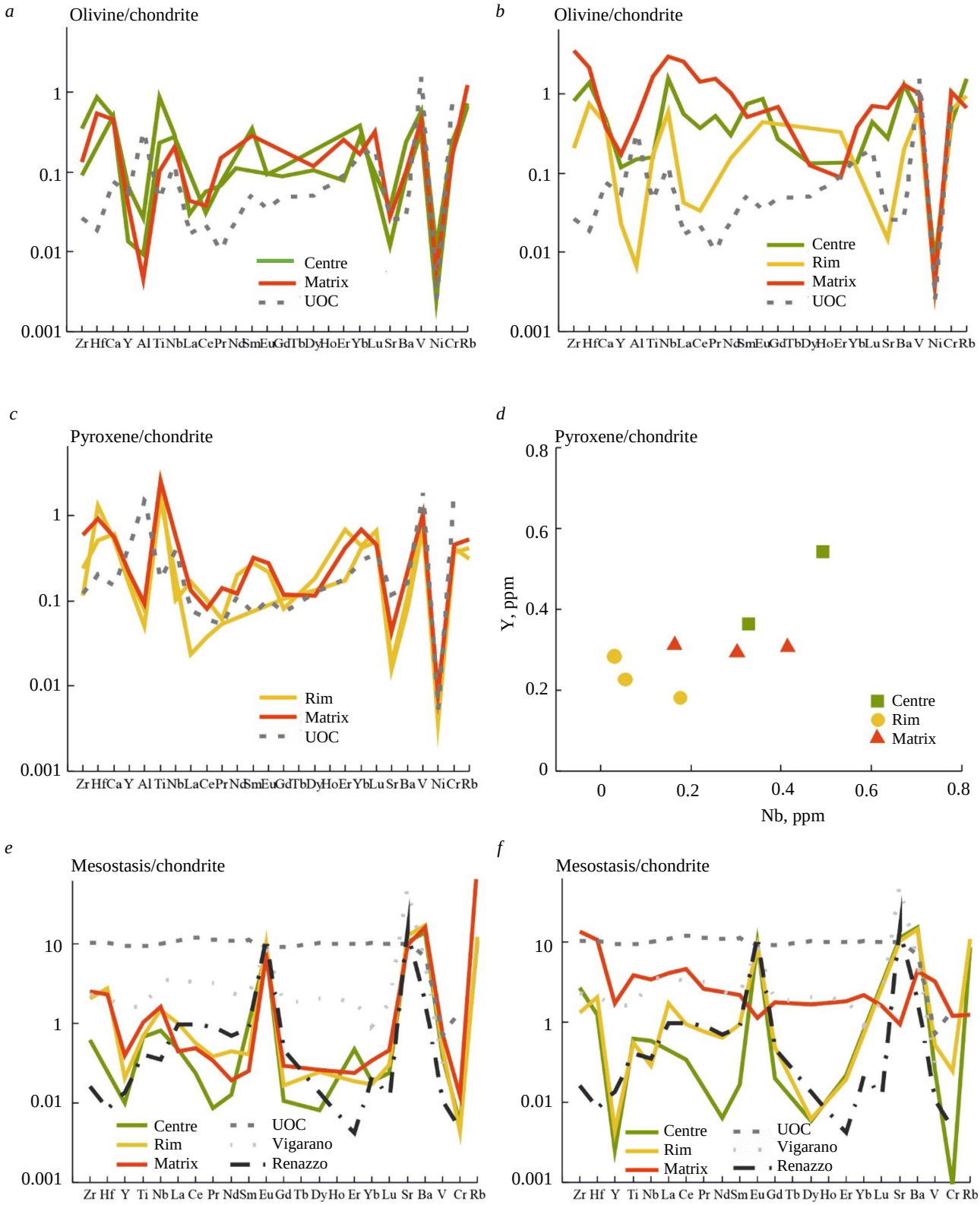

Fig.3. Spider diagrams for trace elements normalized to CI chondrite. Aggregate 14APO-3: olivine (*a*); low-Ca pyroxene (*c*) and mesostasis (*e*). Chondrule 14PO-4: olivine (*b*) and mesostasis (*f*). The Y and Nb ratio in low-Ca pyroxene of the Borodino Meteorite (*d*). Data on the composition of UOC minerals are given according to [20, 21]

Low-Ca pyroxene from aggregate 14APO-3 is present as enstatite (En 81, Wo 1). It occurs as coarse fractured idiomorphic crystals overgrown with olivine grains. Its trace element concentrations are invariable, except for some minor variations: TiO_2 0.12-0.21 wt.% and Cr_2O_3 0.13-0.22 wt.%.

Trace elements in low-Ca pyroxene from aggregate 14APO-3 vary less markedly than those in olivine. Pyroxene at the aggregate rim has a minimum LREE concentration of 0.03 ppm, which is not characteristic of pyroxene from the aggregate, the matrix, and other chondrules.

Trace element distribution spectra for pyroxene from aggregate 14APO-3 are absolutely similar to each other, suggesting their permanent trace element composition (Fig.3, *c*). Trace element concentration in pyroxene from the aggregate is below chondrite values. Trace element fractionation in low-Ca pyroxene from the aggregate is not obvious.

The trace element distribution spectrum for the pyroxene of aggregate 14APO-3 has much in common with a spectrum for pyroxene from UOC. However, it contains high refractory element (Zr, Hf, Ti) and some rare-earth (Sm, Eu) element concentrations.

Mesostasis from aggregate 14APO-3 occurs very seldom. On BSE-images, it looks like absolutely homeneous plagioclase of oligoclase composition (An 11 Or 4). The major element composition of the mesostasis is stable, except for considerable variation in FeO (0.67-2.03 wt.%) and minor variations in Al_2O_3 (20.86-21.33 wt.%).

The trace element composition of mesostasis from aggregate 14APO-3 is slightly variable. The central portion of the mesostasis contains minimum trace element concentrations, especially Zr, Hf, Y and REE. Mesostasis from the aggregate rim is similar to that from the matrix, but its LREE concentrations are higher (1.50 ppm).

Trace element distribution spectra for mesostasis from the pyroxene-olivine aggregate are not differentiated (Fig.3, *e*). Trace element concentrations in the mesostasis are consistent with chondrite values. No HREE and LREE fractionation in mesostasis from the aggregate and matrix of the Borodino Meteorite has been revealed. The trace element distribution spectrum for mesostasis from the aggregate is fully consistent with that for plagioclase from Renazzo coaly chondrite. However, it contains elevated refractory Zr and Hf concentrations and low total REE.

Porphyritic chondrule 14PO-4 consists solely of olivine and mesostasis. It has a perfect rounded shape with a little nose, is small in size (500 μm) and has no silicate or metallic rims. Olivine from the chondrule occurs as coarse idiomorphic grains. The coarsest grains are up to 250 μm lengthwise, while the finest grains are 50-70 μm in size. Mesostasis is evenly distributed throughout the chondrule, it fills interstices between olivine grains and looks homogeneous on BSE-images.

Olivine from chondrule 14PO-4 is present as forsterite (Fo 81). It is coarse, highly fractured and, unlike olivine from the matrix, has well-defined facets. Major element concentrations in olivine from the chondrule are practically invariable (Table 4).

Trace elements in olivine from chondrule 14PO-4 vary markedly. For instance, olivine from the centre of the chondrule contains intermediate trace element concentrations, as compared to olivine from the rim and matrix of the meteorite. Olivine from the chondrule rim contains minimum trace element concentrations. Very low concentrations are characteristic of Y 0.03, Al 56.7, REE 0.19 and Sr 0.11 ppm. Olivine from the matrix of the Borodino Meteorite is richer in Zr, Hf and LREE than olivine from chondrule 14PO-4.

The trace element distribution spectra for olivine from chondrule 14PO-4 are poorly differentiated (Fig.3, *b*). Trace element concentrations increase to chondrite values, which are much higher than trace element concentrations in olivine from UOC. The greatest prevalence is characteristic of refractory Zr, Hf, Nb and REE. In olivine from chondrule 14PO-4, LREE dominate over HREE.

Mesostasis from chondrule 14PO-4 consists of homogeneous poorly recrystallized glass of oligoclase composition (An 11 Or 4). Plagioclase occasionally occurs together with micron-sized troilite and chromite grains. The major element composition of the mesostasis is practically invariable, except for some minor variations in FeO (0.67-2.03 wt.%).

Journal of Mining Institute. 2024. Vol. 265. P. 16-33

Table 4

Major (wt.%) and trace (ppm) element composition of silicate minerals from 14PO-4 chondrule of the Borodino Meteorite

Component	Ol			Mes		
	Centre	Rim	Matrix	Centre	Rim	Matrix
SiO_2	39.45	39.50	39.50	64.37	64.63	–
Al_2O_3	0.00	0.00	0.00	20.86	21.33	–
MgO	42.65	43.05	42.94	0.11	0.09	–
TiO_2	0.00	0.02	0.03	0.04	0.06	–
CaO	0.03	0.04	0.02	2.44	2.47	–
FeO	17.80	17.69	17.89	2.03	0.67	–
MnO	0.47	0.47	0.48	–	–	–
Cr_2O_3	0.02	0.02	0.05	–	–	–
NiO	0.01	0.00	0.00	–	–	–
Na_2O	–	–	–	–	–	–
K_2O	–	–	–	–	–	–
Total	100.44	100.78	100.91	100.71	100.40	–
Zr	3.00	0.76	13.0	9.86	4.81	49.2
Hf	0.15	0.08	0.23	0.13	0.22	1.15
Ca	4340	3753	3513	–	–	–
Y	0.17	0.03	0.25	0.04	0.07	2.50
Al	1239	56.7	3967	–	–	–
Ti	70.4	75.4	739	281	250	1737
Nb	0.44	0.17	0.83	0.17	0.08	0.99
La	0.14	0.01	0.62	0.11	0.41	0.99
Ce	0.23	0.02	0.89	0.21	0.59	2.92
Pr	0.05	b.d.l.	0.15	0.01	0.07	0.25
Nd	0.14	0.07	0.48	0.03	0.31	1.16
Sm	0.11	b.d.l.	0.08	0.03	0.15	0.34
Eu	0.05	0.03	0.04	0.59	0.53	0.07
Gd	0.06	b.d.l.	0.14	0.04	0.10	0.37
Tb	–	–	–	–	–	–
Dy	0.03	b.d.l.	0.03	0.01	0.02	0.43
Ho	–	–	–	–	–	–
Er	b.d.l.	0.06	0.01	0.04	0.03	0.31
Yb	0.02	b.d.l.	0.06	b.d.l.	b.d.l.	0.37
Lu	0.01	b.d.l.	0.02	b.d.l.	b.d.l.	0.04
Sr	2.18	0.12	5.13	90.2	81.2	7.52
Ba	3.16	0.49	3.19	37.8	35.1	10.6
V	29.9	33.3	55.3	13.5	28.2	178
Ni	82.4	39.0	44.1	–	–	–
Cr	1111	1636	2792	24.5	648	3209
Rb	3.65	2.21	1.54	20.3	25.6	2.87
REE	0.85	0.19	2.52	1.07	2.21	7.24
LREE	0.73	0.13	2.25	0.98	2.06	5.72
HREE	0.12	0.06	0.27	0.09	0.15	1.52

Trace elements in mesostasis from chondrule 14PO-4 also vary slightly. Mesostasis contains minimum LREE concentration in the centre of the chondrule, but not at its rim. Mesostasis from the matrix has more trace and rare-earth elements than that from the chondrule, except for Eu.

The trace element distribution spectra obtained are differentiated with respect to the position of mesostasis in or outside the chondrule (Fig.3, *f*). For instance, mesostasis from the centre and at the rim of the chondrule is depleted in trace elements and displays the prevalence of LREE over HREE and a well-defined positive europium anomaly. Mesostasis from the matrix contains more trace elements than that from the chondrule, exhibits a poorly-defined negative anomaly and shows practically no light or heavy rare-earth element fractionation.

Mesostasis from the chondrule overlaps the plagioclase line for Renazzo coaly chondrite to a greater extent. However, it contains high refractory element (Zr and Hf) concentrations. Mesostasis from the matrix has a spectrum similar to that for plagioclase from Vigarano coaly chondrite. However, it contains high Zr and Hf concentrations and displays a negative europium anomaly.

Discussion. Olivines from porphyritic (14POP-1 and 14PO-4) and barred 14BOP-2 chondrules, pyroxene-olivine aggregate 14APO-3 and the Borodino Meteorite matrix have practically the same trace element concentrations, but display some minor differences in trace element composition.

The trace element distribution spectrum obtained for olivine is generally poorly-differentiated. However, there is a group of olivines enriched in incompatible LREE, Sr and Ba (Fig.4, *a*, *b*). These olivines are from the different objects (chondrules and aggregate) of the meteorite, look homogeneous on BSE-images and consist of coarse (over 200 μm) grains. However, there is no difference in the trace element composition of olivine, regardless of its position in the centre of the object, at the rim or in the matrix.

Differences in the objects of the Borodino Meteorite can be seen on plots showing Ca/Ni (Fig.4, *c*) and Cr/Nb ratios (Fig.4, *d*). Olivine from barred chondrule 14BOP-2 is richer in Ca and Ni than other objects of the Borodino Meteorite, forming an isolated cloud of points. Olivine from pyroxene-olivine aggregate 14APO-3 and a barred chondrule contains more Cr and Nb than olivine from porphyritic chondrules. Olivine from the Borodino Meteorite contains more trace refractory and rare-earth elements than olivine from UOC. The bulk of olivine has less Al than UOC.

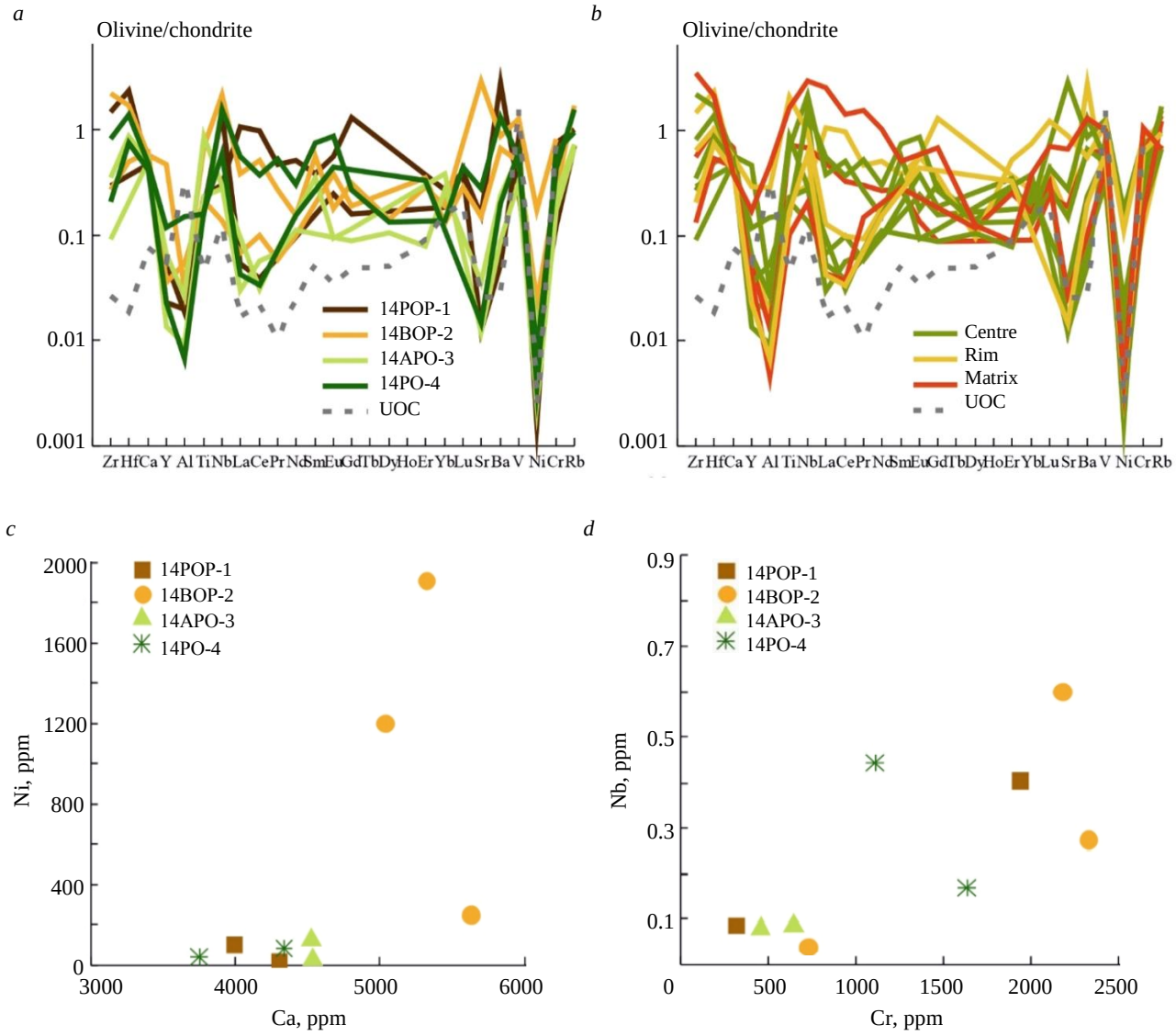

Fig.4. Spider diagrams for trace elements normalized to CI chondrite in olivine from the Borodino Meteorite relative to different chondrules (*a*) and the location of grains inside/outside the chondrule (*b*);
the Ca/Ni (*c*) and Cr /Nb (*d*) ratios. Data on the composition of UOC minerals are given according to [20, 21]

Journal of Mining Institute. 2024. Vol. 265. P. 16-33

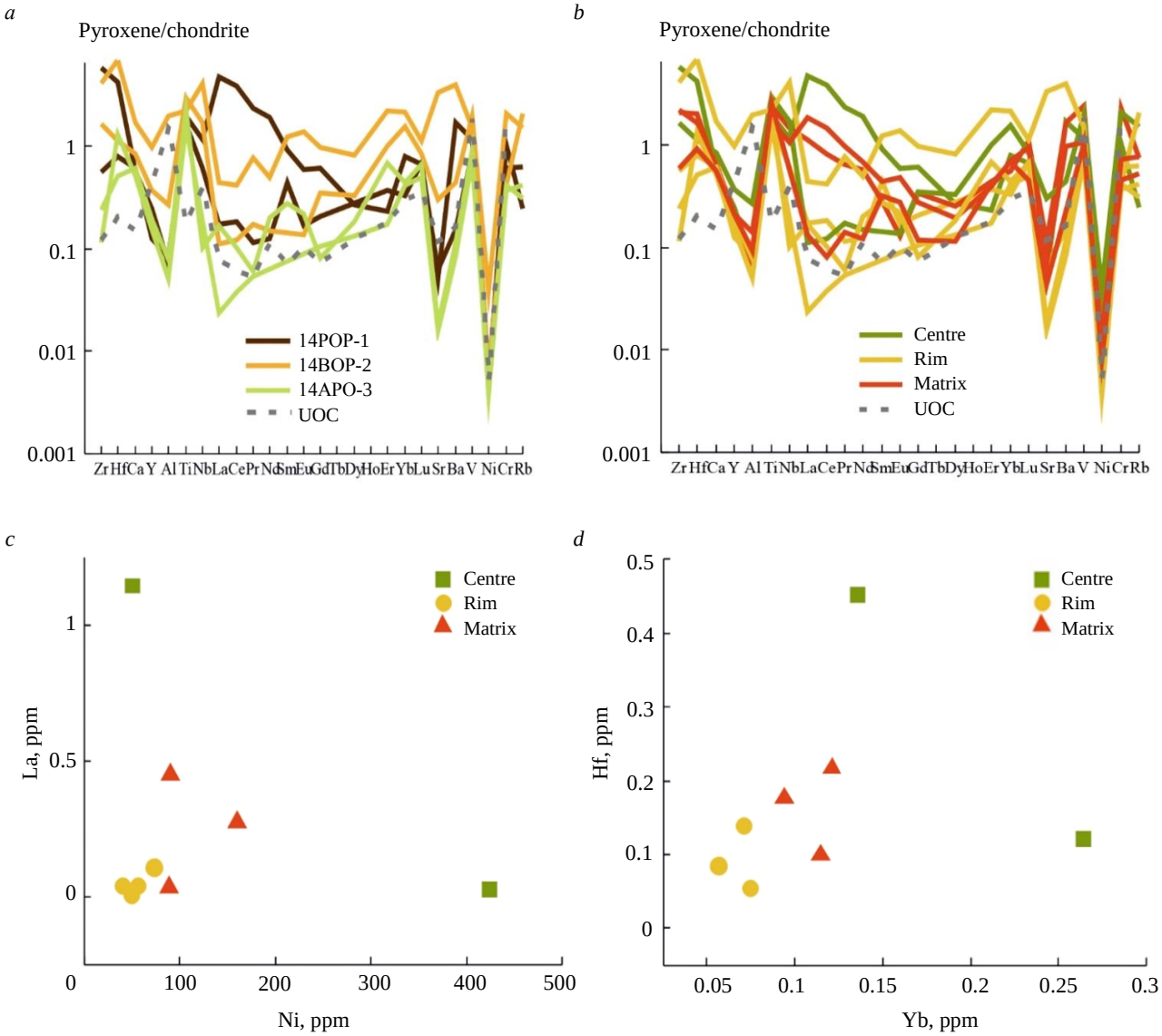

Fig.5. Spider diagrams for trace elements normalized to CI chondrite in low-Ca pyroxene from the Borodino Meteorite relative to different chondrules (*a*) and the location of grains inside/outside the chondrule (*b*);
the Ni/La (*c*) and Yb/Hf (*d*) ratios. Data on the composition of UOC minerals are given according to [20, 21]

Low-Ca pyroxene displays a variety of trace element concentrations, depending on the object in which it occurs. For instance, pyroxene from barred chondrule 14BOP-2 contains more trace elements than pyroxene from porphyritic chondrule 14POP-1 and aggregate 14APO-3 (Fig.5, *a*). Pyroxene from porphyritic chondrule 14POP-1 has low trace element concentrations. Pyroxene from the meteorite matrix is also depleted in trace elements, as compared to a barred chondrule and is more similar to pyroxene from a porphyritic chondrule (Fig.5, *b*).

Pyroxene from the Borodino Meteorite is not different from pyroxene present in porphyritic chondrules (UOC), except for a small amount of Al and high Ti concentration.

The concentration of some trace elements in low-Ca pyroxene is controlled by its position in the meteorite object. Point fields, corresponding to the position of pyroxene – in the centre, at the object rim or in the meteorite matrix, were obtained from Nb/Y (see Fig.3, *d*), Ni/La (Fig.5, *c*) and Yb/Hf (Fig.5, *d*) ratios. Thus, pyroxene from the centre of the meteorite is normally enriched in trace elements, pyroxene from the object rim is depleted in them and pyroxene from the meteorite matrix occupies an intermediate position. The trends revealed are characteristic of pyroxene from porphyritic and barred chondrules and pyroxene-olivine aggregate.

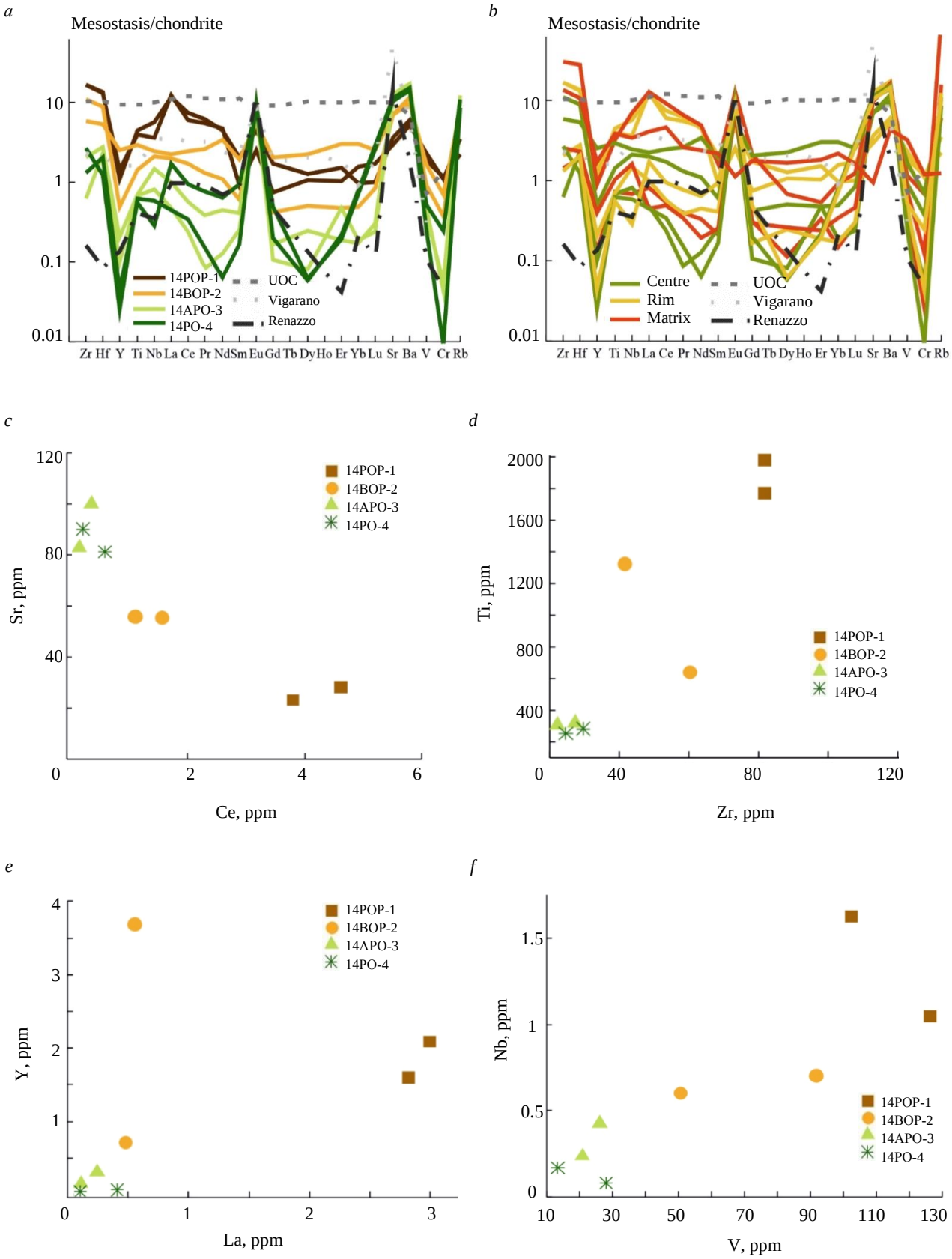

Fig.6. Spider diagrams for trace elements normalized to CI chondrite in mesostasis from the Borodino Meteorite relative to different chondrules (*a*) and the location of grains inside/outside the chondrule (*b*); the Ce/Sr (*c*), Zr/Ti (*d*), La/Y (*e*) and V/Nb (*f*) ratios. Data on the composition of UOC minerals are given according to [20, 21]

Journal of Mining Institute. 2024. Vol. 265. P. 16-33

The trace element composition of mesostasis is more informative than the object of the meteorite in which it occurs, as compared to olivine and low-Ca pyroxene. Mesostasis from barred chondrule 14BOP-2 and porphyritic 14POP-1 chondrules is richer in trace elements than mesostasis from porphyritic chondrule 14PO-4 and pyroxene-olivine aggregate 14APO-3 (Fig.6, *a*, *b*). The trace element distribution spectrum of metostasis 14BOP-2 and 14POP-1 is either similar to that of the Vigarano Meteorite or is slightly poorer.

Mesostasis from other objects of the meteorite is depleted in trace elements and is similar to a spectrum for plagioclase from Renazzo coaly chondrite.

Differences in trace element concentrations in mesostasis between the objects of the meteorite can be seen on plots showing Ce/Sr (Fig.6, *c*), Zr/Ti (Fig.6, *d*), La/Y (Fig.6, *e*) and V/Nb (Fig.6, *f*) ratios. The first three plots show three isolated groups of points corresponding to mesostasis 14PO-4 and 14APO-3 depleted in trace elements. An intermediate position is normally occupied by mesostasis from barred chondrule 14BOP-2, and the richest mesostasis from porphyritic chondrule 14POP-1 usually occupies an opposite marginal position. The plot for Ce-Sr correlation shows an inverse ratio: mesostasis from 14PO-4 and 14APO-3 is enriched in Sr but is depleted in Ce. Mesostasis from chondrule 14POP-1 is enriched in Ce but contains minimum Sr concentration, while mesostasis from the barred chondrule occupies an intermediate position.

In spite of obvious differences in the trace element composition of mesostasis from the various objects of the Borodino Meteorite, the chemical composition of mesostasis is not controlled by its position in the object.

Conclusions. Thus, minerals from porphyritic olivine-pyroxene and barred chondrules contain elevated trace element concentrations. Trace element concentrations in olivine is correlated with grain size. The trace element composition of low-Ca pyroxene is controlled by the position of a pyroxene grain in the meteorite object, and the composition of mesostasis by the object itself. The results obtained show no traces of the equilibration of the trace element composition of silicate minerals in the Borodino Meteorite.

High LREE/HREE values for unequilibrated ordinary chondrites (UOC) are correlated with a decrease in grain size. This trend is assumed to be due to the rapid cooling of fine grains [21]. Experiments have shown that trace element accumulation in olivine and low-Ca pyroxene is intensified by an increase in chondrule crystallization rate and, hence, olivine growth rate in it. Nevertheless, the evidence obtained contradicts the earlier studies referred to in the present paper. Further studies, e.g. analysis of trace element accumulation in olivine depending on controlled by grain cross-section and estimation of the real, rather than observed, size of olivine, are needed.

Low-Ca pyroxene and mesostasis from a barred chondrule contain elevated amounts of trace elements. This evidence is consistent with experimental data indicating the rapid crystallization of chondrule melt in a protoplanetary disc. Low-Ca pyroxene shows an increase in trace element concentrations in the following sequence: rim – matrix – centre, which could be due to chondrule-nebular gas interaction [35].

The author is grateful to Candidate of Physics and Mathematics S.G.Simakin and E.V.Potapov (*Valiev IPT RAS, Yaroslavl Branch*) *for their analytical work.*

REFERENCES

1. Ivanova M.A., Nazarov M.A. History of the meteorite collection of the Russian Academy of Sciences. *Geological Society, London, Special Publications*. 2006. Vol. 256, p. 219-236. DOI: 10.1144/GSL.SP.2006.256.01.11

2. Obolonskaya E.V., Popova E.E. Meteorite Borodino. *Russkaya istoriya*. 2012. N 1, p. 95-96 (in Russian).

3. Obolonskaya E.V., Popova E.E. Meteorite collection from the Mining Museum of St. Petersburg Mining University. Meteorit Chelyabinsk – god na Zemle: Materialy Vserossiiskoi nauchnoi konferentsii, 14-15 fevralya 2014, Chelyabinsk, Rossiya. Chelyabinsk: Chelyabinskii gosudarstvennyi kraevedcheskii muzei, 2014, p. 355-363 (in Russian).

4. Scott E.R.D., Krot A.N. Chondrites and Their Components. *Treatise on Geochemistry* (*Second Edition*). 2014. Vol. 1, p. 65-137. DOI: 10.1016/B978-0-08-095975-7.00104-2

5. Chondrules: Records of Protoplanetary Disk Processes. Ed. by S.S.Russell, Jr.H.C.Connolly, A.N.Krot. Cambridge: Cambridge University Press, 2018, p. 450. DOI: 10.1017/9781108284073

6. Jacquet E., Piralla M., Kersaho P., Marrocchi Y. Origin of isolated olivine grains in carbonaceous chondrites. *Meteoritics & Planetary Science*. 2021. Vol. 56. N 1, p. 13-33. DOI: 10.1111/maps.13583

7. Marrocchi Y., Euverte R., Villeneuve J. et al. Formation of CV chondrules by recycling of amoeboid olivine aggregate-like precursors. *Geochimica et Cosmochimica Acta*. 2019. Vol. 247, p. 121-141. DOI: 10.1016/j.gca.2018.12.038

8. Nardi L., Palomba E., Longobardo A. et al. Mapping olivine abundance on asteroid (25143) Itokawa from Hayabusa/NIRS data. *Icarus*. 2019. Vol. 321, p. 14-28. DOI: 10.1016/j.icarus.2018.10.035

9. Jacquet E., Marrocchi Y. Chondrule heritage and thermal histories from trace element and oxygen isotope analyses of chondrules and amoeboid olivine aggregates. *Meteoritics & Planetary Science*. 2017. Vol. 52. Iss. 12, p. 2672-2694. DOI: 10.1111/maps.12985

10. Libourel G., Krot A.N. Evidence for the presence of planetesimal material among the precursors of magnesian chondrules of nebular origin. *Earth and Planetary Science Letters*. 2007. Vol. 254. Iss. 1-2, p. 1-8. DOI: 10.1016/j.epsl.2006.11.013

11. Tenner T.J., Nakashima D., Ushikubo T. et al. Oxygen isotope ratios of FeO-poor chondrules in CR3 chondrites: Influence of dust enrichment and H_2O during chondrule formation. *Geochimica et Cosmochimica Acta*. 2015. Vol. 148, p. 228-250. DOI: 10.1016/j.gca.2014.09.025

12. Bischoff A., Schleiting M., Wieler R., Patzek M. Brecciation among 2280 ordinary chondrites – Constraints on the evolution of their parent bodies. *Geochimica et Cosmochimica Acta*. 2018. Vol. 238, p. 516-541. DOI: 10.1016/j.gca.2018.07.020

13. Grossman J.N., Brearley A.J. The onset of metamorphism in ordinary and carbonaceous chondrites. *Meteoritics & Planetary Science*. 2005. Vol. 40. Iss. 1, p. 87-122. DOI: 10.1111/j.1945-5100.2005.tb00366.x

14. Chakraborty S. Diffusion Coefficients in Olivine, Wadsleyite and Ringwoodite. *Reviews in Mineralogy and Geochemistry*. 2010. Vol. 72. N 1, p. 603-639. DOI: 10.2138/rmg.2010.72.13

15. Cherniak D.J. REE diffusion in olivine. *American Mineralogist*. 2010. Vol. 95. N 2-3, p. 362-368. DOI: 10.2138/am.2010.3345

16. Pape J., Mezger K., Bouvier A.-S., Baumgartner L.P. Time and duration of chondrule formation: Constraints from ^{26}Al-^{26}Mg ages of individual chondrules. *Geochimica et Cosmochimica Acta*. 2019. Vol. 244, p. 416-436. DOI: 10.1016/j.gca.2018.10.017

17. Marrocchi Y., Villeneuve J., Batanova V. et al. Oxygen isotopic diversity of chondrule precursors and the nebular origin of chondrules. *Earth and Planetary Science Letters*. 2018. Vol. 496, p. 132-141. DOI: 10.1016/j.epsl.2018.05.042

18. Piralla M., Villeneuve J., Batanova V. et al. Conditions of chondrule formation in ordinary chondrites. *Geochimica et Cosmochimica Acta*. 2021. Vol. 313, p. 295-312. DOI: 10.1016/j.gca.2021.08.007

19. Varela M.E. Bulk trace elements of Mg-rich cryptocrystalline and ferrous radiating pyroxene chondrules from Acfer 182: Their evolution paths. *Geochimica et Cosmochimica Acta*. 2019. Vol. 257, p. 1-15. DOI: 10.1016/j.gca.2019.04.025

20. Jacquet E., Alard O., Gounelle M. Trace element geochemistry of ordinary chondrite chondrules: The type I/type II chondrule dichotomy. *Geochimica et Cosmochimica Acta*. 2015. Vol. 155, p. 47-67. DOI: 10.1016/j.gca.2015.02.005

21. Jacquet E., Alard O., Gounelle M. Chondrule trace element geochemistry at the mineral scale. *Meteoritics & Planetary Science*. 2012. Vol. 47. N 11, p. 1695-1714. DOI: 10.1111/maps.12005

22. Jacquet E., Alard O., Gounelle M. The formation conditions of enstatite chondrites: Insights from trace element geochemistry of olivine-bearing chondrules in Sahara 97096 (EH3). *Meteoritics & Planetary Science*. 2015. Vol. 50. N 9, p. 1624-1642. DOI: 10.1111/maps.12481

23. Varela M.E., Sylvester P., Brandstätter F., Engler A. Nonporphyritic chondrules and chondrule fragments in enstatite chondrites: Insights into their origin and secondary processing. *Meteoritics & Planetary Science*. 2015. Vol. 50. N 8, p. 1338-1361. DOI: 10.1111/maps.12468

24. Skublov S.G., Rumyantseva N.A., Vanshtein B.G. et al. Zircon Xenocrysts from the Shaka Ridge Record Ancient Continental Crust: New U-Pb Geochronological and Oxygen Isotopic Data. *Journal of Earth Science*. 2022. Vol. 33. N 1, p. 5-16. DOI: 10.1007/s12583-021-1422-2

25. Rumyantseva N.A., Skublov S.G., Vanshteina B.G. et al. Zircon from Gabbroids of the Shaka Ridge (South Atlantic): U-Pb Age, Oxygen Isotope Ratios and Trace Element Composition. *Proceedings of the Russian Mineralogical Society*. 2022. Part CLI. N 1, p. 44-73 (in Russian). DOI: 10.31857/S0869605522010099

26. Skublov S.G., Gavrilchik A.K., Berezin A.V. Geochemistry of beryl varieties: comparative analysis and visualization of analytical data by principal component analysis (PCA) and t-distributed stochastic neighbor embedding (t-SNE). *Journal of Mining Institute*. 2022. Vol. 255, p. 455-469. DOI: 10.31897/PMI.2022.40

27. Gavrilchik A.K., Skublov S.G., Kotova E.L. Trace Element Composition of Beryl From the Sherlovaya Gora Deposit, South-Eastern Transbaikalia, Russia. *Proceedings of the Russian Mineralogical Society*. 2021. Part CL. N 2, p. 69-82 (in Russian). DOI: 10.31857/S0869605521020052

28. Ashikhmin D.S., Skublov S.G., Melnik A.E. et al. Geochemistry of Rock-Forming Minerals in Mantle Xenoliths from Basalts of Sverre Volcano, Spitsbergen Archipelago. *Geochemistry International*. 2018. Vol. 56, p. 857-864. DOI: 10.1134/S0016702918080025

29. Sukhanova K.G., Kuznetsov A.B., Galankina O.L. Features of olivine crystallization in ordinary chondrites (Saratov meteorite): geochemistry of trace and rare earth elements. *Journal of Mining Institute*. 2022. Vol. 254, p. 149-157. DOI: 10.31897/PMI.2022.39

30. Sukhanova K.G., Skublov S.G., Galankina O.L. et al. Trace Element Composition of Silicate Minerals in the Chondrules and Matrix of the Buschhof Meteorite. *Geochemistry International*. 2020. Vol. 58, p. 1321-1330. DOI: 10.1134/S001670292012006X

Journal of Mining Institute. *2024. Vol. 265. P. 16-33*

31. Sukhanova K.G. Silicate minerals composition as a reflection of equilibrated ordinary chondrite evolution: Avtoref. dis. … kand. geol.-mineral. nauk. Moscow: Moskovskii gosudarstvennyi universitet, 2022, p. 21 (in Russian).

32. Zanetta P.-M., Le Guillou C., Leroux H. et al. Modal abundance, density and chemistry of micrometer-sized assemblages by advanced electron microscopy: Application to chondrites. *Chemical Geology*. 2019. Vol. 514, p. 27-41. DOI: 10.1016/j.chemgeo.2019.03.025

33. Portnyagin M., Almeev R., Matveev S., Holtz F. Experimental evidence for rapid water exchange between melt inclusions in olivine and host magma. *Earth and Planetary Science Letters*. 2008. Vol. 272. Iss. 3-4, p. 541-552. DOI: 10.1016/j.epsl.2008.05.020

34. Palme H., Lodders K., Jones A. Solar System Abundances of the Elements. *Treatise on Geochemistry* (*Second Edition*). 2014. Vol. 2, p. 15-36. DOI: 10.1016/b978-0-08-095975-7.00118-2

35. Engler A., Varela M.E., Kurat G. et al. The origin of non-porphyritic pyroxene chondrules in UOCs: Liquid solar nebula condensates? *Icarus*. 2007. Vol. 192. Iss. 1, p. 248-286. DOI: 10.1016/j.icarus.2007.06.016

Author **Kristina G. Sukhanova,** *Candidate of Geological and Mineralogical Sciences, Junior Researcher, cris.suhanova92@yandex.ru, https://orcid.org/0000-0001-5695-0767* (*Institute of Precambrian Geology and Geochronology RAS, Saint Petersburg, Russia*).

The author declares no conflict of interests.

ISSN 2411-3336; e-ISSN 2541-9404

JOURNAL OF MINING INSTITUTE

Zapiski Gornogo instituta

Journal homepage: pmi.spmi.ru

Research article

Determination of the accuracy of leveling route based on GNSS/leveling and Earth gravitational model data SGG-UGM-2 at some typical regions in Vietnam

BUI THI HONG THAM, PHI TRUONG THANH✉
Hanoi University of Natural Resources and Environment, Hanoi, Vietnam

***How to cite this article*:** Bui Thi Hong Tham, Phi Truong Thanh. Determination of the accuracy of leveling route based on GNSS/leveling and Earth gravitational model data SGG-UGM-2 at some typical regions in Vietnam. Journal of Mining Institute. 2024. Vol. 265, p. 34-44. EDN UGMFEW

Abstract. This paper presents the accuracy of leveling routes determined by using GNSS/leveling at three grades and Earth gravitational model data SGG-UGM-2 in four regions of Vietnam by calculating the difference between the measured height anomalies and the model of pairs of points. The calculation is made based on the total points of three grades for four regions (99 in the Northwest, 34 in the Red River Delta, 130 in the Central Highlands, and 96 in the Mekong River Delta) with the leveling routes, connected between pair of points in each region are 189, 92, 294, and 203. The calculated results of the percentage of accuracy of the leveling routes of the four regions have shown that most of the leveling routes are satisfactory (grades I-IV, and technical leveling). The determination of the accuracy of the leveling route is completely applicable to other areas when the points have simultaneous ellipsoid and leveling heights and it also helps managers and surveyors to predict the accuracy of the height points when the above-mentioned leveling routes are connected and to take reasonable measures when implementing the project.

***Keywords*:** Earth gravitational model; GNSS/leveling; height; accuracy; SGG-UGM-2

Acknowledgment. The article was written as part of the project TNMT.2022.562.04 by the Ministry of Natural Resources and Environment (MONRE), Vietnam.

Received: 25.06.2022 ***Accepted: 20.06.2023*** ***Online: 29.11.2023*** ***Published: 29.02.2024***

Introduction. A height system is a one-dimensional coordinate system used to determine the metric distance of some points from a reference surface along a well-defined path, termed simply the height of that point [1]. Corresponding to the reference surface will give the type of height: the geoid reference surface will give the orthometric height, and the quasigeoid reference surface will give the normal height (also known as the leveling height). The reference surface is the ellipsoid which will give the ellipsoid height.

Most countries in the world have used the normal height system as the national height system. This height system is concretized by benchmarks (called national height points) buried in the field. The normal heights of benchmarks are determined based on the starting surface which is the average sea level for many years. National height points are control points serving the construction of all kinds of works for the socio-economic development, security, and defense of each country.

To establish topographic maps, cadastral maps, construction of civil and industrial works, traffic works, irrigation, mining, etc., height points are built. These points are connected with the national benchmarks from the leveling routes, and leveling closed loops. Therefore, if we know the accuracy of the leveling routes, we can predict the height accuracy of the connection points with those national height points.

In order to determine the accuracy of the leveling routes to achieve grade, it usually takes the following steps: measure in the field; process measurement data to calculate the mean square error

Journal of Mining Institute. 2024. Vol. 265. P. 34-44

per one km leveling route; compare the mean square error per one km leveling route with the permitted measurement error for leveling grades [2-6].

The accuracy of the leveling route is determined after the process of measuring and processing data, which wastes time and money, especially if the leveling route does not reach the required accuracy. Therefore, the idea of this study is to determine the accuracy of the leveling route without having to take measurements in the field. To carry out this study, the Earth gravitational model and GNSS/leveling data were used.

An Earth gravitational model (EGM) is a set of geopotential coefficients used in a spherical harmonic expansion to create a global potential surface to coincide with the Mean Sea Level (MSL). This model is used as the reference geoid in the WGS. Basically, Earth gravity model data are provided in two formats: as a series of spherical harmonic coefficients determining the model and as a geoid height of the point which have a coordinate. A GNSS point that has an ellipsoid height and leveling height is called a GNSS/leveling point.

GNSS/leveling data and Earth gravitational model play an important role in studies of the geoid, and national height systems and it is the input data source to carry out studies, such as:

The GNSS/leveling data is used to evaluate the accuracy of the global gravity model such as: evaluating and comparing models GOCE, EGM2008 in the Mediterranean area [7], Japan [8]; evaluating models EGM08, EIGEN-6C4, GECO in Iran [9], Turkey [10]; evaluating model EGM2008 [11]; comparing model XGM2019e with XGM2016, EIGEN-6C4, EGM2008 [12]; compare models EGM2008 and EGM96 in Iraq [13]; evaluating model EGM2008, EIGEN-6C4, XGM2019e_2159 in Korea [14]; comparing model EIGEN-6C4 with EGM2008 in Europe, USA, Canada, Brazil, Japan, Czech Republic and Slovakia [15]; evaluating the accuracy of models EGM2008, EIGEN-6C4, GECO, and SGG-UGM-1 in Kenya [16]; evaluating models EGM2008, EIGEN6C4, and GECO in the Aegean region [17]; evaluating models EGM96, EGM84, and EGM2008 in Iraq [18]; comparing models EGM96 and EGM2008 in Iraq [19]; comparing models OUS-91A, EGM96, and EGM2008 in Egypt [20]; evaluating model EGM2008 in Bangladesh [21]. GNSS/leveling data was used to build local geoid models such as in Iraq [19], Turkey [22], Evboriaria, Benin City (Nigeria) [23].

GNSS/leveling data were used to correct the global gravity model and build a local geoid model: the model EGM2008 and GNSS/leveling data to build a local geoid model in Indonesia [24], Nigeria [25], Vietnam [26], Turkey [27], Egypt [28], China [29], the USA [30]; model EIGEN6C4, leveling data, GNSS to build a local geoid model in Uganda [31].

GNSS/leveling data and the global gravity model were used to build the height system in Italy [32], the GNSS/leveling data and the model EGM2008 to build the height system in Palestine [33]; the GNSS/leveling was together with GOCE data to estimate the height reference system in Canada [34].

GNSS/leveling data, global gravity model and other data were used to build local geoid model: GNSS/leveling together with EGM2008 data, digital terrestrial model to determine geoid model in Mexico [35]; GNSS/leveling together with EIGEN-6C4 gravity data to build geoid model in Qatar [36]; GNSS/leveling together with GOCE data to build geoid models in the state of São Paulo (Brazil) [37]; GNSS/leveling together with model data XGM2019e_2159, digital terrestrial model ACE2 GDEM to build geoid model in Egypt [28]; GNSS/leveling together with model data EGM2008, EIGEN-6C4, gravity data, high-resolution topographic data, bathymetric data to build geoid model in Vietnam [38].

GNSS/leveling data and Earth gravitational model are indispensable factors when studying height-related issues in countries. It is an input data source to support evaluating the accuracy of the global gravity model, building the national height system, and the local geoid model.

In this study, based on the GNSS/leveling data and Earth gravitational model, the theoretical basis for determining the accuracy of the leveling routes is presented logically and rigorously. Based on the collected data, the experimental areas are selected as the areas in the territory of Vietnam.

Theoretical basis. The relationship between the ellipsoid height *h* and the normal height *H* is presented by the formula

$$\zeta^i_{\text{GNSS/leveling}} \approx h^i - H^i, \tag{1}$$

where $\zeta^i_{\text{GNSS/leveling}}$ – height anomaly of point *i*.

The height anomaly value can also be determined based on the Earth gravitational model.

To determine the accuracy of the leveling route connecting the national GNSS/leveling points, the value of the height anomaly when determined according to the GNSS/leveling data is compared with the corresponding data taken from the Earth gravitational model.

Suggested ζ^i_{model} is the height anomaly of the point *i* extracted from the Earth gravitational model. The formula for calculating the height anomaly of the point *i* is written as follows:

$$\Delta\zeta^i = \zeta^i_{\text{GNSS/leveling}} - \zeta^i_{\text{model}} = h^i - H^i - \zeta^i_{\text{model}}. \tag{2}$$

Calculate the average value of the deviation of height anomaly according to the following formula

$$\Delta\zeta_{\text{average}} = \sum_{i=1}^{n} \Delta\zeta^i / n, \tag{3}$$

where *n* – is point numbers.

The deviation of the pair of points *i* and *j* (Fig.1) are calculated according to the following formula

$$\Delta\zeta^{ij} = \Delta\zeta^j - \Delta\zeta^i. \tag{4}$$

Combination of formula (2) and (3), get

$$\Delta\zeta^{ij} = h^j - h^i - \left(H^j - H^i\right) - \left(\zeta^j_{\text{model}} - \zeta^i_{\text{model}}\right). \tag{5}$$

Assign formulas

$$\begin{gathered} \Delta h^{ij} = h^j - h^i; \quad \Delta H^{ij} = H^j - H^i; \\ \Delta\zeta^{ij}_{\text{model}} = \zeta^j_{\text{model}} - \zeta^i_{\text{model}}; \quad \Delta\zeta^{ij}_{\text{GNSS/leveling}} = \Delta h^{ij} - \Delta H^{ij}, \end{gathered} \tag{6}$$

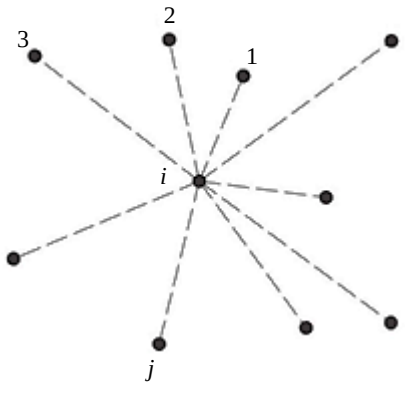

Fig.1. Pairs of points

get the equation

$$\Delta\zeta^{ij} = \Delta h^{ij} - \Delta H^{ij} - \Delta\zeta^{ij}_{\text{model}} = \Delta\zeta^{ij}_{\text{GNSS/leveling}} - \Delta\zeta^{ij}_{\text{model}}. \tag{7}$$

The weight of the equation (6) is calculated according to the formula

$$P^{ij} = \frac{1}{D^{ij}}, \tag{8}$$

where *D* – is the distance between points *i* and *j*, km.

The mean square error of the height anomaly difference over one kilometer is calculated according to the following formula

Journal of Mining Institute. 2024. Vol. 265. P. 34-44

$$m_{\text{km}} = \sqrt{\frac{\left[P\Delta\zeta^i\Delta\zeta^j\right]}{q}}, \tag{9}$$

where q – is the number of pairs of points used to perform the calculation.

The national standard on building height networks, the permited error for leveling route, leveling closed loop according to the grade are specified. In Vietnam, for mountainous areas, the permited error for leveling route, leveling closed loop of grades I, II, III, IV is $3\sqrt{L}$, $5\sqrt{L}$, $12\sqrt{L}$, $25\sqrt{L}$ (L is in mm); respectively; for in the plains, these errors are $2\sqrt{L}$, $4\sqrt{L}$, $10\sqrt{L}$, $20\sqrt{L}$, respectively; for technical leveling, the error is $50\sqrt{L}$ (L is in km).

Vietnam is a country which has mostly low hills and mountains, with plains making up about a quarter of the area. Based on topography and economic development, Vietnam is divided into the following regions:

• Northwest region – terrain with many high mountain ranges;

• Northeast region – low hills;

• Red River Delta – relatively flat terrain, it is the economic center of the northern region of Vietnam;

• North central coast – mixed topography of mountains, hills and plains;

• South central coast – low mountains and plains;

• Highlands region – diverse topography, includes: high mountains, plateaus and large plains;

• Southeast region – midlands and low hills;

• Southwest region or Mekong River Delta – terrain is relatively flat, quite low compared to sea level, often affected by tides.

According to the national standard on building height networks, with different topographical areas, the error of leveling route, leveling closed loop according to their grades is different. Therefore, the areas having a typical topography of Vietnam are selected for research including: Northwest, Red River Delta, Central Highlands, Mekong River Delta. Data sources used in the analysis include GNSS/Leveling data and Earth gravitational model data.

GNSS/leveling data. The points number of national GNSS/leveling in each experimental area is listed in Table 1. The leveling and geodetic heights of the GNSS/leveling points are detailed in Table 2.

Table 1

GNSS/ leveling points

Region	Number of GNSS/ leveling points			Total
	Grade I	Grade II	Grade III	
Northwest	35	16	48	99
Red River Delta	20	11	3	34
Highlands	24	26	80	130
Mekong river Delta	13	52	31	96

Table 2

Data of GNSS/leveling points

Points number	Point index	B^0	L^0	h, m	H, m
1	I(BMT-APD)12	12.28926	107.59477	907.6780	907.9755
2	I(BMT-APD)1-2	12.65835	108.02837	431.3888	431.2042
3	I(BMT-APD)16	12.10935	107.65618	833.2335	832.9730
4	I(BMT-APD)22	11.99578	107.51564	732.3017	732.6708

End of Table 2

Points number	Point index	B^0	L^0	h, m	H, m
5	I(BMT-APD)25	11.93166	107.42908	575.1619	576.0473
6	I(BMT-APD)3	12.58108	107.84340	358.1393	358.6506
7	I(BMT-APD)6	12.49414	107.74019	580.5556	581.0788
8	I(BMT-NH)11-1	12.80411	108.54048	468.5150	466.5640
9	I(BMT-NH)17-1	12.73304	108.75417	423.7629	420.9371
10	I(BMT-NH)22	12.58583	108.85847	561.2232	557.7819
…	…	…	…	…	…
351	III(TT-GR)4	9.95520	105.36885	–5.6633	0.9933
352	III(TT-HN)2	10.92092	105.42574	–4.3237	4.1669
353	III(TT-TS)1	10.25559	105.16435	–5.4807	2.6149
354	III(TV-LS)9	9.71773	106.42700	–0.1141	2.0210
355	III(TY-VD)9	9.22404	104.81945	–6.3808	0.4914
356	III(UM-HDB)7	10.52037	104.70823	–8.4336	2.0185
357	III(VL-MC)7	10.23367	106.18661	–2.0257	1.8265
358	III(VT-PS)5	9.37355	105.39224	–4.1265	1.1779
359	III(VT-VC)7	9.29983	105.93297	–1.2964	1.4918

Earth gravitational model data. The Earth gravitational model SGG-UGM-2 is the latest model published in 2020. The data of this model can be accessed at the website of the International Center for Global Earth Models (ICGEM) (http://icgem.gfz-potsdam.de/tom). Height anomaly data of GNSS/leveling points got from the Earth gravitational model are listed in Table 3.

Table 3

Height anomaly data of GNSS/leveling points got from Earth gravitational model

Points number	Point index	$\zeta_{SGG-UGM-2}$, m	Points number	Point index	$\zeta_{SGG-UGM-2}$, m
1	I(BMT-APD)12	–0.6568	…	…	…
2	I(BMT-APD)1-2	–0.4138	351	III(TT-GR)4	–6.9711
3	I(BMT-APD)16	–0.0710	352	III(TT-HN)2	–9.1764
4	I(BMT-APD)22	–0.6639	353	III(TT-TS)1	–8.7063
5	I(BMT-APD)25	–1.1798	354	III(TV-LS)9	–2.4782
6	I(BMT-APD)3	–1.0340	355	III(TY-VD)9	–7.1055
7	I(BMT-APD)6	–1.0081	356	III(UM-HDB)7	–11.1486
8	I(BMT-NH)11-1	1.3586	357	III(VL-MC)7	–4.1515
9	I(BMT-NH)17-1	2.3220	358	III(VT-PS)5	–5.4536
10	I(BMT-NH)22	3.0755	359	III(VT-VC)7	–3.1043

Results and discussions. The accuracy of the leveling routes is carried out according to the following steps:

1. Calculate the height anomalies from measurement data GNSS/leveling $\zeta^i_{\text{GNSS/leveling}}$ (formula (2).

2. Calculate the deviation of hight anomaly between the measured height anomalies and model $\Delta\zeta^i$. The mean value of high anomaly $\Delta\zeta_{\text{average}}$ is calculated in formula 3.

Journal of Mining Institute. 2024. Vol. 265. P. 34-44

3. Calculate the deviation of height anomalies of the pairs of points $\Delta\zeta^{ij}$ (formula (5).

4. Calculate the weight of the leveling route P^{ij} (formula (8).

5. Calculate the mean square error of the height anomaly difference per kilometer m_{km} (formula (9) for each leveling route and for four regions.

6. Calculate the permited error for each leveling route m_{permited}.

7. Compare the mean square error of the height anomaly difference per kilometer of each leveling route with the permited error.

The calculated results in steps 1 and 2 are shown in Table 4 and Fig.2.

Table 4

Height anomalies from measurement data GNSS/leveling and their deviation and the model value

Points number	Point index	$\zeta^i_{\text{GNSS/leveling}}$, m	$\Delta\zeta^i$, m	Points number	Point index	$\zeta^i_{\text{GNSS/leveling}}$, m	$\Delta\zeta^i$, m
1	I(BMT-APD)12	–0.2975	0.3593	…	…	…	…
2	I(BMT-APD)1-2	0.1846	0.5984	351	III(TT-GR)4	–6.6566	0.3145
3	I(BMT-APD)16	0.2605	0.3315	352	III(TT-HN)2	–8.4906	0.6858
4	I(BMT-APD)22	–0.3691	0.2948	353	III(TT-TS)1	–8.0956	0.6107
5	I(BMT-APD)25	–0.8854	0.2944	354	III(TV-LS)9	–2.1351	0.3431
6	I(BMT-APD)3	–0.5113	0.5227	355	III(TY-VD)9	–6.8722	0.2333
7	I(BMT-APD)6	–0.5232	0.4849	356	III(UM-HDB)7	–10.4521	0.6965
8	I(BMT-NH)11-1	1.9510	0.5924	357	III(VL-MC)7	–3.8522	0.2993
9	I(BMT-NH)17-1	2.8258	0.5038	358	III(VT-PS)5	–5.3044	0.1492
10	I(BMT-NH)22	3.4413	0.3658	359	III(VT-VC)7	–2.7882	0.3161

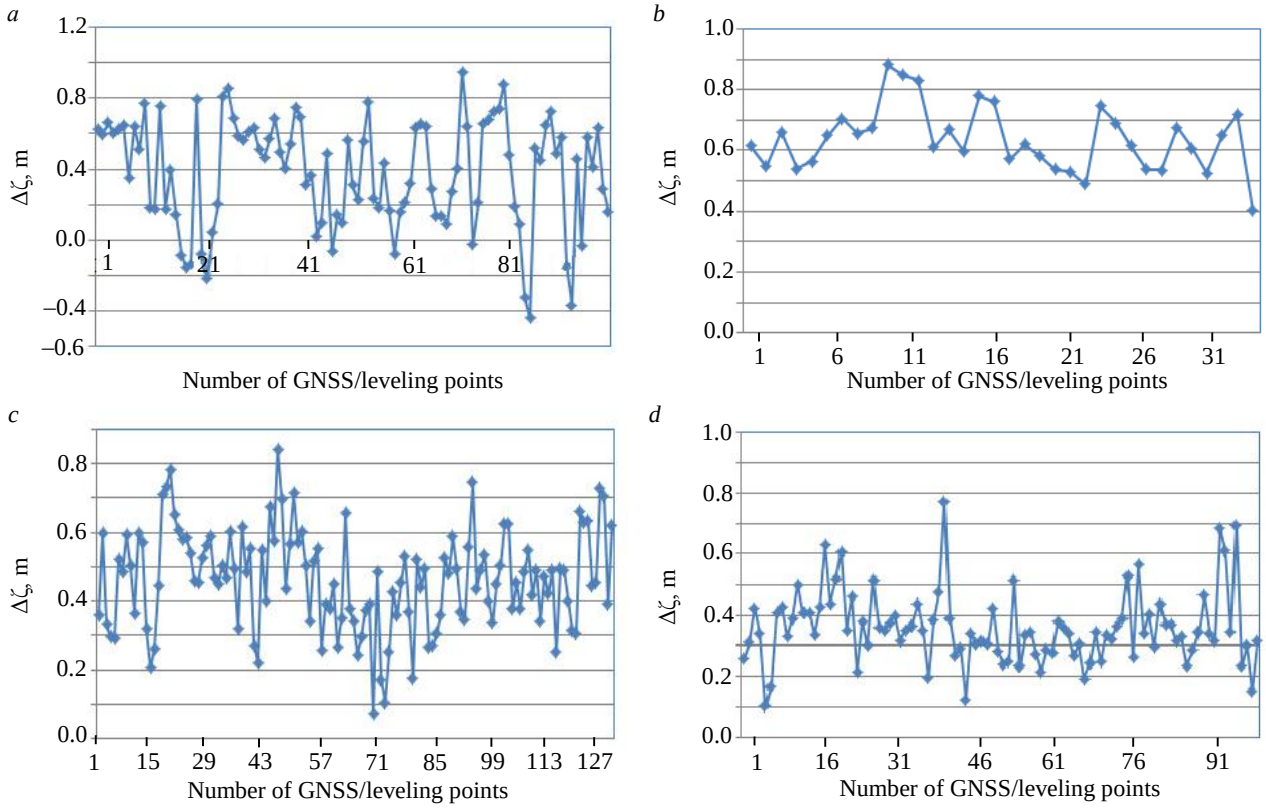

Fig.2. Height anomaly of model SGG-UGM-2 with the height anomaly of the GPS/ leveling:
a – Northwest; *b* – Red River Delta; *c* – Central Highlands; *d* – Mekong River Delta

Figure 2 shows that the topography of the four regions is generally higher than the model SGG-UGM-2. The average value of the deviation of height anomaly of the GNSS/leveling points between the measurements and model makes in the Northwest 0.4249 m, Red River Delta 0.6369 m, Central Highlands 0.4638 m, and Mekong River Delta 0.3588 m.

The calculated results in steps 3 and 4. From the GNSS/leveling points at the four regions, the leveling routes are formed based on pairs of points with the number of routes in the Northwest region 189, Red River Delta 92, Central Highlands 294, and Mekong River Delta 203. The measured height anomaly values and models of GNSS/leveling routes are shown in Table 5.

Table 5

The deviation of height anomalies of the national GNSS/leveling of pairs of points

Points number	Start point	End point	D, km	$\Delta\zeta^{ij}_{\text{GNSS/leveling}}$, m	$\Delta\zeta^{ij}_{\text{model}}$, m	$\Delta\zeta^{ij}$, m	P^{ij}
1	I(BMT-APD)12	I(BMT-APD)16	21.0	–0.5580	–0.5858	0.0278	0.048
2	I(BMT-APD)12	III(DBS-DL)3	23.4	0.3530	0.1683	0.1847	0.043
3	I(BMT-APD)12	III(QS-DN)2	29.8	–1.1846	–1.2386	0.0540	0.034
4	I(BMT-APD)12	III(BDS-QP)5	33.0	–0.7274	–0.4316	–0.2958	0.030
5	I(BMT-APD)22	I(BMT-APD)25	11.8	0.5163	0.5159	0.0004	0.085
6	I(BMT-APD)22	I(BMT-APD)16	19.8	–0.6296	–0.5930	–0.0366	0.050
7	I(BMT-APD)25	I(BMT-APD)30	24.0	0.9462	0.9868	–0.0406	0.042
8	I(BMT-APD)25	III(BGM-MH)3	32.7	1.6841	1.8078	–0.1237	0.031
9	I(BMT-APD)3	I(BMT-APD)6	14.8	0.0119	–0.0259	0.0378	0.068
10	I(BMT-APD)3	III(BDS-QP)5	21.3	–0.9412	–0.8088	–0.1324	0.047
…	…	…	…	…	…	…	…
767	III(TT-HN)2	II(HN-AB)7	23.7	–0.7255	–1.0619	0.3364	0.042
768	III(TT-TS)1	II(CD-VC)8	32.3	–0.1642	–0.5622	0.3980	0.031
769	III(UM-HDB)7	III(OD-CN)1	26.1	–0.7561	–0.6581	–0.0980	0.038
770	III(VL-MC)7	II(TL-TV)5-1	17.5	–0.6959	–0.6593	–0.0366	0.057
771	III(VL-MC)7	II(MT-TV)6-1	17.6	–0.1647	–0.1954	0.0307	0.057
772	III(VL-MC)7	III(LH-TH)1	21.6	0.3888	0.4602	–0.0714	0.046
773	III(VL-MC)7	I(VL-HT)273A	23.1	–0.3478	–0.3374	–0.0104	0.043
774	III(VL-MC)7	II(TX-TL)25	24.9	1.1117	1.1544	–0.0427	0.040
775	III(VL-MC)7	I(VL-HT)284A	29.2	–1.1320	–0.9975	–0.1345	0.034
776	III(VT-PS)5	II(SC-PL)34	20.7	0.9892	0.9625	0.0267	0.048
777	III(VT-PS)5	II(SC-PL)15	21.9	0.6785	0.5949	0.0836	0.046
778	III(VT-VC)7	II(ST-PL)2	27.5	–0.7561	–0.6581	–0.0980	0.036

The calculated results from steps 5 to 7. The mean square error of the height anomaly difference over 1km of the four regions is calculated according to the formula (9):

for Northwest region $m_{\text{km}} = \sqrt{\frac{0.0526}{189}} \approx \pm 0.0516$ m;

for Red River Delta region $m_{\text{km}} = \sqrt{\frac{0.0570}{92}} \approx \pm 0.0249$ m;

Journal of Mining Institute. 2024. Vol. 265. P. 34-44

for Central Highlands region $m_{\text{km}} = \sqrt{\frac{0.2368}{294}} \approx \pm 0.0284$ m;

for Mekong River Delta region $m_{\text{km}} = \sqrt{\frac{0.0521}{203}} \approx \pm 0.0160$ m.

To determine the accuracy of each leveling route, it is necessary to define two types of errors:

• the mean square error of the height anomaly difference over one km shows the accuracy of the leveling route that is calculated according to the formula (9); in case if it has only one leveling route, $q = 1$ and $P = 1$ and the mean square error of the height anomaly difference over 1 km will be calculated according to formula $m_{\text{km}} = \sqrt{\left[\Delta\zeta^i \Delta\zeta^j\right]}$;

• the permitted error is also caculated for each leveling route based on the topography of the area. If the terrain is plain, the value of $L = 1.1D$ (distance between two points), if the terrain is mountainous, the value of $L = 1.3D$.

The error value for each leveling routes is shown in Table 6.

Table 6

Error of the leveling routes

Points number	Start point	End point	$\lvert m_{\text{km}} \rvert$, mm	Absolute value of permitted error, mm					Achieved grade of leveling route
				Grade I	Grade II	Grade III	Grade IV	Technical leveling	
1	I(BMT-APD)12	I(BMT-APD)16	27.8	15.7	26.1	62.7	130.6	313.6	Grade III
2	I(BMT-APD)12	III(DBS-DL)3	184.7	16.5	27.6	66.2	137.9	330.9	Technical
3	I(BMT-APD)12	III(QS-DN)2	54.0	18.7	31.1	74.7	155.6	373.3	Grade III
4	I(BMT-APD)12	III(BDS-QP)5	295.8	19.7	32.8	78.7	163.9	393.3	Technical
5	I(BMT-APD)22	I(BMT-APD)25	0.4	11.8	19.6	47.0	97.9	235.0	Grade I
6	I(BMT-APD)22	I(BMT-APD)16	36.6	15.2	25.4	60.9	126.9	304.5	Grade III
7	I(BMT-APD)25	I(BMT-APD)30	40.6	16.8	27.9	67.0	139.6	335.1	Grade III
8	I(BMT-APD)25	III(BGM-MH)3	123.7	19.6	32.6	78.3	163.0	391.3	Grade IV
9	I(BMT-APD)3	I(BMT-APD)6	37.8	13.2	21.9	52.6	109.6	263.1	Grade III
10	I(BMT-APD)3	III(BDS-QP)5	132.4	15.8	26.3	63.1	131.5	315.6	Technical
…	…	…	…	…	…	…	…	…	…
767	III(TT-HN)2	II(HN-AB)7	336.4	10.2	20.4	51.1	102.1	255.4	Unsatisfactory
768	III(TT-TS)1	II(CD-VC)8	398.0	11.9	23.8	59.6	119.2	298.0	Unsatisfactory
769	III(UM-HDB)7	III(OD-CN)1	98.0	10.7	21.4	53.6	107.2	268.1	Grade IV
770	III(VL-MC)7	II(TL-TV)5-1	36.6	8.8	17.6	43.9	87.8	219.5	Grade III
771	III(VL-MC)7	II(MT-TV)6-1	30.7	8.8	17.6	44.0	87.9	219.9	Grade III
772	III(VL-MC)7	III(LH-TH)1	71.4	9.8	19.5	48.8	97.6	243.9	Grade IV
773	III(VL-MC)7	I(VL-HT)273A	10.4	10.1	20.2	50.4	100.9	252.1	Grade II
774	III(VL-MC)7	II(TX-TL)25	77.8	10.5	20.9	52.4	104.7	261.8	Grade IV
775	III(VL-MC)7	I(VL-HT)284A	42.7	11.3	22.7	56.6	113.3	283.2	Grade III
776	III(VT-PS)5	II(SC-PL)34	134.5	9.5	19.1	47.7	95.4	238.5	Technical
777	III(VT-PS)5	II(SC-PL)15	26.7	9.8	19.6	49.1	98.2	245.4	Grade III
778	III(VT-VC)7	II(ST-PL)2	83.6	11.0	22.0	55.0	110.0	274.9	Grade IV

The sum of leveling routes corresponding to the grades for each region in Table 6 is listed in Table 7. The number of leveling routes of each grade in four regions are calculated as the number of leveling routes of each grade divided by the total number of leveling routes of each respective region.

Table 7

Number of leveling routes achieved grades and percentage of accuracy

Region	Number of leveling routes achieved grades							Accuracy, %					
								Satisfactory					Unsatisfactory
	Grade I	GradeII	Grade III	Grade IV	Technical leveling	Unsatisfactory	Total	Grade I	Grade II	Grade III	Grade IV	Technical leveling	
Northwest	13	7	25	45	68	31	189	6.9	3.7	13.2	23.8	36.0	16.4
Red River Delta	9	7	15	28	30	3	92	9.8	7.6	16.3	30.4	32.6	3.3
Central Highlands	31	15	62	97	85	4	294	10.5	5.1	21.1	33.0	28.9	1.4
Mekong River Delta	16	14	35	51	67	20	203	7.9	6.9	17.2	25.1	33.0	9.9

The percentage of accuracy of the leveling routes of the four regions of Vietnam show that most of the leveling routes in the four regions are satisfactory (grades I-IV and Technical leveling). The highest grade that can be obtained for the leveling routes in all four experimental regions is grade I.

Conclusions. The results of determining the accuracy of the leveling routes from GNSS/leveling data and Earth gravity model SGG-UGM-2 at four regions – Northwest, Red River Delta, Central Highlands, Mekong River Delta – by calculating the difference between the measured height anomalies and the model of pairs of points with the leveling routes, connected between pair of points in each region showed that most of the percentage of accuracy of the leveling routes of the four regions are satisfactory.

The effect of determining the accuracy of leveling routes allows to save time and money, since there is no need to take measurements in the field. The determination of the accuracy of the leveling route is completely applicable to other areas if the points have both geodetic and leveling heights.

From these results, managers and surveyors can predict the accuracy of the elevation points when the above-mentioned leveling routes are connected to take reasonable measures when implementing the project.

REFERENCES

1. Featherstone W.E., Kuhn M. Height systems and vertical datums: A review in the Australian context. *Journal of Spatial Sciences*. 2006. Vol. 51. Iss. 1, p. 21-41. DOI: 10.1080/14498596.2006.9635062

2. El-Ashmawy K.L.A. Accuracy, time cost and terrain independence comparisons of levelling techniques. *Geodesy and Cartography*. 2014. Vol. 40. Iss. 3, p. 133-141. DOI: 10.3846/20296991.2014.962727

3. Karila K., Karjalainen M., Hyyppä J. et al. A Comparison of Precise Leveling and Persistent Scatterer SAR Interferometry for Building Subsidence Rate Measurement. *ISPRS International Journal of Geo-Information*. 2013. Vol. 2. Iss. 3, p. 797-816. DOI: 10.3390/ijgi2030797

4. Kubodera T., Okazawa H., Hosokawa Y. et al. Effects of Surveying Methods between GNSS and Direct Leveling on Elevation Values over Long Distance in Mountainous Area. *International Journal of Environmental and Rural Development*. 2016. Vol. 7. Iss. 1, p. 62-69. DOI: 10.32115/ijerd.7.1_62

5. Perij S., Pokotylo I., Korliatovych T. Investigation of accuracy of methods of trigonometric levelling during the transmission of elevations over water surfaces. *Geodesy, Cartography, and Aerial Photography*. 2017. Vol. 85, p. 18-26. DOI: 10.23939/istcgcap2017.01.018

6. Ding Liang Yang, Jin Gui Zou. Precise levelling in crossing river over 5 km using total station and GNSS. *Scientific Reports*. 2021. Vol. 11. N 7492. DOI: 10.1038/s41598-021-86929-1

7. Carrion D., Vergos G., Albertella A. et al. Assessing the GOCE models accuracy in the Mediterranean area. *Newton's Bulletin*. 2015. Vol. 5, p. 63-82.

8. Odera P.A., Fukuda Y. Evaluation of GOCE-based global gravity feld models over Japan after the full mission using free-air gravity anomalies and geoid undulations. *Earth, Planets and Space*. 2017. Vol. 69. N 135. DOI: 10.1186/s40623-017-0716-1

9. Foroughi I., Afrasteh Y., Ramouz S., Safari A. Local evaluation of Earth gravitational models, case study: Iran. *Geodesy and Cartography*. 2017. Vol. 43. Iss. 1, p. 1-13. DOI: 10.3846/20296991.2017.1299839

10. Yılmaz M., Turgut B., Güllü M., Yılmaz I. The Evaluation of High-Degree Geopotential Models for Regional Geoid Determination in Turkey. *Afyon Kocatepe University Journal of Science and Engineering*. 2017. Vol. 17. N 015501, p. 147-153. DOI: 10.5578/fmbd.50706

11. Pavlis N.K., Holmes S.A., Kenyon S.C., Factor J.K. The development and evaluation of the Earth Gravitational Model 2008 (EGM2008). *Journal of Geophysical Research: Solid Earth*. 2012. Vol. 117. N B04406, p. 1-38. DOI: 10.1029/2011JB008916

12. Zingerle P., Pail R., Gruber T., Oikonomidou X. The combined global gravity field model XGM2019e. *Journal of Geodesy*. 2020. Vol. 94. N 66. DOI: 10.1007/s00190-020-01398-0

13. Aljanbi A.J.A., Dibs H., Alyasery B.H. Interpolation and Statistical Analysis for Evaluation of Global Earth Gravity Models Based on GPS and Orthometric Heights in the Middle of Iraq. *Iraqi Journal of Science*. 2020. Vol. 61. N 7, p. 1823-1830. DOI: 10.24996/ijs.2020.61.7.31

14. Lee J., Kwon J.H. Precision Evaluation of Recent Global Geopotential Models based on GNSS/Leveling Data on Unified Control Points. *Journal of the Korean Society of Surveying, Geodesy, Photogrammetry and Cartography*. 2020. Vol. 38. N 2, p. 153-163. DOI: 10.7848/ksgpc.2020.38.2.153

15. Kostelecký J., Klokočník J., Bucha B. et al. Evaluation of gravity field model EIGEN-6C4 by means of various functions of gravity potential, and by GNSS/leveling. *Geoinformatics FCE CTU*. 2015. Vol. 14. N 1, p. 7-28. DOI: 10.14311/gi.14.1.1

16. Odera P.A. Evaluation of the recent high-degree combined global gravity-field models for geoid modelling over Kenya. *Geodesy and Cartography*. 2020. Vol. 46. Iss. 2, p. 48-54. DOI: 10.3846/gac.2020.10453

17. Yilmaz M., Turgut B., Gullu M., Yilmaz I. Evaluation of recent global geopotential models by GNSS/levelling data: Internal Aegean region. *International Journal of Engineering and Geosciences (IJEG)*. 2016. Vol. 1. Iss. 1, p. 18-23. DOI: 10.26833/ijeg.285221

18. Saray N.S., Ghazal N.K. Evaluation of Global Gravitational Models Based on DGPS/leveling Data over Baghdad University (IRAQ). *Journal of Physics: Conference Series*. 2021. Vol. 1804. N 012044. DOI: 10.1088/1742-6596/1804/1/012044

19. Abdulrahman F.H. Determination of the local geoid model in Duhok Region, University of Duhok Campus as a Case study. *Ain Shams Engineering Journal*. 2021. Vol. 12. Iss. 2, p. 1293-1304. DOI: 10.1016/j.asej.2020.10.004

20. Al-Karargy E.M., Doma M.I., Dawod G.M. Towards an Accurate Definition of the Local Geoid Model in Egypt using GPS/Leveling Data: A Case Study at Rosetta Zone. *International Journal of Innovative Science and Modern Engineering (IJISME)*. 2014. Vol. 2. Iss. 11, p. 10-15.

21. Sikder M.A.A., Falin Wu, Ahmed W.A. et al. Assessment of Orthometric Height Derived from Levelling, GNSS and EGM2008 Geoid Model in Bangladesh. 15th IEEE International Conference on Signal Processing (ICSP), 6-9 December 2020, Beijing, China. IEEE, 2020, p. 689-694. DOI: 10.1109/ICSP48669.2020.9321048

22. Albayrak M., Özlüdemir M.T., Aref M.M., Halicioglu K. Determination of Istanbul geoid using GNSS/levelling and valley cross levelling data. *Geodesy and Geodynamics*. 2020. Vol. 11. Iss. 3, p. 163-173. DOI: 10.1016/j.geog.2020.01.003

23. Eteje S.O., Ono M.N., Oduyebo O.F. Practical local geoid model determination for mean sea level heights of surveys and stable building projects. *IOSR Journal of Environmental Science, Toxicology and Food Technology*. 2018. Vol. 12. Iss. 6, p. 30-37. DOI: 10.5281/zenodo.2525661

24. Heliani L.S. Evaluation of global geopotential model and its application on local geoid modelling of Java Island, Indonesia. *AIP Conference Proceedings*. 2016. Vol. 1755. Iss. 1. N 100005. DOI: 10.1063/1.4958534

25. Oluyori P.D., Ono M.N., Eteje S.O. Computations of Geoid Undulation from Comparison of GNSS/Levelling with EGM 2008 for Geodetic Applications. *International Journal of Scientific and Research Publications*. 2018. Vol. 8. Iss. 10, p. 235-241. DOI: 10.29322/IJSRP.8.10.2018

26. Thanh Son Tran, Mustafin M.G., Kuzin A.A. Creating a Local Quasigeoid Model for the Territory of Vietnam Using the Global Model EGM2008. *Proceedings of the International Symposium "Engineering and Earth Sciences: Applied and Fundamental Research" (ISEES 2019)*, 10-13 June 2019, Grozny, Russia. Amsterdam: Atlantis Press, 2019. Vol. 1, p. 603-608. DOI: 10.2991/isees-19.2019.119

27. Soycan M. Improving EGM2008 by GPS and leveling data at local scale. *Boletim de Ciências Geodésicas*. 2014. Vol. 20. Iss. 1, p. 3-18. DOI: 10.1590/S1982-21702014000100001

28. Al-Karargy E.M., Dawod G.M. Optimum combinations of GGM and GDEM models for precise national geoid modeling. *Proceedings of Engineering and Technology Innovation*. 2021. Vol. 18, p. 15-24. DOI: 10.46604/peti.2021.6452

29. Wei Liang, Roland Pail, Xinyu Xu, Jiancheng Li. A new method of improving global geopotential models regionally using GNSS/levelling data. *Geophysical Journal International*. 2020. Vol. 221. Iss. 1, p. 542-549. DOI: 10.1093/gji/ggaa047

30. Mosayebzadeh M., Ardalan A.A., Karimi R. Regional improvement of global geopotential models using GPS/Leveling data. *Studia Geophysica et Geodaetica*. 2019. Vol. 63, p. 169-190. DOI: 10.1007/s11200-017-1084-9

31. Kyamulesire B., Oluyori P.D., Eteje S.O. Comparative analysis of three plane geometric geoid surfaces for orthometric height modelling in Kampala, Uganda. *FUDMA Journal of Sciences (FJS)*. 2020. Vol. 4. N 3, p. 48-51. DOI: 10.33003/fjs-2020-0403-255

32. Barzaghi R., Carrion D., Reguzzoni M., Venuti G. A Feasibility Study on the Unification of the Italian Height Systems Using GNSS-Leveling Data and Global Satellite Gravity Models. IAG 150 Years. International Association of Geodesy Symposia. Cham: Springer, 2015. Vol. 143, p. 281-288. DOI: 10.1007/1345_2015_35

33. Younis G. The Integration of GNSS/Leveling Data with Global Geopotential Models to Define the Height Reference System of Palestine. *Arabian Journal for Science and Engineering*. 2018. Vol. 43. N 7, p. 3639-3645. DOI: 10.1007/s13369-017-2912-5

34. Hayden T., Amjadiparvar B., Rangelova E., Sideris M.G. Estimating Canadian vertical datum offsets using GNSS/levelling benchmark information and GOCE global geopotential models. *Journal of Geodetic Science*. 2012. Vol. 2. Iss. 4, p. 257-269. DOI: 10.2478/v10156-012-0008-4

35. Alcantar-Elizondo N., Garcia-Lopez R.V., Torres-Carillo X.G., Vazquez-Becerra G.E. Combining Global Geopotential Models, Digital Elevation Models, and GNSS/Leveling for Precise Local Geoid Determination in Some Mexico Urban Areas: Case Study. *ISPRS International Journal of Geo-Information*. 2021. Vol. 10. Iss. 12. N 819. DOI: 10.3390/ijgi10120819

36. Bos M., Fernandes R., Al-Marri M. et al. The New Gravimetric Geoid Model of Qatar: QG2020. *FIG e-Working Week* 2021, 21-25 June 2021, Netherlands.

37. Guimarães G.D.N., Blitzkow D., Barzaghi R., Matos A.C.O.C. The computation of the geoid model in the state of São Paulo using two methodologies and GOCE models. *Boletim de Ciências Geodésicas*. 2014. Vol. 20. N 1, p. 183-203. DOI: 10.1590/S1982-21702014000100012

38. Vu D.T., Bruinsma S., Bonvalot S. A high-resolution gravimetric quasigeoid model for Vietnam. *Earth, Planets and Space*. 2019. Vol. 71. N 65. DOI: 10.1186/s40623-019-1045-3

Authors: **Bui Thi Hong Tham,** *PhD, Dean, https://orcid.org/0000-0002-3932-4040 (Hanoi University of Natural Resources and Environment, Hanoi, Vietnam),* **Phi Truong Thanh,** *Associate Professor, Dean, ptthanhdc@hunre.edu.vn, https://orcid.org/0000-0003-0421-6557(Hanoi University of Natural Resources and Environment, Hanoi, Vietnam).*

The authors declare no conflict of interests.

ISSN 2411-3336; e-ISSN 2541-9404

JOURNAL OF MINING INSTITUTE
Zapiski Gornogo instituta
Journal homepage: pmi.spmi.ru

Research article

Impact of carbon dioxide on the main geotechnical quality criteria and preparation cost of cemented paste backfill

Pitchou M. BUKASA✉, Melvin M. MASHINGAIDZE, Simasiku L. SIMASIKU
University of Namibia, Windhoek, Namibia

***How to cite this article*:** Bukasa P.M., Mashingaidze M.M., Simasiku S.L. Impact of carbon dioxide on the main geotechnical quality criteria and preparation cost of cemented paste backfill. Journal of Mining Institute. 2024. Vol. 265, p. 45-54. EDN ZBZTKN

Abstract. There is a global upsurge in the use of cemented paste backfill (CPB) for various mining functions. However, the cost of the Portland cement binder is prohibitive, thus warranting strategies to reduce cement usage without overly diminishing the CPB quality. Since carbon dioxide is used for patented sand moulding processes, this study is premised on that physicochemical ability of CO_2 to enhance the curing of consolidated inorganic materials. It evaluated the impact of carbon dioxide on the uniaxial compressive strength UCS and preparation cost of CPB standard samples (ASTM C109). The preparation cost was delimited to the purchase cost of the Portland cement. The backfill material was silica sand tailings with 4.5 wt.% Portland cement binder and a water-cement ratio of 7.6. Distilled water of pH 5.4 was used for the control samples while variable amounts of carbon dioxide were dissolved in distilled water to generate carbonated mixing water with pH values of 3.8; 4 and 4.2. The lower the carbonated water pH, the higher is the CO_2 concentration. UCS tests were conducted on the samples after curing for 3, 7, 28, and 90 days. There was an observable increase in the UCSs and reduction in curing time with increasing carbon dioxide. Samples prepared with carbonated water of pH 3.8 had almost double the strength of those prepared with pure distilled water of pH 5.4, implying that more dissolved CO_2 corresponds to higher CPB strength. This is supported by the trendline equations for the graphical simulation of strength on curing time. Thus, CPB with much less binder can be expected to attain the requisite UCS if carbon dioxide is incorporated. The average reduction in Portland cement consumption was 0.61 %, which translates to a cost saving of the same percentage points. If calculated over the operational life of a mine, this is a massive saving of millions of dollars.

***Keywords*:** cemented paste backfill; CPB; curing time; uniaxial compressive strength; binder consumption; carbon dioxide sequestration; tailings management

Received: 20.05.2022 ***Accepted: 03.04.2023*** ***Online: 29.08.2023*** ***Published: 29.02.2024***

Introduction. Hardened mine backfill or cemented paste backfill (CPB) is a synthetic engineering material composed of tailings, water, and hydraulic binders, with the tailings constituting 65-85 % of the combined paste weight [1-3]. CPB has multiple mining applications such as underground mine backfilling [4-6], roof support [7-9], control of surface subsidence [10-12], and mitigation of acid mine drainage [1, 13], while at the same time serving as an environmentally friendly tailings management method utilized in many mines globally [14-16], with its adoption on the increase [17, 18].

A critical geotechnical quality criterion for cured mine backfill is the mechanical strength [10, 19, 20], which is important for load bearing applications such as roof and goaf support [9] in underground mines to safeguard mine personnel and prevent ore dilution [5, 7, 21]. The unconfined compressive strength (UCS) of the hardened or cured backfill is commonly ascertained via the uniaxial compressive strength test to evaluate the CPB's stability on demand due to the test's low cost and ease of integration into standard mine quality control protocols [22-24]. Before curing, the CPB is in slurry form, necessitating transport in pipelines and the use

of slurry pumps to convey it to places where it is needed [25-27]. During this phase, rheological properties of the CPB slurry are critical for timely and efficient deposition at points of interest [28-30]. Numerous works such as [2, 7, 31] have studied the rheology of CPB slurry and characterised it as a non-Newtonian fluid [25, 27, 30], whose yield stress is mainly affected by the solids mass fraction [32-35]. This yield stress is the primary shear stress that the slurry pumping system has to overcome in order for the CPB to flow, thus making it critical for cost-effective placement of the CPB in mine workings [7, 27]. Water-reducing admixtures can be added to the paste to augment its pumpability, and improve the strength of the cured CPB [36-38].

CPB is the most extensively used backfilling technology in Northern America, and in some parts of the globe because of a number of advantages over competing technologies [24, 38, 39]. CPB is produced by homogeneously mixing three major constituents: tailings, water, and binder [12, 40-42]. The binder generates cohesion in the CPB due to the hydration process [21, 43, 44]. A major type of binder which is often used in the mining industry for the production of CPB is Portland cement in weight proportions of 2-7 % owing to its market abundance and flexibility of application [21, 37, 45].

However, while binders advantageously increase the mechanical strength of CPB [17, 20, 46], they can also represent a considerable portion of the mine operating cost [2, 8, 37]. For example, Portland cement binders constitute about 50-75 % of the overall cost of CPBs [8, 27, 45]. For instance, the cement consumption of the mining industry in the province of Ontario, Canada alone is estimated between 5-6 % of the total Canadian Portland cement production with an estimated cost of CA $75 million annually in the consolidation of backfill in underground mining operations [44].

Since binder consumption is the most expensive component in the preparation of CPB, there is a need to explore techniques for reducing the binder consumption of cemented backfill [17, 18, 47]. One approach would be to incorporate carbon dioxide into the cemented backfill during its preparation, as has been reported for concrete [48, 49]. The strength of concrete has been observed to increase due to carbonation, which results in precipitates forming and aggregating inside pores in the cement matrix. The partial closure of the pores or voids, also termed pore refinement improves the cement UCS [48, 49]. If the same phenomenon can occur in CPB, then it may also lead to an increase of its UCS, thereby reducing the binder consumption and affiliated costs. While the study by T.Kasap et al. [50] did consider the effect of pH on CPB, there was no deliberate alteration of the mixing water pH by dissolution of CO_2, but the natural composition of the different tailings used was intentionally selected so as to have basic and acidic CPB samples. Therefore, the present work focuses on assessing the impact of carbonation on the UCS of CPB and the potential cost savings in its preparation arising out of reduced Portland cement binder use.

Methodology. *Silica sand tailings.* Ground silica sand (99.8 wt.% SiO_2) was used as the main mine backfill constituent, consistent with earlier studies [14, 24, 51]. The physical properties of this sand: G_s 2.7; D_{10} 1.9; D_{30} 9.0; D_{50} 22.5; D_{60} 31.5; D_{90} 88.9; C_u 16.2; C_c 1.3 μm. The silica sand can be classified as medium tailings having about 40 % fine particles, which have diameters lower than 20 μm.

Binder. The purpose of the binder in paste backfill is to create adequate mechanical strength to satisfy static and dynamic loading support functions. Portland cement is traditionally used as binder for cemented paste backfill [45]. Paste backfill bonded with Portland cement exhibits improved shear strength, tensile strength, and stiffness [52, 53]. Therefore, 4.5 wt.% by weight Portland Cement Type I (PCI) was used as the binder in this study. The chemical constitution of

Journal of Mining Institute. 2024. Vol. 265. P. 45-54

this PCI: MgO 2.65; CaO 62.82; SiO_2 18.03; Mn_2O_3 4.53; Fe_2O_3 2.70; SO_3 3.82 wt.% and it had a density of 3.15g/cm^3.

Mixing water. Water demand is critical in the preparation of CPB. In the context of this work, it occupied second position (34.2 %) in terms of portions of the constituents after silica tailings.

A water-cement ratio (w/c) of 7.6 (4.5 × 7.6 = 34.2 %) was maintained throughout the CPB samples preparation. Two types of mixing water were used: distilled water with no CO_2 added (DW) and distilled water with varying amounts of CO_2 (CW). Pure distilled water of pH 5.4 was used as the solvent and control. Specific amounts of CO_2 were then added to this distilled water in order to create carbonated mixing water with pH values of 3.8; 4 and 4.2 respectively (Table 1), such that the higher the dissolved CO_2, the lower the pH and hence the more acidic the CW.

Table 1

Mix ratios of the CPB samples produced

Mix name	Tailings type	Binder type	Binder, wt.%	W/c ratio	pH
CPB-3.8	ST	PCI	4.5	7.6	3.8
CPB-4	ST	PCI	4.5	7.6	4.0
CPB-4.2	ST	PCI	4.5	7.6	4.2
CPB-5.4	ST	PCI	4.5	7.6	5.4

Preparation of CPB mixtures. The silica sand tailings, cement and pre-treated water samples were homogeneously mixed in a double spiral mixer. 31 samples were prepared with a fixed binder composition of 4.5 wt.% and water-cement ratio of 7.6. The CPB that was produced was then poured into standard cylindrical curing molds (∅50 mm and H = 100 mm). The filled moulds were then sealed to prevent vaporization of water and cured at a temperature of 22 °C, for periods of 3, 7, 28 and 90 days. The composition mixtures of the different CPBs prepared for this study are as presented in Table 2.

Table 2

Density of constituents used during the preparation of CPB samples

Component	Value, g/cm^3	Constituent portion, %
PCI	3.15	4.5
Distilled water	0.9900198	34.2 = (4.5 × 7.6)
Carbonated water	1	34.2 = (4.5 × 7.6)
Silica sand tailings	1.680	61.3 = (100 – 4.5 × 7.6)

Testing Methods. UCS tests were conducted on all the 31 cylindrical samples in order to evaluate their mechanical strength after 3, 7, 28 and 90 days of curing. An initial load of 10 N was first applied before dynamic loading began at a compression rate of 2.5 mm/min to failure in accordance with ASTM C109 using a 50 kN Z050 ZwickRoell compression machine.

Results and discussion. *Influence of carbon dioxide on CPB strength.* Figure 1 shows that throughout curing times 3, 7, 28 and 90 days respectively, there is an increase of strength in the CPB when the pH level is decreasing, especially between the strength of CPBs of DW (with pH level of 5.4) and the strength of CPBs of DW (with pH level of 3.8). This trend of the increase of compressive strength is also true when pH level is between 4 and 4.2 except at day 3 where the difference between the compressive strength of all the samples is not that significant (Fig.1).

Another exception can also be seen at curing time day 7 where the compressive strength of DW CPB with pH level of 5.4 is greater than the one of CW CPB with pH level 4.2. These two exceptions might have been caused perhaps by the difficulties related to the preparation of high quality CPB samples [9, 24, 37].

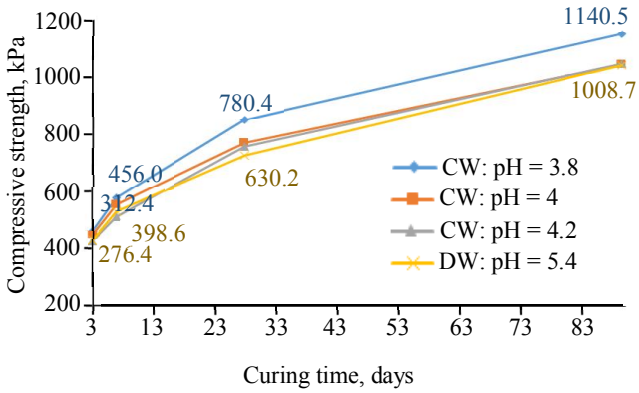

Fig.1. Strength development of CPB with CW and DW

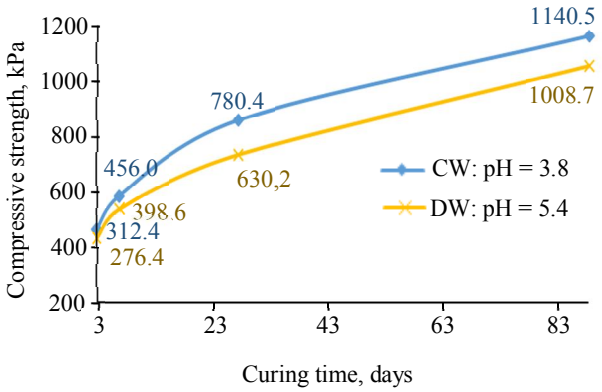

Fig.2. Comparative strength development of DW CPB (pH = 5.4) vs CW CPB (pH = 3.8)

Now since, throughout all the curing times studied (days 3, 7, 28 and 90), there is significant and clear increase of compressive strength between specimen of DW (when pH level is 5.4) and CW (when pH level is 3.8), the rest of the discussions are focused mainly on these two special cases.

At day 3 and day 90 of curing time, Fig.2 shows a 13 % strength increase of CW CPB specimens of pH 3.8 in comparison with the DW CPB specimens of pH 5.4 for the same binder proportion (4.5 wt.%). However, there are even greater strength increases during other curing times.

At "day 7", with the injection of CO_2 into the mixing water resulting in the solution with pH level of 3.8, the UCS of CPB samples increased in 14 % versus the UCS produced with just DW (pH = 5.4). At day 28 for example, it is shown that the strength of CPB made with CW where the pH level is of 3.8 reaches about 780 kPa (Fig.3). The incorporation of carbon dioxide into the mixing water to reach a pH level minimum 3.8 increases the strength by approximately 24 %. That is almost double the minimum strength (400 kPa) required at Matagami Mine, a Glencore underground zinc mine in the province of Quebec, Canada. In fact, the CPB structure strength must reach 400 kPa after 28 days or curing time. At the same curing time (day 28), Fig.3 show that the compressive strength of the CPB obtained using DW was found to be about 630.2 kPa, which is lower than the value of CPB made with CW when pH level is 3.8, yet it is greater than the industrial requirement of UCS at curing day 28 as stated above. This might mean that in the conditions of Matagami Zinc Mine, the required strength of the hardened paste fill (400 kPa) can be developed or reached earlier than the curing time day 28. Consequently, this might therefore contribute to the efficiency of underground mine productions operations of adjacent mine faces since the stope backfilled would have already provided a safe working environment for the miners [4, 32, 38, 46]. Overall, the presence of CO_2 in the water solution for preparing CPB caused the compressive strength to increase by approximately 16 % when considering the average value of all the UCSs increases during the curing time studied (incremental strength of CW CPB over DW CPB (days 3, 7, 28 and 90 – 13; 14; 24; 13 % respectivery).

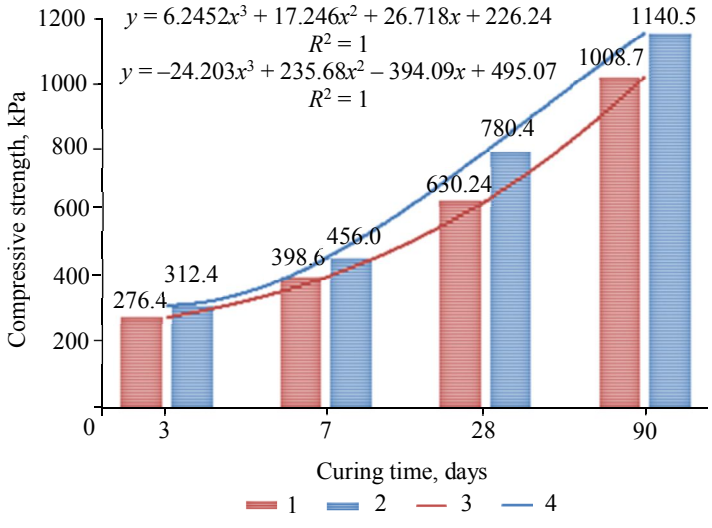

Fig.3. Trendlines of strength development of DW CPB (pH = 5.4) vs CW CPB (pH = 3.8)
1 – DW; 2 – CW; 3 – polynomial (DW); 4 – polynomial (CW)

Carbon dioxide is one of the major greenhouse gases (GHG) produced mainly by human activities. Globally 78 % of CO_2 emissions come from activities related to production and energy

Journal of Mining Institute. 2024. Vol. 265. P. 45-54

consumption [54-57], such as the burning of fossil fuels, iron and steelmaking, and production of cements. Some components of these emissions attack atmospheric ozone and create holes in the ozone layer [58]. It is important to note that the suggested approach of introducing this type of GHG into mixing water for the production of paste backfill implies first the extraction of CO_2 from natural deposits (wells) or its capture and storage [59-63]. This means this approach may eventually become one of the strategic ways of backfill technology for reducing the GHG footprint of the mining industry, particularly in tailings and water management sectors since it promotes the capture, storage, sequestration and utilization of the CO_2 [64]. Hence, it might help contribute towards the achievement of United Nations (UN) SDG 13 (climate action) which recommends urgent action to combat climate change and its impacts*.

The density of carbonated water is dependent on the degree of carbonation. There is no consistent density for carbonated water; however, if certain parameters are known, then the density can be easily calculated. In order to calculate the density of carbonated water, the density of both carbon dioxide and water. Carbon dioxide has a density of 0.00198 g/cm^3. The density of water is 1 g/cm^3. The equation to calculate the density of a substance involves multiplying the percentage of concentration of one substance by its density and adding it to the percentage multiplied by the density of the other substance [37].

Now, knowing the mathematical model of the strength development of CPB produced with CW of pH level 3.8 as function of curing time, it is possible to determine the approximate day when the hardened paste fill would cure and reach the expected 400 kPa:

$$y = -24.203x^3 + 235.68x^2 - 394.09x + 495.07. \quad (1)$$

Solving equation (1) which represents the best fit function obtained using Microsoft Excel when y = 400 kPa, under the conditions of Matagami Mine would yield the following results: x_1 = 7.68552; x_2 = 0.29005; x_3 = 1.76207 days. Among these values, the optimum curing time, would be 7.7 days while the other two can be rejected since they are not realistic according to the experimental data. This means that by incorporating CO_2 into mixing water for the production of CPB, the expected mechanical strength (400 kPa) can be attained after only 8 days instead of 28 days. This is equivalent to the reduction of the CPB curing time by about 71.4 %, which would have tremendous impact on the economic parameters of the considered mining company. Moreover, the schedule of the entire mine operations would be improved and would there anticipate the cash flow of the project, and therefore contribute effectively to the return on the investments and a shortened payback period of the operation project:

$$y = 6.2452x^3 + 17.246x^2 + 26.718x + 226.24. \quad (2)$$

Similarly, if equation (2) is solved considering Matagami Mine conditions when y is equal to 400 kPa, the optimum curing time for DW CPBs would be 2 days or 93 % of the curing time is saved. This high rate of increase of the strength of CPBs observed for both CW and DW solutions can be attributed partially to some physical properties of the silica tailings used, especially density. This is obvious because the tailings material used at Matagami Mine is zinc ore gangue material, which weighs less than the silica tailings used in the present study. The observation confirms the findings of [10, 43, 65] who reported an increase in paste backfill strength for the same binder proportion (4.5 wt.%) when the tailings density increased.

The results obtained demonstrate that there is an important strength improvement when there CO_2 is incorporated in the mixing water intended for the preparation of the CPB and that the pH level of 3.8 yields the highest compressive strengths.

Effect of carbon dioxide on binder consumption. The results obtained demonstrate that the presence of CO_2 in the mixing water for preparing the CPBs results in considerable

* Transforming our world: The 2030 Agenda for sustainable development, 2015, p. 35. URL: https://www.unfpa.org/sites/default/files/resource-pdf/Resolution_A_RES_70_1_EN.pdf (accessed 20.05.2022).

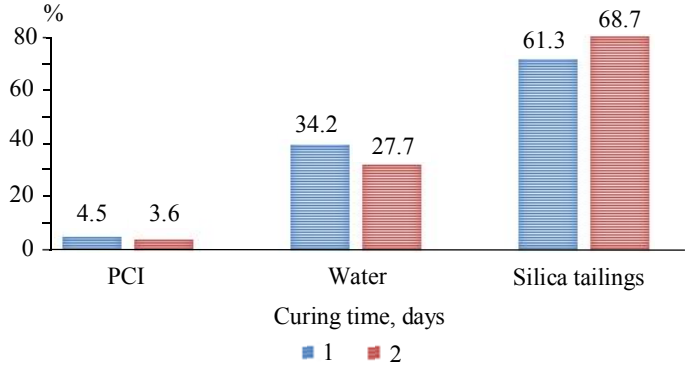

Fig.4. Comparison of consituents portions of DW CPBs and CW CPBs, %
1 – constituents portions DW; 2 – constituents portions CW

Table 3

Economic effect of incorportating CO_2 into CPB, CA $

Day	Costs of binders of CPB		Annual Saved Costs on binder
	DW	CW	
3	7473375	6626392.50	846982.50
7	7473375	6543355.00	930020.00
28	7473375	6045130.00	1428245.00
90	7473375	6626392.50	846982.50

augmentation of the mechanical strength of these CPBs, with a water pH of 3.8 yielding the optimum UCS.

Now, considering that there is a linear proportional relationship between initial binder portions (4.5 %), strength values of DW CPB samples and strength values of CW CPB samples at a pH level of 3.8, the optimized portions of binders can be find by multiplying this binder portion by UCS of DW and divided by the UCS of CW at a specific curing time. Results for day 28 are presented in Fig.4. Therefore, by injecting CO_2 into the mixing water, it is possible based on day 28 results to save not only about 1 % of binders' consumption (PCI), but also about 6.5 % of water consumption while maintaining the same w/c ratio (7.6). This might contribute towards the achievement of United Nations (UN) SDG 14 (Life below water) which advocates for conservation and sustainable use of marine resources for sustainable development*.

Based on the results of curing days 3, 7, 28 and 90 respectively, the overall economy that might be achieved in terms of cement consumption in preparing paste fill, can be found within the respective 0.51; 0.56; 0.86; 0.51 % saving figures. The average value of this saving would be ~0.61 %.

The use of carbon dioxide also has another significant effect on the tailings consumption. After introduction of CO_2 (decreased pH), there is an increased demand for the tailings quantity to be used as major constituents for the production of paste backfill, about 7.4 % of tailing consumptions at the curing day 28. This means that less mine residual materials may remain in the environment to impact the ecosystem. Therefore, this approach might contribute effectively to underground disposal [2, 23, 26]. Hence, the suggested approach might also help reach the UN SDG 15 (Life on the Land) which promotes the protection, restoration and sustainable use of terrestrial ecosystems, sustainable management of forests, combating desertification, halting and reserving land degradation, as well as halting biodiversity loss**.

Effect of CO_2 on CPB binder costs. The optimization of the binder consumption due the concentration of carbon dioxide in the mixing water, leads to important economic results as presented in Table 3.

The findings indicate the incorporation of carbon dioxide in the distilled water used for preparation of CPB would result in a significant improvement of the strength for an equal quantity of binder. This means that there is potential for the development of new optimum recipes of mixture of backfill (reduction of cost of binders) and/or the forecast of its main mechanical property (strength) as function of carbon dioxide concentration in the mixing water. As a result, about 0.51-0.86 % of quantities of binders used during the preparation of backfill can be saved which may have a great impact on productivity and competitiveness of the relevant mines, that is to say also on generating employment.

* Transforming our world: The 2030 Agenda for sustainable development, 2015, p. 35. URL: https://www.unfpa.org/sites/default/files/resource-pdf/Resolution_A_RES_70_1_EN.pdf (accessed 20.05.2022).

** Ibid.

Journal of Mining Institute. 2024. Vol. 265. P. 45-54

In fact, a mine which produces 7000 t of ore per day produces an average of 3500 t of CPB per day with an average binder consumption of about 3.5 % (at times 4.5 % or more). Given, that the average cost of binders is about CA $ 1.30 / 1% binder [26], a reduction of the quantity of binder consumption of 0.51-0.86 % would result in annual savings of about CA $ 846.983 (0.51 % × 3500 t × 365*j*) to CA $ 1.428.245. For a mine that has a lifespan of 20 years, the overall benefit in the reduction of the cost of cemented backfill would be about 17 million (case of 0.23 % reduction) and about 29 million CA $ (case of 0.86 % reduction). The economic effect of incorporating CO_2 into CPB throughtout the life span of the mine on 3, 7, 28 and 90 days would be 17 million CA $, 19 million CA $, 29 million CA $, 17 million CA $ respectively.

Table 4

Variation of UCS of CPB as a function of pH, kPa

pH	Day 3	Day 7	Day 28	Day 90
3.8	312.4	456.0	780.4	1140.5
4	298.8	427.6	685.0	1010.0
4.2	272.6	375.9	668.3	1013.4
5.4	276.4	398.6	630.2	1008.7

Trendline equations of CPB UCS as a function of pH. The best fit functions of strength development of DW CPB (pH = 5.4) and CW CPB (pH = 3.8) versus the curing ages of the samples were found using Microsoft Excel to be a third degree equation (see Fig.3). It is shown that the strength y of hardened backfill increases with increasing curing time x.

Similary, mathematical models of the variation of the compressive strength with curing time illustrated in Fig.1, are also third-degree polynomials equations for pH 5.4, 4.2, 4 and 3.8 respectively, $R^2 = 1$. Based on the coefficients for x, pH 3.8 corresponds to the optimum CO_2 concentration for maximum strength of the CPB. This supports the data in Table 4, which shows that with a decrease of the pH level of the mixing water, the compressive strength of the hardened backfill increases:

$$y = -23.679x^3 + 209.04x^2 - 591.88x + 1547;$$

$$y = -16.689x^3 + 139.48x^2 - 397.01x + 1054.6;$$

$$y = 16.31x^3 - 109.56x^2 + 186.17x + 363.04;$$

$$y = 7.1087x^3 - 48.957x^2 + 83.504x + 270.79.$$

Conclusions. The incorporation of carbon dioxide into the mixing water for the preparation of silica tailings CPB samples diminishes the pH level, as expected, due to the acidic nature of CO_2, but increases the final UCS of the CPB by 13 %, while cutting the curing time by more than 70 %. It also reduces the Portland cement binder consumption by approximately 0.51-0.86 %, and yields CPB preparation cost savings of the same percentage points.

The best fit functions of strength development of DW CPB (pH = 5.4) and CW CPB (pH = 3.8) versus the curing ages of the samples are both third-degree equations, and the trendlines have similar profiles, implying the same curing mechanism in the CPB samples for either test case. The only diffence is the magnitude of the coefficients, which explains the higher UCSs for the CW CPB samples. This increase in strength is due to carbonation on account of reactions between the CO_2, water and Portland cement, producing fine-sized compounds which coalesce inside voids within the CPB matrix. This increases the effective cross-sectional area of the CW CPB samples for compressive load bearing, hence the higher UCSs.

Since CO_2 is the most important GHG, using it for CPB preparation is a strategic way for mitigating the carbon footprint of the mining industry, particularly in tailings and water management sector since it promotes the capture, storage, sequestration and utilization of the CO_2. Hence, if commercialized it might contribute towards the achievement of United Nations SDG 13 (Climate Action) which recommends the taking an urgent action in order to combat climate change

and its impacts. This contribution to climate change mitigation is in fact two-fold, considering that less binder will be required for Portland cement, thus lessening GHG emissions from the cement manufacturing industries.

Therefore, CO_2 in CPB can be one of the pathways for the mining and Portland cement manufacturing industries to achieve net zero GHG emissions by 2050.

Future CPB studies can focus on studying the impact of different volumes of the cement binder on the backfill rheological and mechanical properties, and accounting for the costs of carbon dioxide production, capture, storage, transportation, and incorporation into the backfill mixture in the economic analysis.

The chemical composition of the plant tailings has an effect on the water and cement demands of the CPB, as well the rheological and mechanical properties. This warrants replications of this study for different tailings.

REFERENCES

1. Benzaazoua M., Fall M., Belem T. A contribution to understanding the hardening process of cemented pastefill. *Minerals Engineering*. 2004. Vol. 17. Iss. 2, p. 141-152. DOI: 10.1016/j.mineng.2003.10.022

2. Fall M., Benzaazoua M., Saa E.G. Mix proportioning of underground cemented tailings backfill. *Tunnelling and Underground Space Technology*. 2008. Vol. 23. Iss. 1, p. 80-90. DOI: 10.1016/j.tust.2006.08.005

3. Yilmaz E., Belem T., Bussière B. et al. Curing time effect on consolidation behaviour of cemented paste backfill containing different cement types and contents. *Construction and Building Materials*. 2015. Vol. 75, p. 99-111. DOI: 10.1016/j.conbuildmat.2014.11.008

4. Emad M.Z., Mitri H., Kelly C. State-of-the-art review of backfill practices for sublevel stoping system. *International Journal of Mining, Reclamation and Environment*. 2015. Vol. 29. Iss. 6, p. 544-556. DOI: 10.1080/17480930.2014.889363

5. Helinski M., Fahey M., Fourie A. Behavior of Cemented Paste Backfill in Two Mine Stopes: Measurements and Modeling. *Journal of Geotechnical and Geoenvironmental Engineering*. 2010. Vol. 137. N 2, p. 171-182. DOI: 10.1061/(ASCE)GT.1943-5606.0000418

6. Thompson B.D., Bawden W.F., Grabinsky M.W. In situ measurements of cemented paste backfill at the Cayeli mine. *Canadian Geotechnical Journal*. 2012. Vol. 49. N 7, p. 755-772. DOI: 10.1139/t2012-040

7. Belem T., Benzaazoua M. Design and Application of Underground Mine Paste Backfill Technology. *Geotechnical and Geological Engineering*. 2008. Vol. 26. Iss. 2, p. 147-174. DOI: 10.1007/s10706-007-9154-3

8. Fall M., Pokharel M. Coupled effects of sulphate and temperature on the strength development of cemented tailings backfills: Portland cement-paste backfill. *Cement & Concrete Composites*. 2010. Vol. 32. Iss. 10, p. 819-828. DOI: 10.1016/j.cemconcomp.2010.08.002

9. Minefill 2020-2021: Proceedings of the 13th International Symposium on Mining with Backfill, 25-28 May 2021, Katowice, Poland / Ed. by F.Hassani, J.Palarski, V.Sokoła-Szewioła, G.Strozik. London: CRC Press, 2021. 450 p. DOI: 10.1201/9781003205906

10. Gaili Xue, Erol Yilmaz, Weidong Song, Shuai Cao. Compressive Strength Characteristics of Cemented Tailings Backfill with Alkali-Activated Slag. *Applied Sciences*. 2018. Vol. 8. Iss. 9. N 1537. DOI: 10.3390/app8091537

11. Qiu-song Chen, Qin-li Zhang, Fourie A. et al. Experimental investigation on the strength characteristics of cement paste backfill in a similar stope model and its mechanism. *Construction and Building Materials*. 2017. Vol. 154, p. 34-43. DOI: 10.1016/j.conbuildmat.2017.07.142

12. Lei Yang, Jingping Qiu, Haiqiang Jiang et al. Use of Cemented Super-Fine Unclassified Tailings Backfill for Control of Subsidence. *Minerals*. 2017. Vol. 7. Iss. 11. N 216. DOI: 10.3390/min7110216

13. Benzaazoua M., Marion P., Picquet I., Bussière B. The use of pastefill as a solidification and stabilization process for the control of acid mine drainage. *Minerals Engineering*. 2004. Vol. 17. Iss. 2, p. 233-243. DOI: 10.1016/j.mineng.2003.10.027

14. Chen Hou, Liujun Yang, Lei Li, Baoxu Yan. Mechanical Characteristics and Stress Evolution of Cemented Paste Backfill: Effect of Curing Time, Solid Content, and Binder Content. *Frontiers in Materials*. 2022. Vol. 8, p. 1-10. DOI: 10.3389/fmats.2021.812402

15. Saedi A., Jamshidi-Zanjani A., Darban A.K. A review on different methods of activating tailings to improve their cementitious property as cemented paste and reusability. *Journal of Environmental Management*. 2020. Vol. 270. N 110881. DOI: 10.1016/j.jenvman.2020.110881

16. Yilmaz T., Ercikdi B., Deveci H. Utilisation of construction and demolition waste as cemented paste backfill material for underground mine openings. *Journal of Environmental Management*. 2018. Vol. 222, p. 250-259. DOI: 10.1016/j.jenvman.2018.05.075

17. Koohestani B., Belem T., Koubaa A., Bussière B. Experimental investigation into the compressive strength development of cemented paste backfill containing Nano-silica. *Cement & Concrete Composites*. 2016. Vol. 72, p. 180-189. DOI: 10.1016/j.cemconcomp.2016.06.016

18. Juanrong Zheng, Xiaoxiao Sun, Lijie Guo et al. Strength and hydration products of cemented paste backfill from sulphide-rich tailings using reactive MgO-activated slag as a binder. *Construction and Building Materials*. 2019. Vol. 203, p. 111-119. DOI: 10.1016/j.conbuildmat.2019.01.047

19. Ercikdi B., Yılmaz T., Külekci G. Strength and ultrasonic properties of cemented paste backfill. *Ultrasonics*. 2014. Vol. 54. Iss. 1, p. 195-204. DOI: 10.1016/j.ultras.2013.04.013

20. Juanrong Zheng, Lijie Guo, Xiaoxiao Sun et al. Study on the Strength Development of Cemented Backfill Body from Lead-Zinc Mine Tailings with Sulphide. *Advances in Materials Science and Engineering*. 2018. Vol. 2018. N 7278014. DOI: 10.1155/2018/7278014

21. Saedi A., Jamshidi-Zanjani A., Darban A.K. A review of additives used in the cemented paste tailings: Environmental aspects and application. *Journal of Environmental Management*. 2021. Vol. 289. N 112501. DOI: 10.1016/j.jenvman.2021.112501

22. Cihangir F., Ercikdi B., Kesimal A. et al. Paste backfill of high-sulphide mill tailings using alkali-activated blast furnace slag: Effect of activator nature, concentration and slag properties. *Minerals Engineering*. 2015. Vol. 83, p. 117-127. DOI: 10.1016/j.mineng.2015.08.022

23. Ercikdi B., Baki H., Izki M. Effect of desliming of sulphide-rich mill tailings on the long-term strength of cemented paste backfill. *Journal of Environmental Management*. 2013. Vol. 115, p. 5-13. DOI: 10.1016/j.jenvman.2012.11.014

24. Grabinsky M., Jafari M., Pan A. Cemented Paste Backfill (CPB) Material Properties for Undercut Analysis. *Mining*. 2022. Vol. 2. Iss. 1, p. 103-122. DOI: 10.3390/mining2010007

25. Boger D.V. Rheology of Slurries and Environmental Impacts in the Mining Industry. *Annual Review of Chemical and Biomolecular Engineering*. 2013. Vol. 4, p. 239-257. DOI: 10.1146/annurev-chembioeng-061312-103347

26. Deb D., Sreenivas T., Dey G.K., Panchal S. Paste Backfill Technology: Essential Characteristics and Assessment of its Application for Mill Rejects of Uranium Ores. *Transactions of the Indian Institute of Metals*. 2017. Vol. 70. Iss. 2, p. 487-495. DOI: 10.1007/s12666-016-0999-0

27. Roshani A., Fall M. Flow ability of cemented pastefill material that contains nano-silica particles. *Powder Technology*. 2020. Vol. 373, p. 289-300. DOI: 10.1016/j.powtec.2020.06.050

28. Liu Lang, Ki-Il Song, Dezheng Lao, Tae-Hyuk Kwon. Rheological Properties of Cemented Tailing Backfill and the Construction of a Prediction Model. *Materials*. 2015. Vol. 8. Iss. 5, p. 2076-2092. DOI: 10.3390/ma8052076

29. Niroshan N., Sivakugan N., Veenstra R.L. Flow Characteristics of Cemented Paste Backfill. *Geotechnical and Geological Engineering*. 2018. Vol. 36. Iss. 4, p. 2261-2272. DOI: 10.1007/s10706-018-0460-8

30. Yonghui Niu, Haiyong Cheng, Shunchuan Wu et al. Rheological properties of cemented paste backfill and the construction of a prediction model. *Case Studies in Construction Materials*. 2022. Vol. 16. N e01140. DOI: 10.1016/j.cscm.2022.e01140

31. Deng X.J., Klein B., Hallbom D.J. et al. Influence of Particle Size on the Basic and Time-Dependent Rheological Behaviors of Cemented Paste Backfill. *Journal of Materials Engineering and Performance*. 2018. Vol. 27. Iss. 7, p. 3478-3487. DOI: 10.1007/s11665-018-3467-7

32. Xin Chen, Xiuzhi Shi, Jian Zhou et al. Effect of overflow tailings properties on cemented paste backfill. *Journal of Environmental Management*. 2019. Vol. 235, p. 133-144. DOI: 10.1016/j.jenvman.2019.01.040

33. Deng X.J., Klein B., Zhang J.X. et al. Time-dependent rheological behaviour of cemented backfill mixture. *International Journal of Mining, Reclamation and Environment*. 2018. Vol. 32. Iss. 3, p. 145-162. DOI: 10.1080/17480930.2016.1239305

34. Qiangqiang Cheng, Yaben Guo, Chaowei Dong et al. Mechanical Properties of Clay Based Cemented Paste Backfill for Coal Recovery from Deep Mines. *Energies*. 2021. Vol. 14. Iss. 18. N 5764. DOI: 10.3390/en14185764

35. Hane I., Belem T., Benzaazoua M., Maqsoud A. Laboratory Characterization of Cemented Tailings Paste Containing Crushed Waste Rocks for Improved Compressive Strength Development. *Geotechnical and Geological Engineering*. 2017. Vol. 35. Iss. 2, p. 645-662. DOI: 10.1007/s10706-016-0131-6

36. Chaoqun Dai, Aixiang Wu, Yan Qi, Zhiqiang Chen. The Optimization of Mix Proportions for Cement Paste Backfill Materials via Box-Behnken Experimental Method. *Journal of The Institution of Engineers (India): Series D*. 2019. Vol. 100. Iss. 2, p. 307-316. DOI: 10.1007/s40033-019-00180-7

37. Ercikdi B., Cihangir F., Kesimal A. et al. Utilization of water-reducing admixtures in cemented paste backfill of sulphide-rich mill tailings. *Journal of Hazardous Materials*. 2010. Vol. 179. Iss. 1-3, p. 940-946. DOI: 10.1016/j.jhazmat.2010.03.096

38. Kesimal A., Yilmaz E., Ercikdi B. et al. Effect of properties of tailings and binder on the short-and long-term strength and stability of cemented paste backfill. *Materials Letters*. 2005. Vol. 59. Iss. 28, p. 3703-3709. DOI: 10.1016/j.matlet.2005.06.042

39. Meggyes T., Jefferis S.A. Mine Paste Backfill–The Behaviour of Thickened Tailings and Pipeline Design. GeoCongress 2012: State of the Art and Practice in Geotechnical Engineering: Proceedings of GeoCongress. 2012, 25-29 March 2012, Oakland, California, USA. ASCE, 2012, p. 4116-4125. DOI: 10.1061/9780784412121.423

40. Walske M.L., McWilliam H., Doherty J., Fourie A. Influence of curing temperature and stress conditions on mechanical properties of cementing paste backfill. *Canadian Geotechnical Journal*. 2015. Vol. 52. N 1, p. 148-161. DOI: 10.1139/cgj-2014-0502

41. Yilmaz T., Ercikdi B., Karaman K., Külekçi G. Assessment of strength properties of cemented paste backfill by ultrasonic pulse velocity test. *Ultrasonics*. 2014. Vol. 54. Iss. 5, p. 1386-1394. DOI: 10.1016/j.ultras.2014.02.012

42. Li Li. Analytical solution for determining the required strength of a side-exposed mine backfill containing a plug. *Canadian Geotechnical Journal*. 2014. Vol. 51. N 5, p. 508-519. DOI: 10.1139/cgj-2013-0227

43. Ercikdi B., Kesimal A., Cihangir F. et al. Cemented paste backfill of sulphide-rich tailings: Importance of binder type and dosage. *Cement & Concrete Composites*. 2009. Vol. 31. Iss. 4, p. 268-274. DOI: 10.1016/j.cemconcomp.2009.01.008

44. Jafari M., Shahsavari M., Grabinsky M. Drained Triaxial Compressive Shear Response of Cemented Paste Backfill (CPB). *Rock Mechanics and Rock Engineering*. 2021. Vol. 54. Iss. 6, p. 3309-3325. DOI: 10.1007/s00603-021-02464-5

45. Tariq A., Yanful E.K. A review of binders used in cemented paste tailings for underground and surface disposal practices. *Journal of Environmental Management*. 2013. Vol. 131, p. 138-149. DOI: 10.1016/j.jenvman.2013.09.039

46. Haiqiang Jiang, Fall M. Yield stress and strength of saline cemented tailings in sub-zero environments: Portland cement paste backfill. *International Journal of Mineral Processing*. 2017. Vol. 160, p. 68-75. DOI: 10.1016/j.minpro.2017.01.010

47. Cihangir F., Akyol Y. Effect of Desliming of Tailings on the Fresh and Hardened Properties of Paste Backfill Made from Alkali-Activated Slag. *Advances in Materials Science and Engineering*. 2020. Vol. 2020. N 4536257. DOI: 10.1155/2020/4536257

48. Chi J.M., Ran Huang, Yang C.C. Effects of Carbonation on Mechanical Properties and Durability of Concrete Using Accelerated Testing Method. *Journal of Marine Science and Technology*. 2002. Vol. 10. Iss. 1, p. 14-20. DOI: 10.51400/2709-6998.2296

49. Yoon-Moon Chun, Naik T.R., Kraus R.N. Carbon dioxide sequestration in concrete in different curing environments. *Proc. Int. Conf: Sustainable construction materials and technologies*, 11-13 June 2007, Coventry. Special papers proceedings, 2007, p. 18-24.

50. Kasap T., Yilmaz E., Sari M. Physico-chemical and micro-structural behavior of cemented mine backfill: Effect of pH in dam tailings. *Journal of Environmental Management*. 2022. Vol. 314. Iss. 4. N 115034. DOI: 10.1016/j.jenvman.2022.115034

51. Pokharel M., Fall M. Combined influence of sulphate and temperature on the saturated hydraulic conductivity of hardened cemented paste backfill. *Cement & Concrete Composites*. 2013. Vol. 38, p. 21-28. DOI: 10.1016/j.cemconcomp.2013.03.015

52. Fang K., Fall M. Effects of curing temperature on shear behaviour of cemented paste backfill-rock interface. *International Journal of Rock Mechanics and Mining Sciences*. 2018. Vol. 112, p. 184-192. DOI: 10.1016/j.ijrmms.2018.10.024

53. Raffaldi M.J., Seymour J.B., Richardson J. et al. Cemented Paste Backfill Geomechanics at a Narrow-Vein Underhand Cut-and-Fill Mine. *Rock Mechanics and Rock Engineering*. 2019. Vol. 52. Iss. 12, p. 4925-4940. DOI: 10.1007/s00603-019-01850-4

54. Skobelev D.O., Cherepovitsyna A.A., Guseva T.V. Carbon capture and storage: net zero contribution and cost estimation approaches. *Journal of Mining Institute*. 2023. Vol. 259, p. 125-140. DOI: 10.31897/PMI.2023.10

55. Shaposhnikov N.O., Golubev I.A., Khorobrov S.V. et al. Autoclave modeling of corrosion processes occurring in a gas pipeline during transportation of an unprepared multiphase medium containing CO_2. *Journal of Mining Institute*. 2022. Vol. 258, p. 915-923. DOI: 10.31897/PMI.2022.92

56. Fedoseev S.V., Tcvetkov P.S. Key Factors of Public Perception of Carbon Dioxide Capture and Storage Projects. *Journal of Mining Institute*. 2019. Vol. 237, p. 361-368. DOI: 10.31897/PMI.2019.3.361

57. Cherepovitsyn A., Chvileva T., Fedoseev S. Popularization of Carbon Capture and Storage Technology in Society: Principles and Methods. *International Journal of Environmental Research and Public Health*. 2020. Vol. 17. Iss. 22. N 8368. DOI: 10.3390/ijerph17228368

58. Gür T.M. Carbon Dioxide Emissions, Capture, Storage and Utilization: Review of Materials, Processes and Technologies. *Progress in Energy and Combustion Science*. 2022. Vol. 89. N 100965. DOI: 10.1016/j.pecs.2021.100965

59. Kantyukov R.R., Zapevalov D.N., Vagapov R.K. Analysis of the application and impact of carbon dioxide media on the corrosion state of oil and gas facilities. *Journal of Mining Institute*. 2021. Vol. 250, p. 578-856. DOI: 10.31897/PMI.2021.4.11

60. Ilinova A.A., Romasheva N.V., Stroykov G.A. Prospects and social effects of carbon dioxide sequestration and utilization projects. *Journal of Mining Institute*. 2020. Vol. 244, p. 493-502. DOI: 10.31897/PMI.2020.4.12

61. Vasilev Yu., Cherepovitsyn A., Tsvetkova A., Komendantova N. Promoting Public Awareness of Carbon Capture and Storage Technologies in the Russian Federation: A System of Educational Activities. *Energies*. 2021. Vol. 14. Iss. 5. N 1408. DOI: 10.3390/en14051408

62. Ponomarev A.I., Yusupov A.D. Effect of shear stress on the wall of technological pipelines at a gas condensate field on the intensity of carbon dioxide corrosion. *Journal of Mining Institute*. 2020. Vol. 244, p. 439-447. DOI: 10.31897/PMI.2020.4.6

63. Cherepovitsyn A.E., Ilinova A.A., Evseeva O.O. Stakeholders management of carbon sequestration project in the state – business – society system. *Journal of Mining Institute*. 2019. Vol. 240, p. 731-742. DOI: 10.31897/PMI.2019.6.731

64. Tcvetkov P. Engagement of resource-based economies in the fight against rising carbon emissions. *Energy Reports*. 2022. Vol. 8. S. 10, p. 874-883. DOI: 10.1016/j.egyr.2022.05.259

65. Yilmaz E., Belem T., Benzaazoua M. Effects of curing and stress conditions on hydromechanical, geotechnical and geochemical properties of cemented paste backfill. *Engineering Geology*. 2014. Vol. 168, p. 23-37. DOI: 10.1016/j.enggeo.2013.10.024

Authors: **Pitchou M. Bukasa,** *PhD, Senior Lecturer, pbukasam@unam.na, https://orcid.org/0000-0001-6088-1135* (*University of Namibia, Windhoek, Namibia*), **Melvin M. Mashingaidze,** *Lecturer, https://orcid.org/0000-0002-7558-8369* (*University of Namibia, Windhoek, Namibia*), **Simasiku L. Simasiku,** *Laboratory Technician, https://orcid.org/0000-0003-2434-5604* (*University of Namibia, Windhoek, Namibia*).

The authors declare no conflict of interests.

ISSN 2411-3336; e-ISSN 2541-9404

JOURNAL OF MINING INSTITUTE

Zapiski Gornogo instituta

Journal homepage: pmi.spmi.ru

Research article

Analysis of experience in the use of preformed particle polymer gels in the development of high-water-cut production facilities in low-temperature oil reservoirs

Sergei V. GALKIN✉, Yuliya A. ROZHKOVA
Perm National Research Polytechnic University, Perm, Russia

***How to cite this article*:** Galkin S.V., Rozhkova Yu.A. Analysis of experience in the use of preformed particle polymer gels in the development of high-water-cut production facilities in low-temperature oil reservoirs. Journal of Mining Institute. 2024. Vol. 265, p. 55-64. EDN CNCFIW

Abstract. Foreign practice of oil production in high-water-cut conditions suggests using the technology of injection of preformed particle gel (PPG) suspension into injection wells. After swelling, the polymer particles become elastic and are able to penetrate through highly permeable watered intervals into the remote reservoir zone, forming a polymer "plug". Thus far, the domestic experience of application of this technology boiled down to testing foreign compounds. We have looked into the possibilities of PPG technology application in geological and technological conditions of high-water-cut fields of Perm Krai. The paper proposes PPG reagents effective in low-temperature reservoirs (20-35 °C) and at relatively high salinity of formation water (more than 200 g/l). The world experience of PPG technology application was analyzed to identify the principal scheme of reagent injection, to establish variants of sequence of injection of PPG particles of different sizes, as well as the possibility of regulating the morphological characteristics of polymer gel particles during synthesis depending on the porosity and permeability of the reservoir. A prerequisite for the technology is the ability to remove PPG particles after treatment from the bottom-hole zone of the formation; for this purpose, tests were carried out on a breaker compound based on sodium persulfate with synergizing additives. PPG technology is effective in reservoirs with high permeability heterogeneity. Two types of high-water-cut production facilities potentially promising for PPG realization have been identified for oil fields of Perm Krai. The first type includes carbonate Tournaisian-Famennian reservoirs with pronounced macrofracturing, in which the PPGs are used for colmatation of flushed large fractures. The second type is terrigenous Visean deposits with increased oil viscosity from 5 to 100 mPa·s and high permeability of reservoirs (> 0.5 μm^2). For both types of reservoirs, areas have been selected that are promising for the implementation of PPG technology.

***Keywords*:** water cut in production wells; injectivity profile; injection wells; superabsorbent; preformed particle polymer gel; permeability; injection pressure

Acknowledgments. The research was carried out with the financial support of the Ministry of Education and Science of Russia within the framework of implementation of the program of the world-class research and education center "Rational Subsoil Use". A number of studies were carried out at the unique scientific installation "Complex for the study of the structure of the capacitive space of rocks" of the community center for filtration and capacitive properties of rocks of PNRPU.

Received: 09.02.2021 ***Accepted: 20.09.2023*** ***Online: 21.12.2023*** ***Published: 29.02.2024***

Introduction. At a late stage of oil field exploitation, waterflooding of reservoirs results in formation of washed-out zones through which the injected water seeps. Consequently, production wells are prematurely watered out, while a part of residual recoverable oil reserves (ROR) from less permeable zones do not participate in the displacement process and remain undeveloped. This problem is most pronounced in oil deposits with highly heterogenour permeability and increased oil viscosity. It is especially urgent to reduce watercutting of well products in "old" oil and gas producing areas. The possibility of extending the life of well stock for late-stage fields would help intensify production

and increase the final oil recovery factor. Rational development of such fields should be supported by tertiary enhanced oil recovery methods.

At present, the main method of increasing the efficiency of water injection in domestic fields is the technology based on the use of polymer solutions. As field experience shows, in conditions of high salinity of formation water the standard use of polyacrylamide (PAA) is ineffective. As polymers can be adsorbed by rock surface and interact with metal ions in water (such as Na^+, Ca^{2+}), the rheological characteristics of the injected PAA solution change greatly during treatment. Study [1] shows that due to adsorption of a part of the polymer dissolved in water by the formation rock, the polymer does not enter the anterior part of the displacing water front and the mobility of the water phase does not change significantly. As a result, the polymer front can significantly lag behind the front of oil displacement by water.

In order to influence the reservoir injectivity profile in fields at the late stage of exploitation, the world practice in recent years has been to use the technology of injecting a suspension of preformed particle gel (PPG) into injection wells. After swelling, the polymer particles become elastic and therefore can penetrate into highly permeable watered intervals, bypassing the bottom-hole zone (BHZ) to the remote formation zone (RFZ), and forming a polymer "plug" [2-4].

Problem statement. Russian experience in the application of technology based on preformed polymer gels mostly consists in testing the compounds produced abroad. Among the domestic developments, one should mention Temposcreen reagent based on water-soluble PAA cross-linked by ionizing irradiation and requires dedicated expensive equipment to be produced [5-7]. There is also a limited experience in the application of water-swelling AK-639 polymer, which swells at a temperature of 70 °C, and Ritin polymer gel, at oil fields [8-10].

For Perm Krai, applicability of the aforementioned polymers is limited by their low absorption capacity at low reservoir temperatures (20-35 °C) and increased formation water salinity (more than 200 g/l). In such geological conditions the absorption capacity of preformed particle gels tends to decrease, as particles remain rigid, which significantly reduces their ability to penetrate the RFZ. This process is explained by the Flory – Huggins theory, stating that in the presence of cations in aqueous medium, a double electric layer formed by negatively charged functional groups of the polymer and metal cations is formed on the surface of the polymer particle [11]. The described phenomenon leads to a decrease in the mobility of polymer chains in the pellet and, as a result, to a significant decrease in the absorption capacity.

Study [1] describes the experience of injection of preformed polymer systems at the Kalamkas field (Kazakhstan) and a number of fields in Perm Krai. In general, the geological and technical performance of PPG technology in wells of Yu1C formation of the Kalamkas field was 80 %. At the same time, the maximum technological efficiency was achieved in the zone of paleochannels (91 %), which in addition to increased density of oil reserves are characterized by the highest velocities of injected water. For Perm Krai fields, the analysis of waterflooding experience using standard polyacrylamide has shown low efficiency, as there is almost no residual resistance factor for water injected following the margin. Study [1] makes a conclusion on promising application of PPG technology at oil facilities of Perm Krai and recommends to carry out research work to adapt the properties of synthesized polymers for the geological and physical conditions of this territory.

Generalization of international research experience in application of preformed particle gels in the oil industry is made in review papers [12-14]. Notably, the industrial experience of PPG technology application abroad is much more extensive. Preformed particle gels have been developed and tested for selective blocking of reservoir interlayers with permeability more than 0.5 μm^2 [15-17], along with microgels which aim at conformance control in wells with lower permeability of intervals treated

Journal of Mining Institute. 2024. Vol. 265. P. 55-64

with gel (up to 0.5 μm^2) [18, 19]. Microgels are obtained by inverse emulsion synthesis; there are varieties of microgels that are water-swellable microspheres [20, 21], thermosensitive microgels with two types of cross-linking (stable and unstable) [22], pH-sensitive microgels [18] etc. The PPG technology has been tested at fields in China, USA, Canada, etc., where it is considered an effective method of conformity control of the displacement front of oil reservoirs with water cut from 50 to 95 %. Based on the analysis of scientific publications, we can summarize the experience of technology implementation.

Figure 1 shows the basic scheme of PPG reagent injection [23], which involves preparing a suspension using produced water in a tank with an agitator. PPG suspension is pumped alternately with water. The recommended concentration of the reagent ranges from 2000 to 3500 mg/l, the volume of suspension for one treatment varies from 2500 to 4300 m^3 on average. The required weight of PPG powder for treatment is 5-15 tons.

The advantage of using preformed particle polymer gels is low cost of the polymer, minimal expenditures on equipment for preparation of the suspension for injection into the well, as well as stability of its visco-elastic characteristics in reservoir conditions.

The PPG technology [24] was applied in a wide range of reservoir temperatures from 45 to 110 °C. Formation water with different salinity (up to 150 g/l and higher) was used for treatments. The gel was synthesized on the basis of polyacrylamide with addition of N,N′-methylene-bisacrylamide crosslinker. The absorption capacity of the obtained gel can vary from 10 to 200 g/g depending on the crosslinker concentration and formation water salinity.

The analysis of foreign experience shows that during treatment the volume of injected PPG suspension per well is 2000-4500 m^3, the weight of dry PPG powder is from 5 to 15 tons of reagent. Duration of PPG treatment can be from 1.5 to 6 months. PPG technology application results in the following effects: increase of oil flow rate up to 10 tons per day; treatment effect of 120-250 tons per each ton of PPG powder (in dry form); reduction of water cut of production wells from 5 to 10 %. The technological effect from PPG treatment can last up to 12 months [25-27].

Methodology. The possibilities of PPG technology application are considered for the geological and technological conditions of the Volga-Ural oil and gas province (OGP) where most oil fields are at a late stage of operation. A typical example of prevalence of such mature fields is the territory of Perm Krai, where product water cut exceeds 75 % in more than 50 % of wells. In such geological and technological conditions there is a need for application of complex technologies aimed at conformity control and involvement of previously undeveloped reserves.

Formation conditions of Perm Krai fields are characterized by low temperatures (20-35 °C), which is generally typical for the Paleozoic sediments of the Volga-Ural Basin. Relatively high

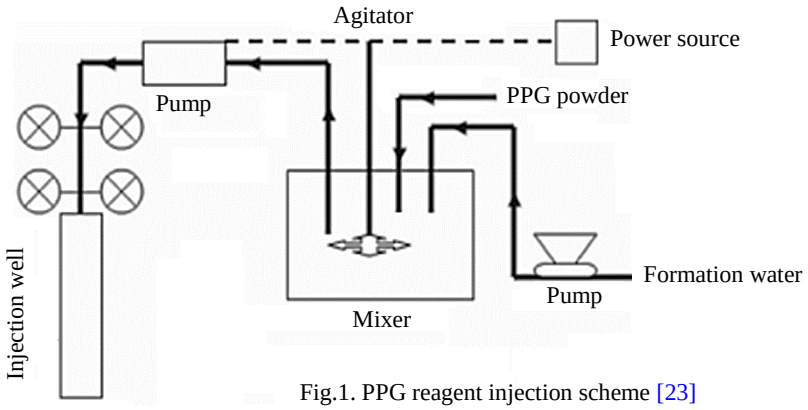

Fig.1. PPG reagent injection scheme [23]

mineralization of formation water (200-230 g/l) is typical for Perm Krai. PPG reagents recommended for the study area should be adapted to the conditions of low-temperature formations with high formation water salinity.

Due to low temperature and increased salinity of formation water, the absorption capacity drops significantly. That is why most imported PPG formulations are ineffective for the study area. The authors have developed an original formulation of PPG gel cross-linked with imide functional groups formed during synthesis between polyacrylamide chains [28]. Under the study conditions, the proposed composition has an absorption capacity of 35-40 g/g, which is twice higher than the available analogs. Optical microscopy has shown that the gel particles increase in size by 4-6 times during swelling. Tests to determine the strength of gel particles showed that they are able to compress and pass through holes 20 times smaller than the diameter of the swollen particle.

The authors have conducted filtration core tests of this reagent on carbonate fractured [29] and terrigenous reservoirs of pore type [30]. Using the X-ray tomography method [31] it was established that PPG suspension colmatizes fractures and highly permeable porous intervals of the core and promotes redistribution of filtration flows into low-permeable channels.

PPG treatment is controlled by three main parameters: injection rate, suspension concentration, and size of gel particles, which are determined, among other things, by permeability of the bottomhole formation zone and injectivity of injection wells. If at the initial stage of treatment there is an increase in pump outlet pressure, the first step is to reduce the injection rate and PPG concentration. The parameters are adjusted during treatment so that the injection pressure does not exced 80 % of the design rock fracture pressure.

The gel particle size is selected based on the void space characteristics, as well as gel characteristics (strength, absorption capacity). The most common algorithm for treatment involves injection of suspension starting with small PPG fractions, and if there is no change in injection pressure, increasingly larger PPG fractions are injected.

A different treatment option is used to treat reservoirs that have been determined to have fully flushed “superchannels”. In this case, injection starts with a larger PPG fraction to colmatize the reservoirs, and then gradually shifts to PPG with a smaller particle size.

During injection, PPG gel particles can adhere to the rock surface and form a crust [32, 33], so the necessary condition is the technological possibility to remove the reagent after treatment from the bottomhole zone. In [34] core studies it is shown that swollen PPG particles in the presence of hydrochloric acid can give away from 60 to 85 % water. Dehydration of PPG particles leads to their multiple shrinking and, consequently, to the restoration of permeability and porosity of the core. Analysis of the experience of the technology application shows that to restore BHZ injectivity, a breaker is usually injected into the injection well after treatment [35, 36].

Both enzymes and oxidizing agents were considered for the development of breakers (destructors) that destroy the structure of preformed gel. Enzymes are capable of effecting polymer chains, which leads to their breaking into shorter fragments of lower molecular weight. The use of enzymes as breakers is limited by their effectiveness in small temperature and pH intervals, as well as by their high cost. Therefore, it is more promising to use breakers that break polymer chains as a result of redox processes.

Study [35] describes tests of PPG breakers based on such oxidizing agents as sodium hypochlorite, calcium hypochlorite, and sodium persulfate, and concludes that the latter is more efficient. With this in mind, the authors tested a breaker based on sodium persulfate as part of the testing of the obtained reagent. During the research PPG particles were kept in model formation water (mineralization 200 g/l) up to the equilibrium absorption capacity, after which a 20 g gel sample was placed

Journal of Mining Institute. 2024. Vol. 265. P. 55-64

in the breaker solution. After 24 hours, the polymer was separated from the breaker solution by filtration. The fractions of dissolved polymer were calculated from the polymer mass values before and after interaction with the breaker. The test showed that 85 % of the PPG gel dissolved during interaction with the breaker within one day, which can be considered a satisfactory result.

One of the main conditions determining the final efficiency of the technology application is the correct choice of the development system section, including the injection and associated production wells. The necessary requirement for the injection well is its high injectivity factor. For successful introduction of the technology in the implementation area, the formation has to have a pronounced heterogeneity in terms of permeability (k) from 10^{-3} μm^2 to single digits. There should be a stable hydrodynamic connection between the injection and production wells, which is most reliably substantiated by tracer studies.

Having summarized the analysis of experience of PPG technology implementation, we can formulate the following geological and technological conditions for selecting sites promising in terms of its effective application. Economic feasibility should be justified by the presence of sufficient residual recoverable oil reserves, which oil and gas producing companies currently estimate based on 3D digital geological and technological models. The site of technology implementation should be characterized by water cut of production wells more than 50 % and high injectivity of injection wells [13]. In this case, based on the methods of hydrodynamic studies of wells, well interference testing and tracing of labeled substances, stable hydrodynamic connection between the injection well and the neighboring producing wells should be established. Examples of evaluation of interference of production and injection wells based on complex analysis of hydrodynamic studies of wells, methods of hydraulic listening and tracing of labeled substances are given in [36].

Effective application of PPG technology also requires high anisotropy of reservoir permeability both in height and in area. With this in mind, this technology can be effective for both fractured reservoirs and pore-type reservoirs with highly heterogeneous geological structure. For deposits with pronounced macrofracturing, the purpose of PPG is colmatization of washed-out large fractures. In Perm Krai, this type is mainly confined to carbonate reservoirs of Tournaisian-Famennian age (T, Fm) [37]. An example is the deposit of reservoir T of the Opalikhinskoe field, which is characterized by high-viscosity oil (μ = 82 mPa·s) and reduced reservoir matrix permeability (k = 0.061 μm^2). In this production facility with the current reserve recovery η = 46.8 %, more than 60 % of wells work with water cut of more than 50 %, which testifies to the expediency of application of tertiary methods of oil recovery.

An area of the deposit with increased density of oil reserves and water cut of all producing wells exceeding 50 % was selected as a promising area for implementation of PPG technology (Fig.2).

The choice of this area for implementation of a production trial is based, among other things, on the fact that it is well studied: apart from standard logging, hydrodynamic studies have shown high permeability of the reservoir (k > 0.5 μm^2). At the same time, its injection wells N 423, 433, 439 have a characteristic bend on the pressure drop curves (Fig.3), which is interpreted as presence of fracturing in Warren – Root model [38, 39].

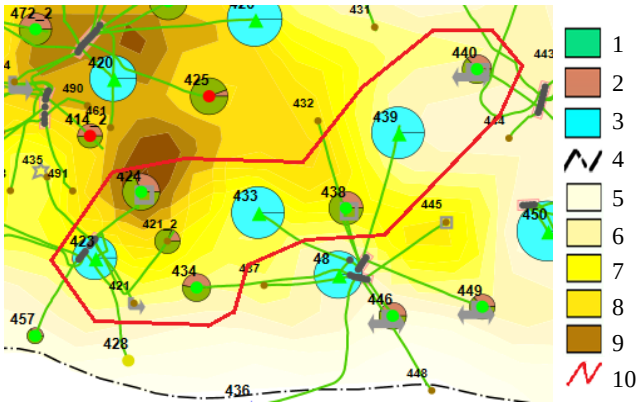

Fig.2. Example of a fractured reservoir development site. Facility T. Opalikhinskoe oil field
1, 2 – current withdrawals, tons per day (1 – water flow rate, 2 – oil flow rate); 3 – injectivity, m^3/day; 4 – outer oil bearing contour; 5-9 – density of reserves, t/m^2 (5 – 0.03-0.17; 6 – 0.17-0.32; 7 – 0.32-0.46; 8 – 0.46-0.61; 9 – 0.61-0.75); 10 – PPG area

According to efficiency calculations, the average fracture openness over the thickness of the perforation interval ranges from 30 to 50 μm. The effect of PPG technology application should be colmatization of the most open cracks, and taking into account the change in particle size after swelling, the minimum size of PPG particles can be estimated at 250 μm.

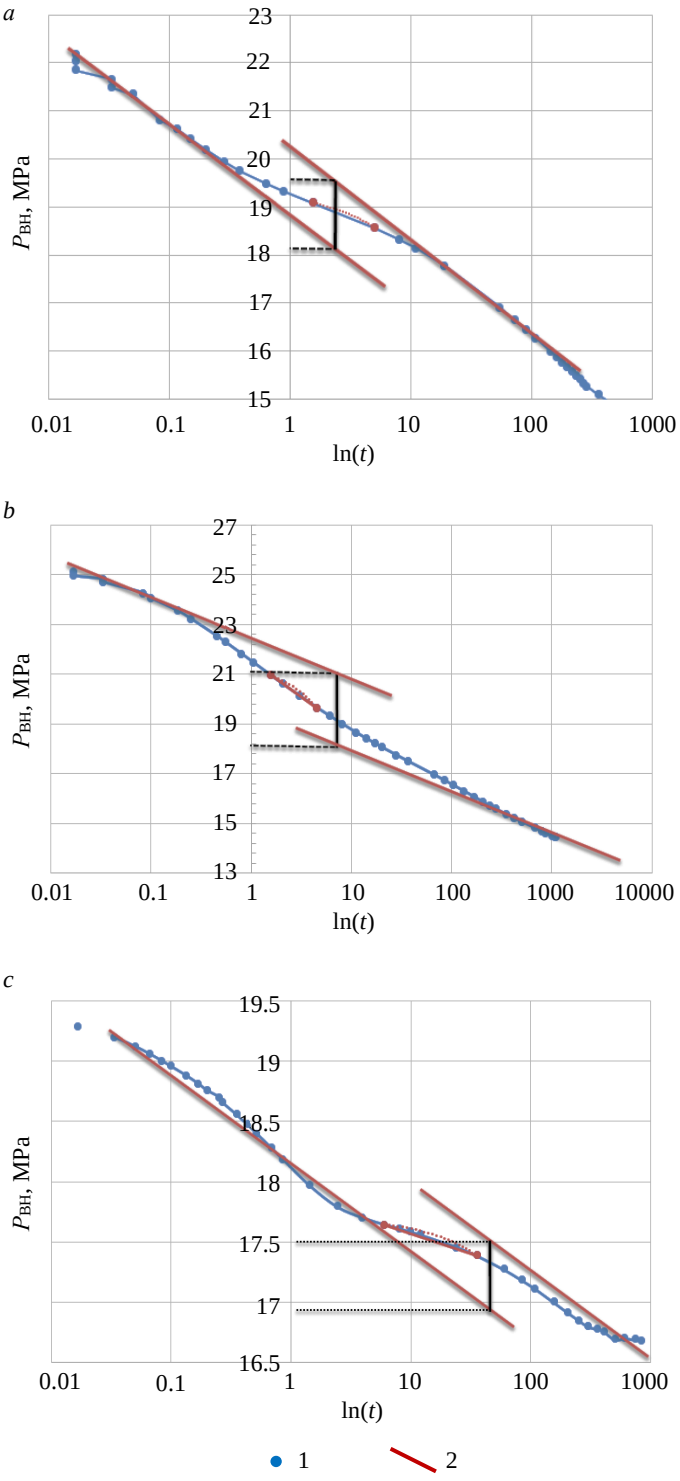

Fig.3. Pressure drop curves for injection wells N 423 (*a*), 433 (*b*), 439 (*c*)
1 – pressure drop curve measurements;
2 – interpretation by Warren – Root model

In a pore type of reservoir, the advanced waterflooding of wells is more pronounced in deposits with increased oil viscosity. Figure 4 shows examples of dependence of well product watercut on oil reserves recovery [40] for pore type reservoirs in different ranges of reservoir oil viscosity.

At $\mu < 2$ mPa·s only after recovery of $\eta > 75$ % reserves, the wells start to quickly become waterflooded. At low μ, the oil displacement front is uniform over the entire reservoir thickness, and water cut does not exceed 45 % during the main development period. Starting from $\mu > 5$ mPa·s, the water cut exceeds 50 % as early as at 40 % recovery. Thus, deposits with increased oil viscosity ($\mu \geq 5$ mPa·s) in highly permeable pore reservoirs ($k \geq 0.5$ μm^2) are promising for PPG realization. The analysis of Perm Krai deposits shows that deposits of this type predominantly belong to terrigenous Visean strata (Tl, Bb, Ml – 41 facilities) of the platform part of Perm Krai. It should be noted that focal areas with $k \geq 0.5$ μm^2 might be present in deposits with lower average permeability, which may also become targets for PPG application.

The Tl-Bb reservoir of the Shagirtsko-Gozhanskoe field ($\mu = 38$ mPa·s, $k = 1.2$ μm^2, $\eta = 60.9$ %) can be considered a promising pore-type facility for PPG technology. In this production facility as a whole, in presence of sufficient ROR, the stock of producing wells operates with water cut of more than 80 % (Fig.5).

According to foreign practice, it is recommended to select candidate wells for injection of PPG reagents by calculating the *PI* (pressure index), which is plotted on a pressure drop curve with values taken at intervals of 5-10 min when the injection well is shut down for 90 min [14, 23, 41]. An index is calculated from the graph of pressure change over time

Journal of Mining Institute. 2024. Vol. 265. P. 55-64

$$PI = \frac{\int_0^T P(t)}{T},$$

where $P(t)$ is pressure change over time when the injection well is shut down; T is well shut-down time.

According to [14], injection wells with lower *PI* values deviating from the average value for the site by more than 5 MPa can be considered the first-priority candidates for PPG injection. According to the data of short-term measurements of efficiency (Fig.6) with participation of the authors, in [42] calculations of *PI* were carried out, according to which for wells N 370 – *PI* = 83.5 MPa; 1113 – *PI* = 104.8; 1128 – *PI* = 113.8; 1133 – *PI* = 78.9.

Thus, the considered development element is characterized by a high degree of heterogeneity (*PI* range of about 35 MPa) and can be recommended for selective isolation of highly permeable intervals. The lowest *PI* index was recorded for injection wells N 370 and 1133, which have a sharp downward trend of efficiency (Fig.6). Taking this into account, wells 370 and 1133 are prioritized for reagent injection when implementing PPG technology.

Conclusion. On the basis of the analysis of international experience of PPG technology application and research conducted for low-temperature oil deposits of Perm Krai, the authors have developed a composition cross-linked with imide functional groups formed during synthesis between poly-acrylamide chains This PPG reagent has an absorption capacity of 35-40 g/g, which is twice as high as available analogs. The effectiveness of colmatization of fractures and highly permeable porous intervals by the developed compound with redistribution of filtration flows into low-permeable channels is confirmed by the results of core filtration trials.

Optical microscopy studies have shown that swollen gel particles increase in size by 4-6 times. Tests to determine the strength of the gel particles show that they are able to compress and pass through holes 20 times smaller than the diameter of the swollen particle.

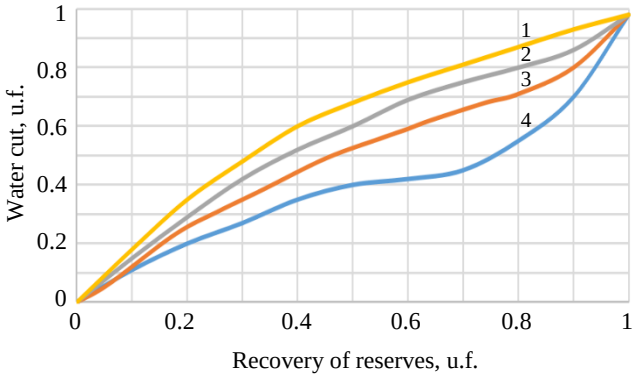

Fig.4. Dependences of product water cut on recovery of reserves depending on different ranges of oil viscosity. Tl-Bb-Ml facilities. Perm Krai [40]

1 – μ < 2 MPa·s; 2 – μ = 2-5; 3 – μ = 5-20; 4 – μ > 20

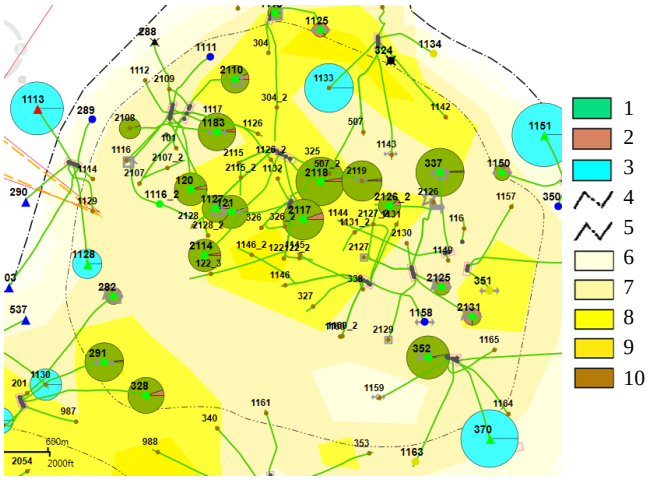

Fig.5. Example of a pore reservoir development site. Tl-Bb facilities. Shagirtsko-Gozhanskoe field

1, 2 – current withdrawals, tons per day (1 – water flow rate, 2 – oil flow rate); 3 – injectivity, m^3/day; 4 – inner oil bearing contour; 5 – outer oil bearing contour; 6-10 – density of reserves, t/m^2 (6 – 1.23-3.97; 7 – 3.97-6.71; 8 – 6.71-9.44; 9 – 9.44-12.18; 10 – 12.18-14.92)

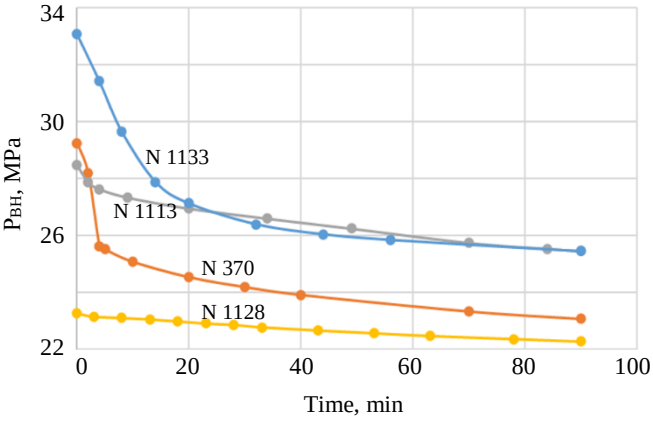

Fig.6. Pressure drop curves of injection wells N 370; 1113; 1128; 1133 for *PI* calculation

Two main areas of PPG technology application have been identified for high-water-cut oil production facilities in Perm Krai: in carbonate reservoirs with established fracturing and in terrigenous reservoirs with high heterogeneity of geological structure. For carbonate deposits, the effect of PPG technology application should consist in colmatization of the most open fractures. At one of the production facilities, based on the data of hydrodynamic studies of wells, the injection section with the established fracture openness of about 30-50 μm was identified, where injection of the reagent is recommended. Minimal size of PPG particles during treatment is estimated at 250 μm.

In terrigenous reservoirs, PPG technology is most effective for oil deposits with viscosity more than 5 mPa·s and permeability more than 0.5 μm^2. The PI index was calculated for this type of reservoir when selecting injection wells for PPG injection using the pressure drop curve. It was found that the considered element of development is characterized by a high degree of heterogeneity (*PI* range of about 35 MPa). As a result of calculations, the wells with a sharp downward trend of the pressure drop curve were recommended for injection of the reagent.

The research has included trials of different types of breakers for PPG, with the conclusion that sodium persulfate is the most effective one. The experiments showed that 85 % of the PPG gel dissolved when interacting with sodium persulfate within one day.

Thus, as a result of the conducted research, a complex of necessary measures for effective application of PPG technology has been determined. The principal scheme of reagent injection was defined, effective scenarios of sequential injection of PPG particles of different sizes were established for various geological and technological conditions. Potentially promising areas of PPG implementation with fractured carbonate and pore terrigenous types of reservoirs were identified. The conducted studies allow singling out promising operational sites for implementation of preformed particle gel injection technology that could increase the period of profitable operation and ultimate oil recovery factor in mature fields in the long run.

REFERENCES

1. Mikhailov N.N., Zakenov S.T., Kiynov K.K. et al. The experience of implementation of polymer flooding technology in oil fields characterized by a high degree of salinity of reservoir and injected waters. *Oil Industry Journal*. 2019. N 4, p. 74-78 (in Russian). DOI: 10.24887/0028-2448-2019-4-74-78

2. Elsharafi M.O., Bai B. Effect of Strong Preformed Particle Gel on Unswept Oil Zones/Areas During Conformance Control Treatments. EAGE Annual Conference & Exhibition incorporating SPE Europec, 10-13 June 2013, London, UK. OnePetro, 2013. N SPE-164879-MS. DOI: 10.2118/164879-MS

3. Goudarzi A., Zhang H., Varavei A. et al. Water Management in Mature Oil Fields using Preformed Particle Gels. SPE Western Regional & AAPG Pacific Section Meeting 2013 Joint Technical Conference, 19-25 April 2013, Monterey, CA, USA. OnePetro, 2013. N SPE-165356-MS. DOI: 10.2118/165356-MS

4. Zhang H., Bai B. Preformed-Particle-Gel Transport Through Open Fractures and Its Effect on Water Flow. *SPE Journal*. 2011. Vol. 16. Iss. 2, p. 388-400. DOI: 10.2118/129908-PA

5. Barabanov V.L., Demyanovsky V.B., Kaushansky D.A. The study of rheological heterogeneity of the liquid systems in the instance of the water-swollen dispersed gels of polyacrylamide. *Georesources, geoenergetics, geopolitics.* 2016. N 1 (13) (in Russian). DOI: 10.29222/ipng.2078-5712.2016-13.art4

6. Kaushansky D.A. Multipurpose innovative technology “Temposkrin-Lyuks” to increase OIL recovery from reservoirs at the late stage of development. *Georesources, geoenergetics, geopolitics.* 2014. N 1 (9) (in Russian).

7. Kaushanskii D.A., Batyrbaev M.D., Duzbaev S.K., Demyanovskii V.B. Results of using Temposcreen technology in the fields of the Republic of Kazakhstan (on the example of PF Embamunaigas). *Geology, geophysics and development of oil and gas fields.* 2006. N 9, p. 51-58 (in Russian).

8. Idiyatullin A.R. Ritin-10: A new effective reagent for reservoir recovery increase. *Oil Industry Journal.* 2007. N 2, p. 54-58 (in Russian).

9. Sladovskaya O.Yu., Bashkirtseva N.Yu., Kuryashov D.A. et al. Application of colloidal systems for oil recovery enhancement. *Vestnik Kazanskogo tekhnologicheskogo universiteta*. 2010. N 10, p. 585-591 (in Russian).

10. Shuvalov S.A., Vinokurov V.A., Khlebnikov V.N. Using polymeric agents for eor and waterproofing. *Trudy Rossiiskogo gosudarstvennogo universiteta nefti i gaza imeni I.M.Gubkina*. 2013. N 4 (273), p. 98-107 (in Russian).

11. Hongbin Yang, Wanli Kang, Shuren Liu et al. Mechanism and Influencing Factors on the Initial Particle Size and Swelling Capability of Viscoelastic Microspheres. *Journal of Dispersion Science and Technology*. 2015. Vol. 36. Iss. 11, p. 1673-1684. DOI: 10.1080/01932691.2014.1000463

12. Rozhkova Y.A., Burin D.A., Galkin S.V., Yang H. Review of Microgels for Enhanced Oil Recovery: Properties and Cases of Application. *Gels*. 2022. Vol. 8. Iss. 2. N 112. DOI: 10.3390/gels8020112

13. Baojun Bai, Jia Zhou, Mingfei Yin. A comprehensive review of polyacrylamide polymer gels for conformance control. *Petroleum Exploration and Development*. 2015. Vol. 42. Iss. 4. DOI: 10.1016/S1876-3804(15)30045-8

14. Yuzhang Liu, Baojun Bai, Yefei Wang. Applied Technologies and Prospects of Conformance Control Treatment in China. *Oil & Gas Science and Technology – Revue IFP Energies nouvelles*. 2010. Vol. 65. Iss. 6, p. 859-878. DOI: 10.2516/ogst/2009057

15. Bai B., Liu Y., Coste J.-P., Li L. Preformed Particle Gel for Conformance Control: Transport Mechanism Through Porous Media. *SPE Reservoir Evaluation & Engineering*. 2007. Vol. 10. Iss. 2, p. 176-184. DOI: 10.2118/89468-PA

16. Imqam A., Bai B., Delshad M. Preformed Particle Gel Propagation Through Super-K Permeability Sand and Its Resistance to Water Flow During Conformance Control. SPE/IATMI Asia Pacific Oil & Gas Conference and Exhibition, 20-22 October 2015, Nusa Dua, Bali, Indonesia. OnePetro, 2015. N SPE-176429-MS. DOI: 10.2118/176429-MS

17. Long Yu, Qian Sang, Mingzhe Dong. Enhanced oil recovery ability of branched preformed particle gel in heterogeneous reservoirs. *Oil & Gas Science and Technology – Revue IFP Energies nouvelles*. 2018. Vol. 73. Iss. 1. N 65. DOI: 10.2516/ogst/2018062

18. Abdilbaki M., Huh C., Sepehrnoori K. et al. A critical review on use of polymer microgels for conformance control purposes. *Journal of Petroleum Science and Engineering*. 2014. Vol. 122, p. 741-753. DOI: 10.1016/j.petrol.2014.06.034

19. Almohsin A., Ding H., Bai B. Experimental Study on the Transport and Improved Oil Recovery Mechanism of Submicron Particle Gel. SPE EOR Conference at Oil and Gas West Asia, 26-28 March 2018, Muscat, Oman. OnePetro, 2018. N SPE-190364-MS. DOI: 10.2118/190364-MS

20. Meiqin Lin, Guiqing Zhang, Zhao Hua et al. Conformation and plugging properties of crosslinked polymer microspheres for profile control. *Colloids and Surfaces A: Physicochemicsal Engineering Aspects*. 2015. Vol. 477, p. 49-54. DOI: 10.1016/j.colsurfa.2015.03.042

21. Chuanjin Yao, Guanglun Lei, Lei Li, Xuemei Gao. Selectivity of Pore-Scale Elastic Microspheres as a Novel Profile Control and Oil Displacement Agent. *Energy Fuels*. 2012. Vol. 26. Iss. 8, p. 5092-5101. DOI: 10.1021/ef300689c

22. Ohms D., McLeod J., Graff C.J. et al. Incremental-Oil Success From Waterflood Sweep Improvement in Alaska. *SPE Production & Operations*. 2010. Vol. 25. Iss. 03. DOI: 10.2118/121761-PA

23. Baojun Bai, Liangxiong Li, Yuzhang Liu et al. Preformed Particle gel for Conformance Control: Factors Affecting its Properties and Applications. SPE/DOE Symposium on Improved Oil Recovery, 17-21 April 2004, Tulsa, OK, USA. OnePetro, 2004. N SPE-89389-MS. DOI: 10.2118/89389-MS

24. Baojun Bai, Mingzhen Wei, Yuzhang Liu. Injecting Large Volumes of Preformed Particle Gel for Water Conformance Control. *Oil & Gas Science and Technology – Revue IFP Energies nouvelles*. 2012. Vol. 67. Iss. 6, p. 941-952. DOI: 10.2516/ogst/2012058

25. Daoyi Zhu, Jirui Hou, Xianxing Meng et al. Effect of Different Phenolic Compounds on Performance of Organically Cross-Linked Terpolymer Gel Systems at Extremely High Temperatures. *Energy Fuels*. 2017. Vol. 31. Iss. 8, p. 8120-8130. DOI: 10.1021/acs.energyfuels.7b01386

26. Long Yu, Qian Sang, Mingzhe Dong. Enhanced oil recovery ability of branched preformed particle gel in heterogeneous reservoirs. *Oil & Gas Science and Technology – Revue IFP Energies nouvelles*. 2018. Vol. 73. Iss. 1. N 65. DOI: 10.2516/ogst/2018062

27. Bo Wang, Meiqin Lin, Jinru Guo et al. Plugging properties and profile control effects of crosslinked polyacrylamide microspheres. *Journal of Applied Polymer Science*. 2016. Vol. 133. Iss. 30. N 43666. DOI: 10.1002/APP.43666

28. Rozhkova Yu.A. Justification of the application of limited swelling polymer gels in the development of high-water-cut oil production facilities in Perm Krai: Avtoref. dis. … kand. tekhn. nauk. Perm: Permskii natsionalnyi issledovatelskii politekhnicheskii universitet, 2021, p. 19 (in Russian).

29. Ketova Y.A., Bai B., Khizhnyak G.P. et al. Testing of preformed particles polymer gel technology on core filtration models to limit water inflows. *Journal of Mining Institute.* 2020. Vol. 241, p. 91-96. DOI: 10.31897/PMI.2020.1.91

30. Ketova Y., Galkin S., Kolychev I. Evaluation and X-Ray tomography analysis of super-absorbent polymer for water management in high salinity mature reservoirs. *Journal of Petroleum Science and Engineering*. 2021. Vol. 196. N 107998. DOI: 10.1016/j.petrol.2020.107998

31. Efimov A.A., Galkin S.V., Savitsky Y.V., Galkin V.I. Estimation of heterogeneity of Oil & Gas field carbonate reservoirs by means of computer simulation of Core X-Ray Tomography data. *Ecology, Environment and Conservation*. 2015. Vol. 21. November S, p. 79-85.

32. Elsharafi M., Bai B. Minimizing Formation Damage for Preformed Particle Gels in Mature Reservoirs. SPE Asia Pacific Enhanced Oil Recovery Conference, 11-13 August 2015, Kuala Lumpur, Malaysia. OnePetro, 2015. N SPE-174645-MS. DOI: 10.2118/174645-MS

33. Imqam A., Bai. B. Optimizing the strength and size of preformed particle gels for better conformance control treatment. *Fuel*. 2015. Vol. 148, p. 178-185. DOI: 10.1016/j.fuel.2015.01.022

34. Imqam A., Bai B., Wei M. et al. Use of Hydrochloric Acid To Remove Filter-Cake Damage From Preformed Particle Gel During Conformance-Control Treatments. *SPE Production & Operations*. 2016. Vol. 31. Iss. 03. № SPE-172352-PA. DOI: 10.2118/172352-PA

35. Ze Wang, Baojun Bai, Enze Zhou et al. Experimental Evaluation of Oxidizing Breakers for a Polyacrylamide-Based Re-Crosslinkable Preformed Particle Gel. *Energy & Fuels*. 2019. Vol. 33. Iss. 6, p. 5001-5010. DOI: 10.1021/acs.energyfuels.9b00709

36. Martyushev D.A. Improving the geological and hydrodynamic model of a carbonate oil object by taking into account the permeability anisotropy parameter. *Journal of Mining Institute.* 2020. Vol. 243, p. 313-318. DOI: 10.31897/PMI.2020.3.313

37. Cherepanov S.S. Integrated research of carbonate reservoir fracturing by Warren – Root method using seismic facies analysis (evidence from tournaisian-famennian deposit of Ozernoe field). *Perm Journal of Petroleum and Mining Engineering.* 2015. Vol. 14. N 14, p. 6-12 (in Russian). DOI: 10.15593/2224-9923/2015.14.1

38. Fei Wang, Shicheng Zhang. Pressure-buildup analysis method for a post-treatment evaluation of hydraulically fractured tight gas wells. *Journal of Natural Gas Science and Engineering*. 2016. Vol. 35. N PA, p. 753-760. DOI: 10.1016/j.jngse.2016.09.026

39. Mordvinov V.A., Martiushev D.A., Ladeishchikova T.S., Gorlanov N.P. Estimation of effects of natural reservoir fracturing on producing well performance. *Perm Journal of Petroleum and Mining Engineering.* 2015. Vol. 14. N 14, p. 32-38 (in Russian). DOI: 10.15593/2224-9923/2015.14.4

40. Ilyushin P.Yu. Justification of oil reservoir water cut forecast using analog-statistical methods (on the example of development of Permian Prikamye fields): Avtoref. dis. … kand. tekhn. nauk. Saint Petersburg: Natsionalnyi mineralno-syrevoi universitet "Gornyi", 2013, p. 20 (in Russian).

41. Dongmei Wang, R.S. Seright, Zhenbo Shao, Jinmei Wang. Key Aspects of Project Design for Polymer Flooding at the Daqing Oilfield. *SPE Reservoir Evaluation & Engineering.* 2008. Vol. 11. Iss. 06. N SPE-109682-PA, p. 1117-1124. DOI: 10.2118/109682-PA

42. Rozhkova Y.A., Gurbanov V.S., Efendiyev G.M., Galkin S.V. Assessment of applicability of preformed particle gels for Perm region oil fields. XIV Russian Conference on Petroleum and Mining Engineering, 09-12 November 2021, Perm, Russia. IOP Conference Series: Earth and Environmental Science, 2022. Vol. 1021. N 012073. DOI: 10.1088/1755-1315/1021/1/012073

***Authors*: Sergei V. Galkin,** *Doctor of Geological and Mineralogical Sciences, Professor, gnfd@pstu.ru, https://orcid.org/0000-0001-7275-5419* (*Perm National Research Polytechnic University, Perm, Russia*), **Yuliya A. Rozhkova,** *Candidate of Engineering Sciences, Researcher, https://orcid.org/0000-0002-3199-455X* (*Perm National Research Polytechnic University, Perm, Russia*).

The authors declare no conflict of interests.

ISSN 2411-3336; e-ISSN 2541-9404

JOURNAL OF MINING INSTITUTE

Zapiski Gornogo instituta

Journal homepage: pmi.spmi.ru

Research article

Improvement of concentrate quality in flotation of low-rank coal

Sergei A. KONDRATEV, Tatyana A. KHAMZINA✉
Chinakal Institute of Mining, Siberian Branch, Russian Academy of Sciences, Novosibirsk, Russia

How to cite this article: Kondratev S.A., Khamzina T.A. Improvement of concentrate quality in flotation of low-rank coal. Journal of Mining Institute. 2024. Vol. 265, p. 65-77. EDN RJTNNI

Abstract. Percentage of high-rank coal with low content of ash, moisture, and sulfur in total coal production output is low. Most of the produced coal has a low quality (lignite, bituminous coal: long-flame and fiery). Under increasing requirements for ecological cleanness of coal, the efficient use of coal products is only possible after improvement of their processing properties. The authors discuss the enhancement of flotation efficiency of low-rank coal using the mechanism of physisorption of a collecting agent in particle – bubble attachment. It is explained why the yield of concentrate with low ash content increases as a result of combination of collectors having different physical properties. It is shown that the surface activity of a heteropolar agent relative to the gas – liquid interface and the adsorption density of the agent govern its collecting properties. Based on the recovery – surface activity relationship, the correlation is found between the collecting activity of a chemical compound and the structure of its molecules. The combination of the collectors with different surface activity enables adjusting collectability and selectivity of the blend. The physisorption mechanism of collectors can be a framework for developing recommendations on modification of concentrate yield and ash content, and on selection of optimized ratios of surface activities of miscible collectors relative to the gas – liquid interface.

***Keywords*:** flotation; coal; concentrate yield; ash content; agent surface activity; extraction selectivity

Acknowledgment. The study was supported by the Russian Science Foundation, Grant N 22-27-00084.

Received: 17.05.2022 ***Accepted: 03.04.2023*** ***Online: 01.09.2023*** ***Published: 29.02.2024***

Introduction. The electric power sector in Russia in recent decades features a steady trend toward a decline in the quality of coal as a consequence of the growing scale of its gross production. Low-rank coals used in power generation in Russia differ drastically by composition and qualities which govern efficiency of coals in terms of energy, ecology, and economy. Ash content of low-rank fuel exceeds 40 %. It is unlikely that the quality of coal can improve in the future as it is planned to increase production of power-station coals by open-pit mining of lower rank coal deposits.

In Russia run-of-mine coal is mostly used in industrial power generation. The use of low-rank coals features lower combustion heat and higher fuel consumption [1]. Combustion of low-rank coal slack involves increased emission of toxic pollutants, as well as elevated cost of transportation and storage of much ash and slag. The long-term development program approved by the Russian Government for the coal industry in Russia up to 2030 requires improvement of energy efficiency and industrial and ecological safety. It is only possible to make low-rank coal a high-rank fuel by beneficiation. Flotation is an efficient way of dressing coal slag and upgrading quality of low-rank coal.

Flotation of low-rank coal slag consumes much more conventional collectors. The process selectivity drops as conventional collectors fed at increased consumption are adsorbed at ash [2-5]. To increase coal recovery and decrease ash content of concentrate, a combination of collectors is commonly used. For instance, a mixture of residual fuel oil containing long-chain hydrocarbons with kerosene substantially improved flotation of oxidized coal [6, 7]. The use of mixed dodecane and 4-dodecylphenol allowed increasing extraction of lignite [8]. The higher yield of concentration can be explained by the increased hydrophobicity of coal as a result of sorption of 4-dodecylphenol preferably at oxidized hydrophilic surfaces, while dodecane adsorbed at hydrophobic surfaces.

Supposedly, higher hydrophobicity of low-rank coal enhances selectivity of its recovery. To this effect, the surface tension of a main collector is reduced by addition of surfactants. Many researchers think that its finer emulsification occurs and allows better spreading and flattening of microdrops attached to coal [9, 10]. It is also possible that an apolar collector spreads over a heteropolar collector attached to oxidized areas of coal [11-13].

It is stated in [14] that reagents containing apolar compounds, which are more akin to aromatic components of coal of medium and high metamorphic degree and are capable of fixing on the coal surface in a droplet form rather than in molecular form at the coal surface, are more effective. It is also believed that a physisorbed collector should attach as microdrops [15].

Insoluble collectors find application not only in coal flotation. The use of insoluble hydroxamic acid (AERO 6493) added with aliphatic alcohols C_6-C_{13} allowed improving the efficiency of apatite ore concentration. A single flotation stage produced a concentrate with a P_2O_5 content of 31 % and the recovery of 95 %, while the flotation feed only contained 5 % P_2O_5 [16, 17]. High selectivity of extraction of apatite ore was explained by spreading of a microdrop of the insoluble complex collector over the mineral surface [18]. Flotation of phosphate from nepheline ore using fat acids and surface-active oxyethylated isotridecanol produced in a single process stage a high-quality concentrate containing 31 % P_2O_5 at the recovery of 95 % [19].

Allyl ethers of xanthates are the best selective agents amongst sulfide collectors. These agents are therefore insoluble in water and are usually fed in the cycle of milling. For making a target mineral hydrophobic, xanthate is fed in the cycle of flotation. A small consumption of xanthate, insufficient to extract the target mineral, ensures hydrophobization, which is sufficient for the target mineral and insufficient for the waste rock minerals. For this reason, insoluble allyl ether of xanthate attaches mostly to hydrophobizated sites of the target mineral, which provides high selectivity of flotation [20].

This study aims to examine the influence exerted by the structure and composition of molecules of a collector on its collectability, and to analyze the effect of the physisorption mechanism of a single or mixed-type collector on coal recovery and concentrate quality.

Methods. The study used the available experimental materials on the influence exerted by the structure and composition of molecules of a collector on its flotation activity and selectivity. To this effect, the flotation activity of various collecting agents was correlated with the structure of their molecules. Then, transition from the structure and composition of the collector molecules to the collector activity in flotation was carried out using the physisorption mechanism of a collector [21]. The analysis of coal recovery in concentrate in correlation with the ash content of coal also used the physisorption mechanism.

First, the role of physisorption in the particle – bubble attachment was determined. The rupture of a water film between a particle and an air bubble involves formation of a local meniscus with an advancing contact angle θ_A. To dry the surface of the coal particle facing the bubble, it is necessary to fulfill the inequality

$$\sigma_{SG} - \sigma_{SL} < \sigma_{LG} \cos\theta_R^D, \quad (1)$$

where σ_{SG} is the surface tension at the solid – gas interface; σ_{SL} is the surface tension at the solid – liquid interface; σ_{LG} is the surface tension at the liquid – gas interface.

Inequality (1) holds true when the contacting angle θ_A, formed after the water film rupture, reaches the value of the dynamic receding angle θ_R^D, which is a characteristic of wettability of a target mineral to be extracted [22]. The value of θ_R^D describes possibility of widening a local dry spot formed

Journal of Mining Institute. 2024. Vol. 265. P. 65-77

on the coal surface after the water film rupture. The value of θ_R^D depends on the mineral surface hydrophobicity, and on its chemical and geometrical heterogeneity. The time of the transition $\theta_A \to \theta_R^D$, i.e. from the angle formed at the moment of the water film rupture to the angle θ_R^D, is governed by the spreading rate of a physisorbed collector and by the physisorption ability to capture water from the film.

The surface tension gradient of physisorbed surfactants at particles and bubbles defines the spreading rate of physisorbed collector on the water film surface. The surface tension gradient decomposes into two cofactors: $G = (\partial\sigma/\partial C)\,(\partial C/\partial x)$. Here, $\partial\sigma/\partial C$ characterizes the surface activity of long-chain (oxyhydryl, sulfhydryl, cation) collectors, and $\partial C/\partial x$ describes the concentration gradient (ΔC) in the direction of the film movement. The concentration gradient is governed by the consumption of a collector and by the difference between the adsorption densities of the collector physisorption at the particle and at the air bubble. In this manner, the spreading rate is proportional to the surface activity of a physisorbed collector and to the difference of the physisorbed collector concentrations at the particle and at the bubble at the moment of the water film rupture between them:

$$V \approx k \frac{\partial\sigma}{\partial C} \Delta C, \tag{2}$$

where k is the constant of proportionality.

It follows from relation (2) that spreading rate increases with the higher surface activity of derivatives of a collecting agent and the greater its sorption on the extracted mineral with a simultaneous decrease on the bubble [22]. In flotation machines, the gas environment undergoes continuous refresh, and the surface concentration at the bubble may be assumed as zero for this reason. A high rate of spreading of a collector over the gas – liquid interface and the high rate of removal of water from the film interlayer reduces the induction time which unambiguously defines floatability. According to [23], the time of water removal from the film interlayer is the dominant factor in the mechanism of the particle – bubble attachment. Experiments have proved the connection between the time of induction and the combustible matter extraction in concentrate [24].

Connection of ash content and extractability of coal from the analysis of physisorption mechanism. In flotation, it is possible to improve the quality of a concentrate by using a weaker collector or by reducing the collector consumption [14, 22]. Let us discuss the way of increasing the flotation selectivity by changing consumption of a collector while maintaining its surface activity ($\partial\sigma/\partial C$ const). An apolar collector at a smaller consumption will exhibit attachment in the form of drops predominantly to higher rank coal particles. The local rupture of the water film will take place at the physisorbed collector attachment site, i.e. at higher quality coal. A small consumption of a collector means no physisorption at ash particles and reduced adsorption at lower rank coal particles. As follows from equation (2), the low concentration of a collector will decrease ΔC, and will extend the transition time $\theta_A \to \theta_R^D$ and the time of induction, which will reduce the content of ash in the concentrate.

An increased consumption of an apolar collector will increase its adsorption density at higher rank coal, but the sorption on oxidized coal will also increase. Due to the increased adsorption of the collector at coal and owing to its zero adsorption at air bubbles, ΔC will grow together with the higher recovery of all coal components. If its consumption is increased more, the apolar collector attachment at lower rank coal will grow, the latter will get in the concentrate, and the flotation froth will contain

much ash. An increase in consumption of dodecane from 1 to 4 kg/t increased coal extraction, but at the same time at a dodecane consumption of more than 3 kg/t, the ash content of concentrate increased (Fig.1) [2].

Flotation of low-rank coal uses heteropolar collectors, for example, carboxylic acids. They increase recovery of combustibles by minimum 30 % compared to alkanes at the same consumption of the collectors (Fig.1) [2]. Increasing consumption of carboxylic acids can increase the concentrate yield. An increase in consumption of octenoic and dodecanoic acids improved the yield of the combustible matter but also substantially increased the ash content of the concentrate (Fig.1). This effect is especially noticeable in case of surface-active acids having a high rate of spreading over the gas – liquid interface (Fig.2).

A physically sorbable agent attaches preferably to hydrophobic surfaces and is a selective collector. It is effective at the gas – liquid interface irrespective of the coal surface condition and is not selective relative to target particles in this regard. Nonselectivity of physisorption grows with the increasing rate of a physisorbed collector spreading over water surface.

Palmitic acid has a low spreading rate (Fig.2) [25]. Its physisorption (molecules) has no material effect on the rate of water removal from the film and on the time of induction. For this reason, extraction embraces only hydrophobic particles with a sufficient value of ΔC, which explains the

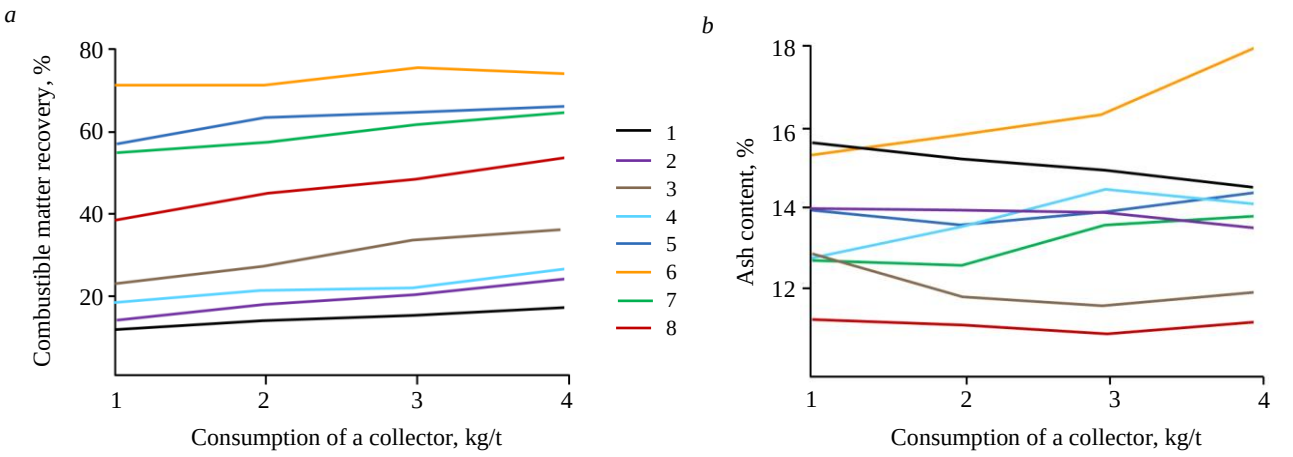

Fig.1. Flotation of coal with apolar collector and carboxylic acids:
a – recovery of combustible matter; *b* – ash content of concentrate [2]
1 – *n*-pentane; 2 – *n*-octane; 3 – dodecane; 4 – *n*-hexadecane; 5 – *n*-pentanoic acid; 6 – *n*-caprylic acid; 7 – dodecanic acid; 8 – palmic acid

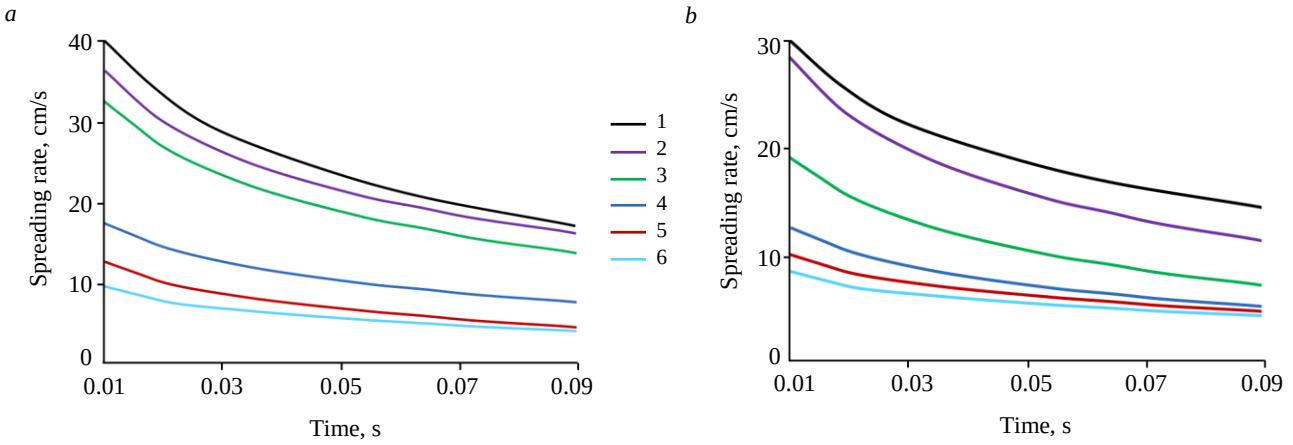

Fig.2. Spreading rate of carboxylic acids over water surface versus time: *a* – pH = 7; *b* – pH = 10 [25]
1 – hexoic acid; 2 – octenoic acid; 3 – decanoic acid; 4 – dodecanoic acid; 5 – tetradecanoic acid; 6 – palmitic acid

Journal of Mining Institute. 2024. Vol. 265. P. 65-77

lowest content of ash in the concentrate among all test acids (see Fig.1, *b*). The low spreading rate and the long induction time result in the decreased recovery of the combustible matter (see Fig.1, *a*).

Octenoic acid, which has the maximal spreading rate ($\partial C/\partial x$ and ΔC have optimal values), offered the maximal extraction of the combustible matter and, because of nonselectivity of its physisorption, the high content of ash in the concentrate.

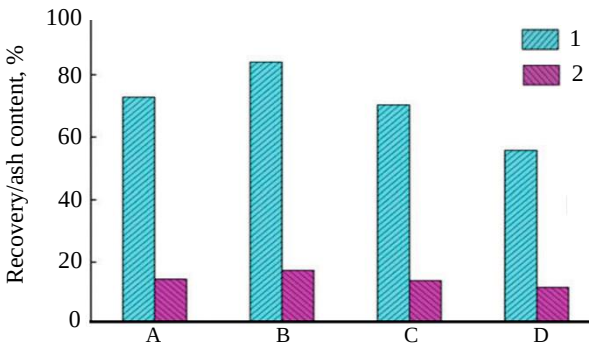

Fig.3. Collectability of carboxylic acids versus carbon atoms in hydrocarbon chain [2]

A – *n*-pentanoic acid; B – *n*-octenoic acid; C – dodecanoic acid; D – tetradecanoic acid; 1 – extraction of combustible matter; 2 – ash content

Let us consider an approach to stimulating selectivity by changing the flotation activity of a collector at the preserved constant consumption (ΔC const). The influence of hydrocarbon chain length (surface activity) of carboxylic acids on flotation performance was studied in [2]. The increase in the number of carbon atoms in hydrocarbon chain of an acid enhanced extraction of the combustible matter from 72 % in case of pentanoic acid and to 84 % in case of octenoic acid (Fig.3). The higher collecting ability results from the higher surface activity $\partial\sigma/\partial C$ of acids with a longer hydrocarbon chain containing 10-12 atoms of carbon, and from the required value of ΔC being achieved. Carboxylic acids perform most actively in the neutral or weakly alkaline range of pH. For instance, oleinic acid generates surface-active dimers which achieve the maximal concentration when pH ~8. These dimers weaken the surface tension of the solution, generate the higher surface pressure at the moment of the water film rupture and, accordingly, accelerate water removal from the film.

Flotation of gas and coking coals using α-olefins was tested in [26]. The maximal yield of the concentrate was achieved with olefin containing 10 carbon atoms in hydrocarbon chain in case of gas coal and with olefin with 12 carbon atoms in case of coking coal [21]. The maximal yield of the concentrate was also obtained with a 12 carbon atoms chain in the radical [9]. Olefins with hydrocarbon fragments C_{11} and C_{12} showed an increased extraction of coal by 2-2.5 % as compared with alkanes [27]. As per the physisorption mechanism, an increase in extraction of a useful element is connected with the higher surface activity $\partial\sigma/\partial C$ and, as a consequence, with the higher spreading rate of a surfactant over the gas – liquid interface (curve (2) in Fig.2), and with the sufficient value of ΔC. The transition time $\theta_A \rightarrow \theta_R^D$ and the induction time become lower with surface-active acids.

Connection of molecule structure and composition with collectability and selectivity of collectors. Alkanes contain no hydrophilic groups and have a low surface tension: it varies from 20.3 mN/m for heptane to 25.35 mN/m for dodecane [28], which points at the higher surface pressure. However, there is no interaction between molecules of alkanes with zero dipole moment and polar molecules of water. For this reason, alkanes show no spreading over the gas – liquid interface [22]. The physisorption activity defined by the surface activity $\partial C/\partial x$ and by the spreading rate is low. An advantage of alkanes consists in their selective attachment at hydrophobic surfaces according to the rule of polarity balancing between adjoining media. The strength of the physisorption attachment is not of vital importance. After the water film rupture, a physisorbed collector goes to bubble surface. When the content of mineral matters is low and the degree of oxidation is high, it is necessary to select a collector with the increased donor – acceptor interaction in surface tension [29].

It is found that a monoalkylate collector containing 89-98 % of isoparaffins features high selectivity [30]. The content of aromatic compounds and unsaturated hydrocarbons is less than 0.3 % and

1.1-1.7 %, respectively. Isoparaffins mostly represent branched compounds with non-zero dipole moment. High selectivity of such collectors is governed by the absence of hydrophilic groups.

Addition of a hydrophilic group into the collector molecule changes its interaction with water molecules, its solubility, and spreading rate. As a hydrocarbon fragment of saturated acids gets longer, their spreading rate lowers because of cohesion between molecules in the film (see Fig.2). The maximal spreading rate is a feature of the short-chain acid, but at small concentrations, the low molecular mass of the acids disables their adsorption at coal surface in a sufficient amount to generate the required value of ΔC. The increased molecular mass of the acids above 144 g/mole enables sufficient adsorption at coal and the increased ΔC. With further increase in the molecular mass and in the hydrocarbon chain length, the spreading rate of the acids over the gas – liquid interface will decrease (see Fig.2). The decrease in the spreading rate will increase the transition time $\theta_A \rightarrow$ $\rightarrow \theta_R^D$ and induction time.

Initially, an increase in the surface activity (hydrocarbon chain length) to a certain value (octenoic and decanoic acids) leads to an increase in recovery (Fig.3). The further addition of atoms affects adversely on the recovery of combustible matter in concentrate due to cohesion of acid molecules and reduced spreading rate. The decrease in the spreading rate of acids over water surface weakens the physisorption effect in spreading. The chemisorption effect remains unchanged. The ratio of the chemisorption and physisorption effects grows; the quality of the concentrate improves accordingly, which is observed in flotation with dodecanoic and tetradecanoic acids (Fig.3) [31].

The dipole moment of a collector molecule characterizes the collector interaction with water molecules. For instance, in coal flotation with alkanes, alkenes and arenes (Table 1) [32], the rise of the dipole moment correlates with the yield of the concentrate and with the recovery of the combustible matter, while it has no correlation with the quality of the concentrate. The dipole moment characterizes the spreading rate of a collector over the gas – liquid interface, i.e. the physisorption activity.

Table 1

Performance of coal flotation with alkanes, alkenes and arenes

Collectors	Yield, %	Ash content, %	Combustible matter recovery, %	Dipole moment *D*
Alkanes	46.0	8.2	50.7	0 (octane)
Olefins	57.8	8.5	63.7	0.25 (octene)
Arenes	76.2	8.7	83.3	0.58 (ethyl benzene)

The experimental results [2, 25, 31] imply: the increase of the surface activity and spreading rate over water surface in physisorption raises the ash content of concentrates.

A way of enhancing extraction of the combustible matter at the good quality of a concentrate is a combination of collectors having different values of $\partial\sigma/\partial C$. The flotation performance with alkane (dodecane) and ionic and anionic (oleinic acid) collectors is compared in [33]. Figure 4 depicts the combustible matter extraction and the concentrate ash content versus the collector consumption. The extraction with dodecane is comparatively low because of the weak surface activity of the latter relative to the gas – liquid interface. The collector spreading at the said interface takes place not due to interaction with water molecules but due to gravity. The increase in the consumption of dodecane only slightly enhances the yield of the concentrate as a consequence of the grown value of ΔC (Fig.4). The ash content of the concentrate lowers owing to the selective attachment of the apolar collector to the hydrophobic areas of coal surface and due to zero spreading of the collector over water surface. In case of oleinic acid, extraction is much higher thanks to the higher value of $\partial\sigma/\partial C$. The spreading

Journal of Mining Institute. 2024. Vol. 265. P. 65-77

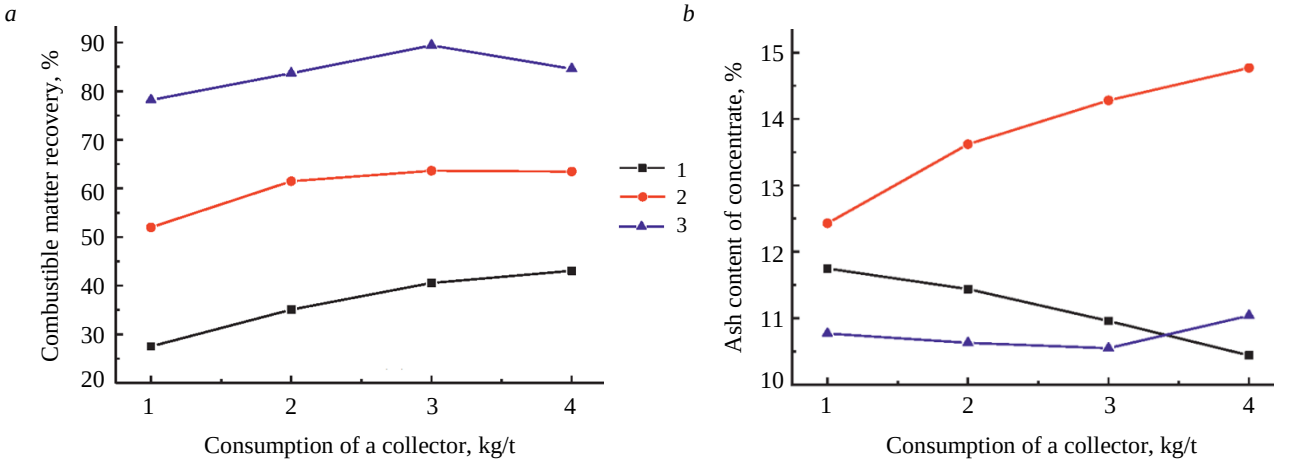

Fig.4. Performance of low-rank coal flotation versus consumption of a collector:
a – extraction of combustible matter; *b* – ash content of concentrate [33]
1 – dodecane; 2 – oleinic acid; 3 – oleinic acid + dodecane

rate of oleinic acid over water surface is more than 20 cm/s. The concentrate quality is low and the ash content is much higher than in flotation with dodecane as molecules of the acid are sensitive to oil and water and the acid physisorption is unselective. And, as said earlier, the physisorption effect is independent of the coal surface condition.

Selective extraction of low-rank coal Yozgat Ayridam was tested in flotation with kerosene, weakly soluble emulsifier, and nonionic surfactant Flotigol CS [12]. The surfactants somewhat promoted connection of the mixture with water molecules but supported no chemical interaction with the surface of hydrophobic coal. At the same time, the cation-active and anion-active substances lowered the concentrate quality. The use of nonionic surfactants is described in [34, 35].

A combination of collectors at moderate acid consumption increased the yield of concentrate and decreased its ash content (Fig.4). The reduced recovery of the combustible matter and the lower quality of the concentrate at the collector consumption higher than 3 kg/t results from the entry of low-rank and impure coal in the froth product.

This example illustrates the fact that every collector performs its own function. Dodecane exhibits selective attachment in the form of drops to hydrophobic areas of coal surface. Oleinic acid with oil and water sensitive molecules is adsorbed by dodecane microdrops, i.e. at the oil – water interface, and enhances the surface activity of the mixture. The surface tension of dodecane – oleinic acid equals the acid surface tension [33]. This property of the mixture provides the wanted value of $\partial\sigma/\partial C$ and the high spreading rate of the mix, i.e. the high extraction of the concentrate. Some acid molecules get attached to oxidized coal and enclosed minerals, and form linkages with their functional groups. In case of high acid consumptions, inorganic matters enter the concentrate. For dodecane and oleinic acid, their ratio in the mixture of collectors was selected as 4:1. In coal flotation with diesel fuel and oleinic acid, the maximal extraction of the combustible matter was reached at the collector ratio of 4:1 [36]. So, a heteropolar collector possessing high surface activity is adsorbed at the oil – water interface and improves the surface activity of a mixture.

The analytical reasoning shows that selectivity of an agent is governed by the ratio of different sorption mechanisms of the agent in removal of water from the film interlayer. An apolar agent is selectively adsorbed at the hydrophobic surface, but has a low surface activity and exhibits a low recovery. The heteropolar collector is attached at microdrops of an apolar collector, makes the mixture surface-active relative to the gas – liquid interface and enhances extraction.

Optimizing the ratio of the sorption mechanisms allows a compromise between the quality and recovery in flotation [31, 37].

An increase in consumption of heteropolar frother Montanol 800 raised the ash content of the concentrates as the frother started interacting with rock-forming minerals and enhanced the surface activity $\partial\sigma/\partial C$ of the frother and collector mixture [38]. The reduced extraction of the combustible matter in the concentrate at the increased consumption of the collector (more than 2.2 kg/t) is probably conditioned by the increased attachment of the collector at the target particles and by the decreased surface tension of bubbles down to minimum after attachment of the first particles. As a result, the surface tension gradient ΔC drops to a critical level when neither spreading of the agent nor removal of water from the film interlayer takes place.

The method of flotation improvement by combining collectors with different values of $\partial\sigma/\partial C$ is also effective in case of composing apolar and cation-active collectors. The tests of low-rank coal floatability with diesel fuel combined with a cation-active collector of dodecyltrimethylammonium bromide (DTAB) proved low extraction in case of individual collectors [39]. The combination of the diesel fuel and cation-active collector at a ratio of 2:1 enabled the maximum yield of the concentrate with a low ash content of ~11 % (Fig.5).

The lab-scale tests of low-rank coal determined petrography and mineral composition of the combustible matter in the low-rank gas coal slack (Kuznetsk Coal Basin): ash content 45.10 %; reflectance 0.58 %; vitrinite 58 %; leuptinite 3 %; semivitrinite 8 %; fusinite 27 %; carbon 73.8 %; hydrogen 6.3 %; nitrogen 2.8 %; oxygen 17.5 %; mineral impurities. Tables 2 and 3 describe the grain size composition, fractional makeup of the test coal and the methods of testing, respectively.

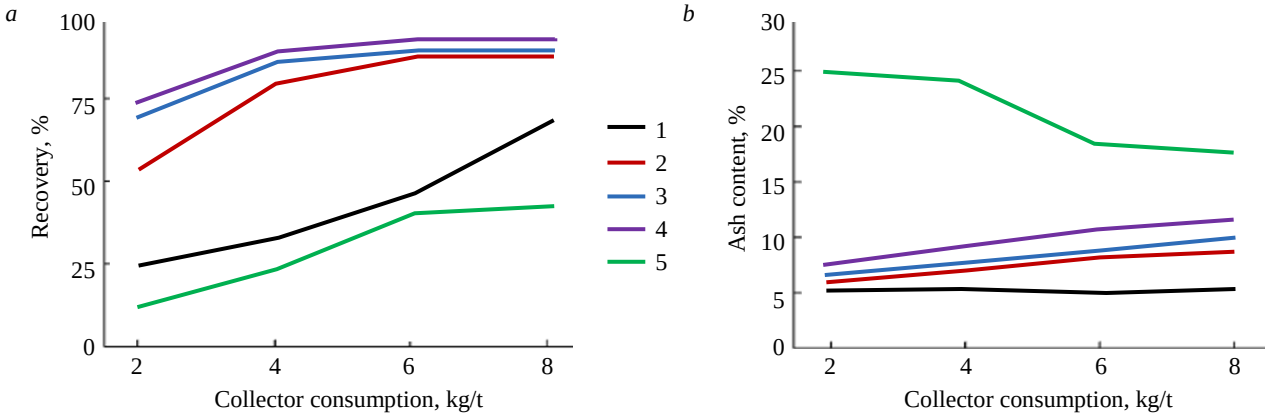

Fig.5. Flotation performance of low-rank coal versus consumption and ratio of collectors: *a* – recovery; *b* – ash content [39]
1 – 0:1; 2 – 1:10; 3 – 1:5; 4 – 1:2; 5 – DTAB

Table 2

Grain size composition and fractional makeup of low-rank gas coal slack (Kuznetsk Coal Basin)

Size grades, mm	Yield, %	Ash content, %	Fraction density, kg/m^3	Yield, %	Ash content, %
			Less than 1400	27.00	5.30
0.2-0.5	37.00	44.42	1400-1500	12.78	9.78
0.1-0.2	17.40	49.80	1500-1600	5.23	20.40
0.05-0.1	7.70	45.60	1600-1800	1.79	36.44
0-0.05	37.90	43.50	More than 1800	53.20	76.51
Total	100.00	45.10	Total	100.0	45.10

Journal of Mining Institute. 2024. Vol. 265. P. 65-77

Table 3

Lab-scale testing of low-rank coal

Test methods	Equipment
Coal slack petrology test in accordance with state standard GOST R 55662-2013 using SIAMS 620 analyzer in automatic mode. Liebig method estimation of carbon and hydrogen in accordance with state standard GOST 32979-2014	
Grain size distribution in accordance with state standard GOST 2093-82 using sieve analyzer MSA-W/D-200. Wet screening at aperture sizes of 0.5; 0.2; 0.1 and 0.05 mm	
Fractional makeup of coal slack in centrifuge cup in accordance with state standard GOST 4790-2017; densities of 1300; 1400; 1500; 1600; 1800 kg/m^3	
Flotation tests on Mekhanobr machine 136A-FL-1, cell volume of 0.5 l, impeller speed 1500 rpm, constant pulp temperature in a range of 19-20 °C. Coal slack size not larger than 0.5 mm, solid content of 100 g/l. Pre-flotation soaking of all test samples for 5 min and loading together with soak water in flotation machine. Flotation time 10 min (complete flotation). One-time feed of agents. Sampling of frother product (flotation concentrate) as bulk concentrate. Flotation performance: flotation concentrate yield γ_c; flotation concentrate ash content A^d_c; combustible matter extraction $E_{c.m}$; tailings ash content A^d_t, $A^d_c = (m_3 - m_1)/(m_2 - m_1)$, where m_1 – mass of roasted boat, g; m_2 – mass of boat with coal sample, g; m_3 – mass of boat with post-roasting residue, g; $E_{c.m} = \gamma_c(100 - A^d_c)/(100 - A^d_{in})$, A^d_{in} – ash content of initial coal slack, %; $A^d_t = (100A^d_{in} - \gamma_c A^d_c)/\gamma_t$, γ_t – flotation tailings, %	
Group analysis of agents using mass-fragmentographic assay (selective ion detection) and software Mass Spectrometry Data Handling System	
Estimation of agent spreading rate in water-filled pan placed under high-speed camera EVERCAM 1000-16-C. Video filming at resolution 1280×304 and speed of 3845 snap/s	

The flotation tests of gas coal slack in the framework of this study proved the trend (Table 4). An apolar collector attaches more selectively to a hydrophobic surface, and a heteropolar collector enables the mixture to interact with water molecules, spreads over water surface and reduces the time of induction. Coal extraction to concentrate grew from 74.18 % in case of dodecane to 78.11 % in case of a mixture of the mentioned collectors, and the ash content of the concentrate lowered from 20.34 to 20.09 %.

Table 4

Flotation of gas coal slack with apolar and heteropolar collectors, and with their combination

Agents	Agent consumption, g/t	Initial ash content, %	Concentrate		Tailings		Extraction of combustible matter to concentrate, %
			Yield, %	Ash content, %	Yield, %	Ash content, %	
Dodecane	300	45.10	51.12	20.34	48.88	70.99	74.18
2-octanol	300	45.10	36.72	22.49	63.28	58.22	51.84
Dodecane 2-octanol	210 90	45.10	53.66	20.09	46.34	74.06	78.11
Hexane	300	45.10	9.06	20.96	90.94	47.50	13.04
Nonane	300	45.10	42.74	21.23	57.26	62.92	61.32

Many studies attempt to enhance flotation performance by combining collectors with similar surface properties. For example, the study into effect of benzene ring in hydrocarbon fragment of the collector on flotation of coal used two surfactants – oxyethylated nonylphenol NPEO and oxyethylated dodecyl ether $C_{12}EO$ [4]. The main apolar collector was kerosene. Pretreatment of coal with NPEO and $C_{12}EO$ increased the extraction from 49.39 to 81.34 and to 83.96 %, respectively. The quality of the concentrate was improved too. Extraction of higher rank coal was somewhat higher with NPEO than with $C_{12}EO$. In the listed agents, the oxyethyl groups are arranged similarly at the beginning of the hydrocarbon fragment. The hydrocarbon chain of $C_{12}EO$ contains 12 carbon atoms. The hydrocarbon chain of NPEO contains 9 atoms of carbon, but the benzene ring is at the beginning of radical, and the surface activity of the ring is equal to 3.5 CH_2-groups of the main unbranched chain [40]. In this manner, the surface activities of these compounds are equal. Nearly similar extraction in case of these collectors is explained by coincidence of their $\partial\sigma/\partial C$ and ΔC, i.e. by their equal spreading rates as per (2).

Results and discussion. The comparative analysis has exhibited correlation between flotation activity and molecular structure of different collectors. The physisorption mechanism in flotation activity allows transition from the structure of molecules to their composition. The flotation activity of an agent depends on the surface activity $\partial\sigma/\partial C$ of the agent, on the difference of the agent adsorption density ΔC at particles and bubbles, and on the cohesion between molecules of the collecting agent. These characteristics are defined by the structure and composition of hydrocarbon fragment. The high flotation activity of collectors having 8-12 carbon atoms chains is explained by the optimal values of $\partial\sigma/\partial C$ and ΔC, and by the low cohesive forces. The double linkage and hydrocarbon radical branching require more atoms of carbon in radical. Activity of many chemical compounds is either known or found experimentally, which enables prediction of their collecting properties. The hydrophilic group of a heteropolar collector governs its connection with water molecules, the value of $\partial\sigma/\partial C$, as well as the possibility to catch water and remove it from the film interlayer between coal particle and gas bubble. Chemical compounds lacking the hydrophilic group have low collectability because of zero interaction with water molecules.

It is possible to enhance selectivity of coal recovery by coal hydrophobization. This statement is proved by selective attachment of alkanes, with their molecules free from the hydrophilic groups, to the organic phase of coal (see Fig.1). Nonselective attachment of molecules of carboxylic acid worsens

Journal of Mining Institute. 2024. Vol. 265. P. 65-77

the concentrate quality, but their surface activity $\partial\sigma/\partial C$ defines the spreading rate of a mixture of collectors and the velocity of water removal from the film interlayer between the objects of interaction in accordance to (2).

Combining collectors with different physical properties allows to achieve the wanted performance of concentrate yield and quality. An apolar collector at moderate consumption attaches selectively to hydrophobic surface of coal in accordance with the rule of polarity balancing between adjoining media. The spreading rate of such collector is relatively low, which explains its low collecting ability (see Fig.1). A heteropolar collector possesses a high surface activity and velocity of water removal from the film, which is reflective of its high collectability. At the same time, this collector exhibits attachment to mineral impurities in coal, which explains the high resultant ash content of the concentrate (see Fig.1). Adsorption of the heteropolar collector at the surface of the apolar collector at the oil – water interface adds the high surface activity and collectability to the mixture. Thus, the surface activity of a physically sorbable collector characterizes the recovery of the combustible matter, and the physically adsorbed apolar collector largely influences the concentrate quality.

Selectivity of a collector is governed by the ratio of the activities of the heteropolar and apolar compounds in the mixed-type collector relative to the gas – water surface, and by the ratio of their consumptions. The physisorption activity is understood as the efficiency of the physically adsorbable collector during its spreading, or as the thickness of its surface flow at the gas – water interface. The increase in the surface activity of the physisorbed heteropolar collector increases the ratio of functions performed by the heteropolar and apolar collectors in terms of removal of water from the film interlayer. The improved selectivity of a collector is achieved via changing the ratio of effects in water removal from the film by chemical compounds with different surface activities. Optimization of both ratios provides a compromise between the recovery and quality in flotation [37]. The illustration of the recovery – quality relation in a concentrate of the combustible matter is provided (see Fig.3).

Conclusion. The analysis of the experimental data on the physisorption mechanism has revealed the connection between the flotation activity of collectors and the structure and composition of their molecules. The combination of an apolar collector, attached as the drops to a hydrophobic surface, and a heteropolar collector, which adds up surface activity of the mix, enables a higher extraction of coal to concentrate at low ash content. The apolar collector at a moderate consumption exhibits attachment by the rule of polarity balancing of adjoining media and ensures selectivity of sorption, while the heteropolar collector, which has a high surface activity, is adsorbed at the oil – water interface and enhances recovery of the useful element.

Owing to the high surface activity, at the moment of rupture of a film between the coal particle and air bubble, the surfactant mixture of the heteropolar and apolar collectors removes water from the film, reduces the time of induction, and increases extraction of the combustible matter. The improved recovery of coal in concentrate with low ash content is achieved by optimizing the ratio of effects exerted on removing water from the film interlayer by the different sorption forms of an agent. Such function optimization provides a compromise between the recovery and quality in flotation [37].

REFERENCES

1. Linev B.I. Theoretical justification and development of rational processing technologies for coal-based fuels using an energy approach: Avtoref. dis. ... d-ra tekhn. nauk. M.: Izd-vo Moskovskogo gosudarstvennogo gornogo universiteta, 2003, p. 48 (in Russian).

2. Quanzhi Tian, Yi Zhang, Guosheng Li, Yongtian Wang. Application of carboxylic acid in low-rank coal flotation. *International Journal of Coal Preparation and Utilization*. 2019. Vol. 39. Iss. 1, p. 44-53. DOI: 10.1080/19392699.2017.1297299

3. Baofeng Wen, Wencheng Xia, Sokolovic J.M. Recent advances in effective collectors for enhancing the flotation of low rank/oxidized coals. *Powder Technology*. 2017. Vol. 319, p. 1-11. DOI: 10.1016/j.powtec.2017.06.030

4. Bao Li, Jianying Guo, Shengyu Liu et al. Molecular insight into the mechanism of benzene ring in nonionic surfactants on low-rank coal floatability. *Journal of Molecular Liquids*. 2020. Vol. 302. N 112563. DOI: 10.1016/j.molliq.2020.112563

5. Akdemir Ü., Sönmez İ. Investigation of coal and ash recovery and entrainment in flotation. *Fuel Processing Technology*. 2003. Vol. 82. Iss. 1, p. 1-9. DOI: 10.1016/S0378-3820(02)00248-5

6. Jena M.S., Biswal S.K., Rudramuniyappa M.V. Study on flotation characteristics of oxidised Indian high ash sub-bituminous coal. *International Journal of Mineral Processing*. 2008. Vol. 87. Iss. 1-2, p. 42-50. DOI: 10.1016/j.minpro.2008.01.004

7. Temel H.A., Majumder A.K. Investigation of the effectiveness of desliming and flotation in cleaning Malatya-Arguvan lignite. *Energy Sources, Part A: Recovery, Utilization, and Environmental Effects*. 2016. Vol. 38. N 8, p. 1048-1054. DOI: 10.1080/15567036.2015.1120819

8. Wencheng Xia, Chao Ni., Guangyuan Xie. Effective flotation of lignite using a mixture of dodecane and 4-dodecylphenol (DDP) as collector. *International Journal of Coal Preparation and Utilization*. 2016. Vol. 36. Iss. 5, p. 262-271. DOI: 10.1080/19392699.2015.1113956

9. Kadagala M.R., Nikkam S., Tripathy S.K. A review on flotation of coal using mixed reagent systems. *Minerals Engineering*. 2021. Vol. 173. N 107217. DOI: 10.1016/j.mineng.2021.107217

10. Dey S. Enhancement in hydrophobicity of low rank coal by surfactants – A critical overview. *Fuel Processing Technology*. 2012. Vol. 94. Iss. 1, p. 151-158. DOI: 10.1016/j.fuproc.2011.10.021

11. Jia R., Harris G.H., Fuerstenau D.W. Chemical reagents for enhanced coal flotation. *Coal Preparation*. 2002. Vol. 22. Iss. 3, p. 123-149. DOI: 10.1080/07349340213847

12. Cebeci Y. The investigation of the floatability improvement of Yozgat Ayrıdam lignite using various collectors. *Fuel*. 2002. Vol. 81. Iss. 3, p. 281-289. DOI: 10.1016/S0016-2361(01)00165-X

13. Zechen Liu, Yinfei Liao, Maoyan An et al. Enhancing low-rank coal flotation using a mixture of dodecane and *n*-valeraldehyde as a collector. *Physicochemical Problems of Mineral Processing*. 2019. Vol. 55 (1), p. 49-57. DOI: 10.5277/ppmp18109

14. Kubak D.A., Petuchov V.N., Semenov D.G. The investigation of the effect of complex reagents sectional chemical composition on coal flotation efficiency. *Vestnik of Nosov Magnitogorsk State Technical University.* 2013. N 4 (44), p. 5-10 (in Russian).

15. Abramov A.A. Requirements to the choice and designing of selective reagents-collectors. Part 2. Requirements to physical-chemical properties of selective reagents-collectors. *Tsvetnye Metally.* 2012. N 5, p. 14-17 (in Russian).

16. Miller J.D., Wang X., Li M. Bench Scale Flotation of Sedimentary Phosphate Rock with Hydroxamic Acid Collectors. Beneficiation of Phosphates: Advances in Research and Practice. Englewood: Society for Mining, Metallurgy & Exploration, 2002, p. 93-101.

17. Miller J.D., Xuming Wang, Minhua Li. Patent N US6341697B1. Selective flotation of phosphate minerals with hydroxamate collectors. Publ. 29.01.2002.

18. Xuming Wang, Nguyen A.V., Miller J.D. Selective attachment and spreading of hydroxamic acid-alcohol collector mixtures in phosphate flotation. *International Journal of Mineral Processing*. 2006. Vol. 78. Iss. 2, p. 122-130. DOI: 10.1016/j.minpro.2005.09.005

19. Aleksandrova T.N., Elbendari A.M. Increasing the efficiency of phosphate ore processing using flotation method. *Journal of Mining Institute.* 2021. Vol. 248, p. 260-271. DOI: 10.31897/PMI.2021.2.10

20. Kondratev S.A., Semyanova D.V. Relation between Hydrocarbon Radical Structure and Collecting Abilities of Flotation Agent. *Journal of Mining Science.* 2018. Vol. 54. N 6, p. 1024-1034. DOI: 10.1134/S1062739118065180

21. Kondratev S.A. Selecting collecting agents for flotation. *Journal of Mining Science.* 2022. N 5, p. 109-124 (in Russian). DOI: 10.15372/FTPRPI20220511

22. Kondratev S.A. Collectability and Selectivity of Flotation Agent. *Journal of Mining Science.* 2021. Vol. 57. N 3, p. 480-492. DOI: 10.1134/S1062739121030133

23. Seongsoo Han, Nguyen A.V., Kwanho Kim et al. Quantitative Analysis of Attachment Time of Air Bubbles to Solid Surfaces in Water. *Langmuir*. 2021. Vol. 37. Iss. 2, p. 616-626. DOI: 10.1021/acs.langmuir.9b02773

24. Lijuan Sun, Yaowen Xing, Haichang Yang et al. A New Experimental Approach to Evaluate Coal Particles Floatability: Bubble-Particle Attachment and Detachment Kinetics. *ACS Omega*. 2020. Vol. 5. Iss. 27, p. 16733-16738. DOI: 10.1021/acsomega.0c01630

25. Kondratyev S.A., Semyanova D.V. A revisit of selection the efficiency criterion for flotation reagents of fatty acids class. *Eurasian Mining*. 2017. N 1, p. 24-29. DOI: 10.17580/em.2017.01.07

26. Lavrinenko A.A., Svechnikova N.Y. The research of quantum-chemical characteristics in selection of coals flotation reagents. *Vestnik Magnitogorsk State Technical University named after G.I.Nosov.* 2008. N 1 (21), p. 85-87 (in Russian).

27. Chuprova L.V. Studying of the mechanism of effect of reagents at floatation enrichment of coal slimes. *International Journal of Applied and Fundamental Research.* 2016. N 11. Part 5, p. 939-942 (in Russian).

28. Ozdemir O., Karaguzel C., Nguyen A.V. et al. Contact angle and bubble attachment studies in the flotation of trona and other soluble carbonate salts. *Minerals Engineering*. 2009. Vol. 22. Iss. 2, p. 168-175. DOI: 10.1016/j.mineng.2008.06.001

29. Xiahui Gui, Yaowen Xing, Tingxia Wang et al. Intensification mechanism of oxidized coal flotation by using oxygen-containing collector α-furanacrylic acid. *Powder Technology*. 2017. Vol. 305, p. 109-116. DOI: 10.1016/j.powtec.2016.09.058

30. Petukhov V.N., Skorobogatova A.A., Ilyasova A.Z. Development reagent conditions of coal flotation using reagents-collectors of different chemical composition. *The Theory and Process Engineering of Metallurgical Production.* 2017. Vol. 20. N 1, p. 16-19 (in Russian).

31. Kondratev S.A. Physisorption and its purpose in flotation. Novosibirsk: Nauka, 2018, p. 182 (in Russian).

32. Osina N.Yu., Gorokhov A.V., Lakhtin S.V. Investigation of the influence of the group chemical composition of agents collectors on the efficiency of bituminous coal flotation. *Gornyi informatsionno-analiticheskii byulleten*. 2006. N 2, p. 393-396 (in Russian).

33. Yinfei Liao, Xiaodong Hao, Maoyan An et al. Enhancing low-rank coal flotation using mixed collector of dodecane and oleic acid: Effect of droplet dispersion and its interaction with coal particle. *Fuel*. 2020. Vol. 280. N 118634. DOI: 10.1016/j.fuel.2020.118634

34. Wencheng Xia, Jianguo Yang. Enhancement in flotation of oxidized coal by oxidized diesel oil and grinding pretreatment. *International Journal of Coal Preparation and Utilization*. 2013. Vol. 33. Iss. 6, p. 257-265. DOI: 10.1080/19392699.2013.816300

35. Ceylan K., Küçük M.Z. Effectiveness of the dense medium and the froth flotation methods in cleaning some Turkish lignites. *Energy Conversion and Management*. 2004. Vol. 45. Iss. 9-10, p. 1407-1418. DOI: 10.1016/j.enconman.2003.09.011

36. Dube R., Honaker R. Improving the flotation performance of an oxidized bituminous coal source. *Minerals Engineering*. 2019. Vol. 142. N 105937. DOI: 10.1016/j.mineng.2019.105937

37. Kondratev S.A., Rostovtsev V.I., Bochkarev G.R. et al. Justification and development of innovative technologies for integrated processing of complex ore and mine waste. *Journal of Mining Science.* 2014. Vol. 50. N 5, p. 959-973. DOI: 10.1134/S1062739114050160

38. Alexandrova T.N., Kuskov V.B., Afanasova A.V., Kuznetsov V.V. Improvement of the fine coking coal flotation technology. *Obogashchenie rud.* 2021. N 3, p. 9-13 (in Russian). DOI: 10.17580/or.2021.03.02

39. Rui Zhang, Yangchao Xia, Fangyu Guo et al. Effect of microemulsion on low-rank coal flotation by mixing DTAB and diesel oil. *Fuel*. 2020. Vol. 260. N 116321. DOI: 10.1016/j.fuel.2019.116321

40. Rosen M.J. Reduction of Surface and Interfacial Tension by Surfactants. Surfactants and Interfacial Phenomena. Hoboken: John Wiley & Sons, 2004, p. 208-242. DOI: 10.1002/0471670561.ch5

***Authors*: Sergei A. Kondratev,** *Doctor of Engineering Sciences*, *Chief Researcher*, *https://orcid.org/0000-0002-8245-2259* (*Chinakal Institute of Mining*, *Siberian Branch*, *RAS*, *Novosibirsk*, *Russia*), **Tatyana A. Khamzina,** *Postgraduate Student*, *bagrowa@bk.ru*, *https://orcid.org/0000-0002-1281-9801* (*Chinakal Institute of Mining*, *Siberian Branch*, *RAS*, *Novosibirsk*, *Russia*).

The authors declare no conflict of interests.

ISSN 2411-3336; e-ISSN 2541-9404

JOURNAL OF MINING INSTITUTE

Zapiski Gornogo instituta

Journal homepage: pmi.spmi.ru

Research article

Selection of the required number of circulating subs in a special assembly and investigation of their performance during drilling of radial branching channels by sectional positive displacement motors

Ilya A. LYAGOV[1], **Aleksandr V. LYAGOV**[2], **Dinislam R. ISANGULOV**[1], **Anastasiya A. LYAGOVA**[3]✉

[1] *LLO "Perfobore", Moscow, Russia*

[2] *Ufa State Petroleum Technological University, Ufa, The Republic of Bashkortostan, Russia*

[3] *Empress Catherine II Saint Petersburg Mining University, Saint Petersburg, Russia*

***How to cite this article*:** Lyagov I.A., Lyagov A.V., Isangulov D.R., Lyagova A.A. Selection of the required number of circulating subs in a special assembly and investigation of their performance during drilling of radial branching channels by sectional positive displacement motors. Journal of Mining Institute. 2024. Vol. 265, p. 78-86. EDN ZBPWKU

Abstract. The task of sludge removal to the surface during construction of directional and horizontal wells and strongly curved radial channels is relevant. For stable operation of technical system "Perfobore", it is proposed to use a circulating sub that ensures efficient cleaning of channel wellbore from the drilled rock. Two schemes of technical system "Perfobore" are considered, consisting of two seven-meter coiled tubing, a positive displacement motor, a bit and one circulating sub in the first scheme and two subs in the second scheme. For each of the schemes CFD modeling was implemented to determine values of pressure and speed. It was found out that the use of two circulating subs in the assembly is more efficient. In order to confirm the numerical experiment, bench tests were carried out. It was determined that the designed circulating sub can eject up to 25 % of pumped drilling fluid. The bench tests of full-size technical system "Perfobore" for drilling 14-meter channels with two circulating subs showed that the axial load on positive displacement motor produced by hydraulic loader was 3000 N and pressure drop depending on flow rate was 1.5-2.0 MPa. This allows the motor to operate at maximum power.

***Keywords*:** the "Perfobore" technical system; deep radial perforation channel; circulating sub; sludge removal; wellbore cleaning; computational fluid dynamics modeling; sectional positive displacement motor

Received: 10.08.2022 ***Accepted: 28.02.2023*** ***Online: 28.04.2023*** ***Published: 29.02.2024***

Introduction. The technical system (TS) "Perfobore" for radial drilling of channels is designed for deep perforation of the productive interval during completion of oil and gas wells or their workover. The system enables increased production rate of production wells, improved injectivity of injection wells and elimination of water-gas-oil cones contacts in the near-bottomhole zone through the creation of a system of spiral-shaped perforation channels with a predictable trajectory. The use of TS "Perfobore" enables to cut a "window" in production casing of different durability groups and further perform drilling of branched channels with length over 21 m, with diameter from 58 to 69 mm and radius of curvature from 3.5 to 17.5 m, and also control their trajectories by zenith and azimuth angles, discretely changing the construction of technical system assembly in rig conditions. The technology enables multiple entries into an already drilled channel, e.g. for repairs or for geological and technical measures.

The technical system "Perfobore" (Fig.1) is used during secondary drilling-in of productive horizons to guarantee the penetration beyond the near-bottomhole zone, contaminated by drilling mud filtrate during primary drilling-in. The main elements of the drill string bottom are a bit/cutter,

Journal of Mining Institute. 2024. Vol. 265. P. 78-86

a special sectional positive displacement motor (PDM) [1], a string of steel pipes with specified bending and torsional rigidity and a hydraulic loader capable of operating in damping or oscillator modes [2, 3]. A special sub with orifice is usually installed above the "Perfobore" PDM to regulate the flow of drilling mud to the PDM with a maximum flow rate of 2 l/s and a discharge of some of the mud into the annular space.

The problem of sludge transport during directional well construction and qualitative wellbore cleaning has been widely discussed in Russian and foreign scientific and technical literature. Thermohydraulic processes during well drilling are studied in works of Russian scientists: A.G.Avetisova, F.A.Akzamova, E.A.Akopova, A.I.Bulatova, E.P.Varlamova, L.K.Gorshkova, M.A.Goldshtik, N.A.Grigoryana, V.I.Isaeva, A.G.Kalinina, V.V.Kafarova, B.B.Kudryashova, E.G.Leonova, A.M.Lihushina, A.H.Mirzadzhanzade, M.R.Mavlyutova, N.I.Nikolaeva, V.S.Prokopenko, V.I.Ryabchenko, R.H.Sannikova, L.I.Sedova, N.I.Slyusareva, B.P.Ustimenko, R.I.Shishchenko, V.I.Shchukina and others.

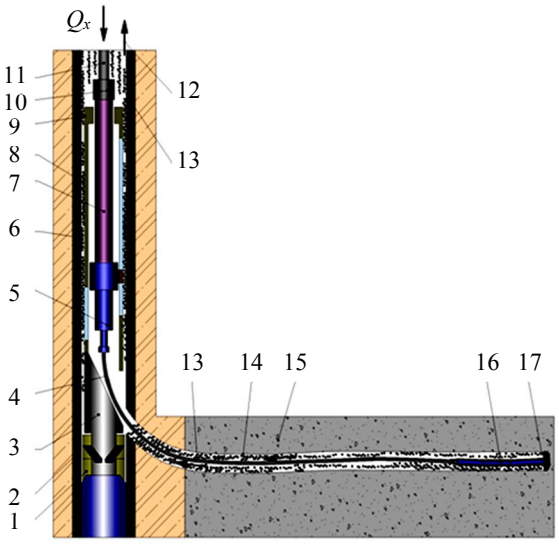

Fig.1. Borehole bottom assembly TS "Perfobore" in a directional channel

1 – anchor; 2 – clutch; 3 – whipstock; 4 – coiled tubing; 5 – hydraulic loader; 6 – cement stone; 7 – pusher; 8 – casing; 9 – modular frames; 10 – overflow valve; 11 – tubing/coiled tubing; 12 – upward flow; 13 – drilled rock; 14 – perforation channel; 15 – productive formation; 16 – positive displacement motor; 17 – bit

In the foreign literature, the most detailed consideration of sludge transport processes in small diameter horizontal boreholes is given by H.Zhang [4], S.Sayindla [5, 6], O.Agwu [7] and B.Basahmin [8]. The thesis [4] presents the results of both experimental investigations on a special test bench and numerical simulation. In [5, 7] there is a comprehensive review of experimental, numerical investigations of sludge settling velocity in drilling mud carried out by researchers during last decades. The paper [8] gives a review of analytical and numerical models of wellbore cleaning in horizontal and vertical wells. It also presents a numerical model of horizontal wellbore cleaning and a comparative analysis of sludge removal process in horizontal and vertical wells. Work [9] gives recommendations for using Monte Carlo simulation method. The method was applied for the comparison of simple probabilistic investigation of traditional models for well circulating in order to evaluate quantitatively the level of certainty/uncertainty in the calculation procedure. Despite of the satisfactory result for a particular type of well, the author describes in the conclusions that in the case of uncertain input data there will be some degree of uncertainty in the well circulating optimization parameters.

The article [10] investigated the influence of different drilling process parameters on sludge removal efficiency. Three most widely used models of sludge transport (Rudi-Shindu, Hopkins, Tobenna) have been compared based on sensitivity analysis of drilling process parameters influencing sludge removal. It has been found out that the considered models are not suitable for horizontal wells because they do not take into account the wellbore cross-sectional profile. The work [11] proves the necessity to take into account geomechanical processes taking place in near-well zone, technological and technical factors such as vibrations and rotation of drill string, formation of grooves during assembly running, pressure pulsations when starting and stopping pumps, hydrostatic and hydrodynamic pressure of drilling mud, its formulation and properties influencing the degree of well cleaning.

Works [12, 13] show the results of experimental investigations on estimation of sludge removal efficiency for three types of drilling mud. The effect of three parameters: viscosity, flow velocity and

zenith angle has been considered. It was found that the use of highly viscous drilling mud in turbulent flow regimes increases the efficiency of sludge removal. However, increasing the viscosity in laminar and transitional regimes gradually or drastically reduces the efficiency of sludge removal. As the zenith angle increases from 60 to 90°, the efficiency of sludge removal increases. At the same time, the paper [14] deals with wellbore cleaning in horizontal and directional wells during coiled tubing drilling, and in particular the effect of the rotation of the drill string on it. It is shown that at average speed of the drilling fluid flow in the annular space (0.56-0.69 m/s) the wellbore cleaning efficiency increases by 68 %. However, at lower speed of the drilling fluid flow in the annular space and zenith angles less than 60° the influence of drill string rotation is less significant. It is concluded that the turbulent flow regime is not effective for cleaning horizontal wells. Similar results were obtained by the authors of works [15, 16] on the experimental test bench, who demonstrated intense difficulty of sludge removal to the surface at the critical well zenith angle 55°.

The article [17] provides a relatively simple and fast graphical method for determining the minimum sludge particles speed in the drilling mud for efficient wellbore cleaning. A distinctive feature of the approach adopted in hydrodynamic modelling of sludge transport in works [18-20] is the use of non-spherical sludge particles. It was noted that the most intensive deposition of sludge occurs at the section of transition from inclined wellbore to vertical one. The works [21, 22] show the urgency of studying sludge transport processes in connection with the development of technologies for construction of wells with complicated profiles. Work [23] shows the results of numerical hydrodynamic simulation of sludge transportation process in a horizontal well. It is established that when the density of drilling mud increases by two times, sludge sedimentation decreases by 32.9 %, while drill string stress and pressure loss increase by 4.59 and 5.97 %.

As can be seen from the review of works devoted to hydrodynamic processes during oil and gas wells drilling, in investigation of sludge transportation process in small diameter wells and deep radial perforation channels, despite the great number of publications in this area, the issues of scientific and methodological support for open wellbore cleaning are still urgent. What is especially important – there are no appropriate analytical solutions and calculation methods for practical application by engineering and technological personnel of oilfield service companies.

Research setting. The main feature of sludge transportation to surface during radial perforating drilling with TS “Perfobore” is the necessity to take into account technical capabilities of special sectional PDM of small diameter (43-49 mm), small gap in annular space of perforation channel (7-10 mm) and low speed of upward flow of drilling mud inside the casing. Sludge particles have smaller size than ones in conventional drilling, because of very small diameter of the abrasive-cutting drilling tool, significantly lower loads on the bit (2-6 kN) and high rotation rate of the spindle in the small-size bottomhole motor (500-800 rpm) [1].

The circulating sub (CS) (Fig.2), due to an upward facing orifice with a special profile and increased mud flow, acts as a hydro-ejector, accelerating the drilling mud flow up the annulus. At the same time, the bottomhole pressure in the wellbore interval below the sub decreases, which in combination with drill string tension and activation of hydraulic loader operation in oscillator mode contributes to decreased probability of possible differential sticking [24]. Periodic activation of this mode allows improving circulating of horizontal channel section and avoiding accumulation of sludge in annular space of the drilled channel. To clean the bit and effectively remove the drilled

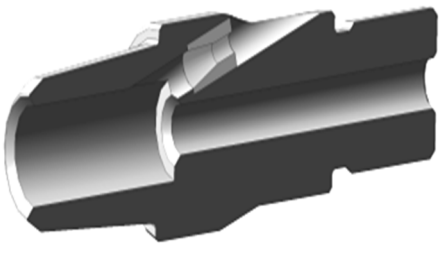

Fig.2. Circulating sub in sectional view

Journal of Mining Institute. 2024. Vol. 265. P. 78-86

rock from the bottomhole (especially when drilling extended channels of small diameter) and its subsequent removal to the surface, it is necessary to provide an upward flow speed exceeding the drop speed of solid particles, which is calculated in transient and turbulent modes of particle flow according to Rittinger's formula.

The inability to rotate the coiled tubing (CT) in the channel during drilling with TS "Perfobore" also significantly complicates the proper cleaning of the wellbore from the drilled sludge. This, in turn, can lead to sludging [24, 25], risks of sticking [26] and reduction of commercial drilling speed [27, 28]. The absence of drill string rotation does not give a reliable answer about the proper cleaning of radial channel from the drilled rock [29, 30]. The problem of sludge removal in intervals with zenith angles of 30-60° is also aggravated by the presence of a horizontal section in the drilled channel, which remains relevant for traditional horizontal wellbore drilling [31, 32].

Methodology. *Mathematical modelling of sludge removal.* Let us consider hydrodynamic process of sludge removal in annular space during drilling of a section for a setting of the zenith angle in a deep radial perforation channel with TS "Perfobore". The modern tendency in analyses of processes, occurring during well drilling, is using of finite elements method, more exactly CFD modelling (Computational Fluid Dynamics modeling). Engineers all over the world use many tools for CFD calculations; however, the international long-term experience of using this type of software shows the superiority of the Ansys CFX for this type of tasks [19, 33, 34].

Two types of schemes were used in the calculations (Fig.3). The installation locations and number of circulating subs were chosen according to the design features of the assemblies. Circulating sub can be installed above PDM as well as between pipes transferring load from hydraulic loader to PDM and bit.

The following inputs and assumptions are used in the calculation and are the same for both calculation schemes:

• Channel length of 14 m is selected for accident-free passage of the motor with two skew angles; curvature radius is 8 m; channel diameter is from 58 to 69 mm depending on the size of the PDM used.

• Abrasive-cutting bit by "Perfobore" with diameter of 69 mm.

• Special small-size positive displacement motor with diameter of 49 mm and two sections of working bodies with 9×10 pitch, curvature angles are 5° and a special spindle section.

• External circulating sub with diameter of 49 mm (4.2 mm internal orifice in the nozzle).

• Steel coiled tubing; outside diameter is 28 mm; wall thickness is 3 mm.

• In each scheme, the outer and inner roughness of the assemblies were assumed to be *Ra* 6.3 μm; the roughness of the drilled channel walls in the carbonate reservoir is 3 mm.

• The length of the coiled tubing is chosen for ease of assembly arrangement at the wellhead, as the height of the derrick does not allow the whole assembly to be lowered and mounted on the scaffolding.

Values of boundary condition parameters for schemes 1 and 2 of mathematical model and numerical solution: inlet pressure is 4.7 and 9.3 MPa; average speed of liquid flow in channel 2.5 and 1.2 m/s; mass flow rate of liquid is 3-6 kg/s. The inlet pressure is specified as the pressure in the

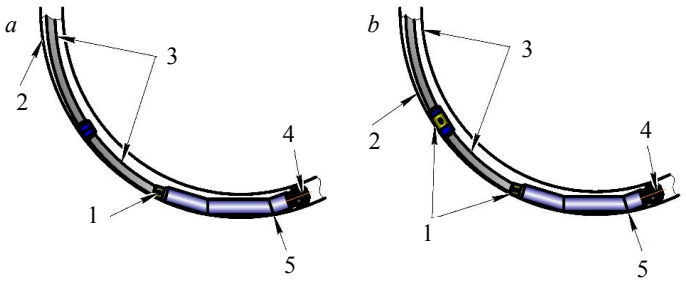

Fig.3. Schemes of borehole bottom assembly: scheme 1 with one CS in radial perforation channel (*a*); scheme 2 with two CS installed: one above the PDM, the other between the lower and upper pipe in the radial perforation channel (*b*)

1 – circulating sub; 2 – channel wall; 3 – coiled tubing; 4 – bit; 5 – PDM

Fig.4. Bench testing of PDM operation

system varies depending on the channel length, density and friction loss in the pipes. According to the basic provisions of GOST 6134-2007 single phase flow (technical water) in stationary formulation with density 998 kg/m^3 is considered.

Numerical investigations were carried out using a system of Navier – Stokes equations averaged by Reynolds (continuity and motion equations), a closed *k*-ε turbulence model (turbulent kinetic energy equation and turbulent kinetic energy dissipation rate equation) [35]. To solve the problem on the geometric model made in the CAD system Kompas-3D, first of all a finite element mesh is generated.

Varying values of liquid mass flow rate from 3 to 6 kg/s are determined by the fact that rated characteristics of special small size PDM, used for drilling of radial channel without circulating sub, allow efficient operation at the flow rate of 2 kg/s [1], and installation of circulating (bleeding) subs in borehole bottom assembly allows increasing the total mass flow rate up to 6 kg/s. As research [1] shows, it is not necessary to increase mass flow rate more than 6 kg/s, moreover, it requires more expensive pumping units, which are difficult to find at remote fields [36].

Carrying out bench and field tests. In preparation for the bench test (Fig.4), the assemblies were arranged: bit, PDM and CS, as well as the assembly without CS. Since the PDM are tested at the factory before they are shipped to the customer, each motor has a known dependence of the spindle shaft rotation frequency on different mass flow rates of this liquid. The motor was started up on a "Perfobore" universal test bench at a rated flow rate of 2 l/s, then a value corresponding to the factory tests was obtained using an AKIP-9202 laser tachometer to measure the rotation frequency. Further, CS was installed into the assembly and the PDM was also started up with a

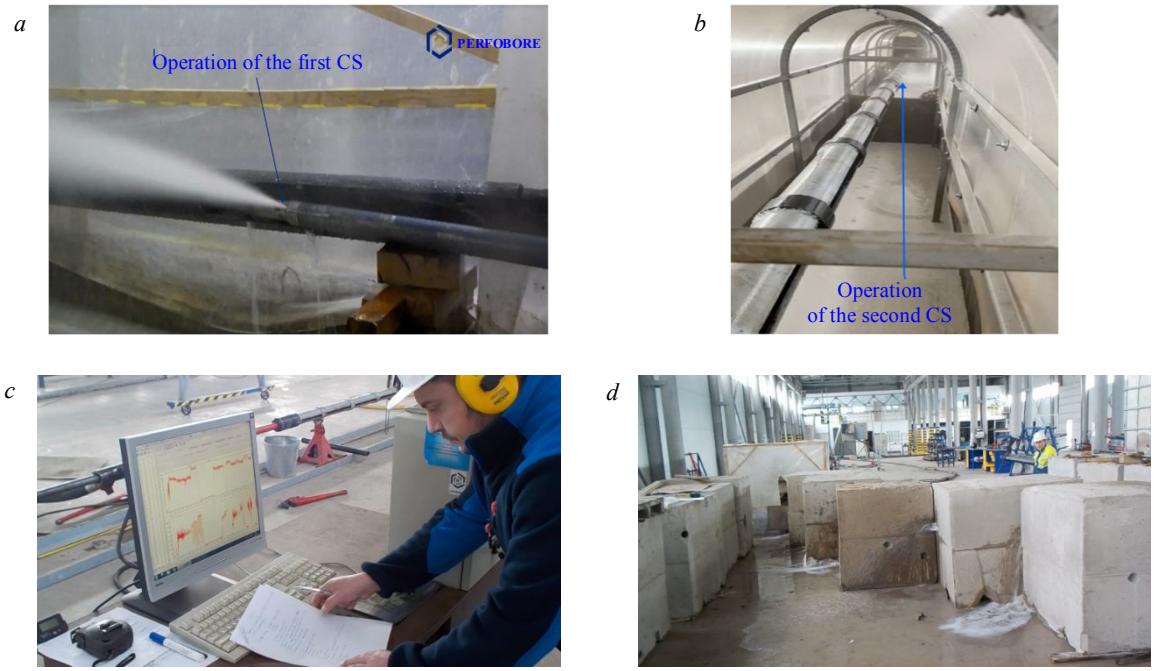

Fig.5. Bench tests of the assembly in configuration with one (*a*) and two (*b*) CS; operator workplace for controlling and monitoring the test bench process (*c*); special blocks, manufactured according to API 19B standards, for carrying out the test (*d*)

Journal of Mining Institute. 2024. Vol. 265. P. 78-86

gradual increase in flow rate at the pumping station SIN-46 until the shaft rotation frequency began to correspond to the values obtained in the previous experiment.

The next stage of the bench tests was to analyze the performance of the assembly with CS in the channel when drilling sand-cement blocks (Fig.5). The dimensions of the blocks, their varying hardness and abrasivity, and their arrangement with calculated spacing between them allowed, firstly, the simulation of rock interference and, secondly but most valuable, gave the ability to control the trajectory and measure the drilling mud flow rate along the entire length of the channel. For this purpose full-scale TS "Perfobore" was assembled for drilling of 14-meter channels in special blocks, with two CS installed in the assembly according to the scheme shown in Fig.3, *b*. Mass flow rate of drilling fluid was controlled in the range of 3-6 kg/s, axial load on PDM produced by hydraulic loader was 3000 N, and pressure drop on PDM depending on flow rate was 1.5-2.0 MPa, which corresponds to rated values at optimum power.

Fig.6. Photograph of the screen of the intake tank with the sludge from the bottomhole of the channel

In order to model flow regime and evaluate reliability and efficiency of TS as a whole, the bench is equipped with control and measuring instruments (CMI): pressure sensors DMP 330L, flow rate meter, which is duplicated by the CMI of SIN-46 pumping unit, as well as axial load sensors (mesdose with pressure transducer MPD-01VD and DVST type vibration sensors), working fluid temperature is registered by Fluke pyrometer.

After successful completion of the bench tests, the equipment and technology were tested in wells. The rate for set of channel curvature was 8-10° per meter of penetration, which corresponded to a curvature radius of 7-9 m and ensured investigation of the whole range of channel zenith angle variation in the intervals from 7 to 120-150° (where 7° is the initial angle of whipstock). Measurement of the trajectory was performed by small-size autonomous inclinometers of the magnetometering "Kvartz-36" and gyroscopic TwinGyro. The presence of sludge in the channels drilled with different curvature was assessed visually and by weighing it during drilling pauses when the special blocks were relocated (Fig.6)

Discussion of the results. Pressure and speed distributions are obtained after mathematical modelling and bench testing (see Table). Figure 7 shows visualization of modelling for design scheme with one CS at 3 kg/s, the required values of speed and pressure are indicated by the marks.

Pressure and speed distribution during modelling in TS "Perfobore"

Mass flow rate, kg/s	Pressure, MPa						Speed, m/s					
	Scheme 1			Scheme 2			Scheme 1			Scheme 2		
	Between CT	Above PDM	At the bit	Between CT	Above PDM	At the bit	Between CT	Above PDM	At the bit	Between CT	Above PDM	At the bit
3	0.107	0.374	0.091	0.202	0.253	0.096	1.7	24	0.65	15	15	1.5
4	1.111	0.425	0.081	0.354	0.334	0.091	2.1	25	2.8	23	22	2
5	0.121	0.607	0.081	0.506	0.607	0.091	2.5	27	3.5	25	30	1.8
6	0.121	0.851	0.111	0.557	0.709	0.081	3.7	35	4.3	30	32	2.2

Analyzing the results of calculations, it can be concluded that the use of assemblies with two CS is efficient, as the speed of fluid flow in problematic intervals is significantly higher in the space between the coiled tubing and the channel walls. The results obtained are consistent with those of [37, 38]. In order to confirm this hypothesis bench and then field tests were conducted. As a result of bench tests at the first stage, it was determined that the developed CS can discharge up to 25 % of drilling fluid.

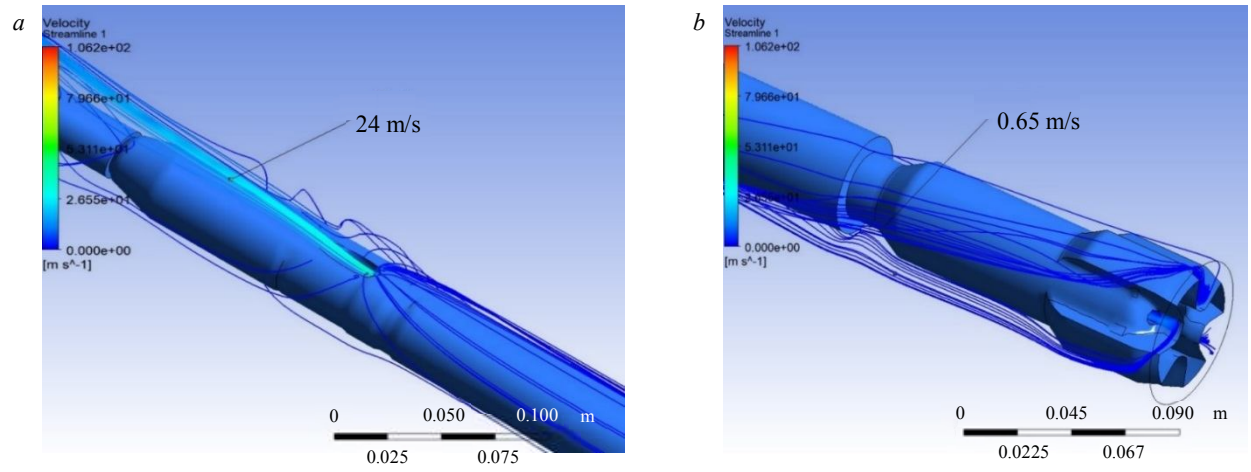

Fig.7. Visualization of fluid flow from CS (*a*) and bit (*b*) during drilling the channel

Conclusion. Experimental investigations have shown that the mathematical model correctly reproduces the character of liquid motion in the channel and provides high correlation with the experimental data. The mathematical modelling and bench tests allowed the authors to conduct pilot tests with minimal risks, first of all for themselves and the created technology, and after their successful completion to proceed to large-scale field works.

The results of calculations to ensure reliable circulating of the channel were verified during bench and field tests at the wells of PAO ANK "Bashneft", OOO "Lukoil-Komi", OAO "Nokratojl", PAO "Novatek", OOO "Gazpromneft-Yamal" fields, PAO "Tatneft", OOO "Novatek-Tarkosaleneftegaz", AO "NK "Neftisa", JV OOO Uz-Kor Gas Chemical (The Republic of Uzbekistan), OOO Sanoat Energetika Guruhi (The Republic of Uzbekistan), TOO KAZPETROL GROUP (The Republic of Kazakhstan), Creative Oil & Gas Operation (USA). To ensure normal operation of TS "Perfobore" and carry sludge to the surface, special assemblies with two CS were used, and at some wells, a clay-free biopolymer drilling mud with special properties was used.

REFERENCES

1. Lyagov I.A., Baldenko F.D., Lyagov A.V. et al. Methodology for calculating technical efficiency of power sections in small-sized screw downhole motors for the "Perfobur" system. *Journal of Mining Institute.* 2019. Vol. 240, p. 694-700. DOI: 10.31897/PMI.2019.6.694

2. Dvoynikov M.V. Technology of oil and gas wells drilling by downhole drilling motors. London: LAP LAMBERT Academic Publishing, 2013, p. 18-29.

3. Dvoinikov M.V., Muraev Y.D. Technical and technological solutions to ensure stability of downhole drilling motors. *Journal of Mining Institute.* 2016. Vol. 218, p. 198-205 (in Russian).

4. Hongyang Zhang. Experimental Study of Cuttings Transport in Coiled Tube Micro-Borehole Drilling: Thesis for degree of doctor of philosophy of Curtin University. Perth: Curtin University, 2018, p. 168. URL: http://hdl.handle.net/20.500.11937/68365 (accessed 10.05.2022).

5. Sayindla S., Lund B., Ytrehus J.D., Saasen A. Hole-cleaning performance comparison of oil-based and water-based drilling fluids. *Journal of Petroleum Science and Engineering.* 2017. Vol. 159, p. 49-57. DOI: 10.1016/j.petrol.2017.08.069

6. Sayindla S., Lund B., Ytrehus J.D., Saasen A. CFD Modelling of Observed Cuttings Transport in Oil-Based and Water-Based Drilling Fluids. SPE/IADC Drilling Conference and Exhibition, 14-16 March 2017, The Hague, The Netherlands. OnePetro, 2017. N SPE-184660-MS, p. 1556-1567. DOI: 10.2118/184660-MS

7. Agwu O.E., Akpabio J.U., Alabi S.B., Dosunmu A. Settling velocity of drill cuttings in drilling fluids: A review of experimental, numerical simulations and artificial intelligence studies. *Powder Technology.* 2018. Vol. 339, p. 728-746. DOI: 10.1016/j.powtec.2018.08.064

8. Basahmin B., Saeid N.H., Alusta G., Zahran E-S.M.M. Review on hole cleaning for horizontal wells. *Journal of Engineering and Applied Sciences*. 2017. Vol. 12. N 16, p. 4697-4708.

9. Tabatabaee Moradi S.S. A probabilistic study on hole cleaning optimization. *Journal of Mining Institute.* 2022. Vol. 258, p. 956-963. DOI: 10.31897/PMI.2022.67

10. Shiddiq A.M.I., Toro B.C., Syafri I. et al. A Comprehensive Comparison Study of Empirical Cutting Transport Models in Inclined and Horizontal Wells. *Journal of Engineering and Technological Sciences*. 2017. Vol. 49. Iss. 2, p. 275-289. DOI: 10.5614/j.eng.technol.sci.2017.49.2.9

11. Blinov P.A. Determining the Stability of the Borehole Walls at Drilling Intervals of Loosely Coupled Rocks Considering Zenith Angle. *Journal of Mining Institute.* 2019. Vol. 236, p. 172-179. DOI: 10.31897/PMI.2019.2.172

12. Piroozian A., Ismail I., Yaacob Z. et al. Impact of drilling fluid viscosity, velocity and hole inclination on cuttings transport in horizontal and highly deviated wells. *Journal of Petroleum Exploration and Production Technology*. 2012. Vol. 2. Iss. 3, p. 149-156. DOI: 10.1007/s13202-012-0031-0

13. Piroozian A., Isshan I. Cuttings Transport in Horizontal and Highly Deviated Wellbores. *Jurnal Teknologi*. 2011. Vol. 56, p. 1-14. DOI: 10.11113/jt.v56.50

14. Muherei M.A., Basaleh S.S., Bamaga M.A. Hole Cleaning in Horizontal and Highly Deviated Wellbores Drilled with Coiled Tubing Drill Pipe Rotation. Draw Back Is It Significant. *International Research Journal of Engineering and Technology*. 2015. Vol. 2. Iss. 9, p. 2280-2286.

15. Kadochnikov V.G., Dvoynikov M.V. Development of Technology for Hydromechanical Breakdown of Mud Plugs and Improvement of Well Cleaning by Controlled Buckling of the Drill String. *Applied Science*. 2022. Vol. 12. Iss. 13. N 6460. DOI: 10.3390/app12136460

16. Kadochnikov V.G., Dvoynikov M.V., Blinov P.A. Influence of the Drill String Spatial Form on Transport of Cuttings in Directional Wells. *Bulletin of the Association of Drilling Contractors.* 2020. N 2, p. 12-19 (in Russian).

17. Joshi S., Braisare A. Graphical method to determine minimum cutting fluid velocity for effective hole cleaning. *International Research Journal of Engineering and Technology*. 2017. Vol. 4. Iss. 6, p. 1684-1689.

18. Epelle E.I., Gerogiorgis D.I. A CFD investigation of the effect of particle sphericity on wellbore cleaning efficiency during oil and gas drilling. *Computer Aided Chemical Engineering*. 2018. Vol. 43, p. 127-132. DOI: 10.1016/B978-0-444-64235-6.50024-3

19. Epelle E.I., Gerogiorgis D.I. A multiparametric CFD analysis of multiphase annular flows for oil and gas drilling applications. *Computers & Chemical Engineering.* 2017. Vol. 106, p. 645-661. DOI: 10.1016/j.compchemeng.2017.08.011

20. Epelle E.I., Gerogiorgis D.I. CFD modeling and simulation of drill cuttings transport efficiency in annular bends: Effect of particle sphericity. *Journal of Petroleum Science and Engineering*. 2018. Vol. 170, p. 992-1004. DOI: 10.1016/j.petrol.2018.06.041

21. Xiaofeng Sun, Kelin Wang, Tie Yan et al. Effect of drillpipe rotation on cuttings transport using computational fluid dynamics (CFD) in complex structure wells. *Journal of Petroleum Exploration and Production Technology*. 2014. Vol. 4. Iss. 3, p. 255-261. DOI: 10.1007/s13202-014-0118-x

22. Wang Kelin, Yan Tie, Sun Xiaofeng et al. Review and Analysis of Cuttings Transport in Complex Structural Wells. *The Open Fuels & Energy Science Journal*. 2013. Vol. 6. Iss. 1, p. 9-17. DOI: 10.2174/1876973X20130610001

23. Zakerian A., Saratraz S., Tabzar A. et al. Numerical modeling and simulation of drilling cutting transport in horizontal wells. *Journal of Petroleum Exploration and Production Technology*. 2018. Vol. 8. Iss. 2, p. 455-474. DOI: 10.1007/s13202-018-0435-6

24. Lyagov I.A., Gubaidullin A.G., Lyagov A.V. et al. Forecasting the Risks of Jamming to Exclude the Possibility of Stitching the Technical System "Perfobur" while Drilling Branched Channels in Terrigenous Reservoirs. *Bulletin of the Tomsk Polytechnic University. Geo Assets Engineering.* 2019. Vol. 330. N 10, p. 126-136 (in Russian). DOI: 10.18799/24131830/2019/10/2304

25. Reichert R.S., Tsukrenko M.S., Organov A.S. Technical and technological solutions for cleaning directional and horizontal wellbores from sludge. *Neft. Gas. Novacii.* 2016. N 3, p. 28-35 (in Russian).

26. Nazari T., Hareland G., Azar J.J. Review of Cuttings Transport in Directional Well Drilling: Systematic Approach. SPE Western Regional Meeting, 27-29 May 2010, Anaheim, California, USA. OnePetro, 2010. N SPE-132372-MS. DOI: 10.2118/132372-MS

27. Aleksandrov S.S., Lugumanov M.G. Regime Regulating of Well Clean-Up During Drilling. *Burenie & neft.* 2013. N 2, p. 36-38 (in Russian).

28. Ulyasheva N.M., Leusheva E.L., Galishin R.N. Development of the drilling mud composition for directional wellbore drilling considering rheological parameters of the fluid. *Journal of Mining Institute.* 2020. Vol. 244, p. 454-461. DOI: 10.31897/PMI.2020.4.8

29. Pushmin P.S., Romanov G.R. Problems of Slant Directed Wells Cleaning. *The Earth Sciences and Subsoil Use.* 2014. N 3 (46), p. 56-60 (in Russian).

30. Vromen T.G.M. Control of stick-slip vibrations in drilling systems: PhD thesis. Eindhoven University of Technology. Eindhoven, 2015, p. 256.

31. Xiaohua Zhu, Liping Tang, Qiming Yang. A Literature Review of Approaches for Stick-Slip Vibration Suppression in Oilwell Drillstring. *Advances in Mechanical Engineering.* 2014. Vol. 6. N 967952. DOI: 10.1155/2014/967952

32. Agzamov F.A., Akbulatov T.O., Khabibullin I.A. et al. Influence of rheological properties of the flushing fluid on sludge transport in a horizontal wellbore. *Oil Gas Territory.* 2008. N 9, p. 16-18 (in Russian).

33. Tie Yan, Jingyu Qu, Xiaofeng Sun et al. Investigation on horizontal and deviated wellbore cleanout by hole cleaning device using CFD approach. *Energy Science & Engineering*. 2019. Vol. 7. Iss. 4, p. 1292-1305. DOI: 10.1002/ese3.346

34. Smorkalov D.V., Tyutyaev A.V., Shterenber A.M., Gorshkalev A.A. Modeling of the egress of a drilling liquid from the nozzle of a drill bit with Ansys Fluent. IOP Conference Series: Materials Science and Engineering. 2017. Vol. 177. N 012067. DOI: 10.1088/1757-899X/177/1/012067

35. Nikitin V.I. Problem solution analysis on finding the velocity distribution for laminar flow of a non-linear viscous flushing fluid in the annular space of a well. *Journal of Mining Institute.* 2022. Vol. 258, p. 964-975. DOI: 10.31897/PMI.2022.93

36. Sidorkin D.I., Kupavykh K.S. Justification on Choosing Screw Pumping Units as Energy Efficient Artificial Lift Technology. *ENERGETIKA. Proceedings of CIS higher education institutions and power engineering associations.* 2021. Vol. 64. N 2, p. 143-151. DOI: 10.21122/1029-7448-2021-64-2-143-151

37. Heshamudin N.S., Katende A., Rashid H.A. et al. Experimental investigation of the effect of drill pipe rotation on improving hole cleaning using water-based mud enriched with polypropylene beads in vertical and horizontal wellbores. *Journal of Petroleum Science and Engineering*. 2019. Vol. 179, p. 1173-1185. DOI: 10.1016/j.petrol.2019.04.086

38. Burke J., Harrison C., Gamarra F. et al. Thru-Tubing Cleanouts and Acidization in Unconventional Wells. SPE/ICoTA Well Intervention Conference and Exhibition, 22-23 March 2022, The Woodlands, Texas, USA. OnePetro, 2022. N SPE-209026-MS. DOI: 10.2118/209026-MS

***Authors*: Ilya A. Lyagov,** *Candidate of Engineering Sciences*, *Executive General Manager*, *https://orcid.org/0000-0002-3780-2133* (*LLO* "*Perfobore*", *Moscow, Russia*), **Aleksandr V. Lyagov,** *Doctor of Engineering Sciences*, *Professor*, *https://orcid.org/0000-0002-7949-7368* (*Ufa State Petroleum Technological University*, *Ufa*, *The Republic of Bashkortostan*, *Russia*), **Dinislam R. Isangulov,** *Engineer First Division*, *https://orcid.org/0000-0003-1188-7594* (*LLO* "*Perfobore*", *Moscow*, *Russia*), **Anastasiya A. Lyagova,** *Candidate of Engineering Sciences*, *Associate Professor*, *lyagova_aa@pers.spmi.ru*, *https://orcid.org/0000-0002-0270-2546* (*Empress Catherine II Saint Petersburg Mining University*, *Saint Petersburg*, *Russia*).

The authors declare no conflict of interests.

ISSN 2411-3336; e-ISSN 2541-9404

JOURNAL OF MINING INSTITUTE

Zapiski Gornogo instituta

Journal homepage: pmi.spmi.ru

Research article

Physico-chemical aspects and carbon footprint of hydrogen production from water and hydrocarbons

Anton L. MAKSIMOV[1], **Aleksandr G. ISHKOV**[2,3], **Andrei A. PIMENOV**[4], **Konstantin V. ROMANOV**[2,5]✉, **Andrei M. MIKHAILOV**[6], **Evgenii A. KOLOSHKIN**[2]

[1] *A.V.Topchiev Institute of Petrochemical Synthesis, RAS, Moscow, Russia*

[2] *PAO Gazprom, Saint Petersburg, Russia*

[3] *D.I.Mendeleev Russian University of Chemical Technology, Moscow, Russia*

[4] *Tatar Oil Research and Design Institute* (*TatNIPIneft*) *of PAO TATNEFT, Kazan, Russia*

[5] *OOO Gazprom Hydrogen, Moscow, Russia*

[6] *OOO Gazprom VNIIGAZ, Saint Petersburg, Russia*

How to cite this article: Maksimov A.L., Ishkov A.G., Pimenov A.A., Romanov K.V., Mikhailov A.M., Koloshkin E.A. Physico-chemical aspects and carbon footprint of hydrogen production from water and hydrocarbons. Journal of Mining Institute. 2024. Vol. 265, p. 87-94. EDN HWCPDC

Abstract. Physico-chemical aspects determine the efficiency and competitiveness of hydrogen production technologies. The indicator of water consumption is especially relevant, since water is one of the main sources of hydrogen in almost all methods of its production. The article analyzes comparative water consumption indicators for various technologies based on published research and actual data from production plants. The volume of water consumption depends on the quality of the source water, which should be taken into account when implementing hydrogen projects in order to minimize the negative impact on the environment. Based on the operating industrial plant, the material balance of hydrogen production by steam reforming was demonstrated, which made it possible to determine the proportion of hydrogen (48.88 %) obtained from water. Currently, the carbon footprint indicator is becoming more important, reflecting greenhouse gas emissions throughout the production chain. According to the results of the total greenhouse gas emissions assessment for hydrogen production by steam reforming (about 10.03 kg CO_2-eq/kg H_2), the carbon footprint of hydrogen from water (4.2-4.5 kg CO_2-eq/kg H_2) and hydrogen from methane (15.4-15.7 kg CO_2-eq/kg H_2) has been determined. Consequently, almost half of the hydrogen produced by steam reforming is produced from water, corresponds to the indicators of “low-carbon” hydrogen and can be considered as “renewable” hydrogen. To make management decisions, an objective assessment in terms of energy and water costs is necessary based on a system analysis by the development of hydrogen energy and the growth of global hydrogen production. The impact of these indicators on the water cycle and global water resources will increase.

Keywords: hydrogen production; low-carbon hydrogen; renewable hydrogen; carbon footprint; water consumption in hydrogen production; material balance of hydrogen production

Received: 27.11.2023 ***Accepted: 27.12.2023*** ***Online: 29.02.2024*** ***Published: 29.02.2024***

Introduction. Currently, there are trends in expanding the field of hydrogen usage worldwide (energy, transport, etc.), however, when planning new hydrogen projects, sufficient attention is often not paid to the real indicators of water consumption. Water is one of the main sources of hydrogen in almost all methods of its production. These methods differ in the method of obtaining and additional sources of hydrogen (hydrocarbons, biomass, etc.).

Water is one of the key resources in energy production, where it is used as a coolant, refrigerant, working fluid, and also in the extraction of fossil energy carriers. On the other hand, energy consumption is necessary for the operation of water supply and sanitation systems, desalination, etc. [1, 2]. In international practice, the term *water-energy nexus* is used to denote the relationship between water use and energy [3, 4], the problem of equilibrium in this field remains relevant in the conditions of decarbonization.

According to the estimates of the International Energy Agency, energy costs here will more than double by 2040*. The dependence between water and energy is particularly relevant for the hydrogen economy considering the impact of increased hydrogen production (primarily from water) on water resources and systems.

Hydrogen production is associated with the consumption of a significant amount of water, and therefore the influence of this factor on the overall growth rate of low carbon footprint production is important. Hydrogen production involves the mandatory use of water as a raw material and its reduction to hydrogen using coal (coal gasification), methane (steam reforming, autothermal reforming, partial oxidation), biomass (biomass gasification) and electricity (electrolysis) [5-8]. As a result, up to 100 % of hydrogen is formed from the water. Water is the only source of hydrogen for processes diametrically opposite in terms of carbon footprint, such as coal gasification and electrolysis. Despite the dominance of hydrogen produced from natural gas in industry [9], hydrogen production from water is gaining momentum; provided that renewable energy is used, it can result in a relatively small carbon footprint [10, 11].

The main purpose of this study is to compare water consumption for various hydrogen production methods, as well as determine the proportion of hydrogen produced from water during steam reforming of natural gas, and estimate the carbon footprint of hydrogen from water and methane based on data from the material balance of hydrogen production by steam reforming.

Comparison of water consumption for various hydrogen production technologies. The assessment of hydrogen in terms of energy and water costs requires verification in terms of water consumption. With the growth of hydrogen production, the factor of provision, consumption and management of water resources will become more important. The initiator of hydrogen projects needs a comprehensive interaction with the water sector in terms of evaluating the methods and consequences of using water in the production of all types of hydrogen. A key success factor is the formation of a sustainable approach to the choice of sources and methods of water utilization, as well as reducing the overall water consumption for hydrogen projects [12]. The implementation of this approach will eliminate the negative impact of hydrogen projects on communities experiencing water scarcity, as well as prevent the aggravation of current water security problems.

An important factor is the requirements for water quality used in the production of hydrogen. At all stages of water purification, losses and the formation of polluted effluents requiring purification are possible [13]. The process of obtaining water of the required quality for electrolysis and steam reforming can be associated with filtration, desalination and/or demineralization (depending on the type and quality of available water sources). During the process of ultrafiltration water losses can reach 10 vol.%, and for reverse osmosis, they amount to 15-25 % for ordinary water, 20-30 % for wastewater, 35-40 % for seawater. Liquid effluents generated during the water treatment process should be disposed of in order to minimize the negative impact on the environment. Their value can range from 7 % for ultrafiltration to 21 % for reverse osmosis [14].

The research uses publications on this topic [15-17], as well as actual data from production plants for steam reforming of natural gas.

When hydrogen is produced by the most common methane steam reforming method, the stoichiometric indicator of water consumption is only 4.5 liters of H_2O per 1 kg of H_2 [18]. It is necessary to take into account the losses of steam and cooling water that occur during the steam conversion process. Steam generation requires 7.35 liters of H_2O, and 38 liters for cooling systems [19]. Taking into account the losses in these processes, the water consumption turns out to be significantly higher and can reach from 5.85 to 13.2 liters [20]. The value is specified to the consumption of demineralized (desalinated) water and its losses.

To determine the actual water consumption, it is necessary to take into account the amount of waste generated during the water treatment process. This indicator depends on the quality of the source or raw water (river, sea or water used in the extraction of methane). Taking into account the

* Introduction to the water-energy nexus. International Energy Agency, 26.10.2022. URL: https://www.iea.org/articles/introduction-to-the-water-energy-nexus (accessed 10.09.2023).

Journal of Mining Institute. 2024. Vol. 265. P. 87-94

listed additional indicators, the real value of water consumption in the production of hydrogen, depending on the water source, may, according to various data, be 13-40 liters of H_2O per 1 kg of H_2 produced [21-22].

Water consumption indicators of alternative natural gas conversion technologies (partial oxidation, autothermal reforming) may initially be lower. For autothermal reforming this value approaches 7.4 liters of H_2O per 1 kg of H_2 produced [23]. The full use of the carbon-containing feed potential to achieve maximum hydrogen yield requires a water-gas shift reaction between carbon monoxide and water steam, i.e. an additional amount of water steam consumption. The actual water consumption in hydrogen production by these methods will be comparable, and in some cases even higher than the same indicator for the steam reforming process*.

Thus, when obtaining "low-carbon" hydrogen (with CO_2 capture), the actual consumption increases by 85 %** [24] and, taking into account CO_2 capture, steam compression and water cooling can be 18-44 liters of H_2O per 1 kg of H_2 produced [21].

For coal based hydrogen production, the actual water consumption can be 30-70 liters of H_2O per 1 kg of H_2 produced for hard coal and 25-60 liters of H_2O per 1 kg of H_2 produced for lignite coal due to its higher humidity. It takes about 12 liters of water directly to carry out the reaction [25, 26].

For steam conversion of biogas, the stoichiometric indicator of water consumption is equal to the same indicator of the steam conversion process of natural gas (4.5 liters of H_2O per 1 kg of H_2). However, taking into account the heat losses for removing CO_2 from biogas before reforming, the actual water consumption may be 15-40 liters of H_2O per 1 kg of H_2 produced [27]. The biogas production itself is very water-intensive in addition [28].

The stoichiometric indicator of water consumption for the water electrolysis process is 9 liters of H_2O per 1 kg of H_2, which is twice as high as the same indicator for the steam conversion of natural gas. Additional factors affecting the water consumption indicators of the water electrolysis process should also be indicated, which are often omitted or not fully taken into account when conducting a feasibility study of projects [29, 30]:

• water cooling of electrolyzers – the one of the key reasons for the decrease in the efficiency of electrode battery during the service life (8-10 years) is additional heating, and therefore the cooling load on the electrolyzer during operation can increase by 40-70 %. The effect of this factor on the water consumption index is 30-40 liters of H_2O per 1 kg of H_2 *** [31];

• water cooling of related equipment, such as compressors to compress hydrogen to the pressure required for storage/application;

• purification of the source (raw) water – depending on the quality of the source water, the amount of waste (effluents) of the purification process can be 20-40 %;

• wastewater disposal – an increased concentration of impurities in the composition of wastewater in most cases prevents the discharge of these wastewater into the environment in its pure form; additional purification or dilution may be required for wastewater disposal.

The actual water consumption for water electrolysis process, taking into account the listed additional factors, may be 60-95 liters of H_2O per 1 kg of H_2. At the same time, 60-70 % of the total amount of water consumed falls on the recharge of water cooling systems. The general scheme of the water consumption in the process of water electrolysis process is shown in Figure*** [31].

The above water consumption indicators are possible when using relatively good quality fresh water as a feedstock. For water with high salinity, seawater or industrial wastewater, raw water consumption and the amount of process effluents may increase significantly [32].

* Green hydrogen production will have a negligible impact on global water use. Hydrogeninsight, 04.08.2023. URL: https://www.hydrogeninsight.com/production/green-hydrogen-production-will-have-a-negligible-impact-on-global-water-use-says-us-think-tank/2-1-1496489 (accessed 10.09.2023).

** Water Usage in Hydrogen or Ammonia Synthesis Scenarios. URL: https://netl.doe.gov/research/Coal/energy-systems/gasification/gasifipedia/water-use-sng (accessed 10.09.2023).

*** Lee K. The Water Impact of Hydrogen. Understanding the effects of green hydrogen production. Sensus, 11.04.2023. URL: https://blog.sensus.com/the-water-impact-of-hydrogen/ (accessed 10.09.2023).

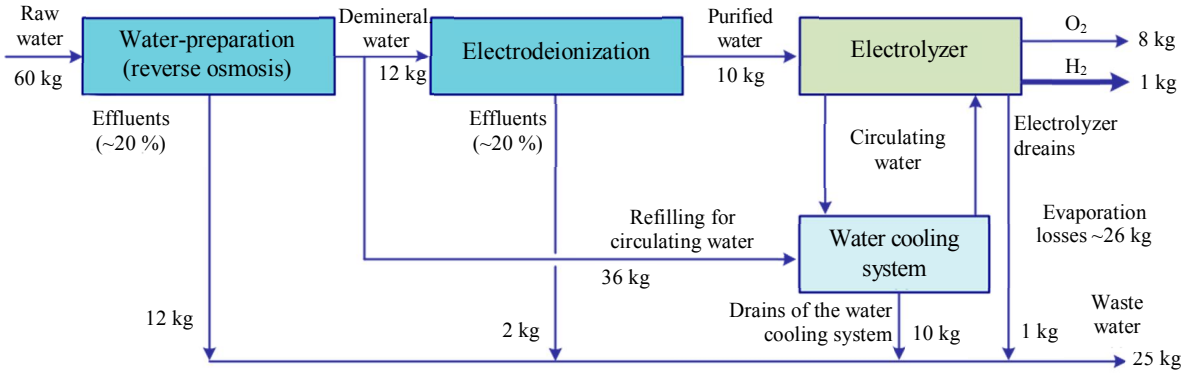

Water consumption in the process of water electrolysis

Table 1

Water consumption for various hydrogen production methods

Production method	Water consumption, liters of H_2O per 1 kg of H_2	
	Stoichiometric	Actual
Steam methane reforming	4.5	15-40
Steam methane reforming + CO_2 capture	4.5	18-44
Steam biogas reforming	4.5	20-45
Hard coal gasification	Depending on C:H ratio and on coal humidity	~70
Lignite coal gasification		~60
Water electrolysis	9	60-95

Table 1 provides a summary of water consumption indicators for the production of various types of hydrogen in accordance with the modern color classification.

An increase in hydrogen production can lead to an increase in water consumption in this segment by 35-100 %. Taking into account the projected volume of hydrogen consumption (70 EJ), in 2050 the total volume of water consumption in the hydrogen production segment may amount to 35-55 thousand tons per year, which is expected to create additional demand for water resources and, as a result, increase the threat of violations of water security in a number of nations.

One of the key tasks of the hydrogen economy development is the ways optimizing for hydrogen storage and the end user delivery. Currently, possible methods of hydrogen transportation, in addition to liquefaction, are the liquid organic carriers (LOHC)* and the use of a chemically bound form (as part of ammonia). The application of each of these methods is associated with an appropriate technology involving the consumption of steam, demineralized and/or cooling water. Despite the fact that water consumption is not a key indicator when choosing a method for storing and transporting hydrogen, it should be taken into account when planning new hydrogen projects.

When developing measures to optimize water consumption in new hydrogen projects, a special attention should be paid to reducing the consumption of make-up cooling water. This indicator is dominant in the overall structure of water consumption and consists of losses for evaporative cooling in cooling towers (~75 %), water cooling blowdown system (~15 %), as well as some additional losses [33-35].

Water consumption for various ways of hydrogen production, depending on the quality of the source water. In addition to optimizing water consumption, an important criterion for the effectiveness of hydrogen projects is the type of water resources. There are three main types of water resources for hydrogen projects: freshwater, seawater, and industrial wastewater. Using fresh water is the least expensive, though not the best option, because in this case hydrogen

* Methylcyclohexane can act as a LOHC (Liquid Organic Hydrogen Carrier).

Journal of Mining Institute. 2024. Vol. 265. P. 87-94

production uses water resources, which could find a more effective use in other segments of the economy and social sphere.

Hydrogen production plants are usually located in close proximity to other industrial enterprises and settlements, which makes it possible to use significant amounts of industrial and domestic wastewater. The use of wastewater is associated with an increase in treatment costs; however, it may have advantages in terms of reducing the length of the water pipeline, transportation costs, as well as the cost of source water [33-35].

The use of seawater is the only realistic source of water resources for most large-scale hydrogen production facilities from water. At the same time, the total water consumption, depending on the quality of the source water, may significantly exceed the analogous indicator when using fresh water [14, 36, 37]. The process of seawater desalination is associated with an increase burden on the environment, in connection with which the procedures for environmental assessment, obtaining permits, approvals, etc. can significantly increase the time and investment costs for the implementation of hydrogen projects. At the same time, energy costs for hydrogen production are also increasing, since water purification is an energy-intensive technology [14].

The prospective energy consumption indicator of a desalination plant averages ~0.5 kWh per 1 kg of H_2, which is insignificant in comparison with ~50 kWh per 1 kg of H_2 required during electrolysis, but in some cases it may be a significantly higher cost for the entire system – from 7 to 20 kWh [31]. The most common modern water desalination process is reverse osmosis, and thermal desalination (distillation) is used on a significant scale (especially in the Middle East). Other processes – direct osmosis, membrane purification, ion exchange, electrodialysis, etc. – are at various stages of commercialization and applied research. The development and optimization of water desalination technologies will have a fundamental impact on the efficiency of hydrogen projects in the future.

In the Table 2 provides comparative estimates of the water consumption of hydrogen projects using freshwater (the best option) and seawater (the worst option).* It should be noted that the water consumption in obtaining hydrogen exclusively from fresh water turns out to be comparable to that for the method with the highest carbon footprint (coal gasification) and with the lowest carbon footprint (electrolysis using "green" electricity). Water consumption when using seawater is proving to be record-breaking. It is assumed that when using industrial or domestic wastewater as a source, water consumption indicators will be in the range between the values obtained for the best and worst options.

Table 2

Water consumption for various hydrogen production methods depending on the quality of the source water

Production method	Water consumption, liters of H_2O per 1 kg of H_2	
	Freshwater, evaporative cooling	Seawater, evaporative cooling
Steam methane reforming	15-40	38-100, occasional up to 200
Steam methane reforming + CO_2 capture	18-44	45-100, occasional up to 220
Steam biogas reforming	20-45	50-113, occasional up to 225
Hard coal gasification	~70	175-350
Lignite coal gasification	~60	150-300
Water electrolysis	60-95	150-238, occasional up to 475

* According to research of GHD Group (Australia). URL: https://www.ghd.com/en-us/insights/navigating-waters-role-in-the-green-hydrogen-economy (accessed 10.09.2023).

Estimation of the carbon footprint of hydrogen production by steam reforming of methane based on the data of the material balance of the production plant. The production of hydrogen from water is often classified as the production of "renewable" hydrogen through the circulation of water, but water is also a source of hydrogen for the steam conversion of methane or hydrocarbons mixtures, one of the main industrial methods for producing hydrogen currently in use. In the framework of hydrogen production at existing industrial steam reforming plants, methane interacts with water vapor in the presence of catalysts in two stages [8] according to the equations:

$$CH_4 + H_2O \rightarrow CO + 3H_2,\ \Delta H°298 = +206\ \text{kJ/mol (I)};$$

$$CO + H_2O \rightarrow CO_2 + H_2,\ \Delta H°298 = -41{,}2\ \text{kJ/mol (II)}.$$

Overall reaction:

$$CH_4 + 2H_2O \rightarrow CO_2 + 4H_2.$$

Considering the amount of hydrogen produced from methane and water, it can be noted that of the total amount of hydrogen in four molecules, two of them belonged to water and two to methane, i.e. the ratio according to the stoichiometric equation is 50/50. In the Table 3 presents data on the material balance of hydrogen production at a real-life industrial plant. It can be seen that the yield of hydrogen from water, taking into account the estimated losses, was 48.88 %, which, taking into account possible errors, can be considered confirmation that during the steam conversion of methane, half of the hydrogen produced base on water and for this part of hydrogen the carbon footprint is significantly lower.

Table 3

Initial data on the material balance of hydrogen production by steam reforming at an industrial plant

Stream	Consumption and share	
	t (m^3)/h	%
Feed		
Natural gas	6.423	19.04
Desalinated water	27.304	80.96
Total	33.727	100
Output		
Hydrogen	2.248	6.67
Water steam 16 Atm.	15.503	45.97
Residual gas	15.356 (15.652)	45.53
Deaerator Air bag	0.171	0.50
Other losses	0.449	1.33
Total	33.727	100

Based on the data of the technological process, it was determined that the cost of methane for the operation of the reformer is 0.1814 MJ/mol H_2. It should be noted that the heat of most natural gas steam reforming processes is utilized for power generation. When calculating greenhouse gas emissions from steam reforming of natural gas, it was determined that the water in the reaction itself has zero CO_2 emissions-eq, the carbon dioxide formed in the process itself belongs to methane, since it is formed in any case regardless of the oxidizer. The calculation is based on the highest calorific value.

In the very process of steam reforming of natural gas, according to stoichiometry, 0.8721 mol CO_2/MJ H_2 is formed from methane. Accordingly, 38.3805 g of CO_2/MJ H_2 is formed for overall hydrogen. For carbon dioxide attribution to hydrogen from methane – 76.761 g CO_2/MJ H_2,

For the reformer to work in the steam reforming of natural gas, it is necessary to ensure its heating by external burner devices, which will be equivalent to 31.6463 g of CO_2/MJ H_2, and it is part of these emissions that can be attributed to hydrogen from water.

Thus, the total greenhouse gas emissions with uniform distribution will amount to 10.03 kg CO_2-eq/kg H_2. Under given conditions, within the framework of steam reforming of natural gas, the carbon footprint of hydrogen from methane will amount to 15.4-15.7 kg CO_2-eq/kg H_2, and the carbon footprint of hydrogen from water will amount to 4.2-4.5 kg CO_2-eq/kg H_2.

Evaluating hydrogen in terms of energy and water costs requires a system analysis. The unilateral practice of supporting only one group of technologies has a significant negative impact on the implementation of scientifically based hydrogen projects [38, 39]. Technological neutrality makes it

Journal of Mining Institute. 2024. Vol. 265. P. 87-94

possible to determine the most optimal solutions in the field of hydrogen energy development based on an interdisciplinary analysis.

Conclusion. The results of the comparative analysis carried out in this study show that water consumption in the steam reforming hydrogen production is significantly lower than by electrolysis hydrogen production.

Based on the data of the material balance of operating hydrogen production plant, it was revealed that hydrogen produced by the traditional steam conversion method is almost 50 % "renewable" and "low-carbon" in terms of the raw materials used – water and the carbon footprint index.

It should be noted that with the development of the hydrogen economy and the growth of global hydrogen production from water, the influence of this segment on the water cycle and global water resources will significantly increase.

REFERENCES

1. Gleick P.H. Water and Energy. *Annual Review of Energy and the Environment*. 1994. Vol. 19, p. 267-299. DOI: 10.1146/annurev.eg.19.110194.001411

2. Grubert E., Sanders K.T. Water Use in the United States Energy System: A National Assessment and Unit Process Inventory of Water Consumption and Withdrawals. *Environmental Science & Technology*. 2018. Vol. 52. Iss. 11, p. 6695-6703. DOI: 10.1021/acs.est.8b00139

3. Helerea E., Calin M.D., Musuroi C. Water Energy Nexus and Energy Transition – A Review. *Energies*. 2023. Vol. 16. Iss. 4. N 1879. DOI: 10.3390/en16041879

4. Bauer D., Philbrick M., Vallario B. The Water-Energy Nexus: Challenges and Opportunities. Overview and Summary. U.S. Department of Energy. 2014, p. 12.

5. Parkinson B., Tabatabaei M., Upham D.C. et al. Hydrogen production using methane: Techno-economics of decarbonizing fuels and chemicals. *International Journal of Hydrogen Energy*. 2018. Vol. 43. Iss. 5, p. 2540-2555. DOI: 10.1016/j.ijhydene.2017.12.081

6. Midilli A., Kucuk H., Topal M.E. et al. A comprehensive review on hydrogen production from coal gasification: Challenges and Opportunities. *International Journal of Hydrogen Energy*. 2021. Vol. 46. Iss. 50, p. 25385-25412. DOI: 10.1016/j.ijhydene.2021.05.088

7. Megía P.J., Vizcaíno A.J., Calles J.A., Carrero A. Hydrogen Production Technologies: From Fossil Fuels toward Renewable Sources. A Mini Review. *Energy & Fuels*. 2021. Vol. 35. Iss. 20, p. 16403-16415. DOI: 10.1021/acs.energyfuels.1c02501

8. Massarweh O., Al-Khuzaei M., Al-Shafi M. et al. Blue hydrogen production from natural gas reservoirs: A review of application and feasibility. *Journal of* CO_2 *Utilization*. 2023. Vol. 70. N 102438. DOI: 10.1016/j.jcou.2023.102438

9. Litvinenko V.S., Tsvetkov P.S., Dvoynikov M.V., Buslaev G.V. Barriers to implementation of hydrogen initiatives in the context of global energy sustainable development. *Journal of Mining Institute*. 2020. Vol. 244, p. 428-438. DOI: 10.31897/PMI.2020.4.5

10. Tabrizi M.K., Famiglietti J., Bonalumi D., Campanari S. The Carbon Footprint of Hydrogen Produced with State-of-the-Art Photovoltaic Electricity Using Life-Cycle Assessment Methodology. *Energies*. 2023. Vol. 16. Iss. 13. N 5190. DOI: 10.3390/en16135190

11. Aghakhani A., Haque N., Saccani C. et al. Direct carbon footprint of hydrogen generation via PEM and alkaline electrolysers using various electrical energy sources and considering cell characteristics. *International Journal of Hydrogen Energy*. 2023. Vol. 48. Iss. 77, p. 30170-30190. DOI: 10.1016/j.ijhydene.2023.04.083

12. Mehmeti A., Angelis-Dimakis A., Arampatzis G. et al. Life Cycle Assessment and Water Footprint of Hydrogen Production Methods: From Conventional to Emerging Technologies. *Environments*. 2018. Vol. 5. Iss. 2. N 24. DOI: 10.3390/environments5020024

13. Simoes S.G., Catarino J., Picado A. et al. Water availability and water usage solutions for electrolysis in hydrogen production. *Journal of Cleaner Production*. 2021. Vol. 315. N 128124. DOI: 10.1016/j.jclepro.2021.128124

14. Plappally A.K., Lienhard V.J.H. Energy requirements for water production, treatment, end use, reclamation, and disposal. *Renewable and Sustainable Energy Reviews*. 2012. Vol. 16. Iss. 7, p. 4818-4848. DOI: 10.1016/j.rser.2012.05.022

15. Dvoynikov M., Buslaev G., Kunshin A. et al. New Concepts of Hydrogen Production and Storage in Arctic Region. *Resources*. 2021. Vol. 10. Iss. 1. N 3. DOI: 10.3390/resources10010003

16. Zhukovskiy Y., Tsvetkov P., Buldysko A. et al. Scenario Modeling of Sustainable Development of Energy Supply in the Arctic. *Resources*. 2021. Vol. 10. Iss. 12. N 124. DOI: 10.3390/resources10120124

17. Buslaev G., Lavrik Al., Lavrik An., Tcvetkov P. Hybrid system of hydrogen generation by water electrolysis and methane partial oxidation. *International Journal of Hydrogen Energy*. 2023. Vol. 48. Iss. 63, p. 24166-24179. DOI: 10.1016/j.ijhydene.2023.03.098

18. Spath P.L., Mann M.K. Life Cycle Assessment of Hydrogen Production via Natural Gas Steam Reforming. Technical Report NREL/TP-570-27637. 2001. N 33067001, p. 33. DOI: 10.2172/764485

19. Saulnier R., Minnich K., Sturgess P.K. Water for the Hydrogen Economy. WaterSMART Solutions Ltd. 2020, p. 13.

20. Ogden J.M. Review of small stationary reformers for hydrogen production. *International Energy Agency*. N IEA/H2/TR-02/002. 2002, p. 52.

21. Lampert D.J., Cai H., Wang Zh. et al. Development of a Life Cycle Inventory of Water Consumption Associated with the Production of Transportation Fuels. U.S. Department of Energy. N ANL/ESD-15/27. 2015, p. 80.

22. Simon A.J., Daily W., Whity R.G. Hydrogen and Water: An Engineering, Economic and Environmental Analysis. U.S. Department of Energy. Technical Report LLNL-TR-422193. 2010. N 110388, p. 26. DOI: 10.2172/101038

23. Matthey J. LCH™ Process for the production of blue hydrogen. Johnson Matthey Group. 2022, p. 10.

24. Rosa L., Sanchez D.L., Realmonte G. et al. The water footprint of carbon capture and storage technologies. *Renewable and Sustainable Energy Reviews*. 2021. Vol. 138. N 110511. DOI: 10.1016/j.rser.2020.110511

25. Milbrandt A., Mann M. Hydrogen Resource Assessment. Hydrogen Potential from Coal, Natural Gas, Nuclear, and Hydro Power. Technical Report NREL/TP-560-42773. 2009, p. 30.

26. Chaowei Wang, Song He, Sheng Li, Lin Gao. Water saving potential of coal-to-synthetic natural gas. *Journal of Cleaner Production*. 2021. Vol. 280. Part 1. N 124326. DOI: 10.1016/j.jclepro.2020.124326

27. Schiaroli N., Volanti M., Crimaldi A. et al. Biogas to Syngas through the Combined Steam/Dry Reforming Process: An Environmental Impact Assessment. *Energy & Fuels*. 2021. Vol. 35. Iss. 5, p. 4224-4236. DOI: 10.1021/acs.energyfuels.0c04066

28. Markard J., Wirth S., Truffer B. Institutional dynamics and technology legitimacy – A framework and a case study on biogas technology. *Research Policy*. 2016. Vol. 45. Iss. 1, p. 330-344. DOI: 10.1016/j.respol.2015.10.009

29. Grubert E. Water consumption from electrolytic hydrogen in a carbon-neutral US energy system. *Cleaner Production Letters*. 2023. Vol. 4. N 100037. DOI: 10.1016/j.clpl.2023.100037

30. Lampert D.J., Cai H., Elgowainy A. Wells to wheels: water consumption for transportation fuels in the United States. *Energy & Environmental Science*. 2016. Vol. 9. Iss. 3, p. 787-802. DOI: 10.1039/C5EE03254G

31. *Brannock M.W.D., Dagg B.J., Mitchell K.P.* Water for hydrogen production: challenges and opportunities supported by real-world case studies. The International Desalination Association International World Congress "Charting Resilient Water Solutions", 9-13 October 2022, Sydney, Australia. № IDAWC22-Brannock, p. 9.

32. Jones E., Qadir M., van Vliet M.T.H. et al. The state of desalination and brine production: A global outlook. *Science of the Total Environment*. 2019. Vol. 657, p. 1343-1356. DOI: 10.1016/j.scitotenv.2018.12.076

33. Hamawand I. Energy Consumption in Water/Wastewater Treatment Industry – Optimisation Potentials. *Energies*. 2023. Vol. 16. Iss. 5. N 2433. DOI: 10.3390/en16052433

34. Tchobanoglous G., Burton F.L., Stensel H.D., Tsuchihashi R. Wastewater Engineering: Treatment and Resource Recovery. New York: McGraw Hill, 2013, p. 2048.

35. Corominas L., Foley J., Guest J.S. et al. Life cycle assessment applied to wastewater treatment: State of the art. *Water Research*. 2013. Vol. 47. Iss. 15, p. 5480-5492. DOI: 10.1016/j.watres.2013.06.049

36. Kavitha J., Rajalakshmi M., Phani A.R., Padaki M. Pretreatment processes for seawater reverse osmosis desalination systems – A review. *Journal of Water Process Engineering*. 2019. Vol. 32. N 100926. DOI: 10.1016/j.jwpe.2019.100926

37. Xiaolei Zhang, Jingjing Jiang, Fang Yuan et al. Estimation of water footprint in seawater desalination with reverse osmosis process. *Environmental Research*. 2022. Vol. 204. Part D. N 112374. DOI: 10.1016/j.envres.2021.112374

38. Kopteva A., Kalimullin L., Tcvetkov P., Soares A. Prospects and Obstacles for Green Hydrogen Production in Russia. *Energies*. 2021. Vol. 14. Iss. 3. N 718. DOI: 10.3390/en14030718

39. Zagashvili Y., Kuzmin A., Buslaev G., Morenov V. Small-Scaled Production of Blue Hydrogen with Reduced Carbon Footprint. *Energies*. 2021. Vol. 14. Iss. 16. N 5194. DOI: 10.3390/en14165194

Authors: Anton L. Maksimov*, Corresponding Member of the RAS, Doctor of Chemical Sciences, Director, https://orcid.org/0000-0001-9297-4950 (A.V.Topchiev Institute of Petrochemical Synthesis, RAS, Moscow, Russia),* ***Aleksandr G. Ishkov****, Doctor of Chemical Sciences, Deputy Head of Department – Head of Directorate, Professor, https://orcid.org/0009-0008-1452-6130 (PAO Gazprom, Saint Petersburg, Russia; D.I.Mendeleev Russian University of Chemical Technology, Moscow, Russia),* ***Andrei A. Pimenov****, Doctor of Engineering Sciences, Director, https://orcid.org/0000-0001-8923-2550 (Tatar Oil Research and Design Institute (TatNIPIneft) of PAO TATNEFT, Kazan, Russia),* ***Konstantin V. Romanov****, Candidate of Economics, Head of Division, General Director, k.romanov@adm.gazprom.ru, https://orcid.org/0009-0004-9130-1155 (PAO Gazprom, Saint Petersburg, Russia; OOO Gazprom Hydrogen, Moscow, Russia),* ***Andrei M. Mikhailov****, Candidate of Engineering Sciences, Head of the Laboratory, https://orcid.org/0009-0001-9884-4329 (OOO Gazprom VNIIGAZ, Saint Petersburg, Russia),* ***Evgenii A. Koloshkin****, Chief Technologist, https://orcid.org/0009-0008-6718-9959 (PAO Gazprom, Saint Petersburg, Russia).*

The authors declare no conflict of interests.

ISSN 2411-3336; e-ISSN 2541-9404

JOURNAL OF MINING INSTITUTE

Zapiski Gornogo instituta

Journal homepage: pmi.spmi.ru

Research article

Study of the properties and action of polyelectrolytes in the treatment of the dressing plant's discharges

Galina V. MITROFANOVA[1]✉, **Elena V. CHERNOUSENKO**[1], **Aleksandr V. ARTEMEV**[1], **Yuliya P. POSPELOVA**[1], **Natalya A. SMIRNOVA**[2], **Igor S. BARMIN**[3]

[1] *Mining Institute of Kola Science Centre of the RAS, Apatity, Russia*

[2] *AO Kovdorsky GOK, Kovdor, Russia*

[3] *AO Mineral and Chemical Company EuroChem, Moscow, Russia*

How to cite this article: Mitrofanova G.V., Chernousenko E.V., Artemev A.V., Pospelova Yu.P., Smirnova N.A., Barmin I.S. Study of the properties and action of polyelectrolytes in the treatment of the dressing plant's discharges. Journal of Mining Institute. 2024. Vol. 265, p. 95-103. EDN CVUHNQ

Abstract. The organization of intrafactory water circulation at mining and processing enterprises, when production wastes and discharges are not sent to an external tailings dump, is an urgent environmental and economic task. Returning even a part of water into the technological process after preliminary treatment will significantly reduce the volume of polluted water discharged into tailings, which will reduce energy costs for waste transportation and the negative environmental impact. One of the wastes sent to the tailings during the ore dressing wastes from the Kovdor deposit to the tailings dump is the discharge of thickeners for the preparation of apatite flotation feed. In order to choose the effective discharge cleaning regime, the authors have evaluated the action of polyacrylamide flocculants. It has been discovered that the apatite and calcite particles interact more effectively with the anionic flocculant. This fact determines its advantage for the treatment of suspended particles. The influence of the residual concentration of a flocculant on the apatite flotation, where a part of the returned treated water goes, has been assessed. Compared to flotation with recycled water, there is a decrease of P_2O_5 extraction into apatite concentrate of equal quality. In order to obtain the required enrichment indicators on the treated water, it is necessary to adjust the collector (tall oil fatty acids) and depressor (liquid glass) costs.

***Keywords*:** apatite flotation; the Kovdor deposit; internal water circulation; polyacrylamide flocculants; water preparation

Received: 31.10.2022 ***Accepted: 21.04.2023*** ***Online: 04.07.2023*** ***Published: 29.02.2024***

Introduction. The development of the mining industry requires an active solution of the tasks on improving environmental safety and reducing the negative environmental impact from dressing enterprises. It is of great interest to involve various liquid dressing wastes into the technological process after their preliminary preparation [1-3]. On the one hand, this reduces the demands of an enterprise for clean water, which is beneficial from an economic point of view; on the other hand, it reduces the amount of polluted water discharged into the tailings [4].

The most promising object in terms of return to the process at the dressing plant is water from thickening and filtration operations [5, 6]. However, rapid return of water into the technological process, without its settling in the tailings dump, results in accumulating dissolved ions, suspended solids and reagents used in previous operations [6-8]. Depending on the name of contaminants, acidic wastes of hydrometallurgical production [9], ash dump effluents of thermal stations [10], and various chemical reagents in the case of oxidative treatment [11, 12] can be used to treat wastewater from a dressing plant.

Purification from fine mineral particles remaining in the discharges of thickeners involves the use of coagulants or flocculants. As a rule, iron, aluminum and magnesium salts are used as coagulants, the adsorption of which on the mineral surface results in neutralizing the surface charge [13].

However, the use of inorganic electrolytes is undesirable if purified water is supposed to be used in the flotation.

The use of organic reagents-flocculants is more preferable; their advantages include good solubility in water, high efficiency at low dosage, and obtaining large, strong and stable flakes [14]. The most popular are polyacrylamide reagents, which differ in charge sign, its density, and molecular weight [15, 16]. Such reagents are used for recycled water treatment in bauxite flotation in alkaline medium [17, 18], in the dissolved-air flotation technology to purify the recycled water of apatite production from interfering impurities [19]. Studies on recycled water sludge from an iron ore dressing plant have shown a high efficiency of an anionic polyacrylamide flocculant, which interacts with the surface of particles due to the formation of hydrogen bonds [20].

The purpose of this study is to justify and select an efficient flocculant for treatment of the liquid phase of the discharges of thickeners for the preparation of feed for apatite flotation. Treatment of the discharge to the required purity (suspended solids content of 50 mg/l) will provide the possible return of the purified water to the technological process of the Kovdor magnetite-apatite ore beneficiation.

Materials and methods. The authors have analyzed Flopam polyacrylamide cationic (FO-4700 SH) and anionic (AN-905 SH, AN-913 SH, AN-934 SH and AN-956 SH) flocculants differing in charge density, produced by SNF Company (see Table).

Characteristics of Flopam flocculants

Flocculant	Molecular weight, $M \cdot 10^6$	Type	Charge density, mol.%	Working range pH	Solution viscosity 1 g/l, cPs
AN-905 SH	11-13.5	Anionic	5	1-12	80
AN-913 SH	11.3-13.5	Anionic	13	0-13	160
AN-934 SH	13.6-16.8	Anionic	30	6-13	195
AN-956 SH	13.6-16.8	Anionic	50	6-13	200
FO-4700 SH	5.0-7.2	Cationic	70	1-10	180

The efficiency of flocculants in the treatment of suspended solids was evaluated by the periodic sedimentation method. A calculated amount of 0.01 % flocculant solution was added to the mineral suspension placed in a 1-liter cylinder. The suspension was stirred in equal conditions and left at rest. When constructing concentration dependences, after a given period of time the volume of liquid above a given (the same for all solutions) depth was taken from the cylinder. The lower boundary of sampling was chosen according to results of preliminary evaluation and was located above the sediment compaction zone. The sampling time was 30 min and was determined based on the preliminary assessment in accordance with the requirement for the water treatment degree. A 100 ml aliquot was taken from the obtained volume of liquid with thorough stirring, for which the residual concentration of suspended particles was determined by the gravimetric method. The aliquot of purified liquid was placed in a tube previously weighed on an analytical scale and centrifuged for 30 min at 3,500 rpm (Elmi CM-6M centrifuge). After decanting the liquid, the solid residue was dried at 102 °C to constant weight. The residual concentration of suspended particles with hydraulic fineness less than the set size was determined after weighing.

The studies were carried out on a model suspension of magnetite-carbonate ore from the Kovdor deposit and on the discharge of thickeners for the preparation of feed for apatite flotation at the dressing plant of AO Kovdorsky GOK. To create the model suspension, the non-magnetic fraction of magnetite-carbonate ore was ground to a size of –0.045 mm; the required density was created by adding recycled water of the dressing plant. The content of solids in the model suspension was 13.7 g/l; suspended particles content in samples of thickener's discharge was 13-14 g/l, and particle size class of minus 0.045 mm – 98 %.

Journal of Mining Institute. 2024. Vol. 265. P. 95-103

The flocculants' adsorption was assessed by using pure apatite with coarseness –0.03 mm. A one-g mineral sample was mixed with a flocculant solution of a given concentration. After separation of solid material by centrifugation the residual concentration of the reagent was determined viscometrically. For this purpose, concentration dependences of the relative viscosity of flocculant solutions at the appropriate value (Sartorius PP-20 pH-meter) were preliminarily plotted. Viscosity was measured by VPZh-2 viscosimeter with a capillary diameter of 0.56 mm.

The suspension effect was evaluated on pure minerals of apatite and calcite, crushed to –0.03 mm particle size. The necessary amount of NaOH or HCl solutions was added to the mineral suspension in distilled water in order to achieve the specified pH level; then the flocculant solution was kept in a hermetically sealed container for 2 h. The suspension effect was defined as the difference between pH values of the initial mineral suspension and its filtrate after a two-hour contact.

The flocculant influence on apatite flotation was estimated on the sample of non-magnetic fraction of magnetite-apatite ore from the Kovdor deposit with 8.45 % P_2O_5. Flotation was carried out in a laboratory flotation machine (Mekhanobr) in open cycle using the water, which was a flocculant-purified thickener's discharge for the preparation of feed for apatite flotation.

The flotation results were evaluated by the main technological indicators of the process: the useful component content β, the product yield γ and the recovery of the determinable component ε. Extraction was calculated by the formula

$$\varepsilon = (\beta\gamma)/\alpha.$$

Discussion of results. Polyacrylamides are the most common flocculants used in the treatment of polluted industrial wastewater and domestic water. A wide range of reagents with different molecular weight, sign and magnitude of charge allows in each specific case to choose the optimal flocculant in terms of composition and structure.

The peculiarities of the technological scheme for magnetite-apatite ore beneficiation determine high requirements to the treatment from suspended water particles, involved in the intra-factory water turnover. The solid phase of the discharge of apatite flotation feed thickeners consists mainly of fine particles of apatite and carbonate minerals. To assess and describe the surface properties of the mineral, causing its interaction with the reagents in the flotation process or in the thickening operations, the value and sign of the electro-kinetic potential (ξ-potential) is commonly used [21, 22].

Analysis of available literature sources shows a wide range of data for both apatite [23, 24] and calcite [25, 26]. The point of zero charge, at which the ξ-potential changes sign to negative, for apatite, according to different authors, lies in the pH range from 1.0 to 8.7 [27, 28]; for calcite the curve ξ-potential lies in the area of negative values almost over the entire pH range [29]. Thus, in the alkaline area of pH ≥ 9.0, corresponding to the pH of the flotation pulp, the surface of apatite and calcite is negatively charged and interaction of cationic flocculants with it should be preferable.

This conclusion is confirmed by the evaluation results of cationic and anionic flocculants adsorption on the apatite surface in the acidic and alkaline pH area. Measurements of adsorption were carried out at pH = 9.5, which corresponds to the pH value of the discharge; at pH = 4 for the FO-4700 reagent, and pH = 6 for the AN-956 reagent. Obtained dependences show that at fixing of reagent on a surface of a mineral having an opposite charge, due to electrostatic interaction (Fig.1, curves 1 and 2), the adsorption significantly exceeds the adsorption of the same flocculants at pH when surface and reagent have the same sign (Fig.1, curves 3 and 4).

Obviously, the anionic reagent in the acidic pH area and the cationic reagent in the alkaline range are in the ionized state. Mutual repulsion of similarly charged ionized groups promotes the unfolding of polymer molecules, which is well traced in the curves of the viscosity dependence of flocculant solutions on pH [30]. Thus, flocculant molecules are in the maximum unfolded state, favorable for

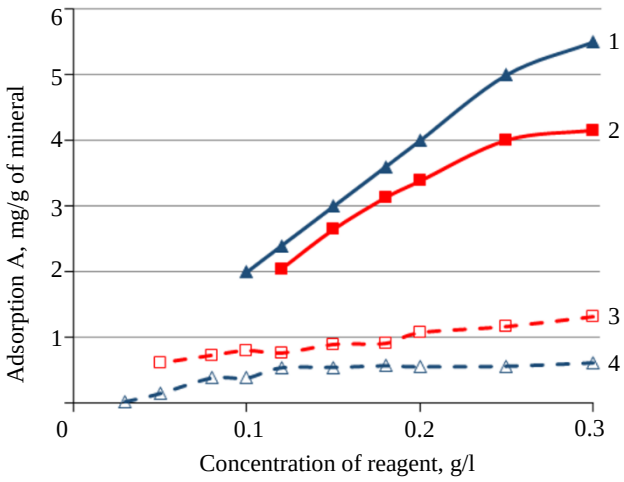

Fig.1. Adsorption of flocculants on apatite
1 – AN-956, pH = 6.0; 2 – FO-4700, pH = 9.5;
3 – FO-4700, pH = 4.0; 4 – AN-956, pH = 9.5

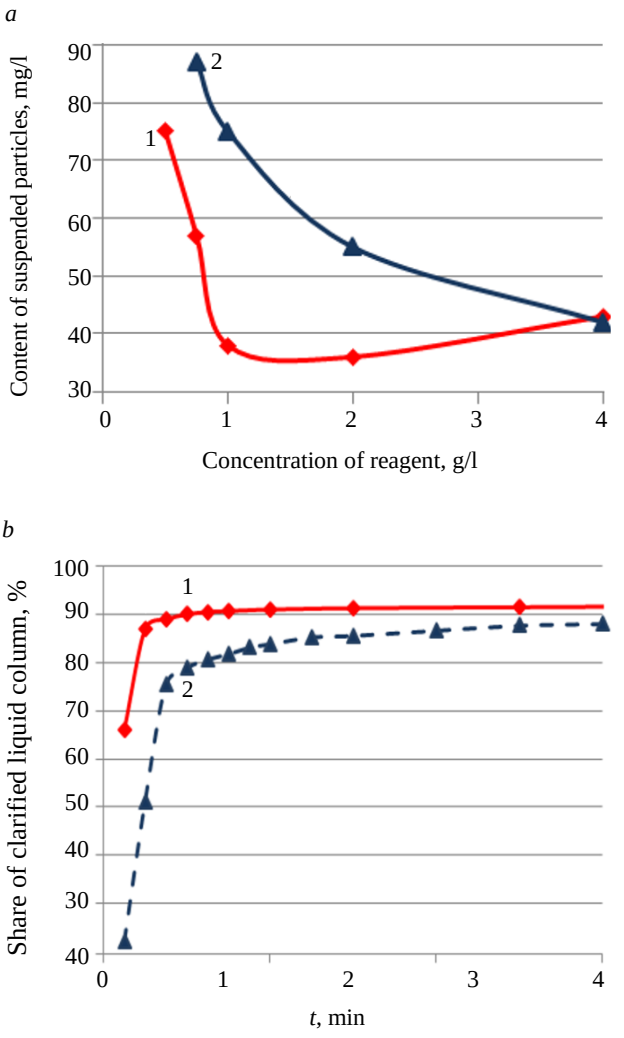

Fig.2. Efficiency of purification of discharge of thickeners (*a*) and velocity of sedimentation of suspended particles (*b*) with the use of flocculants
1 – AN-956; 2 – FO-4700

the binding fine particles into floccule in the pH range, when the surface of the mineral is similarly charged. In this case, fixation of a polymeric molecule on mineral particles occurs due to hydrogen bonds between oxygen and nitrogen atoms of the functional groups with OH-groups on the surface [31].

Experiments on treatment of the discharges of thickeners for the feed of apatite flotation have demonstrated the high efficiency of anionic flocculants (Fig.2, *a*). The use of anionic AN-956 reagent results in a quicker sedimentation of particles (Fig.2, *b*). In the pH alkaline area the molecules of the ionized anionic reagent are in the unfolded state, which contributes to the formation of larger floccules and more rapid release of moisture from the resulting sediment, which volume in the case of FO-4700 is 1.5-1.7 times more than that of the anionic flocculant.

Note that the anionic flocculant retains its effectiveness in a fairly wide range of solid content in the treated discharge, which is an important factor, given the natural fluctuations in the characteristics of the discharge incoming for treatment. When varying the content of solids in the discharge from 0.25 to 5.0 percent, the content of suspended solids in wastewater treated with AN-956 reagent did not exceed 50 mg/l: at 0.25 – 46.4; 0.5 – 39.1; 1.0 – 33.2; 1.25 – 41.5; 1.4 – 38.5; 1.75 – 40.1; 2.5 – 47.0; 5.0 – 50.0.

In order to confirm the mechanism of the interaction of flocculants with the mineral surface the authors evaluated the suspension effect – a parameter characterizing the acid-base properties of the mineral surface.

It is known that the surface of salt-like minerals, including apatite and calcite, is chemically heterogeneous and is characterized by the presence of both basic and acidic centers.

H^+, OH^- and CO_3^{2-} ions are potential-forming with respect to the surface of apatite and calcite in liquid medium, which allowed evaluating the acid-base properties of apatite and calcite by determining the isoionic point of the mineral and its suspension effect. The value of the suspension effect is calculated as the difference between the pH of the initial mineral suspension in water and the pH of the filtrate obtained after separation of the solid phase. The pH change is

Journal of Mining Institute. 2024. Vol. 265. P. 95-103

caused by the specific adsorption of potential-forming ions, as a result of which the surface of the mineral acquires a positive or negative charge.

Studies of acid-base properties of apatite [30, 32] and analysis of literature data [33, 34] have shown a significant influence of ionic composition of the liquid phase on the position of the isoionic point. Therefore, the suspension effect was measured using boiled distilled water without carbonate ions. Dependences of the suspension effect of apatite and calcite on pH are shown in Fig.3. The position of the isoionic point (pH_{ip} = 9.0) of calcite in the alkaline area indicates the predominance of basic centers on its surface. The apatite surface in distilled water is characterized by approximately equal number of acid and basic centers, pH_{ip} = 6.7. In the alkaline area of pH ≥ 9, the suspension effect for both minerals is positive, indicating hydroxide ions binding, which results in a negative charge of the minerals on the surface. Increasing the electrolyte concentration leads to compression of the double electric layer and a decrease in the value of the suspension effect; these events are observed in pH > 8.5 area for apatite and pH > 9.5 for calcite.

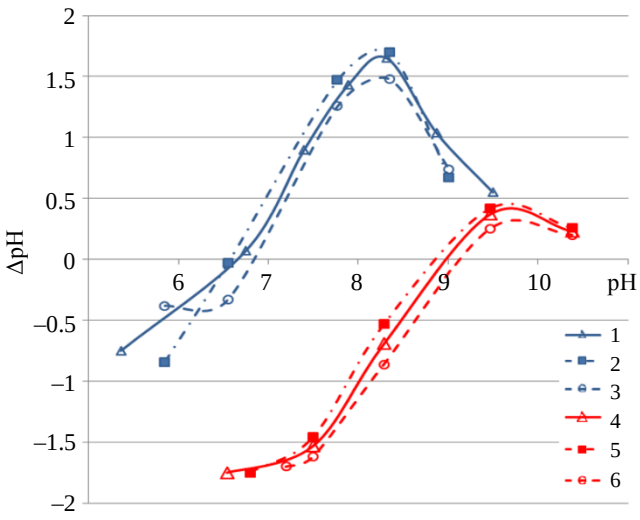

Fig.3. Suspension effect of apatite (1) and calcite (4) depending on pH medium without and with flocculants AN-956 (2, 5) and FO-4700 (3, 6)

Assessment of the apatite suspension effect in the presence of flocculants showed the increase of the positive value of the suspension effect in the alkaline area and the shift of the isoionic point of the minerals to a lower pH under the influence of anionic flocculant. The presence of the cationic reagent demonstrates the opposite relation (Fig.3). Thus, the fixation of the anionic reagent on minerals results in a greater binding of OH^- ions to the solid phase and decreases the number of basic centers on the surface.

It is known that the polymeric compounds are able to sorb and bind counter-ions [35, 36], including H^+ and OH^-. The increase in the value of the suspension effect of minerals in the case of the anionic flocculant shows that the reagent molecule is ionized and fixed on the particle in unfolded conformation, and functional groups are more available for interaction with ions of the solution compared to the cationic reagent.

The ability of organic polymers to bind fine particles in large aggregates depends on the reagent flow rate to a certain limit. At flocculant concentrations above a certain critical value, on the contrary, they stabilize the suspension, which is manifested in a deterioration of the treatment process from suspended solids. Therefore, the authors have analyzed anionic polyacrylamide flocculants, arranged in a series decreasing the density of charge: AN-956 (high 50 %) > AN-934 (average 30 %) > > AN-913 (low ~12 %) > AN-905 (very low ~5 %). The experiments were performed on the model suspension with a solid content of 13.7 g/l.

The data in Fig.4 show that the reagents with high charge density are characterized by a higher treatment degree, and this result is achieved at low flocculant flow rates. At the same time, these reagents are more sensitive to higher flow rates; the flocculant concentration increase leads to lower cleaning efficiency due to some dispersing effect. The reagents with a lower density of charge show less efficiency in treatment of suspended solids.

An important component in determining the possible use of flocculants for water-preparation is an assessment of their effect on flotation process. The apatite flotation tests were performed on a non-magnetic fraction of magnetite-apatite ore with the following chemical composition, %: P_2O_5 – 8.45; CO_2 – 9.65; MgO – 18.80; SiO_2 – 25.67.

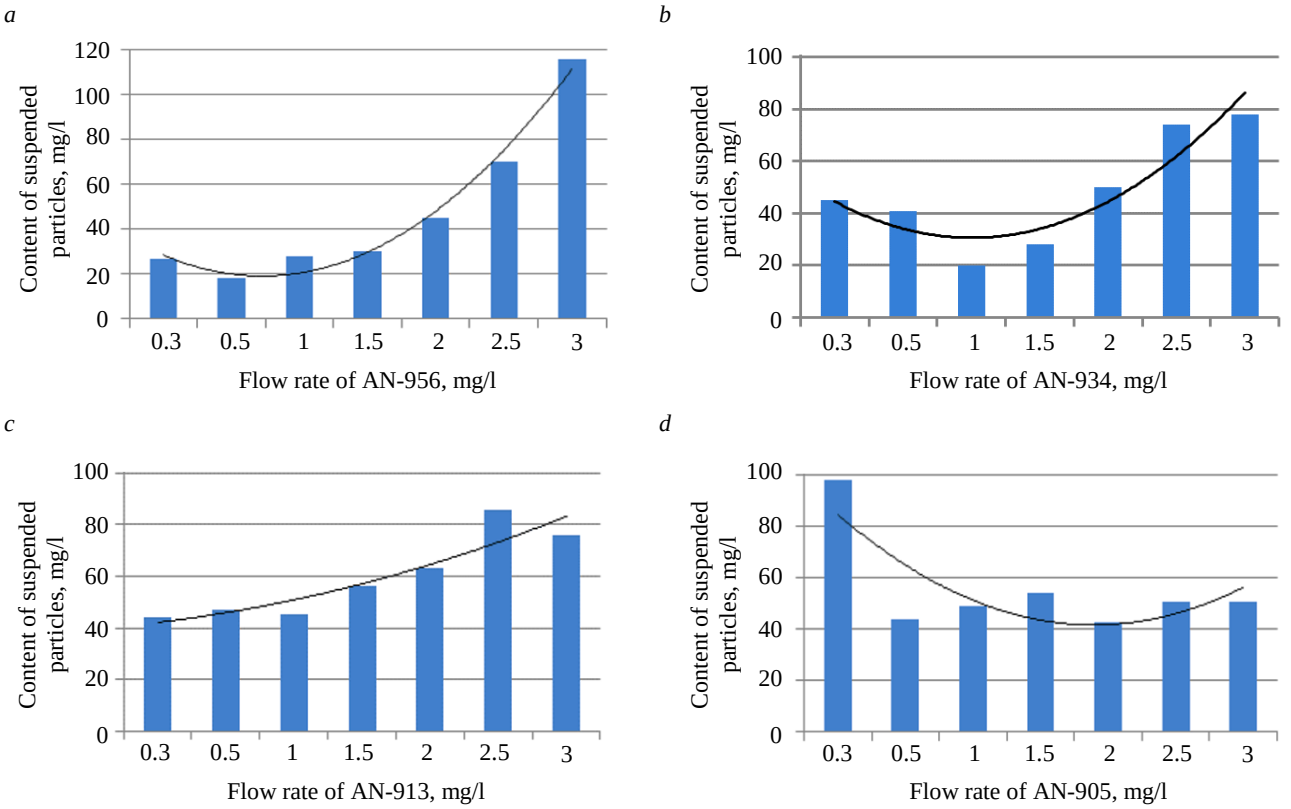

Fig.4. Efficiency of purification from suspended particle by using flocculants: AN-956 (*a*), AN-934 (*b*), AN-913 (*c*), AN-905 (*d*)

Ore was crushed to a grain size of –0.071 mm grade – 36.7 %, +0.16 mm grade – 19.2 %. Flotation was carried out in an open cycle on the recycled water of the dressing plant and on the discharge of thickeners, treated with flocculant AN-956 at a flow rate of 1 mg/l. After flocculant treatment and settling for 30 min, the content of suspended solids in the thickener's discharge was reduced from 13.5 g/l to 40 mg/l.

The flotation parameters were assessed depending on used water at pH = 9.5-9.6 and equal reagents consumption (Na_2CO_3 – 500 g/t, liquid glass (LG) – 200 g/t, tall oil fatty acids (TOFA) – 150 g/t, lupromine – 120 g/t). When using water prepared with flocculant for flotation, the desliming operation was not carried out because of rapid sedimentation of particles. In this case, all fine particles contained in the crushed ore participated in flotation. In average, flotation on the prepared water demonstrates a decrease of extraction into the concentrate of equal quality (37 % P_2O_5) in comparison with the recycled water by 2.9 %. However, increase of TOFA collecting agent consumption allows correcting indicators (Fig.5, *a*).

It is known, that LG added to flotation, on the one hand, plays a role of depressor, and on the other hand, activates flotation at certain rates. The assessment of the impact on the flotation of apatite of various flow rates of the LST was carried out (Fig.5, *b*). As a result, the conclusion was made, that the increase of the liquid glass flow rate also allows receiving the indicators on water prepared with flocculant, close to the indicators received at flotation on recycled water without flocculant.

Polyacrylamide flocculants are produced by various firms, both domestic and foreign. The results allow speaking about the undoubted advantage of anionic reagents for purifying such technological discharges, which can be used when choosing a product from another manufacturer. Thus, the Russian company AlfaKhimProm manufactures products that are similar in their characteristics to

Journal of Mining Institute. 2024. Vol. 265. P. 95-103

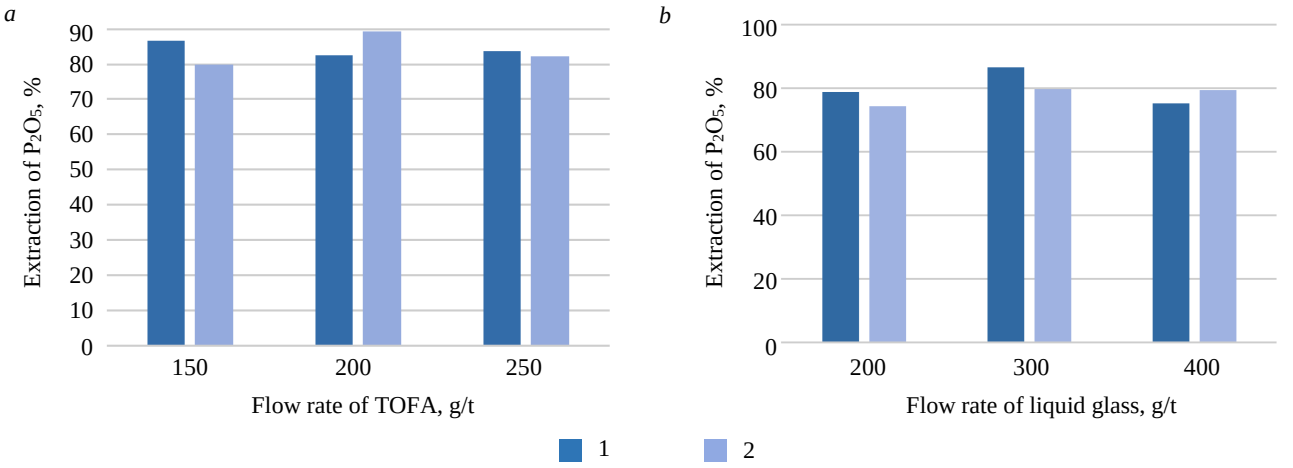

Fig.5. Extraction of P_2O_5 to 37 % concentrate at flotation on different water, depending on TOFA flow rate at pH = 9.6 (*a*) and LG at pH = 9.6 (*b*)

1 – recycled water; 2 – water treated with AN-956

the reagents of the SNF company considered in this study. Difloc 1065 and Difloc 1073 flocculants are analogues of AN-934 and AN-956 reagents.

Conclusion. The interaction of cationic and anionic polyacrylamide flocculants with the surface of apatite and calcite was evaluated. It has been revealed that in the alkaline area of pH~9.0-10.0, typical for suspension of magnetite-apatite ore, the anionic polyacrylamide flocculant acts more efficiently. Hydraulic particle size, which provides the required treatment degree to the residual concentration of suspended solids of 40-50 mg/l, was 1.36-1.56 mm/s at the optimum flow rate of AN-956 SH reagent of 0.75-1 mg/l.

Assessment of the flocculant influence on the flotation process revealed a decrease of P_2O_5 extraction in apatite concentrate of equal quality. However, the adjustment of the TOFA collector and LG depressor flow rates allows levelling the decrease in indicators when using prepared water.

The study shows the possibility of treatment of discharges of the thickeners of apatite flotation feed with the use of anionic polyacrylamide flocculants and their return into the technological process. This will significantly reduce the volume of polluted water currently discharged into the tailings dump.

REFERENCES

1. Kareev N.N., Sukhanov G.S. Methods to optimize solutions for dressing plants and intrafactory water rotation facilities. *Vodoochistka*. 2022. N 1, p. 16-22 (in Russian).

2. Chanturia V.A. Scientific substantiation and development of innovative approaches to integrated mineral processing. *Gornyi Zhurnal.* 2017. N 11, p. 7-13 (in Russian). DOI: 10.17580/gzh.2017.11.01

3. Nevskaya M.A., SeleznevS.G., MasloboevV.A. etal. Geoecological and business problems of mining and mineral processing waste in the Russian Federation. *Herald of Kola Science Centre of the RAS.* 2020. Vol. 12. N 1, p. 11-25 (in Russian). DOI: 10.37614/2307-5228.2020.12.1.002

4. McPhail G.I., Ugaz R., Garcia F. Practical tailings slurry dewatering and tailings management strategies for small and medium mines. Proceedings of the 22nd International Conference on Paste, Thickened and Filtered Tailings. Perth: Australian Centre for Geomechanics, 2019, p. 235-243. DOI: 10.36487/ACG_rep/1910_15_McPhail

5. Witecki K., Polowczyk I., Kowalczuk P.B. Chemistry of wastewater circuits in mineral processing industry – A review. *Journal of Water Process Engineering.* 2022. Vol. 45. N 102509. DOI: 10.1016/j.jwpe.2021.102509

6. Bauman A.V. Concentrating plants thickening circuits and return water systems design problem areas. *ObogashchenieRud.* 2016. N 3, p. 58-62 (in Russian). DOI: 10.17580/or.2016.03.10

7. Shangyong Lin, Runqing Liu, Meirong Wu et al. Minimizing beneficiation wastewater through internal reuse of process water in flotation circuit. *Journal of Cleaner Production.* 2020. Vol. 245. N 118898. DOI: 10.1016/j.jclepro.2019.118898

8. Muzinda I., Schreithofer N. Water quality effects on flotation: Impacts and control of residual xanthates. *Minerals Engineering*. 2018. Vol. 125, p. 34-41. DOI: 10.1016/j.mineng.2018.03.032

9. Jianhua Kang, Chen Chen, Wei Sun et al. A significant improvement of scheelite recovery using recycled flotation wastewater treated by hydrometallurgical waste acid. *Journal of Cleaner Production*. 2017. Vol. 151, p. 419-426. DOI: 10.1016/j.jclepro.2017.03.073

10. Pestriak I., Morozov V., Otchir E. Modelling and development of recycled water conditioning of copper-molybdenum ores processing. *International Journal of Mining Science and Technology*. 2019. Vol. 29. Iss. 2, p. 313-317. DOI: 10.1016/j.ijmst.2018.11.028

11. Jóźwiakowski K., Marzec M., Fiedurek J. et al. Application of H_2O_2 to optimize ammonium removal from domestic wastewater. *Separation and Purification Technology*. 2017. Vol. 173, p. 357-363. DOI: 10.1016/j.seppur.2016.08.047

12. Xiangsong Meng, Khoso S.A., Jiangqiu Wu et al. Efficient COD reduction from sulfide minerals processing wastewater using Fenton process. *Minerals Engineering*. 2019. Vol. 132, p. 110-112. DOI: 10.1016/j.mineng.2018.11.054

13. Khazaie A., Mazarji M., Samali B. et al. A Review on Coagulation/Flocculation in Dewatering of Coal Slurry. *Water*. 2022. Vol. 14. Iss. 6. N 918. DOI: 10.3390/w14060918

14. Zhongfan Zhu, Xiangzhong Xiong, Chaohuang Liang, Ming Zhao. On the flocculation and settling characteristics of low- and high-concentration sediment suspensions: effects of particle concentration and salinity conditions. *Environmental Science and Pollution Research*. 2018. Vol. 25. Iss. 14, p. 14226-14243. DOI: 10.1007/s11356-018-1668-0

15. Shachneva E.Yu. Application of AK-631 Floculants for Floculating Cleaning of Sewage Water of Industrial Enterprises. *Water and Ecology: Problems and Solutions.* 2017. N 4, p. 62-70 (in Russian). DOI: 10.23968/2305-3488.2017.22.4.62-71

16. Jin Park, Young-Soo Han, Sang-Woo Ji. Investigation of Mineral-Processing. Wastewater Recycling Processes: A Pilot Study. *Sustainability*. 2018. Vol. 10. Iss. 9. N 3069. DOI: 10.3390/su10093069

17. Salamatov O.V., Salamatov V.I. To flocculant effect on the kinetics of dewatering and washing processes of red muds from low silicon bauxites in alumina production. *Proceedings of Irkutsk State Technical University.* 2019. Vol. 23. N 2, p. 404-414 (in Russian). DOI: 10.21285/1814-3520-2019-2-404-414

18. Tengfa Long, Xi Liu, Chenbing Ai et al. Treatment technique for wastewater from bauxite flotation and an application for its reuse. *Journal of Cleaner Production*. 2022. Vol. 335. N 130321. DOI: 10.1016/j.jclepro.2021.130321

19. Santos M.A., Capponi F., Ataíde C.H., Barrozo M.A.S. Wastewater treatment using DAF for process water reuse in apatite flotation. *Journal of Cleaner Production*. 2021. Vol. 308. N 127285. DOI: 10.1016/j.jclepro.2021.127285

20. Bahmani-Ghaedi A., Hassanzadeh A., Sam A., Entezari-Zarandi A. The effect of residual flocculants in the circulating water on dewatering of Gol-e-Gohar iron ore. *Minerals Engineering*. 2022. Vol. 179. N 107440. DOI: 10.1016/j.mineng.2022.107440

21. Eskanlou A., Qingqing Huang. Phosphatic waste clay: Origin, composition, physicochemical properties, challenges, values and possible remedies – A review. *Minerals Engineering*. 2021. Vol. 162. N 106745. DOI: 10.1016/j.mineng.2020.106745

22. Shashikant K., Santosh A., Sandeep C. et al. Revisiting Zeta Potential, the Key Feature of Interfacial Phenomena, with Applications and Recent Advancements. *Chemistry Select*. 2022. Vol. 7. Iss. 1. N e202103084, p. 1-40. DOI: 10.1002/slct.202103084

23. Owens C.L., Nash G.R., Hadler K. et al. Apatite enrichment by rare earth elements: A review of the effects of surface properties. *Advances in Colloid and Interface Science*. 2019. Vol. 265, p. 14-28. DOI: 10.1016/j.cis.2019.01.004

24. Fang Zhou, Louxiang Wang, Zhenghe Xu et al. Role of reactive oily bubble in apatite flotation. *Colloids and Surfaces A: Physicochemical and Engineering Aspects*. 2017. Vol. 513, p. 11-19. DOI: 10.1016/j.colsurfa.2016.11.024

25. Mahrouqi D.A., Vinogradov J., Jackson M.D. Zeta potential of artificial and natural calcite in aqueous solution. *Advances in Colloid and Interface Science.* 2017. Vol. 240, p. 60-76. DOI: 10.1016/j.cis.2016.12.006

26. Bonto M., Eftekhari A.A., Nick H.M. Electrokinetic behavior of artificial and natural calcites: A review of experimental measurements and surface complexation models. *Advances in Colloid and Interface Science*. 2022. Vol. 301. N 102600. DOI: 10.1016/j.cis.2022.102600

27. Shuai Li, Leroy P., Heberling F. et al. Influence of surface conductivity on the apparent zeta potential of calcite. *Journal of Colloid and Interface Science*. 2016. Vol. 468, p. 262-275. DOI: 10.1016/j.jcis.2016.01.075

28. Yaoyang Ruan, Zeqiang Zhang, Huihua Luo et al. Effects of Metal Ions on the Flotation of Apatite, Dolomite and Quartz. *Minerals*. 2018. Vol. 8. Iss. 4. N 141. DOI: 10.3390/min8040141

29. Fang Zhou, Qi Liu, Xu Liu et al. Surface Electrical Behaviors of Apatite, Dolomite, Quartz, and Phosphate Ore.*Frontiers in Materials*. 2020. Vol. 7. N 35. DOI: 10.3389/fmats.2020.00035

30. Artemiev A.V., Mitrofanova G.V. The use of anionic flocculant in water treatment for flotation of apatite-nepheline ores. *Vestnik of Murmansk State Technical University.* 2020. Vol. 23. N 2, p. 150-159 (in Russian). DOI: 10.21443/1560-9278-2020-23-2-150-159

31. Wiśniewska M. The temperature effect on the adsorption mechanism of polyacrylamide on the silica surface and its stability. *Applied Surface Science*. 2012. Vol. 258. Iss. 7, p. 3094-3101. DOI: 10.1016/j.apsusc.2011.11.044

32. Garafutdinova M.A., Kolobov Yu.R., Grebtsova E.A., Kolobova E.G. Electrokinetic Characteristics of the Native and Silicon-Substituted Hydroxyapatite. *Belgorod State University Scientific Bulletin.* 2012. N 23 (142), p. 117-121 (in Russian).

33. Skwarek E., Janusz W. The Influence of Carbonate Ions on the Structure of the Electrical Double Layer at the Interface of Hydroxyapatite/Electrolyte Solution. *Materials Science*. 2016. Vol. 22. N 2, p. 174-178. DOI: 10.5755/j01.ms.22.2.7817

34. Nduwa-Mushidi J., Anderson C.G. Surface Chemistry and Flotation Behaviors of Monazite–Apatite–Ilmenite– –Quartz–Rutile–Zircon with Octanohydroxamic Acid. *Journal of Sustainable Metallurgy*. 2017. Vol. 3. Iss. 1, p. 62-72. DOI: 10.1007/s40831-016-0114-0

35. Žuržul N., Ilseng A., Prot V.E. et al. Contribution and Specific Ion Effects in Swelling of Cationic Hydrogels are Additive: Combined High-Resolution Experiments and Finite Element Modeling. *Gels*. 2020. Vol. 6. Iss. 3. N 31. DOI: 10.3390/gels6030031

36. Lipin V.A., Evdokimov A.N., Sustavova T.A., Petrova Yu.A. Synthetic Polyampholyte Hydrogels Based on Various Aliphatic Diamins for Removing Dyes from Aqueous Solutions. *Bulletin of the Tver State University. Series: Chemistry.* 2020. N 4 (42), p. 149-158 (in Russian). DOI: 10.26456/vtchem2020.4.17

***Authors*: Galina V. Mitrofanova,** *Candidate of Engineering Sciences, Leading Researcher, g.mitrofanova@ksc.ru, https://orcid.org/0000-0003-1230-5381* (*Mining Institute of Kola Science Centre of the RAS, Apatity, Russia*), **Elena V. Chernousenko,** *Senior Researcher, https://orcid.org/0000-0003-4266-9418* (*Mining Institute of Kola Science Centre of the RAS, Apatity, Russia*), **Aleksandr V. Artemev,** *Researcher, https://orcid.org/0000-0002-9833-3350* (*Mining Institute of Kola Science Centre of the RAS, Apatity, Russia*), **Yuliya P. Pospelova,** *Leading Industrial Engineer, https://orcid.org/0009-0001-3286-4511* (*Mining Institute of Kola Science Centre of the RAS, Apatity, Russia*), **Natalya A. Smirnova,** *Chief Engineer of Ore Dressing, https://orcid.org/0000-0003-4537-3890* (*AO Kovdorsky GOK, Kovdor, Russia*), **Igor S. Barmin,** *Candidate of Engineering Sciences, Manager of Department, https://orcid.org/0000-0001-7596-5825* (*AO Mineral and Chemical Company EuroChem, Moscow, Russia*).

The authors declare no conflict of interests.

ISSN 2411-3336; e-ISSN 2541-9404

JOURNAL OF MINING INSTITUTE
Zapiski Gornogo instituta
Journal homepage: pmi.spmi.ru

Research article

Isotherm and kinetic adsorption of rice husk particles as a model adsorbent for solving issues in the sustainable gold mining environment from mercury leaching

Asep B. D. NANDIYANTO[1,2]✉, Willy C. NUGRAHA[2], Intan YUSTIA[1], Risti RAGADHITA[1], Meli FIANDINI[1], Hanny MEIRINAWATI[2], Diana R. WULAN[2]
[1] *Universitas Pendidikan Indonesia, Bandung, Indonesia*
[2] *Pusat Riset Lingkungan dan Teknologi Bersih, Badan Riset dan Inovasi Nasional, Jakarta, Indonesia*

***How to cite this article*:** Nandiyanto Asep B. D., Nugraha Willy C., Yustia Intan, Ragadhita Risti, Fiandini Meli, Meirinawati Hanny, Wulan Diana R. Isotherm and kinetic adsorption of rice husk particles as a model adsorbent for solving issues in the sustainable gold mining environment from mercury leaching. Journal of Mining Institute. 2024. Vol. 265, p. 104-120. EDN BZVWDO

Abstract. One of the techniques used in extracting gold in small-scale gold mining is mercury amalgamation. However, the use of mercury presents significant health and environmental hazards, as well as suboptimal efficiency in gold extraction. This study explores the possibility of the use of rice husk as a prototype adsorbent for mercury removal from its leaching in mining environments. To support the analysis, the rice husk adsorbent was characterized by Fourier-transform infrared spectroscopy, scanning electron microscopy, electron dispersive X-ray spectroscopy, atomic absorption spectrophotometers and Brunauer − Emmett − Teller analysis. To investigate the removal of Hg from aqueous solutions, batch adsorption experiments were conducted, and the efficiency was optimized under various parameters such as contact time, rice husk dosage, and initial concentration of mercury. Kinetic and isotherm investigations were also carried out to gain a better understanding of the adsorption properties. The kinetic adsorption was analyzed using the pseudo-first-order and pseudo-second-order. Furthermore, the isotherm adsorption was analyzed using ten adsorption isotherm models (i.e., Langmuir, Freundlich, Temkin, Dubinin – Radushkevich, Flory – Huggins, Fowler – Guggenheim, Hill – de Boer, Jovanovic, Harkin – Jura, and Halsey). The amount of mercury absorption increased with increasing contact time, adsorbent mass, and initial concentration of mercury. The pseudo-second-order kinetic model is the best model that can be applied to describe the adsorption process. Analysis of the adsorption results obtained shows that the adsorption pattern is explained through the formation of a monolayer without any lateral interaction between the adsorbate and adsorbent. In addition, the formation of multilayers due to inhomogeneous pore distribution also occurs which causes a pore filling mechanism. We found that the isotherm phenomena are near the Jovanovic models with the maximum adsorption capacity) of rice husk found to be 107.299 mg/g. As a result, rice husk could be a promising option for wastewater treatment due to its fast and efficient removal capacity, as well as its affordability and eco-friendliness. The predicted thermodynamic studies using the Flory – Huggins isotherm model show that the adsorption process is endothermic, spontaneous, and physisorption. The impact shows that the utilization of rice husk can be used and fit for the current issues in the sustainable development goals (SDGs).

Keywords: gold mining; rice husk; particle technology; mercury leaching; adsorption; SDGs

Received: 07.07.2023 ***Accepted: 20.09.2023*** ***Online: 29.11.2023*** ***Published: 29.02.2024***

Introduction. Community mining has been conducted throughout Indonesia for hundreds of years and is currently experiencing a surge in activity. Indonesia is one of the world's top ten gold producers (www.ceicdata.com/; www.gold.org/goldhub/data/historical-mine-production). It is home to many artisanal and small-scale gold mining (ASGM) firms and operational facilities. ASGM is defined by the Ministry of Environment and Forestry (KLHK) as gold mining undertaken by individual miners or small firms with little capital and production. In Indonesia, there are two

Journal of Mining Institute. 2024. Vol. 265. P. 104-120

sorts of ASGM: those that are licensed and those that are not. The majority of ASGM activities in Indonesia continue to operate illegally since they lack government authorization. Illegal ASGM is detrimental to the state since they are unregistered, do not pay royalties, cannot be regulated, and contribute to environmental damage and adverse health effects caused by mercury usage.

The majority of ASGMs in Indonesia extract gold using a traditional method involving amalgamation with mercury [1]. The mercury and gold precipitate form a mercury-gold amalgam, which is then heated at high temperatures. Finally, the gold is extracted via evaporation by only distilling 10-40 % of the contained gold [2]. Miners are often only able to extract a limited amount of gold with high amounts of mercury (more than 1000 ton of mercury are released into the environment every year) using conventional processing techniques [1], causing environmental and health issues not just for the active miners involved in the processing, but also for the non-mining neighboring communities. Hg emissions from the ASGM industry account for 37 % of all anthropogenic Hg released into the environment, making ASGM the second most prominent source of Hg pollution in Indonesia after coal burning [3, 4]. The pollution of groundwater with mercury poses a severe hazard to humans, animals, and the ecosystem on a global scale. According to the Environmental Protection Agency and the World Health Organization, the maximum permitted limits for total mercury and CH_3Hg are 5.0 and 1.6 g/kg per week, respectively. In addition, Government Regulation of Indonesia N 82 of 2001 states that the amount of mercury found in water is 0.001 ppm. This is backed by the Indonesian Ministry of Health no 907/Menkes/SK/VII/2002, specifying that the highest concentration of permissible mercury is 0.001 mg/l. Therefore, removing mercury from water that has been contaminated is of utmost significance, and this issue requires further focus and consideration. The United Nations for Minamata Convention on Mercury, signed by 128 nations in 2013, was one of the most significant acts against Hg use. Its primary mission is to restrict and reduce the use of mercury, and finally eliminate it by 2030.

Several chemical and physical processes have been applied for Hg removals from wastewater, such as ion exchange [5], coagulation/coprecipitation [6], adsorption, reverse osmosis, membrane separation, liquid-liquid extraction, precipitation, electrodeposition [7, 8]. However, from an engineering standpoint, the technique's cost and efficiency should be compromised. Nonetheless, adsorption-based technologies can remove heavy metal ions due to their simplicity, reusability of the adsorbent, environmental friendliness, ease of operation, and cost-effectiveness [9, 10].

Rice husk is the protective outer covering of rice grains. It is an abundant agricultural waste of rice milling and has various uses and applications. A summary regarding the recent potential application of rice husk and its modification is summarized in Table 1.

Some researchers have already investigated the potential of rice husk sorbents to remove heavy metals from water [11-14]. However, the studies developed using a complex and expensive method due to modifying the rice husk. Hence, this study used raw rice husk as a sorbent material to determine rice husks' adsorption properties so that ASGM small-scale miners can use this method directly in processing mercury waste from gold mining.

This work studied the ability of raw rice husk to remove Hg^{2+} under various competing situations such as initial concentration, contact time, and dosage. In addition, to comprehend the interactions between multiple sorbates and the effect of complexing ligands on the dynamics of Hg, the efficacy of raw rice husk in removing Hg^{2+} from wastewater was investigated using adsorption kinetics and isotherm models. Then, experimental and theoretical research was conducted to elucidate the mercury adsorption mechanism on rice husk and the removal capability of this adsorbent.

Table 1

Recent potential applications and modifications of rice husk

Material	Application	Modification	Results	Source
Rice husk, KOH, HCl, HNO_3	Heavy metals removal from the aqueous phase	Pyrolysis; activated with KOH	Adsorbent	[11]
Rice husk, bamboo sawdust	Heavy metals removal from the aqueous phase	Carbonized at 400 °C for 2 h; mixed with bamboo sawdust ash (BSD-RHA)	Adsorbent	[12]
Rice husk, Na_2CO_3, NaOH, CH_2Cl_2, CH_3NH_2, CH_3COOH, $K_2Cr_2O_7$	Heavy metals removal from the aqueous phase	Na_2CO_3 modified	Adsorbent	[13]
Coal, rice husk, Pb $(NO_3)_2$, $NaNO_3$, HNO_3, NaOH	Heavy metals removal from the aqueous phase	Biofermentation	Adsorbent	[14]
Rice husk, sodium hydroxide solid, tartaric acid, distilled water	Medium of Growth Single Crystal $CaC_4H_4O_64H_2O$	Pyrolysis; filtrate of sodium silicate was reacted with tartrate acid ($C_4H_6O_6$)	Metasilicate gel	[15]
Rice husk ash, soil, bentonite clay	The ceramic membrane in microbial fuel cells	Rice husk ash is mixed with soil	Ceramic membrane	[16]
HNO_3, H_2SO_4, and H_2O_2	Hydrogen production	Ultrasound-assisted inorganic treatment	Catalyst	[17]
Rice husk, polyester resin, methyl ethyl ketone peroxide catalyst, palm fronds	Filler and resin	Dried in the sun for 3 days; rice husk mixed with palm fronds ratio with: 90/10; 70/30; 50/50; 30/70	Composite Based brake pad	[18]
Rice husk, potassium-di-hydrogen phosphate, and potassium nitrate	Soil amendment	Microwave-assisted; pyrolysis	Adsorbent	[19]
NaOH, HCl, sodium aluminate, ethanol, $LiCl·H_2O$, $LaCl_3·7H_2O$ and $CeCl_3·7H_2O$	Carbon capture	Hydrothermal method; impregnated zeolite	Porous material adsorbent nax rare earth La or Ce	[20]
Rice husk, wheat flour, soybean oil, water, and dry yeast	Thermal insulation	Carbonization; fermentation	Carbon foams	[21]
Rice husk, NaOH – 98, HCl – 37, KBr – 98, Mg – 98, EtOH – 98, hydrofluoric acid – 40, lithium hexafluorophosphate ($LiPF_6$ – 99), ethylene carbonate – 99, diethyl carbonate – 99, ethyl methyl carbonate – 98 wt.%; acetylene black, polyacrylic acid, and *n*-methyl-2-pyrrolidone	Scavenger agent	Calcination-KBr	Silicon nanoparticles	[22]
Rice husk and KOH	Carbon-based energy storage ϕnd conversion devices	Calcination and chemical activation-KOH	Graphene	[23]
Rice husk ash and cetyltrimethylammonium bromide	Photocatalyst in the degradation of methylene blue	Sol-gel	Silica-Tin nanotubes	[24]
Rice husk ash, HCl, Ethyl methanesulfonate (EMS)	Cement replacement	Acid modification; mixed with EMS	Cement mortar	[25]

Journal of Mining Institute. 2024. Vol. 265. P. 104-120

End of Table 1

Material	Application	Modification	Results	Source
Rice husk ash, NaOH, HCl, ethanol, carbon dioxide, odorless kerosene, Span 80, Tween 80, sodium dodecyl sulfate, and water	Drug delivery	Sol-gel	Silica aerogel microparticles	[26]
Rice husk	Biofertilizer production	Batch anaerobic digestion	Biogas and digestates	[27]
Rice husk, amoxicillin trihydrate, Cerium(III) nitrate, hexahydrate, Humic acid, sodium dodecyl sulfate, and Diclofenac sodium	Antibiotic removal	Hydrothermal method	Ceo2@sio ad-sorbent	[28]
Rice husk, KOH, and NaOH	Supercapacitor electrode	Chemical activation with dual activation agents	Activated carbons	[29]
Rice husk, HCl, HNO_3, H_2SO_4, and H_3PO_4	Production of silica	Acid leaching method	Mesoporous silica and the magnetic mesoporous silica	[30]

Methods. The materials in this study consisted of raw rice husk (obtained from Farm Shop, Bandung, Indonesia), standard stock solution of mercury to prepare the mercury solution (1000±2 mg/l, Merck (Germany)), nitric acid (EMSURE), and ultrapure water (18.2 MOm/cm, Milli-Q system). In this study, all chemicals used were analytical reagent class.

Raw rice husk was prepared by saw-milled, and sieved to get the desired particle sizes (Yayasan Bumi Publikasi Nusantara, Indonesia) with a hole size of 74, 125, 250, 500, 1000, and 2000 μm, and then preserved at room temperature. The rice husk is placed into a conventional batch-type blade-milling apparatus. Typically, this milling apparatus includes a milling tube made of SAN material with a diameter of 16.6 and a length of 13.5 cm, along with stainless steel blades measuring 6 cm. The milling procedure was conducted at room temperature for 10 min.

Nicolet 6700 Fourier-transform infrared (FTIR) spectrometer, manufactured by Thermo Fisher Scientific Co., USA, was used to determine the functional groups on rice husk at wavelength range 400-4000 cm^{-1}. Additionally, a field emission scanning electron microscope spectroscopy JSM-6360 was utilized to characterize the surface morphology of the adsorbent. Then, the specific surface area and average pore size of the adsorbent were measured using the Brunauer − Emmett − Teller (BET) method at a temperature of 77 K using Quantachrome NOVA 2200E, China. Finally, to utilize the chemical elements in the solution used the atomic absorption Spectrophotometers Agilent 200 Series AA manufactured by Agilent Technologies.

Adsorption Procedure. To conduct the batch adsorption experiments, Hg(II) solutions were prepared by using an analytical grade reagent ($Hg(NO_3)_2$) and using ultrapure water as the solvent. The pH of the prepared solutions was adjusted using 0.05 M solutions of HNO_3 to ensure the presence of metal ions based on the pH-induced chemical speciation.

Various experimental tests were conducted to assess the effectiveness of rice husk in removing Hg from 100 ml aqueous solutions. To determine the most favorable adsorption condition, several factors were investigated, such as contact time (ranging from 30 to 180 min), adsorbent dose (0.02 to 0.2 g), and initial concentration (5 to 20 mg/l). Subsequently, the optimal values, which yielded the highest percentage of removal, were obtained. Then, using the obtained optimum values, kinetics, and isothermal tests were conducted using different contact times.

The mixture solution was shaken at 200 rpm using a magnetic stirrer-SP88850105 manufactured by Thermo Fisher Scientific. After adsorption, the solution was filtered using a 0.45 μm nylon membrane filter to remove adsorbent that might interfere with mercury determination. The residual concentration of Hg(II) was determined at the end of each experiment using Agilent 200 Series AA atomic absorption spectrophotometers (AAS). Then, the adsorption capacity and $Hg_{removal}$ were calculated:

$$Q_e = \frac{(C_0 - C_t)V}{m}; \quad (1)$$

$$Hg_{removal} = \frac{(C_0 - C_e)}{C_0} \cdot 100\,\%, \quad (2)$$

where C_0 and C_e are the initial and residual concentrations of metal ions, mg/l; C_t denotes the analyte concentration at time t, mg/l; V is the volume of solution used, l; m is the adsorbent mass, g.

Kinetic Procedure. The kinetic parameters are necessary to anticipate the rate at which Hg(II) is removed from aqueous solutions, to comprehend the adsorption mechanism, and to define the step that determines the adsorption [31]. In this work, the data obtained from the effect of contact time on the quantity of Hg(II) adsorbed at the surface of rice husk were used in Lagergren pseudo-first-order [32]

$$\ln(Q_e - Q_t) = \ln Q_e - k_1 t,$$

and pseudo-second-order [31, 32] have been used

$$\frac{t}{Q_t} = \frac{1}{k_2 Q_e^2} + \frac{t}{Q_e},$$

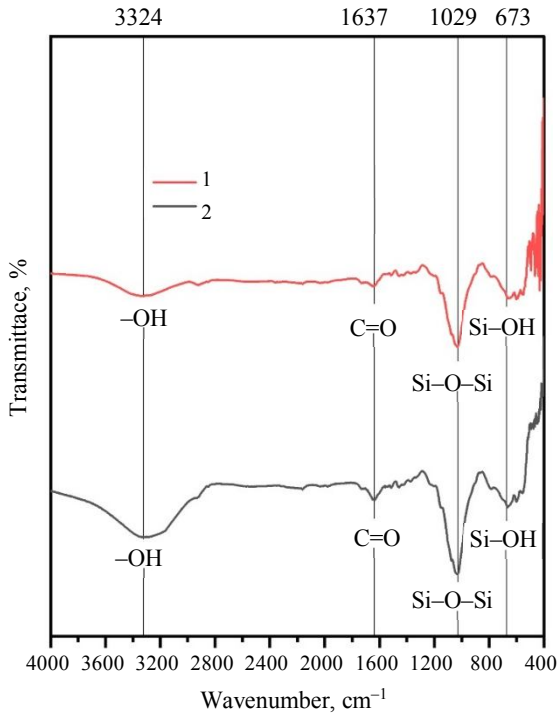

Fig.1. FTIR spectroscopy of rice husk before and after adsorption

1 – after adsorption; 2 – before adsorption

where Q_e is the adsorption capacity at equilibrium, mg Hg/g rice husk; Q_t is the adsorption capacity at time t; mg Hg/g rice husk; k_1 is the rate constant of the Lagergren first-order kinetic model, min^{-1}; t is the time of the experiment, min; k_2 is the rate constant of the pseudo-second-order kinetic model, min^{-1}.

Adsorption kinetics are typically thought to be heavily dependent on the physicochemical qualities of the used substance (adsorbent) [18].

Results and discussion. FTIR analysis of the raw rice husk is conducted after and before adsorption (Fig.1). The band is located at 3282 cm^{-1} be attributed to (–OH) related to the stretching of cellulose and lignin of rice husk before the adsorption process [33-35]. Other peaks in the spectrum of rice husk before Hg^{2+} adsorption, which is the band at around 2918 cm^{-1}, assigned to C–H in CH and C–H_2, the bands at 2160-1978.65 cm^{-1} due to C≡C group, and the band around 1650.69-1514.86 cm^{-1} attributed to the C=O (ester and carboxylic group from hemicellulose) and C=C aromatic ring from lignin, while 1455.11-1330.89 cm^{-1} contributed to –COOH [36].

Journal of Mining Institute. 2024. Vol. 265. P. 104-120

The sharp vibration peak around 1073.75 and 1032.02 cm^{-1} can be correlated to organic silicone (Si–O–Si), while the peak of transmittance appears in the wave number area 788.75-557.36 cm^{-1} is a typical characteristic of amorphous silica (Si–OH) spectrum [35].

Upon analysis of the FTIR spectra after the adsorption of mercury (Fig.1), a discernible peak at 432.08 cm^{-1} was observed. This peak can be attributed to the vibration of oxygen that is perpendicular to the Si–O–Si planes [35]. In addition, rice husk spectra after the removal of Hg^{2+} have revealed a noticeable decrease in the wavelength peaks at 2160.82, 2034.84, 1978.65, and 1073.75 cm^{-1} due to the oxygenated functional groups. The outcomes obtained from the adsorbent materials produced from agroindustry waste bear resemblance to those published in the literature [31-37]. Earlier research has indicated that mercury compounds display characteristic FTIR signals at 3500, 1750, and 600 cm^{-1} [38]. In the case of the rice husk material, the band is noticed at 3500 cm^{-1}, which corresponds to the –OH and Hg interaction. These results are in line with Guo et al. [36] that phenolic hydroxyl groups on the adsorbent surface undergo complexation reactions with Hg^{2+}.

In addition, the SEM image of the rice husk adsorbent is shown in Fig.2. The SEM analysis of the surface of the adsorbent revealed an irregular layer of silica and natural resins in the rice husk structure. The SEM image of rice husk before adsorption (Fig.2, *a*, *b*) reveals the presence of surface pores, which serve as the ideal location for capturing Hg^{2+} molecules from aqueous solutions [39]. Following the adsorption process, the SEM image of rice husk displays the successful capture of Hg^{2+} molecules within its surface pores (Fig.2, *c*, *d*). This was accomplished through a process of diffusion and migration with Hg^{2+} molecules moving from the aqueous solution to the rice husk surface and eventually filling the available pores [40]. The physical adsorption of Hg^{2+} at the surface of rice husk was likely due to mechanical adhesion through electrostatic force, which is consistent with previous research [39-41].

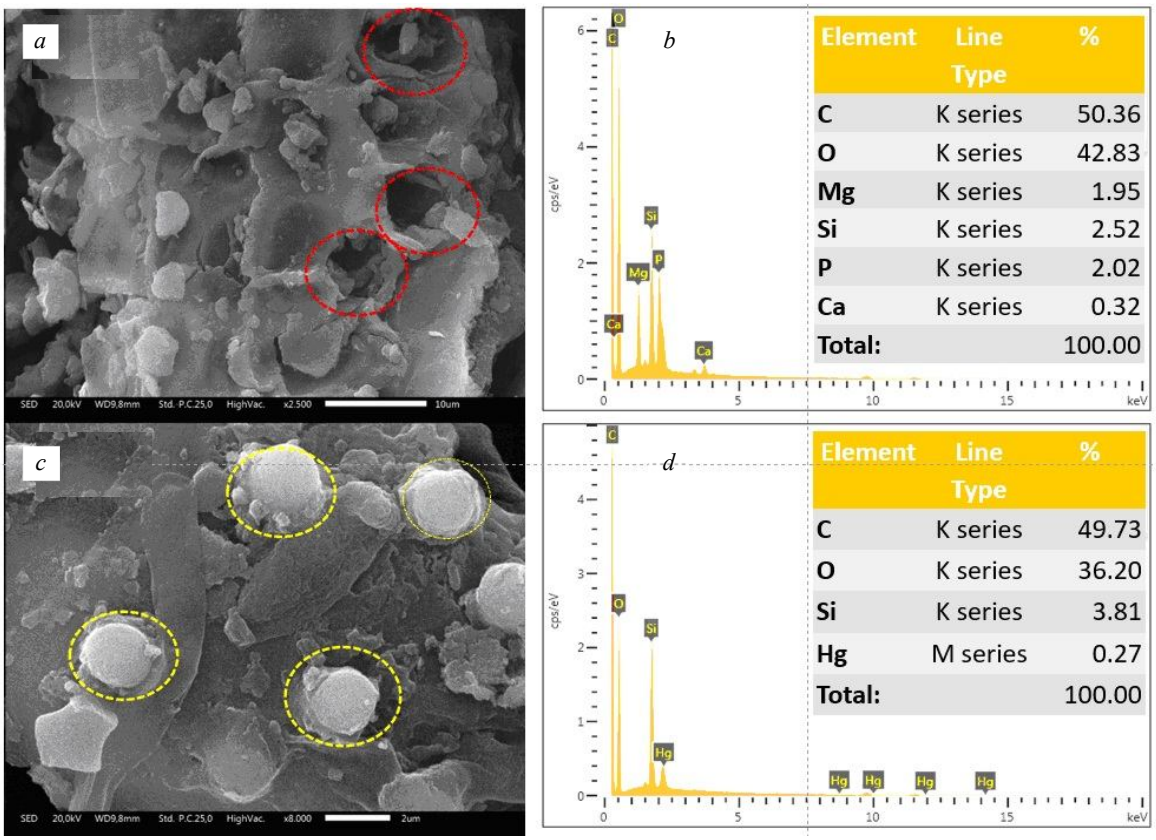

Fig.2. SEM micrograph of rice hush before adsorption (*a*) and Hg-loaded-rice hush after adsorption (*c*); EDX spectrum of rice hush before adsorption (*b*) and Hg-loaded-rice hush after adsorption (*d*)

Figures 2, *b*, *d* display the EDX spectra of the rice husk. Figure 2, *c* shows that the predominant elements in the prepared rice husk are carbon and oxygen, indicating the presence of oxygen functional groups on the carbon surface. Additionally, there are small quantities of silica, calcium, magnesium, and phosphorus from the source. Nevertheless, following the occurrence of the adsorption procedure (Fig.2, *d*), there was a decrease in the cations present in rice husk.

Also, the appearance of Hg peaks in the EDX was found, confirming that Hg fills the pore structure. This outcome suggests that an ion exchange mechanism might have taken place [36].

Nitrogen adsorption isotherms utilizing Quantachrome NOVA 2200E and the BET formalism were employed to determine the isotherm shape, specific surface area, and pore volume of the adsorbent. The outcome of the nitrogen adsorption isotherm test displayed a Type IV pattern as classified by IUPAC and H3 hysteresis (Fig.3, *a*). This suggests a mesoporous substance with a continuous facile pore connection. Additionally, it has a limited multilayer structure that matches the complete filling of the capillaries [42-45]. The BET-specific surface area of the adsorbent was 173.782 m^2/g, and the BJH pore distribution method showed a pore size diameter of about 1.714 nm and a pore volume of about 0.307 cm^3/g (Fig.3, *b*). These results outperformed previous studies [37, 46]. Our findings demonstrate the outstanding quality of the adsorbent.

Adsorption study. Several factors were identified:

• Effect of contact time. To design effective batch adsorption experiments, it is crucial to assess the impact of contact time required to reach equilibrium. Therefore, the effect of contact time on the adsorption of Hg was studied at various adsorbent dosages within 30-180 min. The results indicated that, at room temperature, the mercury concentrations in water decreased within the first 30 min (Fig.4, *a*). The fast initial rates of adsorption are due to the presence of a significant number of binding sites for adsorption at the beginning, followed by saturation and equilibrium [47]. In addition, the presence of major functional groups such as oxygenated aromatic rings in the rice husk structure confirmed by FTIR spectra images (see Fig.1) allows for Hg-π conjugation and stacking interactions with Hg ions [48]. As shown by SEM images (see Fig.2), the presence of cellulose and lignin can also play a role in the removal of heavy metal mercury [37]. The optimal contact time for Hg removal was found to be around two hours for all rice husk dosages, as the percentage removal did not significantly increase beyond this duration. This information is depicted in Fig.4, *a*.

• Effect of adsorbent dosage. Typically, adsorbents have a limited number of active sites which means that their dosage must be optimized. To treat a 100 ml aqueous solution with an initial concentration of 200 μg/l of mercury within 120 min under ambient conditions, various rice husk dosages were evaluated. Figure 4, *b* shows that the percentage of Hg removal increased with increasing adsorbent dosage, reaching 78.8 % at a dosage of 0.2 g. This is because the abundance of active sites on the surface of the adsorbent increases with dosage, allowing it to bind more mercury [32, 37, 47, 48]. However, increasing the adsorbent dosage also decreased the amount of metal ions adsorbed due to the reduced concentration of adsorbate in the solution. Thus, the driving force for the adsorption process was also reduced. As a result, not all available adsorption sites can be occupied (unsaturated), leading to a decrease in adsorption capacity [49, 50].

• Effect of Hg initial concentrations. In Fig.4, *c*, *d*, the impact of the initial concentrations of the adsorbate (Hg) on the efficiency of the adsorption process using 0.05 g of rice husk is presented. The study investigated the impact of different levels of Hg concentration on adsorption properties using a mercury solution as a model for wastewater. The initial concentrations of the mercury solution were set at 5, 10, and 20 mg/l. This concentration is taken based on the actual concentration of mercury in the contaminated wastewater (river) in Indonesia. Based on the data presented in Fig.4, *c*, *d*, it is evident that as the initial concentration of mercury increases, both the adsorption capacity and removal of mercury also increase. When the mercury concentration is higher (20 mg/l), the maximum removal efficiency is approximately 93.1 %, with an adsorption capacity of around 37.3 mg/g.

Journal of Mining Institute. 2024. Vol. 265. P. 104-120

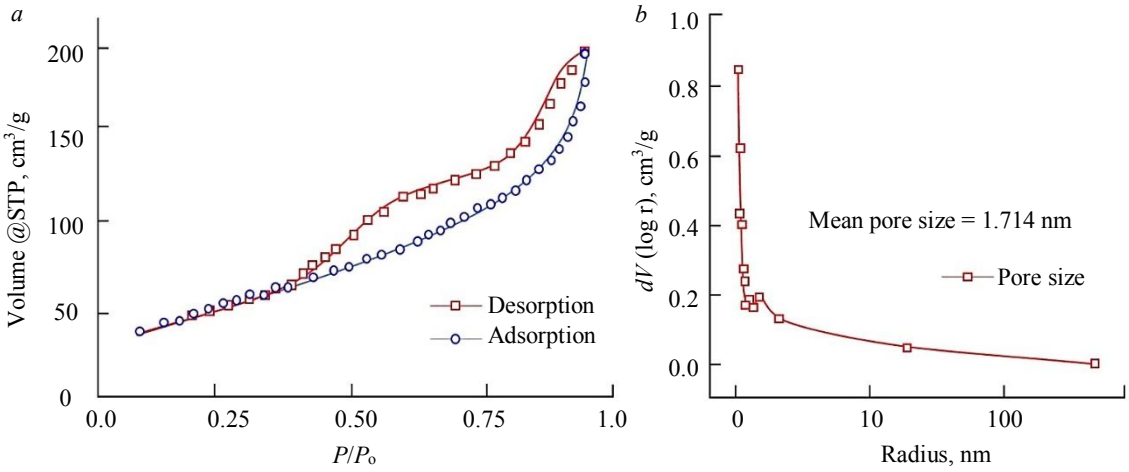

Fig.3. The characteristic Type IV (IUPAC classification) N_2 adsorption isotherm of rice husk adsorbent (*a*); pore distribution of rice husk adsorbent (*b*)

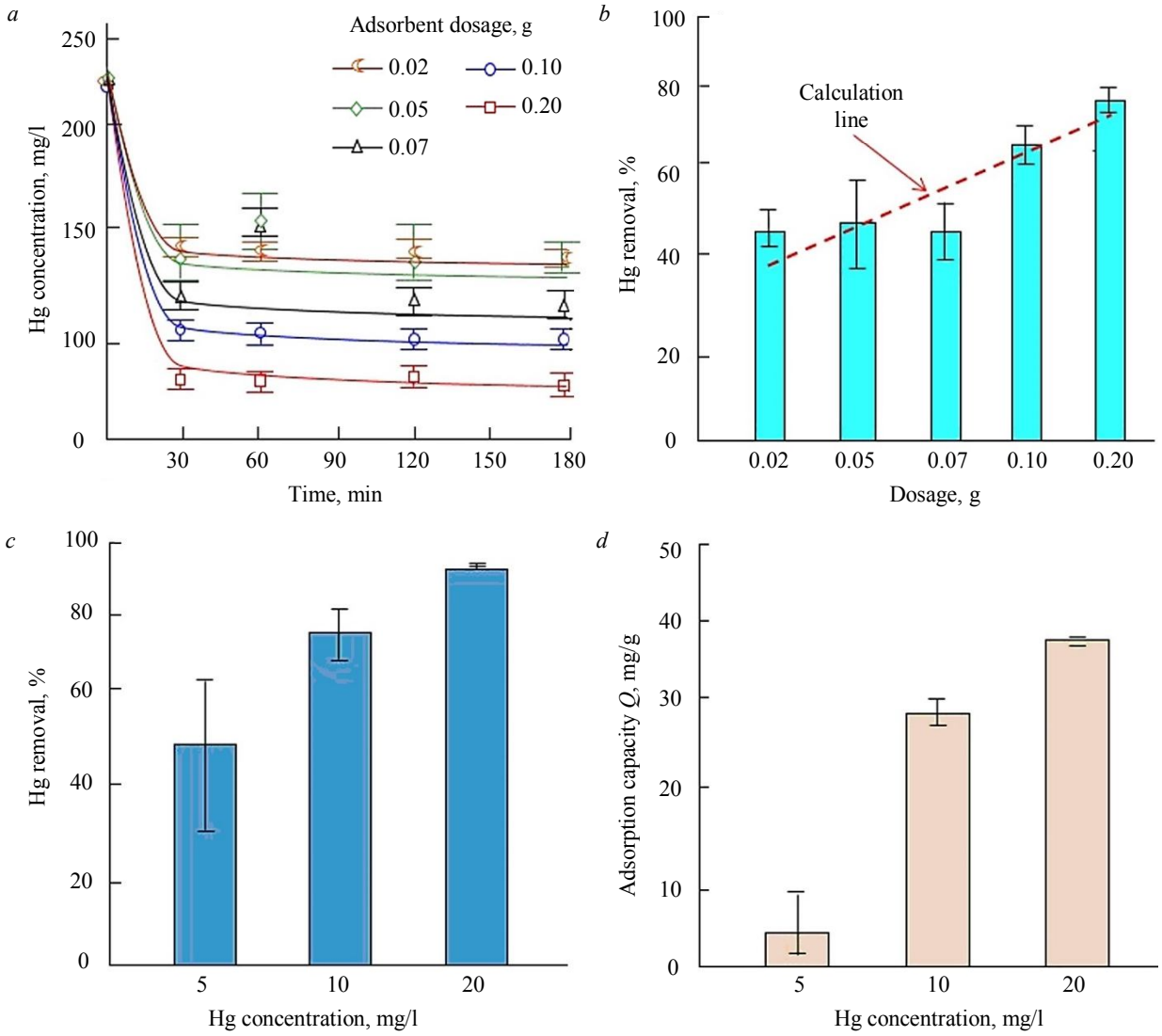

Fig.4. The concentrations of Hg in water as a function of time (*a*); the adsorption performance of rice husk at various adsorbent dosages (*b*); effect of initial mercury concentration on removal (*c*) and adsorbent capacity (*d*)

In comparison, for lower mercury concentrations of 10 and 5 mg/l, the removal efficiencies are approximately 78 and 52 % respectively, with adsorption capacities of approximately 28.6 and 5.2 mg/g after 120 min of contact time. This is because a high initial concentration provides the necessary driving force to overcome adsorbate mass transfer processes between the aqueous and solid phases [47, 51, 52].

Adsorption kinetics. To understand the rate and mechanism of Hg(II) removal from an aqueous solution, knowledge of its kinetic parameters is required, hence a kinetics study was conducted. By graphing kinetic equations (1) and (2) against experimental data, linear connections were formed. Thus, kinetic parameters were determined and provided in Table 2. The effectiveness of the kinetic models was evaluated by the coefficient of determination values R^2. The calculated kinetic constants demonstrated that the pseudo-second-order kinetic model had the highest correlation coefficient R^2 and provided the best fit. Additionally, the results showed that the Hg-uptake obtained through pseudo-first-order kinetic was significantly lower than the experimental value ($Q_{e(cal)} \ll Q_{e(exp)}$). In contrast, the calculated Hg-uptake in pseudo-second-order kinetic was much closer to the experimental value. This finding was consistent with previous research conducted [31, 32]. These results confirm that the best-fit kinetic model is the pseudo-second-order kinetic model and that Hg adsorption on rice husk is most likely through the chemisorption mechanism [8, 53].

Table 2

Kinetic parameters for the mercury adsorption over rice husk

Kinetic information	Parameter	Value
Experimental data	$Q_{e(exp)}$, mg/g	90.63
Lagergren-first-order model	$Q_{e(cal)}$, mg/g	37.07
	k_1, min^{-1}	0.0244
	R^2	0.57238
Pseudo-second-order model	$Q_{e(cal)}$, mg/g	92.65
	k_2, g/mg·min	0.0016
	R^2	0.98859

Adsorption Isotherms. To study the adsorption mechanism, a brief overview of ten adsorption isotherms and the computation for obtaining curves from data fitting results are shown in Table 3. In prior work [54], the calculation of the isotherm adsorption is given in detail.

Table 3

A summary of ten adsorption isotherm models

Isotherm model	Theoretical consideration	Plot (x-axis vs y-axis)	Parameter
Langmuir	The model assumes monolayer adsorption, in which adsorbates are adsorbed to a finite number of identical and equivalent definite localized sites with no lateral interaction, $\frac{1}{Q_e} = \frac{1}{Q_{\max}^{k_L}} \frac{1}{C_e} + \frac{1}{Q_{\max}}$, where k_L represents the Langmuir constant; Q_e represents the number of molecules adsorbed at equilibrium, mg/g; and $Q_{\max}$ represents the adsorption capacity, mg/g. The adsorption factor $R_L = \frac{1}{1 + k_L C_e}$,	$\frac{1}{C_e}$ vs $\frac{1}{Q_e}$	$\frac{1}{Q_{\max}} = intercept$; $k_L = \frac{1}{Q_{\max} slope}$

Journal of Mining Institute. 2024. Vol. 265. P. 104-120

Table 3 continued

Isotherm model	Theoretical consideration	Plot (x-axis vs y-axis)	Parameter
	where R_L describes unfavorable adsorption ($R_L > 1$), linear adsorption (influenced by the number and concentration of adsorbed molecules) ($R_L = 1$), too strong adsorption or irreversible adsorption ($R_L = 0$), and favorable adsorption or absent of desorption ($0 < R_L < 1$)		
Freundlich	The model represents multilayer adsorption on heterogeneous surfaces produced by variances in adsorption heat, $$\log Q_e = \log k_F + \frac{1}{n}\log C_e,$$ where k_F is the Freundlich constant used to determine the adsorption capacity and C_e is the adsorbate concentration at equilibrium, mg/l; n is the degree of nonlinearity and the adsorption strength, following chemisorption $n < 1$ or physisorption $n > 1$; linear adsorption (a concentration-independent partition between two phases $n = 1$; normal adsorption $n^{-1} < 1$; cooperative adsorption $n^{-1} > 1$; favorable adsorption or no desorption $1 < n^{-1} < 0$; and adsorption on a heterogeneous surface $0 < n^{-1} < 1$; the n closer to zero indicates increasing heterogeneous of adsorbent surface	$\ln C_e$ vs $\ln Q_e$	$\ln k_F = intercept$; $\frac{1}{n} = slope$
Temkin	The model covers interactions between adsorbent and adsorbate if the heat of adsorption of molecules reduces linearly in each adsorbed layer and excludes high and low concentration values, $$Q_e = B_\mathrm{T} \ln A_\mathrm{T} + B_\mathrm{T} \ln C_e,$$ where A_T is the Temkin model's equilibrium constant. B_T is the Temkin constant, which determines whether adsorption is physical ($B_\mathrm{T} < 8$ kJ) or chemical ($B_\mathrm{T} > 8$ kJ)	$\ln C_e$ vs Q_e	$B = slope$; $B_\mathrm{T} \ln A_\mathrm{T} = intercept$; $B_\mathrm{T} = \frac{RT}{B}$
Dubinin – Radushkevich	The model is based on the adsorption of gases by porous adsorbents and the pore-filling mechanism $$\ln Q_e = \ln Q_s - \left(\beta\varepsilon^2\right)Q_e,$$ where Q_s is the saturation capacity, mg/g; β is the Dubinin – Radushkevich constant correlating to the average free adsorption energy; ε is the Polanyi potential associated with equilibrium conditions, in which the value correlates to adsorption energy $$\varepsilon = RT \ln\left[1 + \frac{1}{C_e}\right];$$ $$\mathrm{E} = \frac{1}{\sqrt{2\beta}}, \quad (3)$$ E relates to the physical ($E < 8$ kJ) or chemical ($E > 8$ kJ) adsorption	ε^2 vs $\ln Q_e$	$\beta = k_{DR} = slope$; $E = \frac{1}{\sqrt{2k_{DR}}}$
Flory – Huggins	The model is based on the adsorption of gases by porous adsorbents and the pore-filling mechanism $$\log\frac{\theta}{C_e} = \log k_{FH} + n\log\log\left(1-\theta\right),$$ where $\theta = (C_e/C_0)$ is the degree of monolayer coverage; k_FH are the equilibrium constant for the Flory – Huggins model, which correlates to the Gibbs free energy $$\Delta G° = -RT\ln k_{FH}, \quad (4)$$ $\Delta G°$ can describe the spontaneous and temperature-dependent nature of the adsorption when it is negative	$\log\left(\frac{\theta}{C_0}\right)$ vs $\log\left(1-\theta\right)$	$n_{FH} = slope$; $k_{FH} = intercept$; $\Delta G° = RT\ln\left(k_{FH}\right)$; $\theta = 1 - \left(\frac{C_e}{C_0}\right)$

End of Table 3

Isotherm model	Theoretical consideration	Plot (*x*-axis vs *y*-axis)	Parameter
Fowler – Guggenheim	The model is based on the adsorption of gases by porous adsorbents and the pore-filling mechanism $k_{FG}C_e = \frac{\theta}{1-\theta}\exp\left(\frac{2\theta W}{RT}\right)$, where W is the interaction energy between the adsorbed molecules, kJ/mol; informing processes under exothermic ($W > 0$), endothermic ($W < 0$), or no interaction between adsorbed molecules ($W = 0$)	θ vs $\ln\left[\frac{C_e(1-\theta)}{\theta}\right]$	$W = slope$; $-\ln k_{FG} = intercept$; $\alpha(slope) = \frac{2W\theta}{RT}$; $\theta = 1-\left(\frac{C_e}{C_0}\right)$
Hill – de Boer	The model is based on the adsorption of gases by porous adsorbents and the pore-filling mechanism $k_1C_e = \frac{\theta}{1-\theta}\exp\left(\frac{\theta}{1-\theta}-\frac{k_2\theta}{RT}\right)$, where k_1 (l/mg) and k_2 (kJ/mol) are the contact energy constants for the adsorbed molecules; k_2 informing exothermic with intermolecular adsorption ($k_2 > 0$); endothermic with repulsion ($k_2 < 0$); or no interaction between adsorbates ($k_2 = 0$)	θ vs $\ln\left[\frac{C_e(1-\theta)}{\theta}\right]-\frac{\theta}{1-\theta}$	$-\ln k_1 = intercept$; $\alpha(slope) = \frac{k_2\theta}{RT}$; $\theta = 1-\left(\frac{C_e}{C_0}\right)$
Jovanovic	The model evaluates adsorption on a heterogeneous surface where a multilayer forms during the adsorption $\ln Q_e = \ln Q_{\max} - k_J C_e$, where Q_e is the amount of adsorbate in the adsorbent at equilibrium, mg/g; $Q_{\max}$ is the maximum absorption of the adsorbate; k_J is the Jovanovic constant. At a high concentration of adsorbate, the preceding equation becomes the Langmuir isotherm	C_e vs $\ln Q_e$	$k_J = slope$; $\ln q_{\max} = intercept$
Harkin – Jura	The model evaluates adsorption on a heterogeneous surface where a multilayer is formed during the adsorption $\frac{1}{Q_e^2} = \frac{B_{HJ}}{A_{HJ}} - \left(\frac{1}{A}\right)\log C_e$, where B_{HJ} is related to the adsorbent's specific surface area, and A_{HJ} is the Harkin – Jura constant	$\log C_e$ vs $\frac{1}{Q_e^2}$	$A_H = \frac{1}{slope}$; $\frac{B_H}{A_H} = intercept$
Halsey	The model evaluates the multilayer adsorption system far from the surface. Similarly, to the Freundlich model, the Halsey model applies to multilayer adsorption and heterogeneous surfaces with non-uniformly distributed adsorption heat $Q_e = \frac{1}{n_H}\ln k_H - \left(\frac{1}{n_H}\right)\ln C_e$, where k_H and n are Halsey's constants	$\ln C_e$ vs $\ln Q_e$	$\frac{1}{n} = slope$; $\frac{1}{n}\ln k_H = intercept$

Note: *slope* – slope factor; *intercept* – linear part of approximation equation.

The analysis of adsorption isotherms is crucial for determining how the adsorbent surface interacts with adsorbate molecules. The interaction between the metal ion and the adsorbent material, as well as the adsorption capacity of the material, can be determined using isothermal models. The ten isotherm adsorption models were used to match experimental mercury adsorption onto rice husk. The rice husk parameters derived from the ten studied models are presented

Journal of Mining Institute. 2024. Vol. 265. P. 104-120

in Table 4. The experimental values are reconstructed based on the charting of several parameters (using plot equations in Table 3). Then, linear correlation coefficients R^2 are employed to demonstrate the compatibility of correlation curves between experimental data and linearized isotherm models.

The Langmuir factor R_L defines whether the adsorption is favourable. In this instance, values fall in the range $R_L > 1$, indicating that the adsorption process is unfavourable, with maximum adsorption capacities Q_m of 68.140 mg/g. In addition, the degree of adsorbate-adsorbent interaction k_L indicates a weak contact between the adsorbate molecule and the adsorbent surface due to its small value ($k_L = –0.0016$) [54]. Meanwhile, the correlation coefficient value for Langmuir is $R^2 = 0.934$, indicating that the adsorption process employing the present adsorbent can produce a monolayer structure. Nevertheless, the negative value of k_L shows that the data do not fit Langmuir.

The fitting performance of Freundlich is shown in Table 4. The slope derived via data fitting in the form of a gradient is n^{-1}, while the intercept is $\ln k_F$. Analysis of the n value of the rice husk adsorbent revealed a negative value with correlations of $n < 1$ and $n^{-1} < 1$, indicating that adsorption happens chemically via a typical process. In addition, the high value of R^2 0.984 implies that the adsorption profile of rice husk in the adsorption process has a multilayer structure. The adsorption capacities denoted by k_F have a value of 0.788 mg/g.

Temkin's approach was founded on the fact that adsorption decreases the heat of adsorption of all molecules in a linear way [55]. The determined values of its parameters (B_T and A_T) are given in Table 4. The B_T and A_T have small values ($2.02 \cdot 10^{-56}$ and –1.229, respectively), which means less affinity between the adsorbent and adsorbate molecules due to their physical interactions. The correlation coefficient of Temkin ($R^2 = 0.989$) suggests that there is multilayer adsorption with a homogenous distribution between the adsorbate and the surface of the adsorbent. However, because the parameter value is small, this model cannot be used.

Dubinin – Radushkevich's $R^2 = 0.892$ value is the lowest in this study. This value indicates the existence of micropore size in adsorbent surfaces with multilayer structures. The examination of the E value in this model was < 8 KJ/mol proving that adsorption is a physical process [55, 56].

Table 4

Isotherm parameters for the adsorption of Hg (II) on rice husk

Isotherm models	Parameter	Value
Langmuir	Q_{max}	68.140
	R_L	1.1
	k_L	–0.0016
	R^2	0.934
Freundlich	$L_n\, k_F$	5.308
	k_F	0.788
	$1/n_F$	–0.238
	n_F	–4.200
	R^2	0.984
Temkin	B	–19.954
	B_T	–1.229
	A_T	2.02E-56
	R^2	0.989
Dubinin – Radushkevich	β	0.276
	E	1.345
	R^2	0.892
Flory – Huggins	n_{FH}	–4.131
	$\log k_{FH}$	–10.702
	k_{FH}	1.98575E-11
	$\Delta G°$	–604.486
	θ	0.815
	R^2	0.984
Fowler – Guggenheim	W	–11.622
	$-\ln k_{FG}$	11.590
	k_{FG}	9.2573E-06
	α(*slope*)	–0.772
	θ	0.815
	R^2	0.992
Hill – de Boer	k_1	1.47763E-13
	$-\ln k_1$	29.543
	k_2	–1187.105
	α(*slope*)	–39.427
	θ	0.815
	R^2	0.969
Jovanovic	k_1	–0.006
	$\ln Q_{max}$	4.676
	Q_{max}	107.299
	R^2	0.999
Harkin – Jura	A_H	6369.008
	B_H/A_H	–0.00011
	R^2	0.970
Halsey	$1/n_H$	–0.238
	n_H	–4.200
	$\ln k_H$	5.308
	k_H	201.925
	R^2	0.9836

The thermodynamic feasibility and spontaneity of an adsorption process can be predicted using the Flory – Huggins isotherm, which describes the degree of surface covering properties of the adsorbate on the adsorbent [54, 57]. The estimated n_{FH} in this study (Table 4) suggests that the adsorbate occupies more than one active adsorbent zone generating a multilayer structure [54], this is supported by the R^2 value as well $R^2 = 0.984$, indicating that no molecule was bonded to any adsorption site on the rice husk adsorbent [57]. As a result, the Flory – Huggins model cannot predict the adsorption of Hg(II) onto rice husk due to small value parameters and is therefore disregarded. The negative ΔG value demonstrates that the adsorption of Hg(II) onto rice husk is thermodynamically spontaneous and validates the process's viability.

The Fowler – Guggenheim isotherm model takes into consideration the lateral interaction of adsorbate adsorption onto adsorbent [54, 58]. The $R^2 = 0.992$ value of this model shows a good fit. On the contrary, the parameters (W and k_{FG}) show relatively small values. A negative value of W indicates that the interaction occurs repulsively between the adsorbed molecules. Meanwhile, a very small k_{FG} value indicates the weak interaction between the adsorbate and adsorbent due to the Van der Waals bond. Hence, this model is not suitable.

The Hill – de Boer model describes the mobile adsorption and lateral interaction of molecules that have been adsorbed [59]. Using equation (3), Hill – de Boer model adsorption parameters were determined. As seen in Table 4, the regression coefficient R^2 had a value of 0.969 informing of the multilayer structure in the adsorption process. Meanwhile, a negative k_2 value represents repulsion. When there is repulsion among the adsorbed species, the apparent affinity decreases with loading [59]. A modest value of k_1 indicates poor adsorbent-adsorbate interaction because the active site is ineffective in carrying out the adsorption process. Consequently, this model is inappropriate.

The adsorption parameters of the Harkin – Jura model were obtained using equation (2). The R^2 value of 0.970 is the result of a multilayer adsorption process on the surface of an adsorbent with heterogeneous pore distribution.

The coefficient correlation value of Halsey exhibits a good adsorption system ($R^2 = 0.984$), indicating the nature of the adsorbent is heterogeneous with a multilayer structure. These results are in line with the Harkin – Jura model.

The Jovanovic isotherm model has few mechanical contacts between desorbing and adsorbing molecules [54, 58, 59]. The Jovanovic parameters exhibit the most satisfactory value (Table 4), with the correlation coefficient R^2 (0.999) being near unity. In addition, this model has a high maximum capacity (107.299 mg/g). This indicates that the experiment consists of adsorption with a moving and localized monolayer and no lateral contact*.

The R^2 value analysis reveals that the rice husk adsorption system is compatible with various models, excluding Dubinin – Radushkevich. The Langmuir, Freundlich, Temkin, Flory – Huggins, Hill – de Boer, Harkin –Jura, Fowler – Guggenheim, and Halsey models all showed a good fit, but the Jovanovic model provided the best results. This suggests that the adsorption process forms a monolayer structure without any lateral interactions between the adsorbate and adsorbent. Additionally, the rice husk adsorbent is believed to have a multilayer adsorption process due to its heterogeneous pore distribution, which leads to pore filling. Thus, the bond between the adsorbate and adsorbent is characterized by weak chemical and physical interaction (Fig.5). The screening and arrangement are based on an understanding of the coefficient of correlation R^2. In descending order: Jovanovic, Fowler – Guggenheim, Temkin, Flory – Huggins, Freundlich, Halsey, Harkin – Jura, Hill – de Boer, Langmuir, Dubinin – Radushkevich. Although the model is in good agreement with the experimental results, analyses based on Table 4, physicochemical characterization, and kinetic adsorption show that the adsorption profile follows physical

* Saroyda J.R.V., Cruz R.Y.S., Antonio R.J.C. et al. PUPAIM: a collection of physical and chemical adsorption isotherm models. Version 0.2. 0. 2020. URL: https://CRAN. R-project. org/package= PUPAIM (accessed 25.10.2023).

Journal of Mining Institute. 2024. Vol. 265. P. 104-120

and chemical adsorption with multilayer adsorption. In addition, the adsorption process occurs endothermically and spontaneously by forming a multilayer surface with a pore-filling system and mutually repulsive intermolecular interactions.

Proposed adsorption mechanism. Concerning the characterization findings and in conjunction with the reported adsorption results, we propose the following adsorption mechanism. While morphology does indeed factor into the adsorption process, the presence of functional groups on the surface of rice husk is equally significant. There exists a noticeable relationship between Hg^{2+} and the oxygenated functional groups due to their interaction with available pairs of electrons on oxygen and the presence of aromatic structures (π-type bonds) in the materials. This results in them having polar characteristics with partially negative charges and a strong tendency to attract positively charged mercury ions. Thus, the rice husk adsorbent materials predominantly undergo Hg^{2+} adsorption through three processes: electrostatic interaction between the negatively charged density at the surface of rice husk and Hg^{2+} metal cation; formation of $(–COO)_2Hg$ and $(–O)_2Hg$ complexes due to the interaction between Hg^{2+} and conjugate bases of carboxylic and phenolic groups (–COO– and –O–), and interactions between Hg^{2+} and π (or ion exchange), Hg–Cπ electrons from the graphene structure (C=C) and C=O present in the materials. These findings agree with previous studies reported [31, 32, 36, 60]. However, the complexation reaction between –OH groups and Hg^{2+} is the most dominant [36]. The mechanism that happens during the adsorption process is complexation.

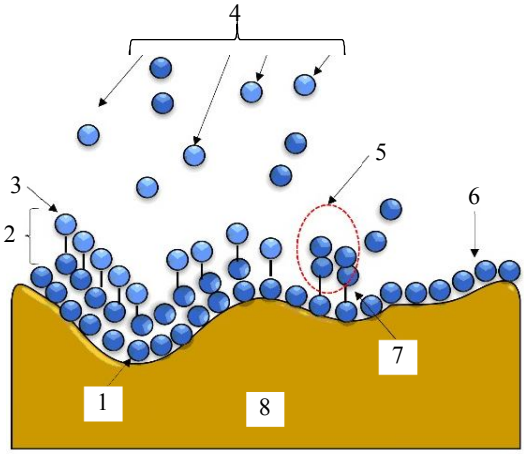

Multilayer, repulsive, mixing adsorption, spontaneous, porefilling

Fig.5. Rice husk adsorbent system prediction model

1 – week physical interaction; 2 – multilayer; 3 – physical adsorption; 4 – Free adsorbate; 5 – the interaction between free molecules and adsorbed molecules; 6 – monolayer; 7 – weak chemical interaction; 8 – adsorbent surface

In addition, this study is preliminary for pilot and large scale process. Some issues must be more detailed analyzed, including the analysis in the formation of Hg into the pore structure, including the final pore structure. Further information relating to surface area (using BET and XRD) and molecule interaction (using FTIR) must be also done and compared to current literature [61-63].

Conclusions. The study successfully removed Hg(II) from realistic environmental concentration levels using rice husk in batch mode. The results showed that the ability to adsorb mercury increased with longer contact time, higher adsorbent dosage, and initial concentration.

The adsorption kinetics followed a pseudo-second-order model, and the Jovanovic model accurately described the adsorption isotherm with a maximum adsorption capacity of 107.299 mg Hg/g rice husk, suggesting a combination of physical and chemical interactions. The study also found that adsorbent materials with low surface area and high oxygenated functional groups are effective in removing Hg(II) because functional groups on the material's surface attract Hg(II) through various interactions. The rice husk material was found to be highly effective in removing Hg(II) from aqueous solutions. In conclusion, this study demonstrates the effectiveness of using rice husk for removing Hg(II) from water.

This study, we summarize the additional advantages of the use of rice husk as follows:

• rice husk is largely available, especially in rice-producing countries; since it is a by-product of rice production, the cost of rice husk is free;

• rice husk is categorized as one of the agricultural wastes, making the use of rice husk as an adsorbent material to solve the current issues in disposal and waste management;

• utilization of rice husk for wastewater treatment needs a simple procedure, requiring less processing steps;

• rice husk has an excellent pore structure, making it have a good adsorption capacity; further development and treatment of this rice husk can increase its selectivity;

• this method is also possible for being applied in the adsorption of heavy metal ions;

• the utilization of rice husk for adsorbing heavy metal can achieve significant results in realizing sustainable development goals (SDGs).

REFERENCES

1. Meutia A.A., Lumowa R., Sakakibara M. Indonesian Artisanal and Small-Scale Gold Mining – A Narrative Literature Review. *International Journal of Environmental Research and Public Health*. 2022. Vol. 19. Iss. 7. N 3955. DOI: 10.3390/ijerph19073955

2. Teknologi Pengolahan Emas Pada Pertambangan Emas Skala Kecil di Indonesia. Buku 4. Ed. by B.D.Krisnayanti, A.S.Probiyantono. Jakarta: UNDP Indonesia, 2020, p. 17. URL: https://goldismia.org/sites/default/files/2020-12/View%20Buku%204%20%281%29.pdf (accessed 25.10.2023).

3. Manzila A.N., Moyo T., Petersen J. A Study on the Applicability of Agitated Cyanide Leaching and Thiosulphate Leaching for Gold Extraction in Artisanal and Small-Scale Gold Mining. *Minerals*. 2022. Vol. 12. Iss. 10. N 1291. DOI: 10.3390/min12101291

4. Green C.S., Lewis P.J., Wozniak J.R. et al. A comparison of factors affecting the small-scale distribution of mercury from artisanal small-scale gold mining in a Zimbabwean stream system. *The Science of The Total Environment*. 2019. Vol. 647, p. 400-410. DOI: 10.1016/j.scitotenv.2018.07.418

5. Bashir A., Malik L.A., Ahad S. et al. Removal of heavy metal ions from aqueous system by ion-exchange and biosorption methods. *Environmental Chemistry Letters*. 2019. Vol. 17. Iss. 2, p. 729-754. DOI: 10.1007/s10311-018-00828-y

6. Karwowska B., Sperczyńska E. Organic Matter and Heavy Metal Ions Removal from Surface Water in Processes of Oxidation with Ozone, UV Irradiation, Coagulation and Adsorption. *Water*. 2022. Vol. 14. Iss. 22. N 3763. DOI: 10.3390/w14223763

7. Hua Kang, Xu Xueliu, Luo Zhiping et al. Effective Removal of Mercury Ions in Aqueous Solutions: A Review. *Current Nanoscience*. 2020. Vol. 16. Iss. 3, p. 363-375. DOI: 10.2174/1573413715666190112110659

8. Ying Li, Yangxian Liu, Wei Yang et al. Adsorption of elemental mercury in flue gas using biomass porous carbons modified by microwave/hydrogen peroxide. *Fuel*. 2021. Vol. 291. N 120152. DOI: 10.1016/j.fuel.2021.120152

9. Saleh T.A., Tuzen M., Sarı A. Polyamide magnetic palygorskite for the simultaneous removal of Hg(II) and methyl mercury; with factorial design analysis. *Journal of Environmental Management*. 2018. Vol. 211. N 323-333. DOI: 10.1016/j.jenvman.2018.01.050

10. Xiaodong Yang, Yongshan Wan, Yulin Zheng et al. Surface functional groups of carbon-based adsorbents and their roles in the removal of heavy metals from aqueous solutions: A critical review. *Chemical Engineering Journal*. 2019. Vol. 366, p. 608-621. DOI: 10.1016/j.cej.2019.02.119

11. Sanka P.M. Application of rice and corn husk biochar for removal of heavy metal ions from industrial wastewater: Dissertation. NM-AIST. Aruska, Tanzania, 2020, p. 51. URL: https://dspace.nm-aist.ac.tz/handle/20.500.12479/968 (accessed 25.10.2023).

12. Kwikima M.M., Chebude Y., Meshesha B.T. Kinetics, adsorption isotherms, thermodynamics, and desorption studies of cadmium removal from aqueous solutions using bamboo sawdust/rice husk biochar. *Biomass Conversion and Biorefinery*. 2023. Vol. 13. Iss. 11, p. 9367-9379. DOI: 10.1007/s13399-022-03472-3

13. Lala M.A., Ntamu T.E., Adesina O.A. et al. Adsorption of hexavalent chromium from aqueous solution using cationic modified rice husk: Parametric optimization *via* Taguchi design approach. *Scientific African*. 2023. Vol. 20. N e01633. DOI: 10.1016/j.sciaf.2023.e01633

14. Peng Zhao, Zhanbin Huang, Ping Wang, An Wang. Comparative study on high-efficiency Pb(II) removal from aqueous solutions using coal and rice husk based humic acids. *Journal of Molecular Liquids*. 2023. Vol. 369. N 120875. DOI: 10.1016/j.molliq.2022.120875

15. Putri S.E., Hasri, Side S. et al. Synthesis of Metasilicate Gel from Rice Husk and Its Application as Medium of Growth Single Crystal Calcium Tartrate Tetrahydrate (CaC4H4O6.4H2O). Joint Conference on Green Engineering Technology & Applied Computing, 4-5 February 2019, Bangkok, Thailand. IOP Conference Series: Materials Science and Engineering, 2019. Vol. 551. N 012112. DOI: 10.1088/1757-899X/551/1/012112

16. Raychaudhuri A., Behera M. Ceramic membrane modified with rice husk ash for application in microbial fuel cells. *Electrochimica Acta*. 2020. Vol. 363. N 137261. DOI: 10.1016/j.electacta.2020.137261

17. Ababaii M.A., Gilani N., Pasikhani J.V. Modification of Rice Husk with Ultrasound-Assisted Inorganic Treatment and Its Application for Catalytic Hydrogen Production. *BioEnergy Research*. 2023, p. 11. DOI: 10.1007/s12155-023-10643-1

18. Nandiyanto A.B.D., Ragadhita R., Girsang G.C.S. et al. Effect of palm fronds and rice husk composition ratio on the mechanical properties of composite-based brake pad. *Moroccan Journal of Chemistry*. 2022. Vol. 10. N 4, p. 663-677. DOI: 10.48317/IMIST.PRSM/morjchem-v10i4.34291

19. Shukla N., Sahoo D., Remya N. Biochar from microwave pyrolysis of rice husk for tertiary wastewater treatment and soil nourishment. *Journal of Cleaner Production*. 2019. Vol. 235, p. 1073-1079. DOI: 10.1016/j.jclepro.2019.07.042

20. Yisong Wang, He Jia, Peng Chen et al. Synthesis of La and Ce modified X zeolite from rice husk ash for carbon dioxide capture. *Journal of Materials Research and Technology*. 2020. Vol. 9. Iss. 3, p. 4368-4378. DOI: 10.1016/j.jmrt.2020.02.061

21. Lazzari L.K., Zimmermann M.V.G., Perondi D. et al. Production of Carbon Foams from Rice Husk. *Materials Research*. 2019. Vol. 22. Suppl. 1. N e20190427. DOI: 10.1590/1980-5373-MR-2019-0427

22. Daulay A., Andriayani, Marpongahtun, Gea S. Synthesis and application of silicon nanoparticles prepared from rice husk for lithium-ion batteries. *Case Studies in Chemical and Environmental Engineering*. 2022. Vol. 6. N 100256. DOI: 10.1016/j.cscee.2022.100256

23. Hiroyuki Muramatsu, Yoong Ahm Kim, Kap-Seung Yang et al. Rice Husk-Derived Graphene with Nano-Sized Domains and Clean Edges. *Small*. 2014. Vol. 10. Iss. 14, p. 2766-2770. DOI: 10.1002/smll.201400017

24. Adam F., Appaturi J.N., Thankappan R., Nawi M.A.M. Silica–tin nanotubes prepared from rice husk ash by sol–gel method: Characterization and its photocatalytic activity. *Applied Surface Science*. 2010. Vol. 257. Iss. 3, p. 811-816. DOI: 10.1016/j.apsusc.2010.07.070

25. Khan K., Ullah M.F., Shahzada K. et al. Effective use of micro-silica extracted from rice husk ash for the production of high-performance and sustainable cement mortar. *Construction and Building Materials*. 2020. Vol. 258. N 119589. DOI: 10.1016/j.conbuildmat.2020.119589

26. Rajanna S.K., Kumar D., Vinjamur M., Mukhopadhyay M. Silica Aerogel Microparticles from Rice Husk Ash for Drug Delivery. *Industrial & Engineering Chemistry Research*. 2015. Vol. 54. Iss. 3, p. 949-956. DOI: 10.1021/ie503867p

27. Olugbemide A.D., Likozar B. Assessment of Liquid and Solid Digestates from Anaerobic Digestion of Rice Husk as Potential Biofertilizer and Nutrient Source for Microalgae Cultivation. *Processes*. 2022. Vol. 10. Iss. 5. N 1007. DOI: 10.3390/pr10051007

28. Tien-Duc Pham, Thi-Mai-Anh Le, Thi-My-Quynh Pham et al. Synthesis and Characterization of Novel Hybridized CeO_2@SiO_2 Nanoparticles Based on Rice Husk and Their Application in Antibiotic Removal. *Langmuir*. 2021. Vol. 37. Iss. 9, p. 2963-2973. DOI: 10.1021/acs.langmuir.0c03632

29. Khu Le Van, Thuy Luong Thi Thu. Preparation of Pore-Size Controllable Activated Carbon from Rice Husk Using Dual Activating Agent and Its Application in Supercapacitor. *Journal of Chemistry*. 2019. Vol. 2019. N 4329609. DOI: 10.1155/2019/4329609

30. Kamari S., Ghorbani F. Extraction of highly pure silica from rice husk as an agricultural by-product and its application in the production of magnetic mesoporous silica MCM–41. *Biomass Conversion and Biorefinery*. 2021. Vol. 11. Iss. 6, p. 3001-3009. DOI: 10.1007/s13399-020-00637-w

31. Giraldo S., Robles I., Ramirez A. et al. Mercury removal from wastewater using agroindustrial waste adsorbents. *SN Applied Sciences*. 2020. Vol. 2. Iss. 6. N 1029. DOI: 10.1007/s42452-020-2736-x

32. Al-Yaari M., Saleh T.A. Mercury Removal from Water Using a Novel Composite of Polyacrylate-Modified Carbon. *ACS omega*. 2022. Vol. 7. Iss. 17, p. 14820-14831. DOI: 10.1021/acsomega.2c00274

33. Nandiyanto A.B.D., Oktiani R., Ragadhita R. How to read and interpret FTIR spectroscope of organic material. *Indonesian Journal of Science and Technology*. 2019. Vol. 4. N 1, p. 97-118. DOI: 10.17509/ijost.v4i1.15806

34. Tariq M., Durrani A.I., Farooq U., Tariq M. Efficacy of spent black tea for the removal of nitrobenzene from aqueous media. *Journal of Environmental Management*. 2018. Vol. 223, p. 771-778. DOI: 10.1016/j.jenvman.2018.06.080

35. Rengga W.D.P., Sediawan W.B., Imani N.A.C. et al. Adsorption Studies of Rice Husk-Based Silica/Carbon Composite. *EKSAKTA: Journal of Sciences and Data Analysis*. 2020. Vol. 1. Iss. 2, p. 98-104. DOI: 10.20885/EKSAKTA.vol1.iss2.art1

36. Xiaoli Guo, Menghong Li, Aijv Liu et al. Adsorption Mechanisms and Characteristics of Hg^{2+} Removal by Different Fractions of Biochar. *Water*. 2020. Vol. 12. Iss. 8. N 2105. DOI: 10.3390/w12082105

37. Tokay B., Akpınar I. A comparative study of heavy metals removal using agricultural waste biosorbents. *Bioresource Technology Reports*. 2021. Vol. 15. N 100719. DOI: 10.1016/j.biteb.2021.100719

38. Gutierrez I.R. Evaluación de los cambios en los parámetros fisicoquímicos del suelo procedente de San Joaquín, Querétaro; después del tratamiento electrocinético para la remoción de mercurio: Tesis doctoral. Mexico: Centro de Investigación y Desarrollo Tecnológico en Electroquímica, 2015. URL: https://www.lareferencia.info/vufind/Record/MX_e7e02b542beacd21972161cd720c5b76 (accessed 25.10.2023).

39. Songnan Li. Combustion synthesis of porous MgO and its adsorption properties. *International Journal of Industrial Chemistry*. 2019. Vol. 10. Iss. 1, p. 89-96. DOI: 10.1007/s40090-019-0174-7

40. Jabar J.M., Odusote Y.A., Alabi K.A., Ahmed I.B. Kinetics and mechanisms of congo-red dye removal from aqueous solution using activated *Moringa oleifera* seed coat as adsorbent. *Applied Water Science*. 2020. Vol. 10. Iss. 6. N 136. DOI: 10.1007/s13201-020-01221-3

41. Boulaiche W., Hamdi B., Trari M. Removal of heavy metals by chitin: equilibrium, kinetic and thermodynamic studies. *Applied Water Science*. 2019. Vol. 9. Iss. 2. N 39. DOI: 10.1007/s13201-019-0926-8

42. Metz P.C. Total Scattering Analysis of Disordered Nanosheet Materials: A Thesis Submitted To The Faculty Of Alfred University In Partial Fulfillment Of The Requirements For The Degree Of Doctor Of Philosophy In Ceramic Engineering. New York: Alfred University, 2017. 157 p. URL: https://s3-eu-west-1.amazonaws.com/pfigshare-u-files/8231207/42017_Metz_Thesis_Final.pdf (accessed 25.10.2023).

43. Yurdakal S., Garlisi C., Özcan L. et al. Chapter 4 – (Photo)catalyst Characterization Techniques: Adsorption Isotherms and BET, SEM, FTIR, UV–Vis, Photoluminescence, and Electrochemical Characterizations. Heterogeneous Photocatalysis. Elsevier, 2019, p. 87-152. DOI: 10.1016/B978-0-444-64015-4.00004-3

44. Thommes M., Kaneko K., Neimark A.V. et al. Physisorption of gases, with special reference to the evaluation of surface area and pore size distribution (IUPAC Technical Report). *Pure Applied Chemistry*. 2015. Vol. 87. N 9-10, p. 1051-1069. DOI: 10.15.15/pac-2014-1117

45. Kumar K.V., Gadipelli S., Wood B. et al. Characterization of the adsorption site energies and heterogeneous surfaces of porous materials. *Journal of Materials Chemistry A*. 2019. Vol. 7. Iss. 17, p. 10104-10137. DOI: 10.1039/C9TA00287A

46. Kolar P., Jin H. Baseline characterization data for raw rice husk. *Data in brief*. 2019. Vol. 25. N 104219. DOI: 10.1016/j.dib.2019.104219

47. Ahmaruzzaman M., Gupta V.K. Rice Husk and Its Ash as Low-Cost Adsorbents in Water and Wastewater Treatment. *Industrial & Engineering Chemistry Research*. 2011. Vol. 50. Iss. 24, p. 13589-13613. DOI: 10.1021/ie201477c

48. Al-Yaari M., Saleh T.A., Saber O. Removal of mercury from polluted water by a novel composite of polymer carbon nanofiber: kinetic, isotherm, and thermodynamic studies. *RSC Advances*. 2021. Vol. 11. Iss. 1, p. 380-389. DOI: 10.1039/D0RA08882J

49. Zili Tang, Hui Wu, Qingbo Wen, Liming Hu. Effect of Adsorbent Dosage to Adsorbate Concentration Ratio on the Adsorption of Cd(II) on Coal Gangue. Proceedings of the 8th International Congress on Environmental Geotechnics, 28 October – 1 November 2018, Hangzhou, China. Springer, 2019. Vol. 1, p. 428-435. DOI: 10.1007/978-981-13-2221-1_45

50. Akpomie K.G., Eluke L.O., Ajiwe V.I.E., Alisa C.O. Attenuation Kinetics and Desorption Performance of *artocarpus altilis* Seed Husk for Co (II), Pb (II) and Zn (II) Ions. *Iranian Journal of Chemistry and Chemical Engineering*. 2018. Vol. 37. Iss. 3 (89), p. 171-186. DOI: 10.30492/IJCCE.2018.30205

51. Syafiuddin A., Fulazzaky M.A. Decolorization kinetics and mass transfer mechanisms of Remazol Brilliant Blue R dye mediated by different fungi. *Biotechnology Reports*. 2021. Vol. 29. N e00573. DOI: 10.1016/j.btre.2020.e00573

52. Jain N., Dwivedi M.K., Waskle A. Adsorption of Methylene Blue Dye from Industrial Effluents Using Coal Fly Ash. *International Journal of Advanced Engineering Research and Science*. 2016. Vol. 3. Iss. 4, p. 9-16.

53. Dada A.O., Adekola F.A., Odebunmi E.O. et al. Two–three parameters isotherm modeling, kinetics with statistical validity, desorption and thermodynamic studies of adsorption of C(II) ions onto zerovalent iron nanoparticles. *Scientific Reports*. 2021. Vol. 11. N 1. N 16454. DOI: 10.1038/s41598-021-95090-8

54. Ragadhita R., Nandiyanto A.B.D. How to Calculate Adsorption Isotherms of Particles Using Two-Parameter Monolayer Adsorption Models and Equations. *Indonesian Journal of Science and Technology*. 2021. Vol. 6. N 1, p. 205-234. DOI: 10.17509/ijost.v6i1.32354

55. Alabbad E.A. Effect of Direct yellow 50 removal from an aqueous solution using nano bentonite; adsorption isotherm, kinetic analysis and thermodynamic behaviour. *Arabian Journal of Chemistry*. 2023. Vol. 16. Iss. 2. N 104517. DOI: 10.1016/j.arabjc.2022.104517

56. Nandiyanto A.B.D. Isotherm Adsorption of Carbon Microparticles Prepared from Pumpkin (Cucurbita maxima) Seeds Using Two-Parameter Monolayer Adsorption Models and Equations. *Moroccan Journal of Chemistry*. 2020. Vol. 8. N 3, p. 745-761. DOI: 10.48317/IMIST.PRSM/morjchem-v8i3.21636

57. Shikuku V.O., Mishra T. Adsorption isotherm modeling for methylene blue removal onto magnetic kaolinite clay: a comparison of two-parameter isotherms. *Applied Water Science*. 2021. Vol. 11. Iss. 6. N 103. DOI: 10.1007/s13201-021-01440-2

58. Dada A.O., Ojedira J.O., Okunola A.A. et al. Modeling of Biosorption of Pb(II) and Zn(II) Ions onto PAMRH: Langmuir, Freundlich, Temkin, Dubinin – Raduskevich, Jovanovic, Flory – Huggins, Fowler – Guggenheim and Kiselev Comparative Isotherm Studies. *International Journal of Mechanical Engineering and Technology*. 2019. Vol. 10. Iss. 2, p. 1048-1058.

59. Yousef N.S., Farouq R., Hazzaa R. Adsorption kinetics and isotherms for the removal of nickel ions from aqueous solutions by an ion-exchange resin: application of two and three parameter isotherm models. *Desalination and Water Treatment*. 2016. Vol. 57. Iss. 46, p. 21925-21938.

60. Yao Huang, Siyu Xia, Jingjing Lyu, Jingchun Tang. Highly efficient removal of aqueous Hg^{2+} and CH_3Hg^+ by selective modification of biochar with 3-mercaptopropyltrimethoxysilane. *Chemical Engineering Journal*. 2019. Vol. 360, p. 1646-1655. DOI: 10.1016/j.cej.2018.10.231

61. Irwansyah F.S., Amal A.I., Diyanthi E.W. et al. How to Read and Determine the Specific Surface area of Inorganic Materials Using the Brunauer – Emmett – Teller (BET) Method. *ASEAN Journal of Science and Engineering*. p. 10. URL: https://ejournal.upi.edu/index.php/AJSE/article/view/60748 (Online First) (accessed 25.10.2023).

62. Sukamto S., Rahmat A. Evaluation of FTIR, Macro and Micronutrients of Compost from Black Soldier Fly Residual: in Context of Its Use as Fertilizer. *ASEAN Journal of Science and Engineering*. 2023. Vol. 3. N 1, p. 21-30. DOI: 10.17509/ajse.v3i1.42798

63. Fatimah S., Ragadhita R., Husaeni D.F.A, Nandiyanto A.B.D. How to Calculate Crystallite Size From X-Ray Diffraction (XRD) Using Scherrer Method. *ASEAN Journal of Science and Engineering*. 2022. Vol. 2. N 1, p. 65-76. DOI: 10.17509/ajse.v2i1.37647

***Authors*: Asep B. D. Nandiyanto,** *Professional Doctorate in Engineering*, *Professor*, *nandiyanto@upi.edu*, *https://orcid.org/0000-0002-9753-1267* (*Universitas Pendidikan Indonesia, Bandung, Indonesia*; *Pusat Riset Lingkungan dan Teknologi Bersih, Badan Riset dan Inovasi Nasional, Jakarta, Indonesia*), **Willy C. Nugraha,** *Doctor of Science*, *Researcher*, *https://orcid.org/0000-0003-1542-6701* (*Pusat Riset Lingkungan dan Teknologi Bersih, Badan Riset dan Inovasi Nasional, Jakarta, Indonesia*), **Intan Yustia,** *Researcher*, *https://orcid.org/0000-0003-0553-6579* (*Universitas Pendidikan Indonesia, Bandung, Indonesia*), **Risti Ragadhita,** *Researcher*, *https://orcid.org/0000-0002-8634-4001* (*Universitas Pendidikan Indonesia, Bandung, Indonesia*), **Meli Fiandini,** *Researcher*, *https://orcid.org/0009-0008-7449-9816* (*Universitas Pendidikan Indonesia, Bandung, Indonesia*), **Hanny Meirinawati,** *Researcher*, *https://orcid.org/0000-0001-7728-5524* (*Pusat Riset Lingkungan dan Teknologi Bersih, Badan Riset dan Inovasi Nasional, Jakarta, Indonesia*), **Diana R. Wulan,** *Researcher*, *https://orcid.org/0000-0001-7054-1708* (*Pusat Riset Lingkungan dan Teknologi Bersih, Badan Riset dan Inovasi Nasional, Jakarta, Indonesia*).

The authors declare no conflict of interests.

ISSN 2411-3336; e-ISSN 2541-9404

JOURNAL OF MINING INSTITUTE

Zapiski Gornogo instituta

Journal homepage: pmi.spmi.ru

Research article

Improving the efficiency of oil vapor recovery units in the commodity transport operations at oil terminals

Vladimir V. PSHENIN ✉, **Gulnur S. ZAKIROVA**
Empress Catherine II Saint Petersburg Mining University, Saint Petersburg, Russia

How to cite this article: Pshenin V.V., Zakirova G.S. Improving the efficiency of oil vapor recovery units in the commodity transport operations at oil terminals. Journal of Mining Institute. 2024. Vol. 265, p. 121-128. EDN FFTUZK. DOI: 10.31897/PMI.2023.29

Abstract. In this paper the problem of losses from evaporation of light fractions of hydrocarbons during loading operations of tanker fleets vessels is considered. It was found that there is no unified approach to modeling the system "tanker – gas phase pipeline – vapor recovery units" in open sources. The absence of a generally recognized model makes it impossible to scientifically justify the application of instruments to reducing losses and the development of corresponding measures. In work it is showed that the dynamics of growth of pressure in the inner tanker capacity is described by a differential equation, considering for non-stationary essence of the process. This equation is converted to a non-dimensional form and investigated in relation to the similarity criteria of this system. This research has allowed to establish unambiguously the general character of pressure changes in the inner tanker capacity, and to predict the peak values of its growth at the initial stage of the loading operation. The obtained equations were tested on real tanker loading data and showed satisfactory convergence with the experimental data. At different stages of the loading operation the component composition of vapor changes, which is shown by chromatographic analysis of the gas mixture. With the availability of a model of hydrocarbon vapor displacement from the inner of tanker, it is possible to propose measures to minimize the negative impact on the environment and return valuable vapors of the product to the technological chain of transportation.

***Keywords*:** oil tanker; marine terminals; evaporation loss; crude; oil terminal; vapor recovery units; volatile organic compounds; oil losses

Received: 30.09.2022 ***Accepted: 13.02.2023*** ***Online: 12.04.2023*** ***Published: 29.02.2024***

Introduction. In the process of tanker loading oil or oil products evaporate intensively, which leads to an increase of the excess pressure in their internal space. In case of high loading rates and insufficient capacity of gas venting systems, when the pressure reaches a critical value a part of the gas-air mixture is released into the atmosphere. Venting vapors to the atmosphere through breathing valves or mast riser is undesirable for the following reasons:

• irretrievable loss of valuable materials occurs (for comparison, for a tanker of Aframax class the size of losses during one operation of crude oil loading can make approximately half of the volume of one railway tank);

• a risk of emergency stop of loading due to triggering of automatic systems at the berth because of high gas level;

• evaporation of light fractions worsens quality indicators of oil products;

• pollution of atmospheric basin occurs [1, 2].

The way of controlling losses from vaporization at oil loading terminals is introduction and efficient operation of vapor recovery units (VRU) [3, 4]. If in domestic practice oil loading terminals have just begun to be equipped with such devices since about 2010 (mainly imported), then abroad they have gained a great practical experience of their application [5, 6]. In the world practice of research in this field the leaders are the countries which are characterized by large volumes of tanker

EDN FFTUZK
DOI: 10.31897/PMI.2023.29

traffic: the USA, Japan, Norway, China [7, 8]. Despite the relatively successful use of these units, there is also a negative experience. Research in this area, especially the project VocSim implemented by Norwegian Marine Technology Research Institute [1], despite substantial financing, could not provide a universal solution for modeling system "tanker – gas phase pipeline – vapor recovery unit" [9, 10]. The reasons are the following: oil (or oil products) evaporation process has a complicated non-stationary character; uniqueness of every separate oil terminal and tanker; a great number of influencing factors. Some research in the field of heat transfer in the internal tanker space [11], determination of vapor composition [12, 13], evaporation processes for different products [14, 15], improvement of individual systems and emission reduction means [16, 17] etc. are of a detached type and can not efficiently solve the task of emission reduction and operative control within an oil terminal as a whole [18, 19].

An important issue is the total volume of volatile hydrocarbon emissions through the mast riser. This value is not monitored, there are simply no flow measurement devices installed on the mast riser line, and calculated estimates are impossible or inaccurate due to the lack of a model of pressure changes in the tanker's gas space. The air-gas mixture being vented through the mast riser enters the atmosphere directly, bypassing the vapor recovery unit, which makes it impossible to recover at least part of the vapor. Vapors are vented when the critical pressure is exceeded through the special piping of the tanker. The flow mode is characterized by non-linearity in pressure, and there is also uncertainty in the duration of opening the mast riser. As a rule opening takes place at the direction of the tanker captain for a short period at the moment of peak pressure growth dynamics in order to stabilize it. From the terminal side, these processes are fixed as unavoidable costs of the technological process. Such approach is not quite correct, since it is impossible to exclude irregular situations completely, but it is possible to minimize their negative impact.

The aim of the study is to provide a scientific basis for measures to reduce losses and improve the efficiency of operation of vapor recovery units. The work consistently solved a number of related problems: the dynamics of pressure growth in the gas space of the tanker has been simulated; the obtained solution has been tested on the data of real loading in the port of Kozmino; the quantitative content of hydrocarbons C_1-C_{10} at different stages of the loading operation has been experimentally determined. Within the framework of the given model, estimates were obtained for possible emission reduction reserve in case of prevention of opening of the mast riser.

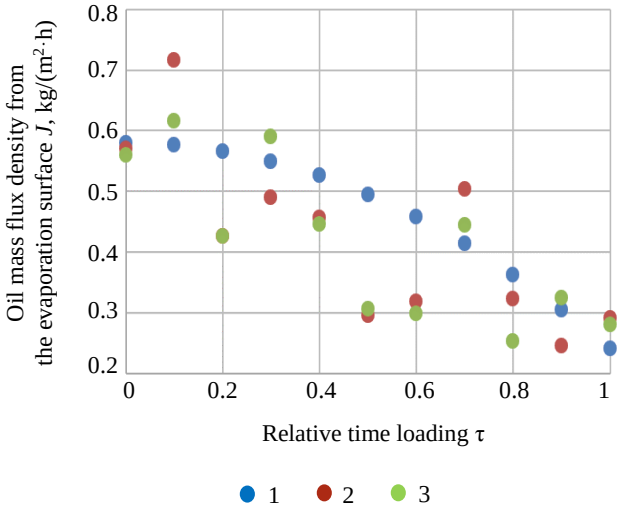

Fig.1. Dynamics of mass transfer from the surface of the oil in the process of tanker loading operation
1 – "ANTONIS"; 2 – "FRONT CASTOR"; 3 – "MASTERA"

Methodology. In the part of obtaining experimental data on the quantitative content of C_1-C_{10} hydrocarbons at different stages of the loading operation the results of chromatographic analysis of selected samples of the displaced gas-air mixture on the "Chromatec-Crystal 5000" unit were used [20, 21]. The results were obtained from laboratory studies with the author's involvement, and the results were published earlier in the open press [22, 23]. Within the framework of studies of hydrocarbon evaporation process the total mass transfer from the surface of oil (oil product) of C_1-C_{10} hydrocarbons is of interest (Fig.1) [24, 25].

Mass transfer decreases over time, as the gas space above the oil (oil product) surface becomes saturated and prevents further evaporation [26, 27]. However, there are a number of secondary effects that can prevent the smooth nature of this function:

EDN FFTUZK
DOI: 10.31897/PMI.2023.29

Journal of Mining Institute. 2024. Vol. 265. P. 121-128

tanker's motions/rolling; non-uniformity of the gas removal system; internal convective fluxes; changes in temperature [27, 28]. The principal diagram of vapor release during cargo loading provides a line: "tanker gas system – gas phase pipeline – vapor recovery unit – gas vent" (Fig.2) [29, 30].

Values for pressure and temperature in the loading process are taken from data of the automated workstation of the vapor recovery unit dispatcher [31, 32]. Part of the information is obtained from the tanker's automation systems (pressure in tanks, oxygen content, and temperature in tanks) [33, 34]. A representation of oil vapor displacement during tanker loading is shown in Fig.3.

The equation of state of the gas-air mixture in differential form is:

$$\frac{dP}{dt}V + \frac{dV}{dt}P = \frac{dG}{dt}RT\,, \tag{1}$$

where V – the volume of the tanker's gas space, m^3; P – pressure in the gas space of the tanker, Pa; R – the gas constant for the component mixture (based on the average molar mass of the vapor), J/kmol·K; T – the temperature inside the gas space of the tanker.

As a result of reducing the equation to a non-dimensional form, it is found that the rate of pressure growth in the inner tanker volume capacity is determined by the following differential equation:

$$\frac{dy}{d\tau}(1-\tau) = y + \psi\left(1-(1-\xi)\tau^2\right) - \frac{\sqrt{y^2-1}}{\theta}\,, \tag{2}$$

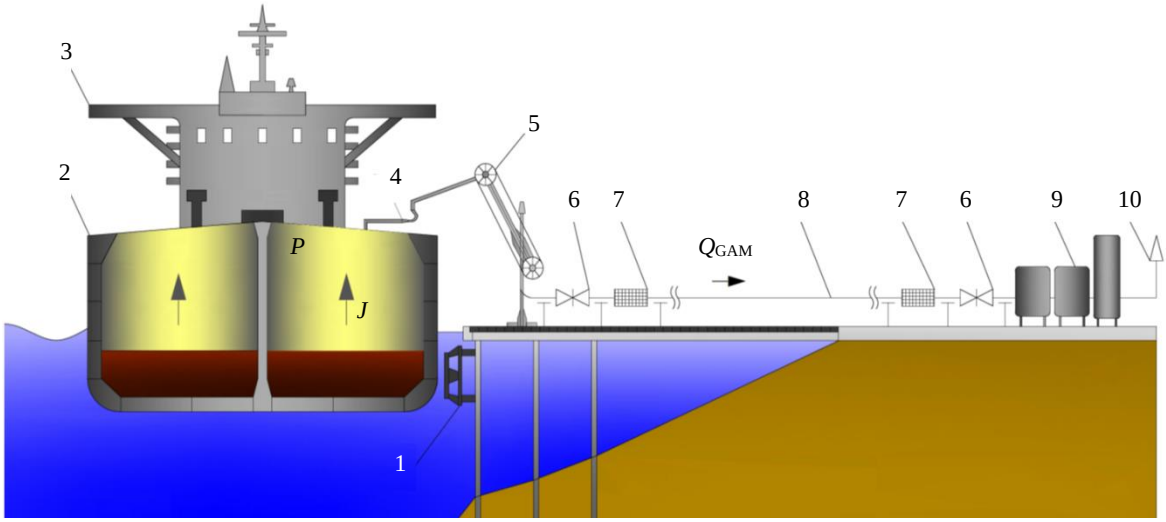

Fig.2. Schematic diagram of gas vent systems of the tanker, coastal and berthing facilities

1 – node protection berthing facilities fender; 2 – double housing; 3 – tanker; 4 – mast riser; 5 – a stander removal of the gas phase; 6 – shut-off and control valves; 7 – detonation arrestor; 8 – the pipeline of the gas phase; 9 – VRU; 10 – gas vent; Q_{GAM} – flowrate gas-air mixture; J – mass transfer

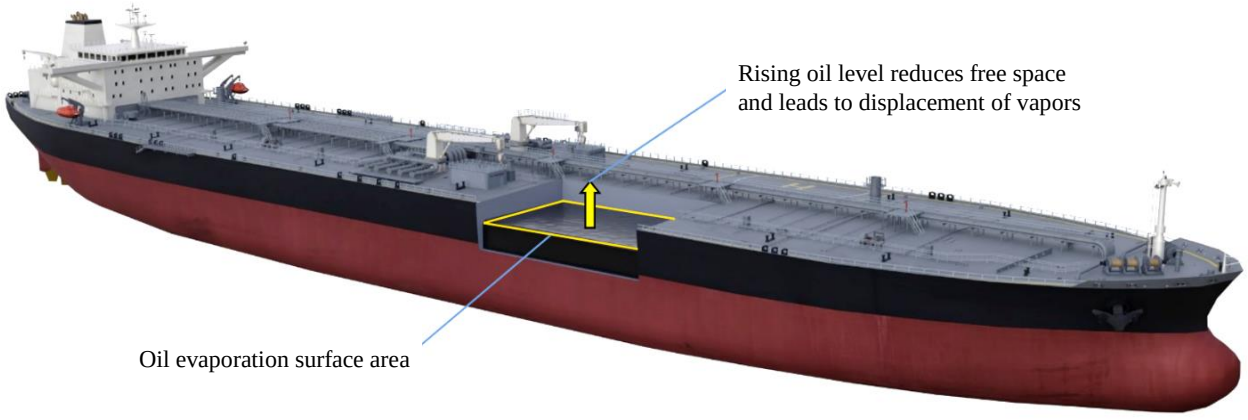

Fig.3. Schematic representation of oil level rise (one compartment is shown in section) and oil vapor displacement during tanker loading

EDN FFTUZK
DOI: 10.31897/PMI.2023.29

where y – dimensionless pressure; τ – dimensionless time; ψ – similarity criterion for the contribution of mass transfer to the pressure growth dynamics; θ – similarity criterion for the contribution of hydraulic resistance to the pressure growth dynamics; ξ – dimensionless ratio for mass transfer;

$$y = \frac{P}{P_{end}}; \tag{3}$$

$$\psi = \frac{JFRT}{Q_{load} P_{end}}; \tag{4}$$

$$\theta = \frac{Q_{load}\sqrt{\lambda \frac{L_{eff}}{D}}}{S\sqrt{RT}}; \tag{5}$$

$$\tau = \frac{t}{\tau_{load}}; \tag{6}$$

$$\xi = \frac{J_{end}}{J_{start}}, \tag{7}$$

P_{end} – pressure at the endpoint; F – evaporation surface area; Q_{load} – oil filling flow rate of the tanker; λ – hydraulic resistance coefficient; D – pipeline diameter; S – cross-sectional area of the gas phase pipeline; t – the current time since the beginning of loading; τ_{load} – full filling time; J_{end}, J_{start} – mass transfer at the final and starting points of time.

From the dimensionless point of view the dynamics of pressure changes are described by a functional dependence of the form:

$$y = \tilde{f}(\psi, \theta, \xi, \tau). \tag{8}$$

The dependence (8) can be used as a reference in the construction of bench equipment to test working hypotheses on the operation of vapor recovery systems and gas removal systems on small-scale units in laboratory conditions [35]. The value of hydrocarbon losses at the opening of mast riser should be determined based on the mass flow rate of the gas-air mixture through the ventilation system of the tanker:

$$G_{mr} = \frac{S_{vent}\sqrt{[P_{mr}]^2 - P_{atm}{}^2}}{\sqrt{RT}\sqrt{2\ln\frac{[P_{mr}]}{P_{atm}} + \lambda\frac{L_{eff}}{D_{vent}}\varepsilon_f}}, \tag{9}$$

where S_{vent} – flow area of the pipeline of the tanker ventilation system; $[P_{mr}]$ – mast riser opening pressures; P_{atm} – atmospheric pressure; T – gas-air mixture temperature; L_{eff} – effective length including local friction drag; D_{vent} – pipeline's diameter of the tanker ventilation system; R – universal gas constant; ε_f – a factor that takes into account the degree of opening of the mast riser.

The mass flow rate is related to the volumetric flow rate by the following equation:

$$G_{mr} = Q_{mr}\rho_{GAM}, \tag{10}$$

where Q_{mr} – volumetric flow rate of the gas-air mixture through the mast riser; ρ_{GAM} – gas-air mixture density.

The total hydrocarbon losses through the mast riser per year should be determined from the equation:

$$G_{all} = Q_{mr}\, c_{av}\, \tau_{mr}\, N_{num}, \tag{11}$$

where c_{av} – average concentration of hydrocarbons in the emission, g/m^3; τ_{mr} – average length of time the mast riser is open; N_{num} – the number of cases of opening a mast riser per year.

EDN FFTUZK
DOI: 10.31897/PMI.2023.29

Journal of Mining Institute. 2024. Vol. 265. P. 121-128

Estimated calculation of damage in value terms:

$$ED = G_{all}\,\sigma_{VOC} + G_{all}\,S_{eff}\,\sigma_{crude}, \quad (12)$$

where σ_{VOC} – fee rate for the emission of 1 t of the amount of hydrocarbons C_1-C_{10}; S_{eff} – predicted degree of the gas-air mixture refining; σ_{crude} – cost per 1000 m^3 of oil.

Discussion of the results. The developed model was tested on the data of real tanker loading, and a number of practical results were obtained (results in Table). Basic data on tanker loading: tanker deadweight – 106208 t; dimensions – 241×44 m; inert gas – exhaust gases; oil density – 0.872 t/m^3 at 20 °C; saturated oil vapor pressure – 54.3 kPa; duration of loading – 14.21 h. The results of approbation of the developed model on the data of real loading operation are shown in Fig.4.

Because the model showed satisfactory convergence, (discrepancies do not exceed 10 %) with the data collected during the loading operation, it is proposed to apply its results to estimate losses in case of opening of the mast riser. The highest pressure is reached from two hours after the start of loading at a linearly increasing pumping rate [36]. At these moments it is not rare for tankers to open the mast riser. Calculations are given by the example of operation of the tanker gas removal system and vapor recovery adsorption unit in the port of Kozmino (Fig.5).

Results of approbation of the mathematical model

Time from the beginning of the loading operation, h	Pressure according to the tanker's automatics systems, Pa	Pressure in the inner space of the tanker according to simulation results, Pa
0	101815	101815
1	103596	104081
2	103899	104159
3	107643	108083
4	108681	108651
5	108894	108544
6	108837	108357
7	108702	108742
8	108550	108730
9	108399	108274
10	108253	108268
11	104983	105313
12	104891	104886
13	105585	105820
14	103946	104236

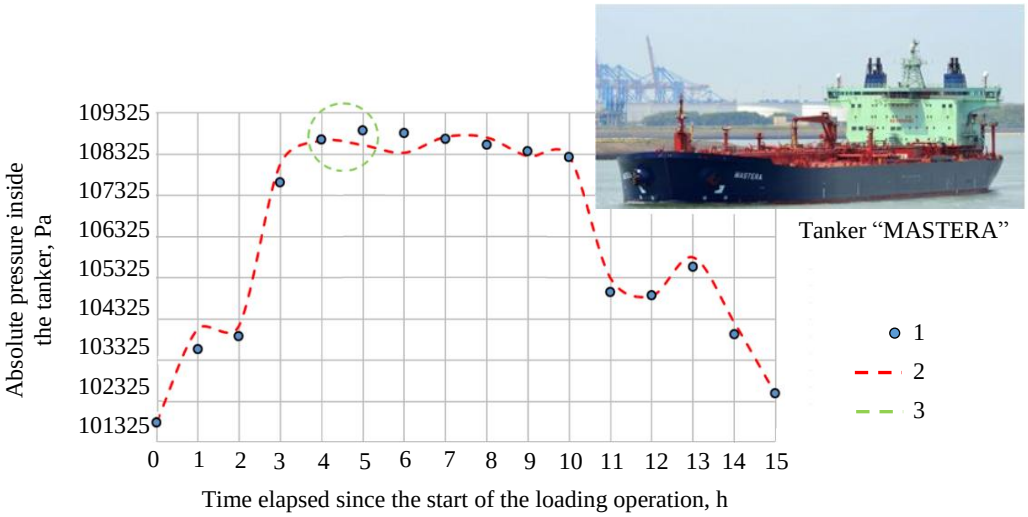

Fig.4. Results of approbation of the mathematical model

1 – automatics data of tanker "MASTERA"; 2 – the results within the developed model; 3 – opening area mast riser

EDN FFTUZK
DOI: 10.31897/PMI.2023.29

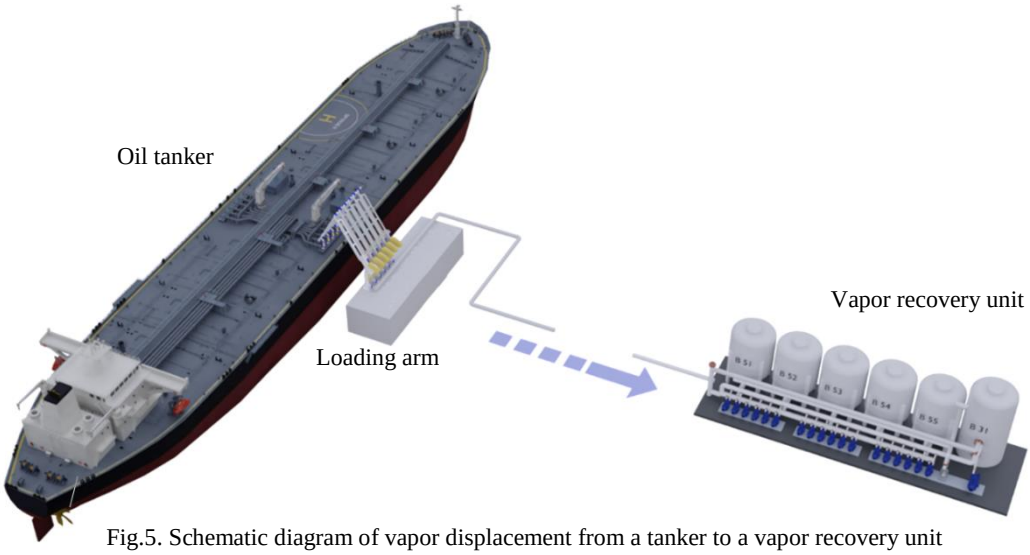

Fig.5. Schematic diagram of vapor displacement from a tanker to a vapor recovery unit

On the basis of the developed technique of the damage estimation, connected with opening of the mast riser, there were made forecast calculations of the given value with the average mass content of hydrocarbons C_1-C_{10} 273.52 g/m^3 and degree of cleanup of the gas-air mixture of 72.6 % [37, 38].

The results of calculations of damage caused by opening the mast riser (based on 50 mast riser openings per year, which is taken from the average operating data) [39]: estimated hydrocarbon losses per loading – 12.3 t; estimated annual hydrocarbon losses – 615 t; damage in value terms for 1 year (including the value of the irretrievably lost product) – 26.623 million rub.

The damage in cost terms can either be completely eliminated or minimized in the case of operational management of tanker loading and control over the operation of the vapor recovery unit systems [40, 41].

Conclusion. As part of the study, for the first time a generalized model of the dynamics of pressure growth in the gas space of the tanker was obtained, and the resulting solution was tested on the data of real loading in the oil terminal. It was found that the pressure change during the loading operation is non-linear and has a local maximum. In order to avoid the opening of the mast riser, it is necessary to ensure such loading modes, which are outside the area of critical pressures. It has been established experimentally, that the quantitative content of hydrocarbons C_1-C_{10} increases with the process of loading, at its initial stage light components (methane, ethane, propane, butane) evaporate, and at the final stages hexane and higher hydrocarbons C_{6+} evaporate. Within the framework of the developed model the possible reserve for the reduction of emissions into the environment at the opening of the mast riser was rated. Operational management of tanker loading allows reducing emissions by saving about 26 million rub. per year.

The conducted research provides a scientific basis for the measures to reduce losses and improve the efficiency of vapor recovery units' operation. In the future, this research will allow not only to increase efficiency of domestic units within the own developments in line with the import substitution programs, but also to provide secure, resource-saving, environmentally friendly operation of oil terminals.

REFERENCES

1. Invernizzi M., Sironi S. Odour Emission Rate Estimation Methods for Hydrocarbon Storage Tanks. *Chemical Engineering Transactions*. 2021. Vol. 85, p. 67-72. DOI: 10.3303/CET2185012

2. Milazzo M.F., Ancione G., Lisi R. Emissions of volatile organic compounds during the ship-loading of petroleum products: Dispersion modelling and environmental concerns. *Journal of Environmental Management*. 2017. Vol. 204. Part 1, p. 637-650. DOI: 10.1016/j.jenvman.2017.09.045

3. Woohyun Kim, Munkyu Yoon, Moonyong Lee, Sunwon Park. CFD Analysis of Cavitation in a Crude Oil Pipeline to an Oil Tanker. *Computer Aided Chemical Engineering*. 2012. Vol. 31, p. 580-584. DOI: 10.1016/B978-0-444-59507-2.50108-6

Journal of Mining Institute. 2024. Vol. 265. P. 121-128

4. Nwachukwu A.N. Volatile Organic Compounds Characterization: a Case Study of a Tank Farm in the United States. *JSM Environmental Science and Ecology*. 2015. Vol. 3 (2). N 1019. DOI: 10.47739/2333-7141/1019

5. Nwachukwu A.N. Characterization of Volatile Organic Compounds (VOCs) at an Industrial Lagoon Site in North-West England, UK. *International Journal of Current Research and Academic Review*. 2015. Vol. 3. N 10, p. 164-177.

6. Nguyen V.T., Pham T.V., Rogachev M.K. et al. A comprehensive method for determining the dewaxing interval period in gas lift wells. *Journal of Petroleum Exploration and Production Technology*. 2023. Vol. 13, p. 1163-1179. DOI: 10.1007/s13202-022-01598-8

7. Dmitriev M.E., Sadreeva K.K., Pshenin V.V., Gaysin M.T. Determination of the Voc Vapor Relativeflowrate During Tanker Loading Operations. *Transport and storage of oil products and hydrocarbons.* 2019. N 1, p. 10-13 (in Russian). DOI: 10.24411/0131-4270-2019-10102

8. Davletjarov R.R., Lapina O.A., Polovkov S.A. Ensuring Environmental Safety around the Oil Loading Port Primorsk. *Science & Technologies: Oil and Oil Products Pipeline Transportation*. 2015. N 2, p. 84-87 (in Russian).

9. Shlekova I.Yu., Ignatenko N.V. Loading hermetic sealing and hydrocarbon vapor recuperation during petroleum product shipment. Bezopasnost gorodskoi sredy: Materialy V Mezhdunarodnoi nauchno-prakticheskoi konferentsii, 21-23 noyabrya 2017, Omsk, Rossiya. Omsk: Omskii GAU, 2018, p. 224-228.

10. Cherepovitsyn A.E., Tcvetkov P.S., Evseeva O.O. Critical analysis of methodological ap-proaches to assessing sustainability of arctic oil and gas projects. *Journal of Mining Institute.* 2021. Vol. 249, p. 463-479. DOI: 0.31897/PMI.2021.3.15

11. Karbasian H.R., Dae Yeon Kim, Sang Youl Yoon et al. A new method for reducing VOCs formation during crude oil loading process. *Journal of Mechanical Science and Technology*. 2017. Vol. 31. Iss. 4, p. 1701-1710. DOI: 10.1007/s12206-017-0318-7

12. Tokuslu A. Estimating greenhouse gas emissions from ships on four ports of Georgia from 2010 to 2018. *Environmental Monitoring and Assessment*. 2021. Vol. 193. Iss. 7. N 385. DOI: 10.1007/s10661-021-09169-w

13. Virdi S.S., Lee L.Y., Li C., Dev A.K. Simulation of VOC Emission During Loading Operations in a Crude Oil Tanker. *International Journal of Maritime Engineering*. 2021. Vol. 163. Part A1, p. 1-16. DOI: 10.5750/IJME.V163IA1.1

14. Nwachukwu A.N., Uwa C.U., Nwagu K.E., Ephraim B.E. Determination of Volatile Organic Compounds at a Marine Terminal in United States Using in-Borehole Gas Monitoring. *Journal of Marine Science and Technology*. 2020. Vol. 28. N 3, p. 219-228. DOI: 10.6119/JMST.202006_28(3).0007

15. Tamaddoni M., Sotudeh-Gharebagh R., Nario S. et al. Experimental study of the VOC emitted from crude oil tankers. *Process Safety and Environmental Protection*. 2014. Vol. 92. Iss. 6, p. 929-937. DOI: 10.1016/j.psep.2013.10.005

16. Guilin Hu, Butler J., Littlejohns J. et al. Simulation of cargo VOC emissions from petroleum tankers in transit in Canadian waters. *Engineering Applications of Computational Fluid Mechanics*. 2020. Vol. 14. Iss. 1, p. 522-533. DOI: 10.1080/19942060.2020.1728386

17. Poornan P.D., Ali Hasan Ali Abdulla Al Hindi. Takreer's Approach to Minimize Environmental Emissions by Vapor Recovery During Gasoline and Naphtha Ship Loading. Abu Dhabi International Petroleum Exhibition and Conference, 7-10 November 2016, Abu Dhabi, UAE. OnePetro, 2016. SPE-183323-MS. DOI: 10.2118/183323-MS

18. Salomone S. Reducing Emissions from Oil & Gas Facilities by Use of Field Proven VOC Technology. SPE Asia Pacific Oil and Gas Conference and Exhibition, 25-27 October 2016, Perth, Australia. 2016. OnePetro, 2016. SPE-182204-MS. DOI: 10.2118/182204-MS

19. Litvinenko V.S., Dvoynikov M.V., Trushko V.L. Elaboration of a conceptual solution for the development of the Arctic shelf from seasonally flooded coastal areas. *International Journal of Mining Science and Technology*. 2021. Vol. 32. Iss. 1, p. 113-119. DOI: 10.1016/j.ijmst.2021.09.010

20. Shammazov A.M., Aminev A.N., Pirogov A.N. et al. Solving problems of reconstruction and development optimization of a pipeline system. *Oil Industry.* 2018. Iss. 8, p. 80-83 (in Russian). DOI: 10.24887/0028-2448-2018-8-80-8

21. Hao Xu, Xiafan Xu, Liubiao Chen et al. A novel cryogenic condensation system combined with gas turbine with low carbon emission for volatile compounds recovery. *Energy*. 2022. Vol. 248. N 123604. DOI: 10.1016/j.energy.2022.123604

22. Pshenin V.V., Korshak A.A., Gaisin M.T. Method of structural minimization of the average risk for identification of mass transfer of evaporating oil at tanker loading. *Oil Industry.* 2019. N 10, p. 108-111 (in Russian). DOI: 10.24887/0028-2448-2019-10-108-111

23. Zemenkova M.Y., Chizhevskaya E.L., Zemenkov Y.D. Intelligent monitoring of the condition of hydrocarbon pipeline transport facilities using neural network technologies. *Journal of Mining Institute.* Vol. 258, p. 933-944. DOI: 10.31897/PMI.2022.105

24. Sangick Lee, Inhwan Choi, Daejun Chang. Multi-objective optimization of VOC recovery and reuse in crude oil loading. *Applied Energy*. 2013. Vol. 108, p. 439-447. DOI: 10.1016/j.apenergy.2013.03.064

25. Rogachev M.K., Aleksandrov A.N. Justification of a comprehensive technology for preventing the formation of asphalt-resin-paraffin deposits during the production of highlyparaffinic oil by electric submersible pumps from multiformation deposits. *Journal of Mining Institute.* 2021. Vol. 250, p. 596-605. DOI: 10.31897/PMI.2021.4.13

26. Rajabi H., Mosleh M.H., Mandal P. et al. Emissions of volatile organic compounds from crude oil processing – Global emission inventory and environmental release. *Science of the Total Environment*. 2020. Vol. 727. N 138654. DOI: 10.1016/j.scitotenv.2020.138654

27. Shammazov I., Dzhemilev E., Sidorkin D. Improving the Method of Replacing the Defective Sections of Main Oil and Gas Pipelines Using Laser Scanning Data. *Applied Sciences*. 2023. Vol. 13. Iss. 1, p. 48-75. DOI: 10.3390/app13010048

28. Ilinova A.A., Chanysheva A.F. Algorithm for assessing the prospects of offshore oil and gas projects in the Arctic. *Energy Reports*. 2020. Vol. 6. N 2, p. 504-509. DOI: 10.1016/j.egyr.2019.11.110

29. Yungmeister D.A., Lavrenko S.A., Yacheikin A.I., Urazbakhtin R.Y. Improving the shield machine cutter head for tunneling under the conditions of the Metrostroy Saint Petersburg mines. *ARPN Journal of Engineering and Applied Sciences*. 2020. Vol. 15. N 11, p. 1282-1288.

30. Mayet A.M., Alizadeh S.M., Nurgalieva K.S. et al. Extraction of Time-Domain Characteristics and Selection of Effective Features Using Correlation Analysis to Increase the Accuracy of Petroleum Fluid Monitoring Systems. *Energies*. 2022. Vol. 15. Iss. 6. N 1986. DOI: 10.3390/en15061986

31. Aleksandrova T.N., Potemkin V.A. Development of a methodology to assess the hydrocyclone process with account of the rheological properties of the mineral slurry. *Journal of Mining Institute.* 2021. Vol. 252, p. 908-916. DOI: 10.31897/PMI.2021.6.12

32. Yoo Youl Choi, Seok Hee Lee, Jae-Cheul Park et al. The impact of corrosion on marine vapour recovery systems by VOC generated from ships. *International Journal of Naval Architecture and Ocean Engineering*. 2019. Vol. 11. Iss. 1, p. 52-58. DOI: 10.1016/j.ijnaoe.2018.01.002

33. Bayirhan İ., Mersin K., Tokuşlu A., Gazioğlu C. Modelling of Ship Originated Exhaust Gas Emissions in the Strait of Istanbul (Bosphorus). *International Journal of Environment and Geoinformatics*. 2019. Vol. 6. Iss. 3, p. 238-243. DOI: 10.30897/ijegeo.641397

34. Alver F., Saraç B.A., Şahin U.A. Estimating of shipping emissions in the Samsun Port from 2010 to 2015. *Atmospheric Pollution Research*. 2018. Vol. 9. Iss. 5, p. 822-828. DOI: 10.1016/j.apr.2018.02.003

35. Litvinenko V.S., Bowbrick I., Naumov I.A., Zaitseva Z. Global guidelines and requirements for professional competencies of natural resource extraction engineers: Implications for ESG principles and sustainable development goals. *Journal of Cleaner Production*. 2022. Vol. 338. N 130530. DOI: 10.1016/j.jclepro.2022.130530

36. Pashkevich M.A., Bykova M.V. Methodology for thermal desorption treatment of local soil pollution by oil products at the facilities of the mineral resource industry. *Journal of Mining Institute.* 2022. Vol. 253, p. 49-60. DOI: 10.31897/PMI.2022.66

37. Gobbi G.P., Liberto L.D., Barnaba F. Impact of port emissions on EU-regulated and non-regulated air quality indicators: the case of Civitavecchia (Italy). *Science of the Total Environment*. 2020. Vol. 719. N 134984. DOI: 10.1016/j.scitotenv.2019.134984

38. Tokuşlu A., Burak S. Examination of Exhaust Gas Emissions of Transit Ships in the Istanbul Strait. *Academic Platform Journal of Engineering and Science*. 2021. Vol. 9. Iss. 1, p. 59-66. DOI: 10.21541/apjes.705918

39. Mihajlović M., Jovanović M., Pešić R.V. Volatile organic compounds (VOC) policy innovation in petrochemicals river barge transportation. *Journal of Cleaner Production*. 2016. Vol. 112. Part 2, p. 1559-1567. DOI: 10.1016/j.jclepro.2015.04.080

40. Rahman M.M., Canter C., Kumar A. Well-to-wheel life cycle assessment of transportation fuels derived from different North American conventional crudes. *Applied Energy*. 2015. Vol. 156, p. 159-173. DOI: 10.1016/j.apenergy.2015.07.004

41. Barykin S.E., Smirnova E.A., Chzhao D. et al. Digital echelons and interfaces within value chains: End-to-end marketing and logistics integration. *Sustainability*. 2021. Vol. 13. Iss. 24. N 13929. DOI: 10.3390/su132413929

***Authors*: Vladimir V. Pshenin,** *Candidate of Engineering Sciences, Associate Professor, pshenin_VV@pers.spmi.ru, https://orcid.org/0000-0003-4604-3172* (*Empress Catherine II Saint Petersburg Mining University, Saint Petersburg, Russia*), **Gulnur S. Zakirova,** *Candidate of Engineering Sciences, Assistant Lecturer, https://orcid.org/0000-0003-3877-8566* (*Empress Catherine II Saint Petersburg Mining University, Saint Petersburg, Russia*).

The authors declare no conflict of interests.

ISSN 2411-3336; e-ISSN 2541-9404

JOURNAL OF MINING INSTITUTE
Zapiski Gornogo instituta
Journal homepage: pmi.spmi.ru

Research article

Increasing the quality of zeolite-bearing rocks from Eastern Transbaikalia by applying directed energy

Konstantin K. RAZMAKHNIN ✉, **Alisa N. KHATKOVA, Lidiya V. SHUMILOVA**
Transbaikal State University, Chita, Russia

***How to cite this article*:** Razmakhnin K.K., Khatkova A.N., Shumilova L.V. Increasing the quality of zeolite-bearing rocks from Eastern Transbaikalia by applying directed energy. Journal of Mining Institute. 2024. Vol. 265, p. 129-139. EDN VNPZCT

Abstract. This paper presents the use of accelerated electrons to treat zeolite-bearing rocks from Eastern Transbaikalia to increase the efficiency of separating zeolites from rock-forming minerals via electromagnetic separation. The effectiveness of the liberation of zeolite minerals using accelerated electrons was analyzed. The results of dry electromagnetic separation of zeolite-bearing rocks are presented. The dependence of the extraction of iron-bearing minerals from zeolite-bearing rocks by electromagnetic separation on the magnetic field intensity for different particle sizes has been established. The main methods of zeolite-bearing rock enrichment and ore preparation were determined. A technological scheme for processing zeolite-bearing rocks, based on the use of accelerated electron treatment at the ore preparation stage, is presented, significantly improving the zeolite production quality.

***Keywords*:** zeolite-bearing rocks; enrichment; accelerated electrons; adsorption capacity; quality improvement; mining waste

Acknowledgment. This work was performed with the support of the Russian Science Foundation project 22-17-00040 “Scientific substantiation and development of environmentally friendly waste-free technologies for processing natural and technogenic mineral raw materials” (2022-2023).

Received: 20.05.2022 ***Accepted: 20.06.2023*** ***Online: 30.10.2023*** ***Published: 29.02.2024***

Introduction. The intense development of the mining industry is accompanied by technologies that generate a considerable amount of industrial waste that is not subject to disposal and processing [1, 2]. The accumulation of substantial volumes of waste rock and beneficiation tailings leads to serious economic and environmental problems in the areas where they are located [3, 4]. Most waste rock dumps and tailings storage facilities, which are a legacy of the 1990s and 2000s, lack responsible management, and combined with newly generated waste from the mining industry, they inflict significant harm on the environment [5, 6].

The solution to the problem of the negative impact of mining and processing waste on the environment is to use effective tools for managing industrial materials [7, 8]. This includes the adoption of best available technologies and materials capable of reducing the contents of toxic and radioactive elements in waste, preventing or significantly reducing dust and gas emissions from them and restoring land disturbed by anthropogenic activities while adhering to principles of conserving mi-neral resources, rationality, and complexity in their utilization [9, 10].

One of the most versatile tools in implementing environmental protection measures is sorbents, which possess the required properties, primarily adsorption properties [11, 12]. Among naturally occurring sorbents, zeolite-bearing rocks (ZCR) are highly effective, widely available, and cost-

effective [13, 14]. The unique sorption and ion exchange properties of natural zeolites can be effectively utilized in waste management systems of mining production [15].

Currently, ZCR are primarily used in backfilling mined-out spaces (mines and quarries) in combination with waste rock and tailings from mineral resource storage and in road construction for technical purposes [14, 15]. Considering their unique properties, the potential of natural zeolites is in the identification of effective approaches for their application in waste management systems of mining production, significantly minimizing and preventing the negative impact of anthropogenic formations on the environment [16, 17]. These tasks include the purification of exhaust gases, se-wage, and circulating water, land reclamation, the preservation of tailings and waste rock, and the burial of toxic and radioactive waste [18, 19].

The main limitation of ZCR application is the relatively low quality of mineral resources (zeolite mineral content ranging from 35 to 60 %), despite significant reserves. Additionally, industry requirements for the quality of natural zeolites, including the adherence to international standards owing to Russia's membership in various trade organizations, stipulate that impurities in zeolite products cannot exceed 1-3 % [20, 21]. The vast majority of Russia's ZCR reserves consist of medium- and low-quality common rocks containing a high percentage of rock-forming minerals (mainly quartz, feldspars, and iron oxides), limiting the widespread use of this raw material [22, 23]. This necessitates the development of efficient beneficiation and modification technologies for ZCR to obtain zeolite products. On the one hand, these products will allow us to rationally solve the complex issue of comprehensive utilization, disposal, neutralization, and processing of mining and production waste. On the other hand, they will allow the creation of technologies used to control the physicochemical properties of natural zeolites to produce high-quality products [24, 25].

Previous studies [20, 26] have shown that utilizing accelerated electrons for pretreating raw mineral materials is an effective approach to modify their physicochemical and mechanical properties selectively. This alteration results in reduced ore strength characteristics, increased selective disintegration, and a considerable reduction in the duration of subsequent ore preparation operations, such as milling. The impact of accelerated electrons promotes the selective liberation of mineral intergrowths and enhances the efficiency of subsequent ore enrichment [20, 27].

The enrichment of ZCR depends on the similarities and differences in the technological properties of zeolites and rock-forming minerals, their textures and structures, and the mineral forms of iron and silica in rocks as isomorphic inclusions and native minerals [20, 28]. The necessity of using accelerated electron exposure and determining the optimal radiation treatment parameters lies in achieving selective modification of the properties of Eastern Transbaikalia ZCR. Such alterations will enhance the efficiency of their purification from rock-forming minerals, particularly through magnetic separation, and increase the adsorption capacity of zeolite minerals such as clinoptilolite, mordenite, and chabazite [20, 29].

The methodological and theoretical foundations of research in this field have been laid by well-known domestic scientists [26, 30]. This study aimed to explore the feasibility of applying energy-based treatments to significantly improve the quality of ZCR and obtain zeolite products with high sorption properties.

Methods. Montmorillonite-clinoptilolite-bearing rocks from the Shivyrtuy, clinoptilolite-bearing rocks from the Holinsky, and chabazite-bearing rocks from Talan-Gozagorsk deposits were used as the research objects. The research methodology included exposing the ZCR to accelerated electrons using an ILU electron accelerator developed at the Institute of Nuclear Physics of the Siberian Branch of the Russian Academy of Sciences.

The ZCR samples were fed through a dosing hopper and conveyor into the accelerator, where they were exposed to a beam of accelerated electrons. The irradiation dose ranged from 2 to 5 kGy.

Journal of Mining Institute. 2024. Vol. 265. P. 129-139

Mössbauer spectroscopy measurements were performed using an Ms-1104Em spectrometer. The particle size of the studied rocks in the samples was 0.05-0.07 mm, and the mass of each sample was 50-70 mg. The data processing of Mössbauer spectra was performed using the Univem MS program. The thermal studies of Eastern Transbaikalia ZCR after accelerated electron treatment were conducted in an argon atmosphere at 20-1400 °C using an STA 449C instrument (Germany). The heat capacity was determined to be 40-400 °C based on the baseline, standard (sapphire), and sample.

The liberation coefficient of zeolite minerals was determined using optical microscopy after milling zeolite minerals in a laboratory ball mill (MSHL, Russia) in two modes: conventional ZCR milling and milling after pretreatment with accelerated electrons. The obtained data were mathematically processed, and the corresponding functions and graphs were created. The electromagnetic separation of ZCR was performed using a 138-CE electromagnetic separator and a high-intensity isodynamic field separator SIM-1 (particle size of 0.1 mm). The research involved granulometric, mineralogical, chemical, and X-ray phase analyses, infrared spectroscopy, scanning electron microscopy, and optical-geometric image analysis.

The ZCR were studied using a JEOL-5300 analytical electron microscope with a Link-ISIS energy-dispersive attachment, which allows to determine the chemical composition of the minerals in the ZCR. The mineral composition of the ZCR was determined through quantitative X-ray phase analysis using an ADRON-1 diffractometer. The study of the mineralogical characteristics of the ZCR included determining the mineral composition and identifying the peculiarities of zeolite mineral inclusions and their association with rock-forming minerals. The properties of minerals extracted through directional ore preparation in combination with classical beneficiation methods (gravity, magnetic, and electrical) were also investigated.

Optical microscopy was employed to determine the textural and structural characteristics of Eastern Transbaikalia ZCR. Their phase composition was identified, and the properties and forms of the minerals were studied. An ADP-1.5 diffractometer was used for the X-ray diffraction analysis. The technological assessment of ZCR and the study of the distribution of minerals within them and in the processing products were conducted through image analysis based on the optical-geometric research methodology using the "Video-Master" complex.

Iron-bearing minerals in the Eastern Transbaikalia ZCR were present as mechanical microinclusions and isomorphic impurities; therefore, Mössbauer (nuclear gamma resonance) spectroscopy was employed for this analysis. The sorption characteristics of ZCR were studied at 77 K via the nitrogen adsorption method using an ASAP-2400 instrument (USA).

Discussion. The chemical analysis data of the ZCR from the Eastern Transbaikalia deposits are presented in Table 1. The main components of ZCR were SiO_2, Al_2O_3, Fe_2O_3, and magnesium, sodium, and potassium oxides. The liberation coefficients of zeolite minerals during the milling of ZCR from the investigated deposits, both without and with radiation exposure, are shown in Fig.1. The rock size after milling is represented by curves 1 and 2, the size of zeolite minerals is shown in curves 3 and 4, and the liberation coefficient was determined as the ratio of the areas under the curves.

The use of low-dose (2-4 kGy) directional electron beam irradiation before milling increased the liberation coefficient of clinoptilolite minerals from the Shivyrtuy deposit from 38 to 54 % and from 46 to 62 % for clinoptilolite minerals from the Talan-Gozagorsk deposit. This confirmed the effectiveness of this ore preparation method. Functions describing the relationship between extraction and particle size during the milling of Eastern Transbaikalia ZCR were obtained, allowing to determine the increase in the liberation coefficient values of zeolite minerals after the electron beam pretreatment:

Table 1

Chemical composition of Eastern Transbaikalia ZCR

Components	Average component content in deposits, %		
	Shivyrtuy	Holinsky	Talan-Gozagorsk
SiO_2	62.90	65.62	53.12
P_2O_5	0.08	0.0004	0.33
Al_2O_3	13.61	12.21	16.63
TiO_2	0.34	0.07	1.50
Fe_2O_3	3.00	1.25	11.40
FeO	0.14	0.06	0.32
CaO	0.61	2.07	5.82
MgO	1.51	0.64	1.97
Na_2O	1.36	1.90	3.45
K_2O	4.04	4.14	1.78
S_{total}	0.007	0.016	0.041
MnO	0.11	0.14	0.08
H_2O	3.88	3.82	1.08
Others	8.173	8.0636	2.479

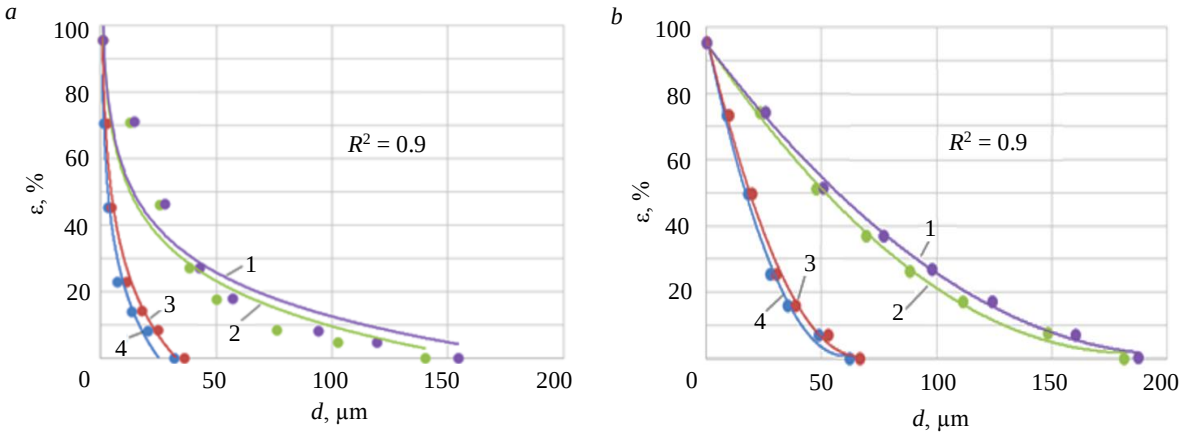

Fig.1. Influence of accelerated electron irradiation on the grain size distribution of ZCR (1, 2), zeolite minerals within the ZCR (3, 4), and the liberation coefficient of zeolites (clinoptilolite and chabazite): *a* – grinding without accelerated electron treatment; *b* – grinding with accelerated electron treatment at a dose of 2 kGy

• milling without accelerated electron treatment: ZCR from the Shivyrtuy deposit – the size of the milled rock is $y = -24.08\ln(x) + 77.6$; the size of zeolite in the milled rock is $y = -19.67\ln(x) + 100.1$; ZCR from the Talan-Gozagorsk deposit – the size of the milled rock is $y = -19.13\ln(x) + 100.5$; the size of zeolite in the milled rock is $y = -25.46\ln(x) + 88.7$;

• milling after accelerated electron treatment: ZCR from the Shivyrtuy deposit – the size of the milled rock is $y = 0.027x^2 - 3.2307x + 97.4$; the size of zeolite in the milled rock is $y = 0.0223x^2 - 2.9383x + 97.5$; ZCR from the Talan-Gozagorsk deposit – the size of the milled rock is $y = 0.0028x^2 - 1.0157x + 95.2$; the size of zeolite in the milled rock is $y = 0.0022x^2 - 0.9164x + 95$.

Figure 2 shows the temperature dependence of the heat capacity of the original and treated ZCR from the Talan-Gozagorsk deposit. Treating ZCR with accelerated electrons considerably affects this parameter.

The results of measuring the heat capacity of the original and accelerated electron-treated ZCR from the Shivyrtuy deposit showed that the initial heat capacities of both materials were identical (1.6 J/g) with a maximum value recorded at 130 °C. The maximum absolute value of the heat capacity of the ZCR from the Shivyrtuy deposit was considerably lower than that of the ZCR from the Talan-Gozagorsk deposit, which was 2.3 J/g. The higher heat capacity is attributed to the higher hematite content in the ZCR from the Talan-Gozagorsk deposit.

Journal of Mining Institute. 2024. Vol. 265. P. 129-139

The analysis of the Mössbauer spectroscopy results of the initial and accelerated electron-treated ZCR from the Talan-Gozagorsk deposit revealed that the sextets correspond to hematite, while the doublets correspond to montmorillonite (Table 2).

Treating ZCR with accelerated electrons considerably reduces the fine-dispersed hematite fraction and increases the coarse crystalline fraction. The accelerated electrons increased the iron content in the ZCR by removing volatile components and altering the magnitude of the resonance effect associated with the total iron content.

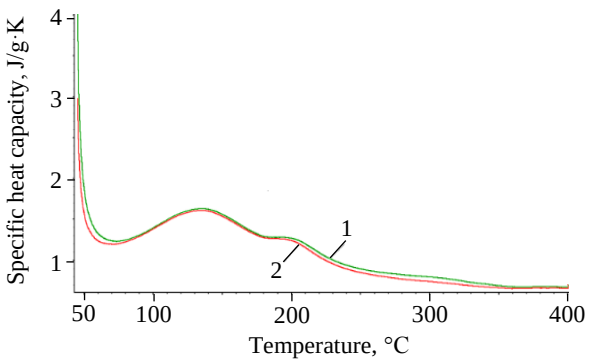

Fig.2. Temperature dependence of the specific heat capacity of ZCR from the Talan-Gozagorsk deposit
1 – before exposure to accelerated electrons;
2 – after exposure to accelerated electrons

Table 2

Results of Mössbauer studies of ZCR from Eastern Transbaikalia

ZCR	Spectrum component	Isomeric shift δ, mm/s	Magnetic fields on $Fe^{57}H$ nuclei, kOe	Component area *S*, %	Effect magnitude ε, %	Interpretation
Talan-Gozagorsk field, original	C1(Fe^{3+})	0.37	512	55.9	3.185	Hematite
	C2(Fe^{3+})	0.39	491	18.4		
	C3(Fe^{3+})	0.36	362	0.6		Goethite hydrogoethite
	D1(Fe^{3+})	0.38	0	10.1		Montmorillonite, hydromicas
	D2(Fe^{3+})	0.38	0	15.0		
Talan-Gozagorsk field, processed	C1(Fe^{3+})	0.37	512	51.4	3.262	Hematite
	C2(Fe^{3+})	0.37	492	24.5		
	C3(Fe^{3+})	0.36	362	1.5		Goethite hydrogoethite
	D1(Fe^{3+})	0.38	0	9.4		Montmorillonite, hydromicas
	D2(Fe^{3+})	0.36	0	13.2		
Shivyrtuy field, original	C1(Fe^{3+})	037	513	6.8	1.069	Hematite
	D1(Fe^{2+})	1.16	0	1.8		Olivine
	D2(Fe^{2+})	1.07	0	4.5		Chlorite
	D3(Fe^{3+})	0.43	0	7.7		Montmorillonite, hydromicas
	D4(Fe^{3+})	0.37	0	12.8		
	D5(Fe^{3+})	0.37	0	66.4		
Shivyrtuy field, processed	C1(Fe^{3+})	0.37	512	5.5	1.250	Hematite
	D1(Fe^{2+})	1.16	0	1.7		Olivine
	D2(Fe^{2+})	1.07	0	4.4		Chlorite
	D3(Fe^{3+})	0.41	0	9.3		Montmorillonite, hydromicas
	D4(Fe^{3+})	0.37	0	7.6		
	D5(Fe^{3+})	0.37	0	71.5		

The impact of accelerated electrons on ZCR intensifies the process of liberating intergrowths and separating zeolite minerals from rock-forming ones. The most significant effect on altering the technological properties of ZCR from the Shivyrtuy and Talan-Gozagorsk deposits was observed at low doses of accelerated electron exposure, specifically 2-4 kGy. When processing ZCR with a beam of accelerated electrons at low current densities, defects form in them. With a further increase in the absorbed energy (from 1 to 10 J/g), charge accumulates, leading to electrical breakdown in the ZCR. In this case, the discharge has a pulsating character, resulting in the formation of microcracks [21, 26], which considerably weaken the rocks, particularly along the boundaries of intergrowth between zeolite minerals and rock-forming minerals, determining the efficiency of subsequent selective disintegration [30, 31].

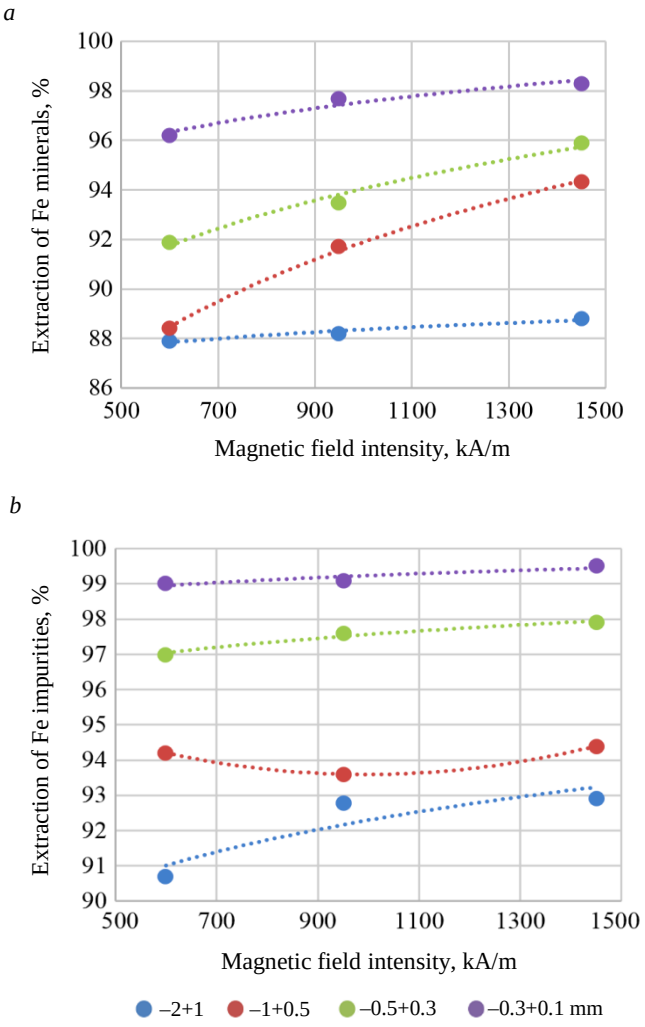

Fig.3. Dependence of the extraction of iron-containing minerals from ZCR from Shivyrtuy (*a*) and Talan-Gozagorsk (*b*) deposits on the magnetic field intensity for various particle sizes

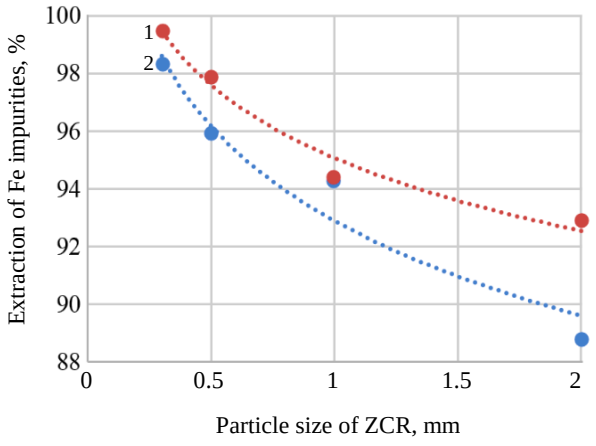

Fig.4. Dependence of the extraction of iron-containing minerals by electromagnetic separation on the particle size of ZCR

1 – Talan-Gozagorsk deposit; 2 – Shivyrtuy deposit

When ZCR from the Shivyrtuy and Talan-Gozagorsk deposits were exposed to accelerated electrons, it significantly altered their granulometric composition during milling and allowed for a more selective liberation of zeolite minerals (clinoptilolite and chabazite), improving subsequent magnetic and electrostatic separation processes. The electricity consumption was 0.6 kWh/t. The use of radiation treatment as a part of ore preparation operations, in combination with electromagnetic and electrostatic separation methods, reduced iron-containing minerals in the ZCR concentrates from the Shivyrtuy deposit from 3.14 to 0.36 % and from 11.2 to 0.12 % from the Talan-Gozagorsk deposit. Radiation treatment increased the content of coarse-grained hematite and the magnetic susceptibility of hematite from $14\text{-}25 \cdot 10^{-8}$ to $460\text{-}660 \cdot 10^{-8}$ m^3/kg, indicating the effective application of electromagnetic separation in the enrichment of ZCR.

When the results from the treatment of Eastern Transbaikalia ZCR with accelerated electrons were analyzed, we established technological dependencies, as presented in Fig.3, 4. The coefficient of determination for these dependencies was 0.9. Figure 3, *a* shows the relationship between the extraction of iron-containing minerals from ZCR from the Shivyrtuy deposit and the magnetic field intensity for different particle sizes. The relationship between the extraction of iron-containing minerals from ZCR from the Talan-Gozagorsk deposit and the magnetic field intensity for different particle sizes is shown in Fig.3, *b*.

Figure 4 illustrates the relationship between the extraction of iron-containing minerals by electromagnetic separation and the particle size of ZCR during treatment with accelerated electrons.

The following functions are used to show the dependence of the extraction of iron-containing minerals from ZCR subjected to accelerated electron treatment on the magnetic field intensity of the separator for different particle sizes (see Fig.3). For ZCR from the Shivyrtuy deposit: $y = 1.015\ln(x) + 81.35$ (particle size −2+1 mm), $y = 6.693\ln(x) + 45.65$ (particle size −1+0.5 mm), $y = 4.518\ln(x) + 62.84$ (particle size −0.5+0.3 mm),

Journal of Mining Institute. 2024. Vol. 265. P. 129-139

$y = 2.393\ln(x) + 81.02$ (particle size −0.3+0.1 mm). For ZCR from the Talan-Gozagorsk deposit: $y = 2.5232\ln(x) + 74.86$ (particle size −2+1 mm), $y = 4E - 06x^2 - 0.01x + 97.45$ (particle size −1+0.5 mm), $y = 1.0241\ln(x) + 90.49$ (particle size −0.5+0.3 mm), $y = 0.561\ln(x) + 95.35$ (particle size −0.3+0.1 mm).

The study of the dependence of iron-containing mineral content on the particle size of ZCR treated with accelerated electrons (after magnetic separation) showed that as the rock particle size increased from 0.07 to 0.1 mm, the iron content increased as follows. For the ZCR from the Shivyrtuy deposit, the iron content increased from 0.35 to 0.85 %. For the ZCR from the Talan-Gozagorsk deposit, the iron content increased from 0.1 to 1.1 %. The dependence of the extraction of iron-containing minerals from ZCR on the particle size (Fig.4) (after treatment with accelerated electrons) is described by the following functions: $y = -3.647\ln(x) + 95.07$ (for ZCR from the Shivyrtuy deposit) and $y = -4.74\ln(x) + 92.89$ (for ZCR from the Talan-Gozagorsk deposit).

The study on the possibility of extracting iron-containing minerals from fine-dispersed accelerated electron-treated ZCR from Eastern Transbaikalia with a particle size of −0.1+0.074 mm using magnetic separation in an isodynamic field allowed to determine the dependence of iron impurity content in zeolite (nonmagnetic) products on their particle size. The corresponding functions characterizing the parameters of this dependence were determined: $y = 6.539x + 1.3262$ (for ZCR from the Shivyrtuy deposit) and $y = 30.385x - 0.2685$ (for ZCR from the Talan-Gozagorsk deposit).

The radiation treatment with accelerated electrons of ZCR from the Shivyrtuy and Talan-Gozagorsk deposits increased the extraction of iron-containing minerals by electromagnetic separation to 98.3 and 99.5 %, respectively. This ensures the production of high-quality zeolite products that can be used in various industrial sectors and in waste management technologies in mining. The greatest effect was achieved at a magnetic field intensity of 1450 kA/m and a particle size of −0.3+0.1 mm (Table 3). The enrichment of ZCR in an isodynamic field is characterized by high iron impurity extraction rates at a particle size of 0.1 mm (Table 4).

Table 3

Results of dry electromagnetic separation of ZCR from Eastern Transbaikalia with a particle size of −2+0.1 mm

Deposit	Particle size, mm	Average Fe impurity content in raw material, %	Zeolite content in product, %	Fe minerals content in zeolite product, %	Other impurities content, %	Yield, %
Shivyrtuy	−2+1	3.14	73.50	1.78	24.72	9.4
	−1+0.5		84.20	1.11	14.69	18.4
	−0.5+0.3		85.90	0.88	13.22	27.7
	−0.3+0.1		88.90	0.36	10.74	44.5
Talan-Gozagorsk	−2+1	11.2	70.10	8.17	21.73	8.8
	−1+0.5		75.20	3.74	21.06	17.1
	−0.5+0.3		84.90	1.08	14.02	23.2
	−0.3+0.1		89.60	0.12	10.28	50.9

Table 4

Results of dry electromagnetic separation of fine-dispersed ZCR in an isodynamic field

Deposit	Magnetic field intensity, kA/m	Current strength, A	Particle size, mm	Extraction of Fe minerals from magnetic product, %	Mass fraction of Fe in magnetic product, %	Yield, %
Shivyrtuy	600	0.50	−0.1+0.074	89.7	92.4	44.7
			−0.074+0.05	96.4	94.4	55.3
	950	1.0	−0.1+0.074	93.3	95.6	47.5
			−0.074+0.05	97.9	96.2	52.5
	1450	1.57	−0.1+0.074	95.4	96.7	49.8
			−0.074+0.05	98.2	97.1	50.2

End of Table 4

Deposit	Magnetic field intensity, kA/m	Current strength, A	Particle size, mm	Extraction of Fe minerals from magnetic product, %	Mass fraction of Fe in magnetic product, %	Yield, %
Talan-Gozagorsk	600	0.50	−0.1+0.074	98.7	96.3	49.6
			−0.074+0.05	99.1	96.8	50.4
	950	1.0	−0.1+0.074	98.5	96.2	47.4
			−0.074+0.05	99.2	98.1	52.6
	1450	1.57	−0.1+0.074	98.3	97.4	46.1
			−0.074+0.05	99.6	98.7	53.9

The application of directional methods, such as treatment with accelerated electrons, in the beneficiation schemes of ZCR considerably enhances the adsorption capacity of natural zeolites (from 147 to 164 mg/g for ZCR from the Shivyrtuy deposit and from 246 to 287 mg/g for ZCR from the Talan-Gozagorsk deposit) [28]. The increase in the sorption capacity of ZCR is achieved via the extraction of iron-bearing minerals and the purification of the pore space of natural zeolites from organic compounds, which is achieved through preprocessing using directional methods in combination with magnetic and electrostatic separations [32-34].

One crucial factor in developing beneficiation and processing technologies for ZCR is the ability to comprehensively process ZCR and separate them from rock-forming minerals [30, 31]. The obtained dependencies in the processing and beneficiation of ZCR from Eastern Transbaikalia allowed to determine a rational sequence of operations in the technological scheme: crushing; enhancing contrast and altering physicochemical properties through directional treatment (treatment with accelerated electrons); milling; and magnetic and electrostatic separation to obtain high-quality zeolite concentrate, iron-bearing (hematite, hydrogoethite, olivine, and pyroxene), and polymineral (quartz, plagioclases, calcite, montmorillonite) products, which are sent for further processing or practical use. In particular, the iron-bearing product can serve as a source of iron, while the polymineral product can be used as a binder for backfilling mined-out areas [35-37].

Creating beneficiation technologies for ZCR involves the following: directed impact before crushing and milling of the material used for disintegration and altering the contrast properties of minerals; maximum extraction of Fe-bearing minerals by electromagnetic separation using separators with an isodynamic field; and extraction of nonmagnetic impurities through electrostatic separation.

Theoretical and experimental studies allowed us to identify the main methods of beneficiation and ore preparation for ZCR, which are crucial for developing the technology selection algorithm for the beneficiation of ZCR from Eastern Transbaikalia (Table 5).

Table 5

Separation methods for ZCR depending on the mineral composition

Separated mineral	Main associated minerals	Concentration methods
Zeolite	Feldspars, micas > 50 μm	Crushing in rotary crushers and milling in ball mills. Directed treatments (accelerated electrons). Electromagnetic separation (for fine-dispersed ZCR using an electromagnetic separator with an isodynamic field). Electrostatic separation
	Clay minerals < 50 μm	Directed treatments (accelerated electrons). Electromagnetic separation using an electromagnetic separator with an isodynamic field. Electrostatic separation with heating and electrification
	Minerals of the quartz group, clay minerals	Crushing in rotary crushers and milling in ball mills. Accelerated electrons. Electrostatic separation

Journal of Mining Institute. 2024. Vol. 265. P. 129-139

The proposed systematization allows us to determine the number of stages in ore preparation, select the necessary type of impact on ZCR, and develop rational processes for their enrichment and processing, which determines the efficiency of separating zeolite minerals from rock-forming minerals, taking into account technological properties (electrical conductivity and magnetic susceptibility) and technological performance indicators. The experimental studies on the enrichment of ZCR serve as the basis for the development of technological schemes for their enrichment.

The developed scientific and methodological foundations for the processing and enrichment of ZCR have been tested under industrial conditions. The possibility of implementing the developed technology for the enrichment of ZCR from the Talan-Gozagorsk and Shivyrtuy deposits in the production complex of OOO "Scientific and Production Entrepreneurship Society "Zeolite" (Krasnokamensk) was studied, resulting in the production of high-quality zeolite products. To achieve the required quality parameters of zeolite products, which meet the technical specifications, the following processes should be introduced into the technological scheme:

- directed impact on ZCR before milling;
- electromagnetic separation in an isodynamic field to achieve the maximum extraction of iron-containing minerals;
- electrostatic separation;
- electrification of ZCR with salicylic acid vapor to enhance the contrast of minerals separated by electrostatic separation.

The technological scheme for the enrichment of ZCR is shown in Fig.5. The practical significance of the results was confirmed by implementing the developed technology for ZCR enrichment

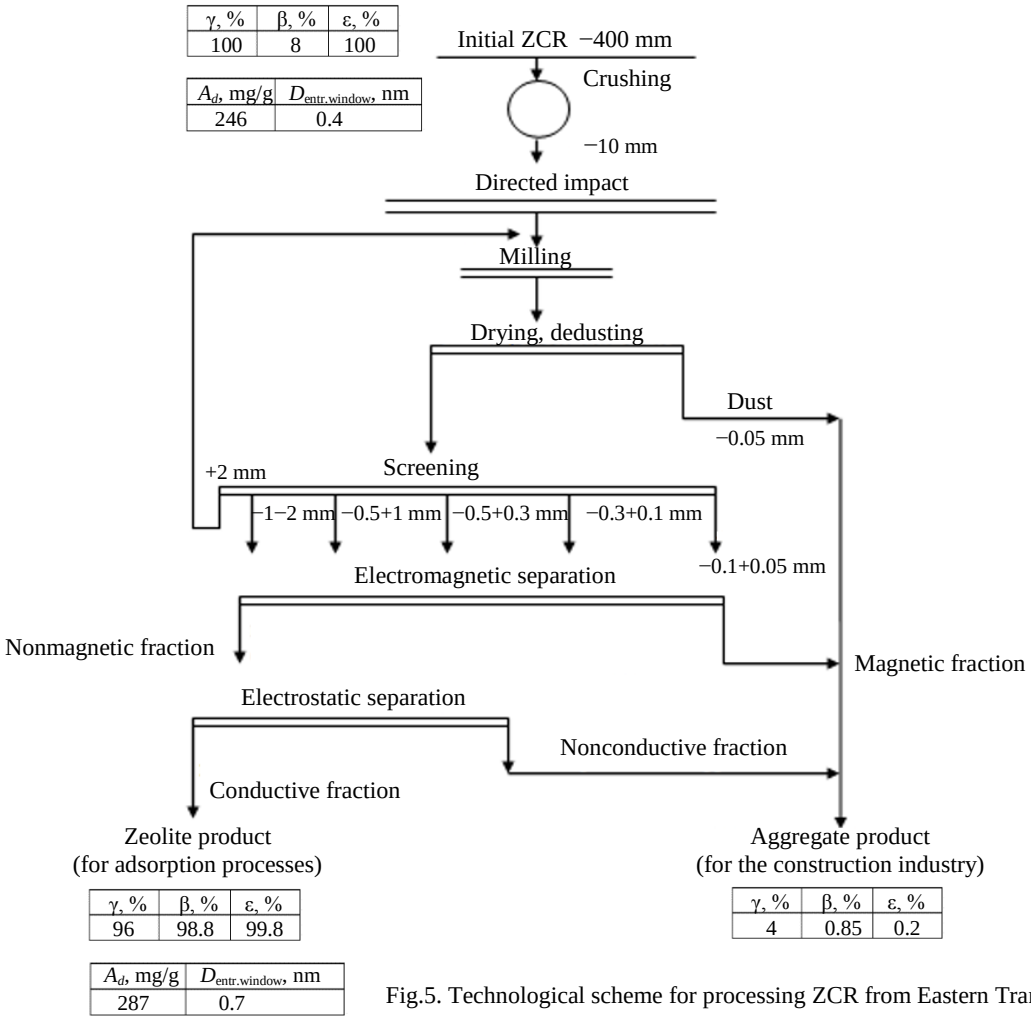

Fig.5. Technological scheme for processing ZCR from Eastern Transbaikalia [21]

in the techno-economic calculations of OOO "Scientific and Production Entrepreneurship Society "Zeolite".

The assessment of the economic efficiency of implementing the technology for processing natural ZCR at the beneficiation plant of OOO "Scientific and Production Entrepreneurship Society "Zeolite" showed that the cost for obtaining high-quality zeolite product with a monomineral content of up to 99.1 % will be approximately 10,000 rubles per ton, and the market price of the pro-duct of the appropriate quality will be up to 100,000 rubles per ton. The calculations justify the environmental and economic feasibility of using directed interventions during the preparation stage of ZCR from Eastern Transbaikalia. Thus, the implementation of the proposed technologies for the beneficiation and processing of ZCR from Eastern Transbaikalia is sufficiently effective, with a discounted payback period of one year.

Conclusion. In this study, it was determined that accelerated electron treatment of ZCR from Shivyrtuy and Talan-Gozagorsk deposits significantly altered the granulometric composition during milling and provided a more selective liberation of zeolite minerals (clinoptilolite and chabazite), thus improving the subsequent processes of magnetic and electrostatic separation. The use of radiation treatment as an ore preparation operation in combination with the electromagnetic and electrostatic separation methods contributes to the reduction of the Fe-containing mineral content in concentrates from 3.14 to 0.36 % and from 11.2 to 0.12 % for ZCR from Shivyrtuy and Talan-Gozagorsk deposits, respectively. The radiation treatment increased the content of coarse-crystalline hematite and the magnetic susceptibility parameter of hematite from $14\text{-}25 \cdot 10^{-8}$ to $460\text{-}660 \cdot 10^{-8}$ m^3/kg. This enables the effective use of electromagnetic separation during ZCR beneficiation and the production of high-quality zeolite products, which can be used in various industries and in waste management technologies in the mining industry.

REFERENCES

1. Gorlova O.E., Shadrunova I.V., Zhilina V.A. Development of deep and comprehensive processing processes of technogenic mineral raw materials in a view of sustainable development strategy. IMPC 2018 – 29th International Mineral Processing Congress, 17-21 September 2018, Moscow, Russian Federation. Canadian Institute of Mining, Metallurgy and Petroleum, 2019, p. 3279-3287.

2. Solodukhina M.A., Yurgenson G.A. Arsenic in the landscapes of the Sherlovogorsk Ore District (Eastern Transbaikalia). Chita: Zabaikalskii gosudarstvennyi universitet, 2018, p. 176 (in Russian).

3. Kudelko J. Effectiveness of mineral waste management. *International Journal of Mining, Reclamation and Environment*. 2018. Vol. 32. N 6, p. 440-448. DOI: 10.1080/17480930.2018.1438036

4. Zaharyan S.V., Gedgagov E.I., Yun A.B. Increase in an Ecological Safety at the Entities of Non-Ferrous Metallurgy Due to Use of Sorption Processes. *Ecology and Industry of Russia*. 2018. Vol. 22. N 1, p. 26-32 (in Russian). DOI: 10.18412/1816-0395-2018-1-26-32

5. Shadrunova I.V., Gorlova O.E., Zhilina V.A. The new paradigm of an environmentally-driven resourcesaving technologies for processing of mining. *IOP Conference Series: Materials Science and Engineering*. 2019. Vol. 687. Iss. 6. N 066048. DOI: 10.1088/1757-899X/687/6/066048

6. Kauppila P., Ryaisyanen M.L., Myullyuoya S. Best environmental practices in the mining industry. Khelsinki: Tsentr okruzhayushchei sredy Finlyandii, 2013, p. 241 (in Russian).

7. Abdrakhmanova R.N., Orehkova N.N., Gorlova O.E. Adaptation of the SAVMIN process for mine water treatment. *IOP Conference Series: Materials Science and Engineering*. 2019. Vol. 687. Iss. 6. N 066077. DOI: 10.1088/1757-899X/687/6/066077

8. Zakondyrin A.E. Best Available Techniques in mining industry: topical issues and solution methods. *Mining Informational and Analytical Bulletin.* 2020. N 6-1, p. 55-64 (in Russian). DOI: 10.25018/0236-1493-2020-61-0-55-64

9. Skobelev D.O. Information and methodological support to the implementation of Best Available Techniques in the Russian Federation. *Upravlenie.* 2019. Vol. 7. N 4, p. 5-15 (in Russian). DOI: 10.26425/2309-3633-2019-4-5-15

10. Savon D.Yu. Improvement of system of paid environmental management. *Mining Informational and Analytical Bulletin.* 2014. N 6, p. 314-320 (in Russian).

11. Alam R., Ahmed Z., Howladar M.F. Evaluation of heavy metal contamination in water, soil and plant around the open landfill site Mogla Bazar in Sylhet, Bangladesh. *Groundwater for Sustainable Development*. 2020. Vol. 10. N 100311. DOI: 10.1016/j.gsd.2019.100311

12. Shushkov D.A., Shuktomova I.I. Sorption of radioactive elements by zeolite-bearing rocks. *Proceedings of the Komi Science Centre of the Ural Division of the Russian Academy of Sciences.* 2013. Iss. 1 (13), p. 69-73 (in Russian).

13. Sivashankari L., Rajkishore S.K., Lakshmanan A., Subramanian K.S. Optimization of dry milling process for synthesizing nano zeolites. *International Journal of Chemical Studies*. 2019. Vol. 7. N 4, p. 328-333.

14. Tyaglov S.G., Voskresova G.N. Features of determination of technology as NDT: Russian and foreign experience. *Journal of Economic Regulation.* 2019. Vol. 10. N 2, p. 96-112 (in Russian). DOI: 10.17835/2078-5429.2019.10.2.096-112

15. Kotova O.B., Shushkov D.A. A process of zeolites production from fly ash. *Obogashchenie rud.* 2015. N 5, p. 60-63 (in Russian). DOI: 10.17580/or.2015.05.10

16. Manchuk J.G., Birks J.S., McClain C.N. et al. Estimating Stable Measured Values and Detecting Anomalies in Groundwater Geochemistry Time Series Data Across the Athabasca Oil Sands Area, Canada. *Natural Resources Research*. 2021. Vol. 30. N 2, p. 1755-1779. DOI: 10.1007/s11053-020-09801-5

17. Cecinati F., Matthews T., Natarajan S. et al. Mining Social Media to Identify Heat Waves. *International Journal of Environmental Research and Public Health*. 2019. Vol. 16. Iss. 5. N 762. DOI: 10.3390/ijerph16050762

18. Li H., Watson J., Zhang Y. et al. Environment-enhancing process for algal wastewater treatment, heavy metal control and hydrothermal biofuel production: A critical review. *Bioresource Technology*. 2020. Vol. 298. N 122421. DOI: 10.1016/j.biortech.2019.122421

19. Uçkun Ş., Sarıkaya M., Top S., Timür İ. Removal of Heavy Metals from Wastewater Solution Using a Mechanically Activated Novel Zeolitic Material. *Journal of Mining Science*. 2020. Vol. 56. N 6, p. 1010-1023. DOI: 10.1134/S1062739120060137

20. Khatkova A.N., Rostovtsev V.I., Razmakhnin K.K., Emelyanov V.N. Effect of Accelerated Electrons on Zeolite-Containing Rocks of the East Transbaikalia. *Journal of Mining Science.* 2013. Vol. 49. N 6, p. 1004-1010. DOI: 10.1134/S1062739149060221

21. Razmakhnin K.K. Development and justification of treatment and modification technology for East Transbaikalia zeolite rocks. *Journal of Mining Science.* 2021. Vol. 57. N 3, p. 493-501. DOI: 10.15372/FTPRPI20210314

22. Ping Wang, Zehang Sun, Yuanan Hu, Hefa Cheng. Leaching of heavy metals from abandoned mine tailings brought by precipitation and the associated environmental impact. *Science of the Total Environment*. 2019. Vol. 695. N 133893. DOI: 10.1016/j.scitotenv.2019.133893

23. Xueyan Zou, Yanbao Zhao, Zhijun Zhang. Preparation of hydroxyapatite nanostructures with different morphologies and adsorption behavior on seven heavy metals ions. *Journal of Contaminant Hydrology*. 2019. Vol. 226. N 103538. DOI: 10.1016/j.jconhyd.2019.103538

24. Mei Hong, Lingyun Yu, Yanding Wang et al. Heavy metal adsorption with zeolites: The role of hierarchical pore architecture. *Chemical Engineering Journal*. 2019. Vol. 359, p. 363-372. DOI: 10.1016/j.cej.2018.11.087

25. Yiping Su, Jing Wang , Shun Li et al. Self-templated microwave-assisted hydrothermal synthesis of two-dimensional holey hydroxyapatite nanosheets for efficient heavy metal removal. *Environmental Science and Pollution Research*. 2019. Vol. 26. Iss. 29, p. 30076-30086. DOI: 10.1007/s11356-019-06160-4

26. Rostovtsev V.I. Theoretical fundamentals and practice of electrochemical and radiation effects application in ore preparation and mineral processing. *Vestnik Chitinskogo gosudarstvennogo universiteta.* 2010. N 8 (65), p. 91-99 (in Russian).

27. Yusupov T.S., Baksheeva I.I., Rostovtsev V.I. Analysis of Different-Type Mechanical Effects on Selectivity of Mineral Dissociation. *Journal of Mining Science.* 2015. Vol. 51. N 6, p. 1248-1253. DOI: 10.1134/S1062739115060552

28. Milyutin V.V., Nekrasova N.A., Razmakhnin K.K., Khatkova A.N. Natural Zeolites of Eastern Transbaikalia in Technologies for Mining Enterprises Wastewater Treatment. *Journal of Environmental Research, Engineering and Management*. 2020. Vol. 76. N 3, p. 62-70. DOI: 10.5755/j01.erem.76.3.24220

29. Litvinenko V.G., Razmakhnin K.K. Natural zeolites in technologies to ensure environmental safety of mining industries. *Fundamentalnye i prikladnye voprosy gornykh nauk*. 2021. Vol. 8. N 2, p. 158-162 (in Russian). DOI: 10.15372/FPVGN2021080224

30. Chanturia V.A., Shadrunova I.V., Zhilina V.A. Recovery of mining waste in the complex development of mineral resources. Moscow: Publishing house Sputnik+, 2019, p. 120.

31. Chanturia V.A., Shadrunova I.V., Zhilina V.A. et al. Environmentally focused processing of mining waste. Moscow: OOO "Izd-vo "Sputnik+", 2018, p. 200 (in Russian).

32. Itzel-Hernández G., Hernández M.A., Portillo R. et al. Hierarchical structure of nanoporosity of Mexican natural zeolites of clinoptilolite type. *Bulletin of the Tomsk Polytechnic University. Geo Assets Engineering.* 2018. Vol. 329. N 10, p. 107-117 (in Russian). DOI: 10.18799/24131830/2018/10/2110

33. Ying Wang, Yange Yu, Haiyan Li, Chanchan Shen. Comparison study of phosphorus adsorption on different waste solids: Fly ash, red mud and ferric-alum water treatment residues. *Journal of Environmental Sciences.* 2016. Vol. 50, p. 79-86. DOI: 10.1016/j.jes.2016.04.025

34. Kotova O.B., Shabalin I.L., Kotova E.L. Phase transformations in synthesis technologies and sorption properties of zeolites from coal fly ash. *Journal of Mining Institute.* 2016. Vol. 220, p. 526-531. DOI: 10.18454/PMI.2016.4.526

35. Sugonyako D.V., Zenitova L.A. Silicon dioxide as a reinforcing filler of polymeric materials. *Herald of Technological University.* 2015. Vol. 18. N 5, p. 94-100 (in Russian).

36. Bogdanov A.V., Fedotov K.V., Kachor O.L. Development of scientific and practical foundations for the recuperative technology of ecoconcreting of arsenic-containing waste from the mining and processing industry. Irkutsk: Izd-vo IrGTU, 2014, p. 182 (in Russian).

37. Aleksandrova T.N., Afanasova A.V., Nikolaeva N.V. On the Use of Microwave Treatment of Gold-Containing Concentrates for Its Efficient Processing. New Materials: Preparation, Properties and Applications in the Aspect of Nanotechnology. 2020, p. 179-188.

***Authors*: Konstantin K. Razmakhnin,** *Doctor of Engineering Sciences, Associate Professor, constantin-const@mail.ru, https://orcid.org/0000-0003-2944-7642* (*Transbaikal State University, Chita, Russia*), **Alisa N. Khatkova,** *Doctor of Engineering Sciences, Vice-Rector, https://orcid.org/0000-0001-6527-0026* (*Transbaikal State University, Chita, Russia*), **Lidiya V. Shumilova,** *Doctor of Engineering Sciences, Professor, https://orcid.org/0000-0001-5991-9204* (*Transbaikal State University, Chita, Russia*).

The authors declare no conflict of interests.

ISSN 2411-3336; e-ISSN 2541-9404

JOURNAL OF MINING INSTITUTE
Zapiski Gornogo instituta
Journal homepage: pmi.spmi.ru

Research article

Optimization of the location of a multilateral well in a thin oil rim, complicated by the presence of an extensive gas cap

Kirill O. TOMSKII ✉, **Mariya S. IVANOVA**
Mirny Polytechnic Institute (*branch*) *of North-Eastern Federal University, Mirny, Russia*

How to cite this article: Tomskii K.O., Ivanova M.S. Optimization of the location of a multilateral well in a thin oil rim, complicated by the presence of an extensive gas cap. Journal of Mining Institute. 2024. Vol. 265, p. 140-146. EDN XOVEYF

Abstract. The specific share of the reserves of hard-to-recover hydrocarbon raw materials is steadily growing. The search for technologies to increase the hydrocarbon recovery factor is one of the most urgent tasks facing the oil and gas industry. One of the methods to expand the coverage of oil reserves and increase oil recovery is to use the technology of drilling multilateral wells with a fishbone trajectory. In the Russian Federation, the most branched well was drilled in the Republic of Sakha (Yakutia) at the Srednebotuobinskoye oil and gas condensate field. The main object of development is the Botuobinsky horizon (Bt reservoir). About 75 % of the geological reserves of the reservoir are concentrated in a thin oil rim with an average oil-saturated layer thickness of 10 m with an extensive gas cap. This circumstance is one of the main complicating factors in the development of the Srednebotuobinskoye oil and gas condensate field. For such complex wells, one of the most important design stages is to determine the optimal location of the fishbone well in an oil-saturated reservoir. The article shows the results of sector modeling in the conditions of the Srednebotuobinskoye field to determine the optimal location of multilateral wells using Tempest simulator.

***Keywords*:** Srednebotuobinskoye oil and gas condensate field; multilateral well; cumulative oil production; oil flow rate; gas cap; gas factor; bottom water; thin oil rim; inclined oil-water contact

Received: 30.09.2022 ***Accepted: 03.04.2023*** ***Online: 18.07.2023*** ***Published: 29.02.2024***

Introduction. The Srednebotuobinskoye oil and gas condensate field (SBNGKM) in the Republic of Sakha (Yakutia) was discovered in 1971 and put into commercial operation in 2013 as a result of the expansion of Rosneft's activities and the development of the region [1-3].

The main development target is the Bt reservoir of the Botuobinsky horizon, which contains 77 % of the initial recoverable oil reserves and provides 99 % of its production. The main design solution for the Botuobinsky horizon provides for the use of a system of horizontal wells 1250 m long with a distance between well rows of 300 and 100 m [4-6].

The Botuobinsky horizon is represented by terrigenous sandstones deposited in coastal-marine conditions. The bar-like body, the axial part of which strikes northeast, was formed during the slow transgression of the marine basin. To the northwest of the deposit, a vast lower beach zone extended along the gently sloping coast. The bar-like body itself is probably formed by tidal and alongshore (northeastward) currents [7-9].

Taking into account the complex geological structure of the field, one of the main directions of development of the SBNGKM is the construction of multilateral fishbone wells [10-12]. Multilateral fishbone wells got their name because of the external similarity of the structure with a fish bone (Fig.1). Due to their design features, they cover a much larger field area compared to a single horizontal well, thereby increasing well productivity and reducing drilling costs [13]. A multilateral well with several branches from the main horizontal wellbore makes it possible to replace several single horizontal wells, increasing the profitability of the entire project [14, 15]. In addition, this technology

Journal of Mining institute. 2024. Vol. 265. P. 140-146

is practically the only way to effectively develop thin under-gas oil rims, since other common technologies for increasing productivity, such as hydraulic fracturing, cannot be applied with similar complications that are typical for SBNGKM [16-18].

The technical characteristics of the fishbone well, which were used in the simulation, are as follows: the total horizontal part in the reservoir is 6052 m; main shaft length 1406.6 m; number of sidetracks 9 m; sidetrack length 334-1006 m; depression on the reservoir 5 atm; oil-saturated capacity 14.4 m.

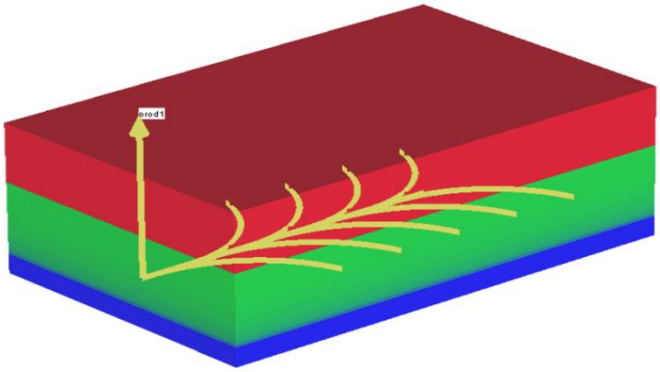

Fig.1. Sector model used in calculations

The problem of choosing the optimal well placement in the gas-oil-water zone of the reservoir is primarily due to the presence of an extensive gas cap, which can break through to the wells, thereby stopping the production process from the well [19-21].

The closer the well is located to the gas-oil contact (GOC), the earlier we observe gas breakthrough, respectively, the shutdown of the well occurs in a relatively short time, which leads to a significant decrease in cumulative oil production. On the other hand, if the well is located in the immediate vicinity of the oil-water contact (OWC), thereby moving it as far as possible from the GOC level, there is a breakthrough of bottom water, rapid watering of the produced product, which in turn also leads to a decrease in cumulative production oil.

Due to the high salinity of reservoir waters of the SBNGKM, the problem of reservoir water breakthrough in wells is not as acute as gas breakthroughs from the gas cap [22].

It can be concluded that for a certain sector of the field there is an optimal location of the well, in which we can get the maximum cumulative oil production, and, accordingly, the maximum economic benefit. An effective solution to the problem can be obtained solely with the help of hydrodynamic modeling, considering different options for the location of the well in the oil-saturated thickness, analyzing the main technological indicators of field development at each location and focusing on such an indicator as cumulative oil production [23, 24].

The novelty of the project is to substantiate, using hydrodynamic modeling, the optimal location of a multilateral fishbone well with nine branches with a total length of a horizontal wellbore of 5050 m in an oil rim with a thickness of 11 m in difficult geological conditions of the SBNGKM.

Methods. The calculations were carried out on the Tempest MORE hydrodynamic simulator manufactured by Roxar (Emerson Group Company). The simulator is a tool for numerically solving the problems of fluid movement in a reservoir and allows performing the following basic operations: numerical solution of the equations of conservation and filtration of phases and components, analysis of filtration flows and calculated technological indicators, modeling of measures to control the development process.

The calculations were carried out on a sector model consisting of 112746 cells with dimensions of 1425×901×23 m (Fig.1). The absolute depth of the gas-oil contact is 1562 m, the depth of the water-oil contact is 1573 m. The calculations were carried out for a multilateral well (MGZS) fishbone, consisting of the main horizontal wellbore 1050 m long and nine branches 500 m long. The total length of the horizontal wellbore is 5050 m. The main goal work is to determine the optimal location of the MSGS in the oil-saturated part of the reservoir. Calculations were carried out according to the following main technological indicators: cumulative production of oil, gas, liquids; flow rate of oil, gas, liquid; gas factor.

The calculations were carried out for 50 years for different options for the location of the MGZS along the oil-saturated thickness in the range of 1563-1572 m (the options for the location of the fishbone well varied from 1 to 10 m from the gas-oil contact zone).

a

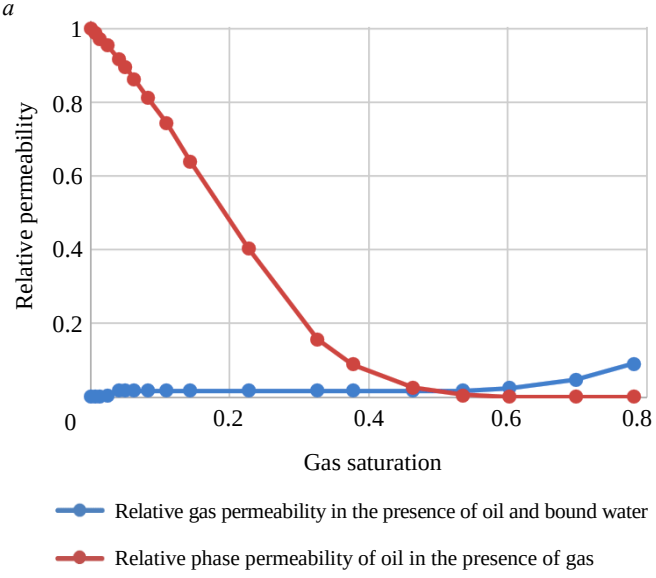

b

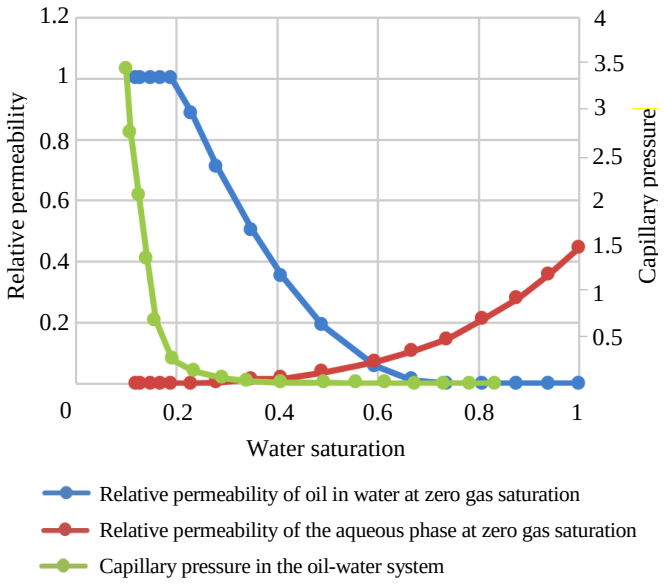

Fig.2. Relative gas-oil (*a*) and water-oil (*b*) phase permeabilities

Figure 2 shows the relative phase permeability of the fluids included in the model.

The main pressure-volume-temperature (*PVT*) properties of the fluid and the porosity and permeability properties of the reservoir, included in the model: oil density 864.2 kg/m^3; molecular weight 1000 kg/m^3; gas density 0.822 kg/m^3; reservoir water density at reservoir conditions 1236 kg/m^3; water compressibility 0.255 atm^{-1}; reduced pressure 140.1 atm; viscosity 8.0 cPs; critical water saturation 0.23; critical gas saturation 0.05; residual oil saturation in water 0.31; residual oil saturation for gas 0.43; residual water saturation 0.08; permeability 369.3 mD; porosity 0.16.

The discussion of the results. As a result of the simulation, the following results were obtained. Figure 3 shows the dynamics of oil production for different well locations. Well location depths ranging from 1563 m (the closest location t o the GOC) to 1572 m (the furthest location from the GOC) were used as designation of the well location options.

From the analysis of dependences in Fig.3, one can see how the well flow rate will change during the development period (50 years). When modeling in the Tempest software product, a limitation was set – the maximum liquid flow rate was 60 m^3/day. In addition, for this field, a GOR limit of 2400 m^3/m^3 was set (Fig.4) that corresponds to gas breakthrough. Figure 4 shows a stepwise decrease in the flow rate, which is typical for the estimated achievement of the gas factor and corresponds to a decrease in the flow rate in order to limit the gas inflow. From the analysis of the GOR data, one can clearly see how long it will take gas to break through from the gas cap into the well, which is equivalent to stopping the well for SBNGKM conditions. Due to inherent limitations in the Tempest simulator, when the maximum value of the GOR is reached, a decrease in the flow rate is observed. Gas breakthrough into the well for the case of the maximum distance from the GOC (1572 m) will occur by 2031, for a well with a depth of 1571 m – by 2030, and for a well with a depth of 1570 m – by 2029.

Analysis of the water cut calculation results (Fig.5) at different depths of the MGZS location shows that the water cut of the well production reaches 0.24 m^3/m^3 by the time of gas breakthrough for the case where the well is located at a distance of 1 m from the OWC. For depths up to 1567 m, there is a slight increase in water cut to 0.01, for depths of 1568; 1569; 1570; 1571 and 1572 m – increase in water cut up to the moment of gas breakthrough up to 0.02; 0.07; 0.13; 0.18 and 0.24 m^3/m^3, respectively.

Figure 6 shows the cumulative oil production at different depths of the fishbone well.

Journal of Mining institute. 2024. Vol. 265. P. 140-146

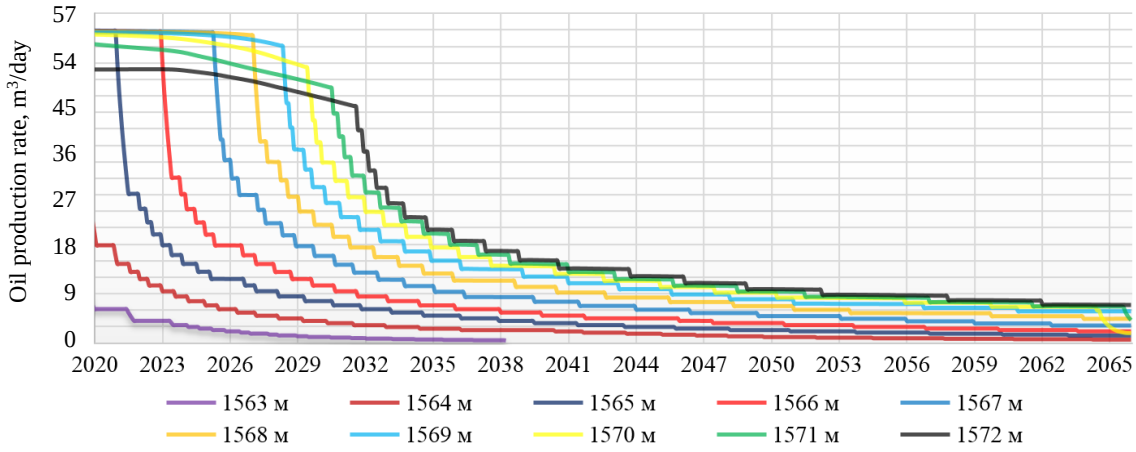

Fig.3. Dynamics of oil production at different depths of MGZS location

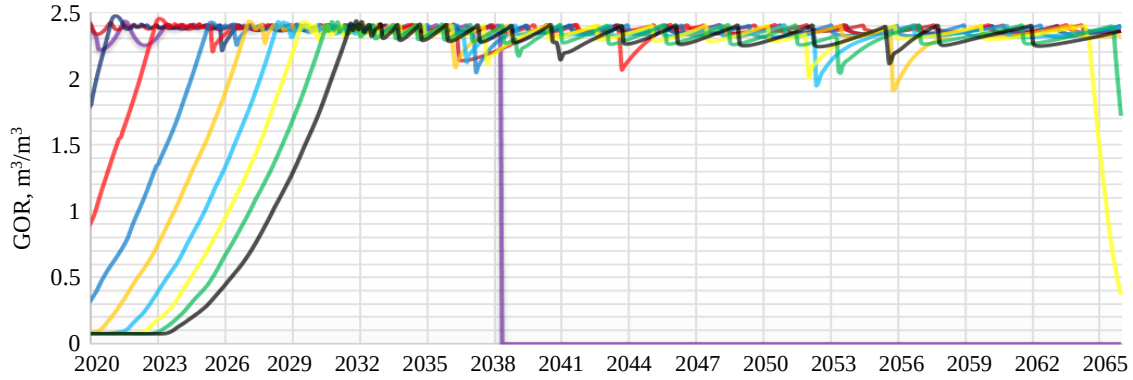

Fig.4. GOR dynamics at different depths of MGZS location
Symbols see in Fig.3

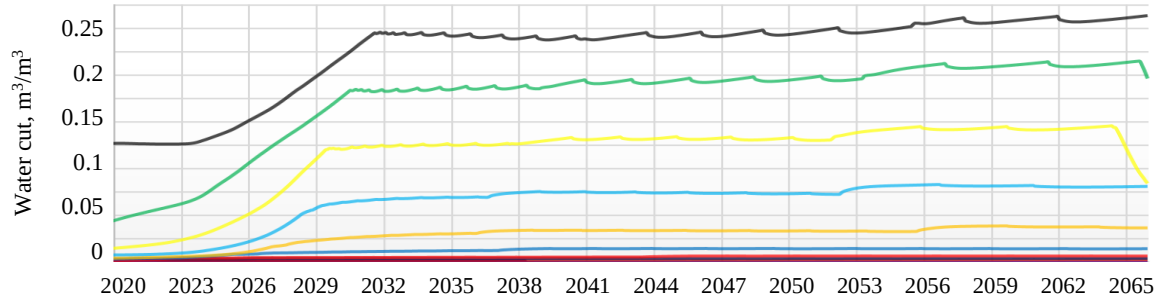

Fig.5. Dynamics of water cut at different depths of MGZS location
Symbols see in Fig.3

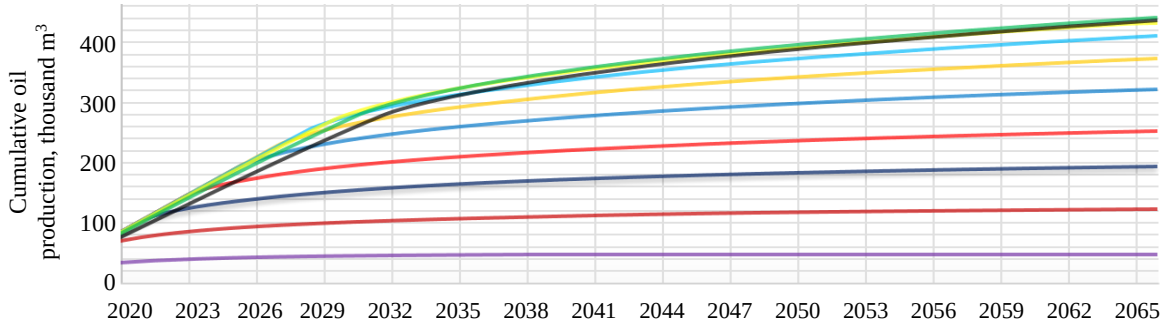

Fig.6. Dynamics of cumulative oil production at different depths of MGZS location
Symbols see in Fig.3

Based on the results of calculating the main technological indicators for different location of the fishbone well in the oil-saturated thickness, it can be concluded that the location of the multilateral well at a depth of 1571 m (9 m from the GOC) is optimal in terms of cumulative oil production, which will be 440,000 m^3 after 50 years of operation. At the same time, the cumulative oil production by the beginning of the gas breakthrough is of greater interest, which is tantamount to shutting down the well. With such a consideration, it can be concluded that the well with a depth of 1571 m shows the best results in terms of "cumulative oil production". By 2031, the cumulative oil production from a 1572 m well will be 274,000 m^3; by 2030, the cumulative oil production from a 1571 m well – 280,000 m^3; by 2029, the cumulative oil production from a 1570 m well – 267,000 m^3.

The adopted optimal wiring for gas-water-oil zones at the SBNGKM corresponds to the option with a 2-3 m distance from the water-oil contact, which is confirmed by the calculations. However, it should be taken into account that for the conditions of development of the SBNGKM, due to the thickness of the oil-saturated layer and the size of the gas cap changing over the area of the field, it is necessary to drill the well individually for a certain area of the field depending on the existing restrictions [25, 26].

An important feature of the SBNGKM, which should be taken into account when drilling a well, is the presence of an inclined oil-water contact. According to the results of the data from the wells of the SBNGKM, it is possible to map the inclined oil-water contact. In this case, a layer with increased viscosity is found in the contact zone. The current working version of the presence of a non-horizontal OWC is accepted as "relatively young neotectonic movements, the consequences of which are currently not fully compensated by gravitational forces due to the high viscosity of oil in the lower part of the deposit and the low phase permeability of water" [28].

The existence of inclined oil-water contacts in fields, especially those associated with the ancient deposits is an established fact. Attempts to explain the nature of the OWC slope are still debatable [30].

At the SBNGKM, in the intervals of 1564-1580 m, there is a slight inclination of the OWC in the southeast direction. According to the results of well logging, core study and analysis of reservoir samples approximately in the indicated intervals, an oil layer with an increased viscosity is established. This observation is confirmed by the results of field and laboratory studies of reservoir fluids and core. According to laboratory analyzes of deep interval oil samples, an increase in oil viscosity in the reservoir section is noted from 6.5-9 cP in the upper part of the section to 24-28 cP at the level of water contact. The thickness of the high viscosity zone is 1-1.5 m [29-31].

Let us conclude that well drilling in the presence of high-viscosity oil zones can be carried out even closer to the OWC. In this case, the high-viscosity oil zone will be a kind of screen against water breakthrough into production wells. Thus, it is possible to justify the drilling of the well at the closest possible distance from the OWC (closer than 2 m), thereby obtaining the maximum possible increase in oil production.

The results of the work allowed us to draw the following conclusions:

1. With the help of hydrodynamic modeling, using the sector model of the SBNGKM, the optimal location of the fishbone well was determined at an absolute mark of 1571 m, which corresponds to a distance of 9 m from the GOC and 2 m from the OWC. At this location, the maximum value of cumulative oil production is observed both until the moment of gas breakthrough into the well (which is observed after 10 years of operation) and for the estimated period of 50 years.

2. The need for an individual approach to well drilling was determined, taking into account changes in the thickness of the oil-saturated layer and gas cap in the field, as well as the presence of zones with high-viscosity oil. Given these limitations and circumstances, it is possible to justify and carry out well drilling at the closest possible distance from the OWC.

Conclusion. In the work, using hydrodynamic modeling, the optimal location of a multilateral fishbone well with nine branches with a total length of a horizontal wellbore of 5050 m in an oil rim

with a thickness of 11 m in difficult geological conditions of the SBNGKM was revealed. It is necessary to further study and refine the zones of high-viscosity oils of the SBNGKM to make additions and changes to the filtration model, at the same time it, is possible to justify the drilling of a complex multilateral fishbone well at a minimum distance from the oil-water contact in certain zones of the field, which will lead to an increase in the oil recovery factor in this field.

REFERENCES

1. Grinchenko V.A., Valeev R.R., Abdullin M.M. et al. Specific PLT features in complex conditions of East Siberia to assist reservoir management. *Oil Industry.* 2020. N 11, p. 56-61 (in Russian). DOI: 10.24887/0028-2448-2020-11-56-61

2. Levanov A.N., Belyansky V.Y., Volkov I.A. et al. Concept Baseline for the Development of a Major Complex Field in Eastern Siberia using Flow Simulation. SPE Russian Petroleum Technology Conference, 26-28 October 2015, Moscow, Russia. OnePetro, 2015. N SPE-176636-MS. DOI: 10.2118/176636-MS

3. Ivanov E.N., Akinin D.V., Valeev R.R. et al. Development of Reservoir with Gas Cap and Underlying Water on Srednebotuobinskoye Field. SPE Russian Petroleum Technology Conference and Exhibition, 24-26 October 2016, Moscow, Russia. OnePetro, 2016. P. 579-593. № SPE-182055-MS. DOI: 10.2118/182055-MS

4. Bakirov D.L., Akhmetshin I.K., Fattakhov M.M. et al. Planning and Construction of Extended-Reach Multilateral Wells. *Geology, geophysics and development of oil and gas fields.* 2015. N 9, p. 41-50 (in Russian).

5. Paveleva O.N., Rubtsova M.E. Optimization of the development of fields in Western Siberia when drilling multilateral wells. Materialy I Mezhdunarodnoi nauchno-prakticheskoi konferentsii “Nauka novogo pokoleniya: konvergentsiya znanii, tekhnologii, obshchestva”, 3 iyunya 2019, Smolensk, Rossiya. Smolensk: MNITs “Naukosfera”, 2019, p. 54-57.

6. Bakirov D.L., Akhmetshin I.K., Fattakhov M.M. et al. Experience in planning, construction and completion of multilateral wells with long horizontal sections. Materialy 6 Tyumenskogo mezhdunarodnogo innovatsionnogo foruma “NEFT GAZTEK”, 16-17 sentyabrya 2015, Tyumen, Rossiya. Salekhard: Pechatnik, 2015, p. 51-68 (in Ryssian).

7. Nosachev A.A. Forecast of the application of enhanced oil recovery methods based on geological and field data: Avtoref. dis. … kand. geol.-min. nauk. Ufa: Bashkirskii nauchno-issledovatelskii i proektnyi institut neftyanoi promyshlennosti, 2000, p. 23 (in Russian).

8. Ivanova M.S., Tomskii K.O. Effectiveness of demulsifiers for the destruction of highly mineralized water-oil emulsions of the Srednebotuobinsky oil and gas condensate field. International Scientific and Practical Conference “Environmental Risks and Safety in Mechanical Engineering”, 20-23 October 2020, Rostov-on-Don, Russia. E3S Web of Conferences, 2020. Vol. 217. N 04001. DOI: 10.1051/e3sconf/202021704001

9. Yermekov R.I., Merkulov V.P., Chernova O.S., Korovin M.O. Features of permeability anisot-ropy accounting in the hydrodynamic model. *Journal of Mining Institute.* 2020. Vol. 243, p. 299-304. DOI: 10.31897/PMI.2020.0.299

10. Bakirov D.L., Ovchinnikov V.P., Fattakhov M.M. et al. Construction of Multi-Bottle (Multilateral) Wells with Horizontal Ending. *Burenie & neft.* 2020. N 10, p. 28-33 (in Russian).

11. Neskoromnykh V.V., Popova M.S. Development of a drilling process control technique based on a comprehensive analysis of the criteria. *Journal of Mining Institute.* 2019. Vol. 240, p. 701-710. DOI: 10.31897/PMI.2019.6.701

12. Fattakhov M.M., Bakirov D.L., Sentsov A.Yu. et al. Development of Technologies of Horizontal and Multilateral Wells Completion in Lukoil-West Siberia LLC. *Oil Industry.* 2016. N 8, p. 25-27 (in Russian).

13. Fattakhov M.M., Bakirov D.L., Bondarenko L.S. et al. Technical-Technological Solutions to Enhance the Efficiency of Multilateral Wells Drilling. *Geology, geophysics and development of oil and gas fields*. 2017. N 9, p. 58-63 (in Russian).

14. Al-Rbeawi S., Artun E. Fishbone type horizontal wellbore completion: a study for pressure behavior, flow regimes, and productivity index. *Journal of Petroleum Science and Engineering*. 2019. Vol. 176, p. 172-202. DOI: 10.1016/j.petrol.2018.12.076

15. Blinov P.A. Determining the stability of the borehole walls at drilling intervals of loosely coupled rocks considering zenith angle. *Journal of Mining Institute.* 2019. Vol. 236, p. 172-179. DOI: 10.31897/PMI.2019.2.172

16. Drozdov N.A. Filtration studies on cores and sand packed tubes from the Urengoy field for determining the efficiency of simultaneous water and gas injection on formation when extracting condensate from low-pressure reservoirs and oil from oil rims. *Journal of Mining Institute.* 2022. Vol. 257, p. 783-794. DOI: 10.31897/PMI.2022.71

17. Dumakova A.K., Trandin I.I., Polivanov S.A. Experience in Multilateral Drilling Using Fish-bone Technology in Orenburgneft Company. *Nedropolzovanie XXI vek.* 2020. N 5 (88), p. 41-45 (in Russian).

18. Bakirov D.L., Fattakhov M.M. Multilateral wells: practical experience of Western Siberia.Tyumen: OAO “Tyumenskii dom pechati”, 2015, p. 232 (in Russian).

19. Maikov D.N., Borkhovich S.Yu. Analytical Model of Multilateral Well with Complete Vertical Opening. *Neft. Gas. Novacii.* 2020. N 11 (240), p. 61-65 (in Russian).

20. Arzhilovsky A.V., Zernin A.A., Shirokov A.S. et al. Evaluation of Multilateral Wells Efficiency in the Fields of Vankorsky Cluster in Different Geological Environments. *Nedropolzovanie XXI vek.* 2020. N 6 (89), p. 64-73 (in Russian).

21. Dvoynikov M.V., Budovskaya M.E. Development of a hydrocarbon completion system for wells with low bottomhole temperatures for conditions of oil and gas fields in Eastern Siberia. *Journal of Mining Institute.* 2022. Vol. 253, p. 12-22. DOI: 10.31897/PMI.2022.4

22. Glebov E.A., Shokarev I.A., Gulov A.B. et al. Yurkharovskoye Extended Reach Drilling Campaign Resulted in the Successful Completion of Record Multilateral Well. SPE Russian Petroleum Technology Conference, 26-28 October 2015, Moscow, Russia. OnePetro, 2015. N SPE-176507-MS. DOI: 10.2118/176507-MS

23. Tuzov E.V., Makhmutov D.Z., Lisitsin M.A. et al. Methodology for construction of multi-borehole wells at Srednebotuobinskiy oil and gas condensate field, Eastern Siberia. *Construction of Oil and Gas Wells on Land and Sea.* 2020. N 12 (336), p. 35-45 (in Russian). DOI: 10.33285/0130-3872-2020-12(336)-35-45

24. Lukyantseva E.A., Oparin I.A., Sultanov R.B. Size Matters: "Birch leaf" Project or New World Record in Drilling of Multilateral Wells. 6th International Conference GeoBaikal, 5-9 October 2020, Irkutsk, Russia. Bunnik: European Association of Geoscientists & Engineers, 2020. Vol. 2020, p. 1-4. DOI: 10.3997/2214-4609.202052012

25. Bazitov M.V., Golovko I.S., Konosov D.A. et al. First Fishbone Well Drilling at Vankorskoe Field. SPE Russian Petroleum Technology Conference, 26-28 October 2015, Moscow, Russia. OnePetro, 2015. N SPE-176510-MS. DOI: 10.2118/176510-MS

26. Shpidko K.V., Gimazitdinov I.I. Multilateral wells - the way to additional oil. Materialy XIV Mezhdunarodnoi konferentsii "Problemy razrabotki mestorozhdenii uglevodorodnykh i rudnykh poleznykh iskopaemykh", 9-12 noyabrya 2021. Perm: Permskii natsionalnyi issledovatelskii politekhnicheskii universitet, 2021. Vol. 1, p. 72-75 (in Russian).

27. Osipova M.V., Sivtsev A.I. Tilted oil-water contact in the botuobinsky horizon of the Srednebotuobinskoe oil gas condensate field as an indication of peculiarities of oil and gas formation and accummulation in Nepsko-Botuobinskaya anticline. *Neftyanaya Provintsiya.* 2019. N 2 (18), p. 1-24 (in Russian). DOI: 10.25689/NP.2019.2.1-24

28. Zernin A.A., Makarova K.A., Tyulkova A.I. Features of production geophysical and hydrodynamic research of horizontal multilateral wells in the fields Rosneft Oil Company. *Oil Industry.* 2021. N 7, p. 94-98 (in Russian). DOI: 10.24887/0028-2448-2021-7-94-98

29. Rylance M.A., Tuzov Y.B., Aliyev S.B. et al. Fishbones, Wishbones and Birch-Leaves, Multilateral Well Design on the Srednebotuobinskoye Field in Eastern Siberia. SPE Russian Petroleum Technology Conference, 26-29 October 2020. OnePetro, 2020. N SPE-201849-MS. DOI: 10.2118/201849-MS

30. Zernin A.A., Ziuzev E.S., Sergeev A.S. et al. Recommendations for the multilateral wells de-sign selection in various geological conditions based on lessons learned. *Oil and Gas Studies.* 2021. N 5, p. 159-167 (in Russian). DOI: 10.31660/0445-0108-2021-5-159-167

31. Birchenko V. M., Al-Khelaiwi F.T., Konopczynski M.R., Davies D.R. Advanced Wells: How to make a Choice between Passive and Active Inflow-Control Completions. SPE Annual Technical Conference and Exhibition, 21-24 September 2008, Denver, Colorado, USA. OnePetro, 2008. N SPE-115742-MS. DOI: 10.2118/115742-MS

***Authors*: Kirill O. Tomskii,** *Candidate of Engineering Sciences, Associate Professor, kirilltom@mail.ru, https://orcid.org/0000-0001-7612-5393* (*Mirny Polytechnic Institute* (*branch*) *of North-Eastern Federal University, Mirny, Russia*), **Mariya S. Ivanova,** *Candidate of Chemical Sciences, Associate Professor, https://orcid.org/0000-0003-3272-9253* (*Mirny Polytechnic Institute* (*branch*) *of North-Eastern Federal University, Mirny, Russia*).

The authors declare no conflict of interests.

ISSN 2411-3336; e-ISSN 2541-9404

JOURNAL OF MINING INSTITUTE

Zapiski Gornogo instituta

Journal homepage: pmi.spmi.ru

Research article

Combined method of phytoremediation and electrical treatment for cleaning contaminated areas of the oil complex

Nikolai S. SHULAEV, Ramil R. KADYROV, Valeriya V. PRYANICHNIKOVA✉
Ufa State Petroleum Technological University, Ufa, Russia

***How to cite this article*:** Shulaev N.S., Kadyrov R.R., Pryanichnikova V.V. Combined method of phytoremediation and electrical treatment for cleaning contaminated areas of the oil complex. Journal of Mining Institute. 2024. Vol. 265, p. 147-155. EDN WJRQDO

Abstract. The scale of land pollution with oil waste necessitates the use of economical and effective methods of recultivation. Phytoremediation is one of the simplest methods, but it has a number of limitations, so additional preparation of the territory is often required before it is carried out. Preliminary electrical preparation and subsequent seeding of special phytoremediants are of interest. Passing a constant electric current through the soil volume under a low voltage removes toxicants from deep soil layers even with flooding. In addition, it reduces pollutant content in the upper layer, where the plants root system is located, which creates more favorable conditions for phytoremediants. Adequately selected types of plants will ensure additional soil cleaning, improve its structure and air exchange. The results of two research directions are presented. Experiments on the study of plant resistance to oil-contaminated soil substrate allowed establishing contamination thresholds at which it is advisable to sow a particular species, and to choose optimal phytoremediants. The study of the oil-containing soil cleaning in a monocathodocentric electrochemical installation with the fixation of main characteristics (oil products concentration, soil temperature, volt-ampere characteristics) allows us to develop technical measures to prepare territories for phytoremediation taking into account the relief features.

***Keywords*:** phytoremediation; electrochemical cleaning; oil-contaminated soil; salinization; amperage; voltage; plants; cleaning efficiency

Acknowledgment. This study was funded by the Ministry of Science and Higher Education of the Russian Federation "Priority 2030" (National Project "Science and University").

Received: 30.10.2022 ***Accepted: 20.09.2023*** ***Online: 03.10.2023*** ***Published: 29.02.2024***

Introduction. Anthropogenic pollution and degradation of soils are one of the most acute environmental problems. The total area of disturbed lands in the Russian Federation reached 1084.6 thousand hectares and continues to grow (an annual increase is to 7.7 thousand hectares) according to the official report of the Ministry of natural resources and ecology in 2020. Most of the disturbed territories belong to the category "industrial and other purpose lands". The list of the main soils pollutants varies depending on the prevailing industries (heavy metals and oil products, residual pesticides and salts). The priority pollutants of oil-producing and oil-refining regions are oil products and various accompanying salt solutions. An accurate assessment of the oil-contaminated area is not possible due to the difficulty of identifying relatively small local leaks and spills [1]. The negative effects of the oil products on the environment are water-air imbalance, gluing, soil structural elements enlargement, violation of the soils bearing capacity, micro- and mesofauna suppression [2-4]. There is a wide range of soil-cleaning and remediation technologies with different characteristics. The combination of such methods taking into account the specificity of the practical tasks is the most effective [5-9].

Soil phytoremediation (i.e. the use of plants to remove pollutants and improve soil properties) is one of the most cost-effective technical directions [10-12]. However, it does not always provide sufficiently fast and effective cleaning. The intensity of phytoremediation significantly depends on the temperature of the soil-air environment, the light regime, the presence of biogenic elements, the form in which the toxicants are in the ground, etc. [13-16]. It should be taken into account that the ability of plants to absorb chemicals changes under phytogeochemical stress [17]. The combination of phytoremediation with preliminary preparation of the territory by other technologies allows improving the quality and speed of degradated lands remediation [18-22].

The preliminary preparation of the contaminated area by passing direct current through the soil massif to remove toxicants and further phytoremediant sowing is very interesting [23-26].

The electro-induced processes prepare the surface layer for sensitive phytoremediant plants and reduce the toxic components content at depth. So special wells are prepared in the soil by automatic or manual drilling, taking into account the degree of oil products vertical distribution. Cathodes and anodes connected to the power supply are mounted into wells. Small currents stimulate electro-oxidative [27-30] and electrokinetic reactions [31-34], promote stable complexes destruction and toxicants transformation into more bioavailable forms and cause other physicochemical phenomena [35]. The size, composition and texture of the electrodes are selected depending on soil properties, the characteristics of the horizontal and vertical toxicants distribution, the required treatment time and other conditions. The result of electrical remediation is the removal of various components (petroleum products, heavy metals, desalination). Periodic change of the electrodes polarity are practiced to avoid soil acidification during electrical treatment.

Objectives of this work are to establish the threshold values of oil pollution based on the analysis and synthesis of experimental data, at which seed germination and further growth of the studied plants are possible; to select tolerant plants species that are optimal for variable terrain and watering conditions; to study the specifics of energy-efficient soil preparation to species – phytoremediants due to preliminary electrochemical cleaning.

The presented research materials are aimed at developing the technology of complex recultivation of oil-contaminated soils. This technology includes higher flora species sowing with preliminary electrochemical soil preparation, taking into account the relief and the moisture degree.

The considered combined remediation method can be implemented on various soils. The type of plant (from the studied ones) that is optimal for specific conditions is selected at the phytoremediation stage of research. Also additional measures can be taken to improve the soil structure (mulching, organic fertilizers, claymation, etc.), if it is necessary. Electrochemical treatment is applicable on both sand, loam and clay.

The possibility of growing some types of plants on oil-contaminated soil was considered in the early works of the authors [36]. General patterns of electro-induced reduction of the oil products content in soils were established [37, 38]. This work continues and expands the cycle of research in these areas.

Methodology. The first stage of the experiments was studying the resistance of certain types of higher plants to oil pollution by germinating them on soil with different oil concentrations and determining the seeds germination percentage. The ultimate goal of these experiments was to select temperate zone plant species tolerant to oil pollution and to determine the threshold values of the toxicant content during their germination. The second stage included the electrical treatment of oil-contaminated soil at an experimental laboratory installation with an assessment of the cleaning degree and monitoring of the voltage, temperature, and acidity of the soil. These parameters allow defining the intensity and features of the cleaning process. This stage is aimed at developing effective measures for the preliminary preparation of heavily oil-contaminated soils for the subsequent selection of phytoremediants.

Journal of Mining Institute. 2024. Vol. 265. P. 147-155

Experiments were carried out with a model soil based on leached chernozem. In all cases, oil with a density of 0.876 g/cm^3 and a content (% by weight) of sulfur – 2.95, paraffins – 3.1, resins – 14.6, mechanical impurities – 0.880 was used to pollute the soil. Variations of the model soil were prepared for different series of experiments. The model soil composition corresponded to the contaminated soil taken from the spill sites at the oil field of the Republic of Bashkortostan. Research was carried out at an air temperature of 20 °C and atmospheric humidity of 67 %.

Fig.1. Containers with seedlings of tested *Ipomoea purpurea* (first row on the left) and *Fagopýrum esculéntum* (2-4 rows)

The first stage. Experiments to determine the resistance of higher plants species to soil oil pollution were carried out in spring and summer in the laboratory, and in autumn and winter with the use of the LCC-1000MP Diahan Labtech climate camera (to clarify the results). The illumination in the climate camera was maintained 4000 lux with the "day – night" photoperiod. The reaction of plants was studied by the method of seed germination in model soils with different concentrations of the toxicant with the calculation of the germination percent and further determination of the viable seedlings number.

First, the soil (leached chernozem) was prepared by removal of roots and small stones, sifting, weighing. 100 g of soil was poured into plastic containers. Different volume of crude oil (1; 2; 5; 10; 50; 100 ml) was put into each sample using a pipette, and then the soil was thoroughly rubbed and mixed to evenly contaminant distribution. Twenty seeds were sown in each container so that the soil layer covering them was about 1 cm. Then 60 ml of tap water was added. The control was soil without oil contamination. Three samples with each oil dose were prepared for experiments. The containers were kept at a temperature of 20 °C and the illumination mode corresponding to the daytime of spring-summer period. The number of seedlings was counted and the percentage of germination was determined after seven days in each container (Fig.1). The number of viable seedlines was recalculated to determine their survival after two weeks.

The results were used to identify the main effects exerted by different volumes of toxicant on the germination, with further detailed statistical processing.

The second stage. Electrotreatment of contaminated soil, which was carried out on a laboratory installation with a cylindrical cell, centric placement of the cathode and peripheral placement of anodes (Fig.2).

It is necessary to remember that highly mineralised reservoir water become the limiting factor of plant development during the remediation of oil field spills. Therefore, it is important that the technology of preliminary preparation of the contaminated area for sowing phytoremediants not only reduces the oil products amount, but also desalinizes the soil. Therefore, the model soil variants containing oil (1 and 10 % by weight) and a solution of salts (40.8 % by weight) were prepared for the electrical treatment experiments. The composition of the salt solution corresponded to the reservoir waters of the deposit included (mg/kg) [39]: sodium chloride – 86000, calcium chloride – 10500, magnesium chloride – 5200, sodium sulfate – 4000, sodium bicarbonate – 400.

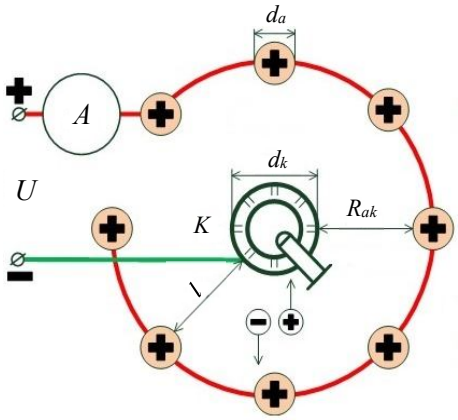

Fig.2. The diagram of the central cathode and peripheral anodes installation

d_a – anodes diameter; d_k – cathode diameter; l – interelectrode distance; R_{ak} – distance between the centers of the cathode and anodes; K – central cathode; U – voltage between the cathode and anodes

The central element of the electrochemical cell is a hollow cylindrical steel cathode with perforation on a surface

(a drainage system for removing soil electrophoretic flow can be also connected, if it is necessary). Anodes are installed along the perimeter of the radial cell, at an equal distance from the cathode. All electrodes are connected to the corresponding pole of the power supply.

The installation used in the experiments had following characteristics: electrochemical cell diameter – 0.3 m; the soil layer height is 0.1 m; the cathode was made of a perforated steel tube, the anodes (with diameter 2.5 cm) are mesh cylinders (tubes) made of titanium with an oxide-ruthenium coating; the cell capacity reached 3 kg of model soil.

Several series of experiments on passing currents through chernozem containing different oil volumes were carried out. The constant amperage was maintained during the experiments: 0.8 A – in a series of experiments with 1 % soil contamination, 1 A in – a series with 10 % contamination. The use of these current values in each case is due to the fact that they are minimal, at which the voltage change between the electrodes is recorded, so we can talk about the appearance of electro-induced processes. The period of electric current passing was 360 min.

The oil products content in the soil was determined by IR spectrometry with the use of KN-2m. The parameters of voltage, temperature, humidity, and acidity were recorded every 30 minutes in the cathode, anode, and interelectrode zones. Multimeter, RGK thermal imager, digital soil moisture analyzer MC-7828SOIL, soil temperature and humidity analyzer HI9921 were used. Monitoring of these parameters allows determining the electrophysical reactions intensity.

Results and their discussion. Experiments on the plants reaction to soil pollution conducted over several years revealed some species resistant to the toxicants (*Typha latifolia*, *Phragmites communis* [36], *Fagopýrum esculéntum* and *Ipomoea purpurea*). These species have very different ecological niches, which allows them to be used at various territories.

Reliable inverse dependences of seed germination on the pollutants concentration were established in all cases after results statistical processing (Fig.3). The seeds of *Ipomoea* and *Fagopýrum* germinated more evenly, the seedlings condition was also more uniform in the same samples.

Experimentally obtained data on the toxicant level at which the seeds germination is equal to or exceeds the control values (i.e. a stimulating effect) are summarized in the Table. These values can be taken as a threshold level of pollution at which the use of a particular type of plants on oil-contaminated soils is effective. Moisture-loving *Typha latifolia* and *Phragmites communis* were additionally germinated with reservoir waters (the seedlings appeared in the sample with 5 ml content).

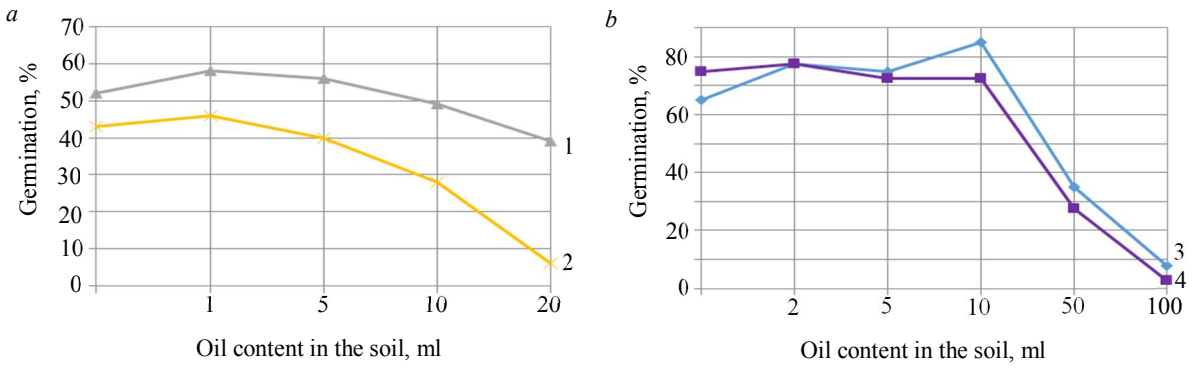

Fig.3. The dependence of the seeds germination on the oil content in the soil:
a – experiments with *Typha latifolia* (1) and *Phragmites communis* (2);
b – experiments with *Fagopýrum esculéntum* (3) and *Ipomoea purpurea* (4)

Journal of Mining Institute. 2024. Vol. 265. P. 147-155

The main parameters of germination

Parameter	*Typha latifolia*	*Phragmites communis*	*Fagopýrum esculéntum*	*Ipomoea purpurea*
Seed germination in the control, %	52	43	65	75
Oil volume in the sample (germination is not less than control), ml	10	5	10	2
Oil volume in the sample at zero germination, ml	30	30	100 (single seedling)	100 (single seedling)
Regression equation, describing the dependence	$y = -2.642x^2 + 12.35x + 42.8$	$y = -4x^2 + 14.8x + 32.2$	$y = -6.964x^2 + 37.17x + 33$	$y = -5.312x^2 + 22.54x + 56.25$
Approximation reliability	$r^2 = 0.988$	$r^2 = 0.999$	$r^2 = 0.918$	$r^2 = 0.955$

The seedlings remained viable for 14 days after their appearance in all series of experiments (the period of monitoring their condition). They retain a green color without any damage to the leaf blades or yellowing. Thus, the data obtained indicate high resistance of all four species to oil pollution. These species can be used for seeding in polluted areas to improve soil properties both independently and during the final stage of complex remediation (for example, after the preliminary electrochemical treatment in our case).

Typha latifolia and *Phragmites communis* are moisture-loving wild-growing widely distributed plants and can be used for the recultivation of oil-contaminated lowlands and swampy areas. They can be sown at the territories of oil and reservoir water spills of oil deposits. It is necessary to create an irrigation system, if sowing is carried out during the dry summer period for normal germination and growth. These species are characterized by a decrease in the oil products content in the root zone, including due to the increased activity of hydrocarbon-oxidizing microorganisms [40].

The use of *Amaranthus retroflexus L.* after electrical treatment is also promising. It is a ubiquitous weed resistant to an increased content of oil products and mineral salts in the soil (experiments are planned).

Ipomoea purpurea is a climbing ornamental plant. It is suitable for use at urban territories with moderate moisture, for example, for sowing after electrical treatment of gas stations soils, areas along roads with fuel and lubricants spills, etc.

Fagopýrum esculéntum is a food and honey crops. However, it is recommended to use it exclusively as an agrotechnical culture in the context of studies, since it has a very intensive interchange of metabolic products between roots and leaves [41]. The issue of accumulation of harmful products of toxicants transformation in various parts of the plant requires study; therefore, it is rational not to eat the plant, when using it for final remediation.

All the studied species are unpretentious to environmental conditions, they are often found in a temperate climate zone, seed material is easy to collect in the field (significant expenses for its purchase are not required).

Studies of oil-containing soil cleaning by low currents with cathodocentric electrode separation, which precede further phytoremediation, have shown significant efficiency. There was a decrease in the level of oil pollution in electrotreated soil (the cleaning degree is 47-65 %) in all cases. In addition, the oil products distribution over the interelectrode zones gradually occurs: there are an increase in their content at the cathode and a decrease at the anode (Fig.4).

The voltage increased from 8.9 to 9.4 V, when an electric current is passed through the soil with 1 % contamination. It varied in the range of 9.8-10.9 V in the soil with 10 % contamination. There is an increase in soil temperature in the cathode zone (temperature gradient is up to 8 °C), while the

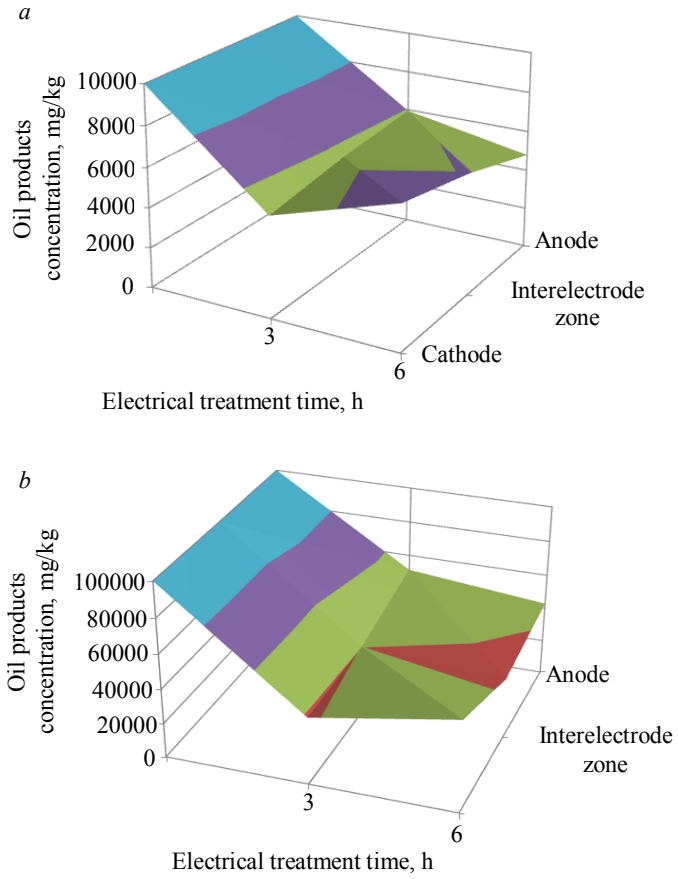

Fig.4. Spatio-temporal distribution of the oil products concentration in the soil in various series of experiments:
a – the minimum level of pollution (1 %);
b – the maximum level of pollution (10 %)

temperature in the anode and in the middle zones is almost the same (Fig.5). The use of a thermal imager makes it possible to analyze the soil temperature profile in the cell. The temperature zones highlighted in the images allow us to assess the electrical conductivity of individual areas. Higher heating indicates the medium resistance increase and electrical conductivity decrease (the area with white-red coloring in Fig.5). This means that salts dissociation, migration and reduction of active ions (i.e. desalination occurs) is taking place at this areas. The pH distribution also confirms it. The alkaline medium is formed at the cathode as a result of the hydroxyl ions formation. The acidity increases in the rest of the electrochemical cell.

It is necessary to use special equations to estimate the energy consumption of this method on cathodocentric installations, taking into account the oil-contaminated soils parameters changes (in particular, resistivity) during the electrical process. The energy parameters of electrochemical cleaning (including in the real conditions) will be determined in this way. The total amperage between the anodes and the cathode is determined by the equation [37]

$$I = \frac{USN}{\rho l}, \quad (1)$$

where N – is the number of anodes, pcs.; ρ – is the treating soil specific resistivity, Ω·m; l – is the interelectrode distance between the central cathode and the anodes, m.

The effective area of the electric current channel between the opposite charged electrodes are determined as follows:

$$S = \frac{d_k + d_a}{2} H, \quad (2)$$

where H – is the contamination depth, m.

The interelectrode distance is calculated by the equation

$$l = R_{ak} - \frac{d_k + d_a}{2}. \quad (3)$$

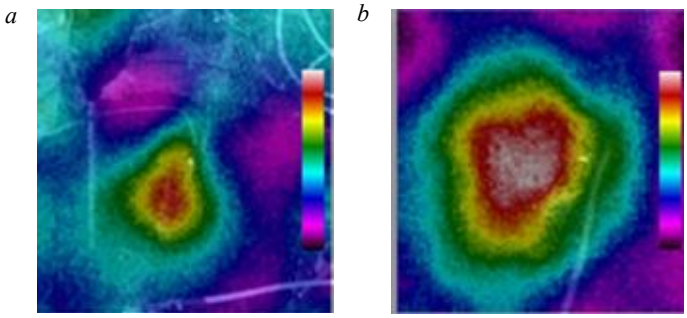

Fig.5. Thermal imaging of a radial cell with soil:
initial (*a*) and final (*b*) treatment stages

Specific electricity costs (J/kg of petroleum products) is determined by the equation

$$\varepsilon_{sp} = \frac{1}{c_0 V} \int UIdt, \quad (4)$$

where V – is the oil-contaminated soil volume, m^3; c_0 – initial concentration of oil products, kg/m^3.

Journal of Mining Institute. 2024. Vol. 265. P. 147-155

The soil resistivity increases during the electrical treatment, as follows from experimental studies [39]. The specific resistance change in time can be estimated in the first approximation by the equation

$$\rho = \rho_0 (1 + \alpha t); \tag{5}$$

$$\alpha = \frac{\rho_k - \rho_0}{\rho_0} \frac{I}{q_{sp} c_0 V}, \tag{6}$$

where ρ_0 – is the soil resistivity at the initial moment of time, Ω·m; ρ_k – is the final value of the soil resistivity at the last stage of electrical treatment, Ω·m; q_{sp} – is the specific electric charge, which should ensure the oil-contaminated soil cleaning, C/kg, q_{sp} values were established for clay, sandy soil and chernozem previously [39].

The specific energy consumption depending electrotheatment modes with constant value of amperage or voltage. So specific energy consumption for the constant voltage will be calculated with the use of equations (4) and (5):

$$\varepsilon_{spU} = \frac{1}{c_0 V} \int \frac{U^2 dt}{R} = \frac{1}{c_0 V} \int \frac{U^2 S dt}{\rho_0 (1 + \alpha t) l} = \frac{1}{c_0 V} \frac{U^2 S}{\rho_0 l} \int \frac{dt}{(1 + \alpha t)} = \frac{1}{c_0 V} \frac{U^2 S}{\rho_0 l \alpha} \ln (1 + \alpha t); \tag{7}$$

specific energy consumption with a constant amperage is

$$\varepsilon_{spI} = \frac{1}{c_0 V} \int I^2 \rho_0 (1 + \alpha t) \frac{l}{S} dt = \frac{1}{c_0 V} I^2 \rho_0 \frac{l}{S} \left(t + \frac{\alpha t^2}{2} \right). \tag{8}$$

The calculation of the energy efficiency of the laboratory installation using the above equations and the experimental data obtained showed that the specific energy consumption is 0.1139 MJ per 1 kg of soil containing 1 % of oil.

The above methodology for determining energy consumption can be used in the design of specialized electrical cleaning installations for specific conditions, taking into account the properties of oil-contaminated areas and their contamination degree.

Conclusion. The conducted experimental and theoretical studies in two scientific fields allowed us to identify the main approaches for the implementation of a complex technology of oil-contaminated territories remediation.

Four types of plants – potential tolerant phytomeliorants suitable for the remediation of oil-contaminated soils of various territories have been selected. The thresholds values of the oil products content in the soil, which are recommended to phytoremediation were defined. Reliable dependences of seed germination on the oil products content have been established. It is proposed to use *Typha latifolia* and *Phragmites communis* species on highly moist soils, including hollows and ravines filled with water-oil emulsion and oil production brines (germination reaching and exceeding the control value with oil content up to 10 and 5 ml in the sample). It is advisable to use the *Ipomoea purpurea* in urban areas (the threshold volume of oil in the sample is 2 ml). *Fagopýrum esculéntum* is useful at the moderately moist agricultural areas exposed to oil spills (the threshold volume is 10 ml in the sample).

It is recommended to carry out electrochemical soils cleaning using a monocathode centric electrode placement scheme for preliminary preparation for phytoremediation and for oil products content reduction to the threshold values of specific species. This arrangement of the electrodes will allow to prepare the soil effectively even with a significantly rugged landscape, i.e. in the presence of lowlands and hills, in watered areas. The oil products cleaning degree in accordance with the conducted experiments reached 65 %. Temperature gradient during electric heating of soil was up to 8 °C.

A method for determining some energy parameters of electroremediation process using a cathodocentric arrangement of electrodes, taking into account changes in soil resistance has been developed.

The results obtained will contribute to the practical implementation of the technology of complex oil-contaminated soils cleaning based on phytoremediation with preliminary electrotreatment in real conditions.

REFERENCES

1. Pashkevich M.A., Bykova M.V. Improvability of measurement accuracy in determining the level of soil contamination with petroleum products. *Mining Informational and Analytical Bulletin.* 2022. N 4, p. 67-86 (in Russian). DOI: 10.25018/0236_1493_2022_4_0_67

2. Pashkevich M.A., Antciferova T.A. Assessment of the impact of fuel and energy complex on the environment in the enlargement of production. *Journal of Mining Institute.* 2013. Vol. 203, p. 229-232 (in Russian).

3. Dashko R.E., Lange I.Y. Forecasting bearing capacity change of sandy-argillaceous soils in course of their contamination by oil-products. *Journal of Mining Institute.* 2015. Vol. 211, p. 16-21 (in Russian).

4. Pashkevich M.A., Bech J., Matveeva V.A., Alekseenko A.V. Biogeochemical assessment of soils and plants in industrial, residential and recreational areas of Saint Petersburg. *Journal of Mining Institute.* 2020. Vol. 241, p. 125-130. DOI: 10.31897/PMI.2020.1.125

5. Wukui Zheng, Tian Cui, Hui Li. Combined technologies for the remediation of soils contaminated by organic pollutants. A review. *Environmental Chemistry Letters*. 2022. Vol. 20. Iss. 3, p. 2043-2062. DOI: 10.1007/s10311-022-01407-y

6. Yan Xu, Yangjie Lu, Chang Tian, Jianqiang Yang. Application of combined remediation in heavy metal polluted soil. *IOP Conference Series: Earth and Environmental Science*. 2019. Vol. 300. N 032006. DOI: 10.1088/1755-1315/300/3/032006

7. Guoxuan Fan, Xitao Liu, Xiaowan Li et al. Mechanochemical treatment with CaO-activated PDS of HCB contaminated soils. *Chemosphere*. 2020. Vol. 257. N 127207. DOI: 10.1016/j.chemosphere.2020.127207

8. Ferreira M.B., Sales Solano A.M., Dos Santos E.V. et al. Coupling of Anodic Oxidation and Soil Remediation Processes: A Review. *Materials*. 2020. Vol. 13. Iss. 19. N 4309. DOI: 10.3390/ma13194309

9. Dos Santos E.V., Sáez C., Cañizares P. et al. Treatment of *ex-situ* soil-washing fluids polluted with petroleum by anodic oxidation, photolysis, sonolysis and combined approaches. *Chemical Engineering Journal*. 2017. Vol. 310, p. 581-588. DOI: 10.1016/j.cej.2016.05.015

10. Shehata S.M., Badawy R.K., Aboulsoud Y.I.E. Phytoremediation of some heavy metals in contaminated soil. *Bulletin of the National Research Centre*. 2019. Vol. 43. N 189. DOI: 10.1186/s42269-019-0214-7

11. Tripathi S., Kumar Singh V., Srivastava P. et al. Phytoremediation of organic pollutants: current status and future directions. *Abatement of Environmental Pollutants*. 2020, p. 81-105. DOI: 10.1016/B978-0-12-818095-2.00004-7

12. Krasnoperova S. The morphological analysis and resistance of plants recommended for phytoremediation of the oil-polluted soils. *Modern High Technologies. Regional Application.* 2015. N 4 (44), p. 184-188 (in Russian).

13. Mader A.E., Holtman G.A., Welz P.J. Treatment wetlands and phyto-technologies for remediation of winery effluent: Challenges and opportunities. *Science of the Total Environment*. 2022. Vol. 807. Part 1. N 150544, p. 1-17. DOI: 10.1016/j.scitotenv.2021.150544

14. Mamirova A., Baubekova A., Pidlisnyuk V. et al. Phytoremediation of Soil Contaminated by Organochlorine Pesticides and Toxic Trace Elements: Prospects and Limitations of Paulownia tomentosa. *Toxics*. 2022. Vol. 10. Iss. 8. N 465. DOI: 10.3390/toxics10080465

15. Hauptvogl M., Kotrla M., Prčík M. et al. Phytoremediation Potential of Fast-Growing Energy Plants: Challenges and Perspectives – a Review. *Polish Journal of Environmental Studies*. 2020. Vol. 29. N 1, p. 505-516. DOI: 10.15244/pjoes/101621

16. Macci C., Peruzzi E., Doni S., Masciandaro G. Monitoring of a long term phytoremediation process of a soil contaminated by heavy metals and hydrocarbons in Tuscany. *Environmental Science and Pollution Research*. 2020. Vol. 27, p. 424-437. DOI: 10.1007/s11356-019-06836-x

17. Alekseenko V.A., Shvydkaya N.V., Alekseenko A.V. et al. Element Accumulation Patterns of Native Plant Species under the Natural Geochemical Stress. *Plants*. 2021. Vol. 10. Iss. 1. N 33. DOI: 10.3390/plants10010033

18. Prabakaran K., Li Jian, Anandkumar A. et al. Managing environmental contamination through phytoremediation by invasive plants: A review. *Ecological Engineering*. 2019. Vol. 138, p. 28-37. DOI: 10.1016/j.ecoleng.2019.07.002

19. Bajagain R., Lee S., Jeong S.-W. Application of persulfate-oxidation foam spraying as a bioremediation pretreatment for diesel oil-contaminated soil. *Chemosphere*. 2018. Vol. 207, p. 565-572. DOI: 10.1016/j.chemosphere.2018.05.081

20. Kafle A., Timilsina A., Gautam A. et al. Phytoremediation: Mechanisms, plant selection and enhancement by natural and synthetic agents. *Environmental Advances*. 2022. Vol. 8. N 100203. DOI: 10.1016/j.envadv.2022.100203

21. Bykova M.V., Alekseenko A.V., Pashkevich M.A., Drebenstedt C. Thermal desorption treatment of petroleum hydrocarbon-contaminated soils of tundra, taiga, and forest steppe landscapes. *Environmental Geochemistry and Health*. 2021. Vol. 43, p. 2331-2346. DOI: 10.1007/s10653-020-00802-0

22. Strizhenok A.V., Korelskiy D.S., Choi Y. Assessment of the Efficiency of Using Organic Waste from the Brewing Industry for Bioremediation of Oil-Contaminated Soils. *Journal of Ecological Engineering*. 2021. Vol. 22. Iss. 4, p. 66-77. DOI: 10.12911/22998993/133966

23. Rada E.C., Andreottola G., Istrate I.A. et al. Remediation of Soil Polluted by Organic Compounds Through Chemical Oxidation and Phytoremediation Combined with DCT. *International Journal of Environmental Research and Public Health*. 2019. Vol. 16. Iss. 17. N 3179. DOI: 10.3390/ijerph16173179

24. Chirakkara R.A., Reddy K.R., Cameselle C. Electrokinetic Amendment in Phytoremediation of Mixed Contaminated Soil. *Electrochimica Acta*. 2015. Vol. 181, p. 179-191. DOI: 10.1016/j.electacta.2015.01.025

25. Cameselle C., Gouveia S. Phytoremediation of mixed contaminated soil enhanced with electric current. *Journal of Hazardous Materials*. 2019. Vol. 361, p. 95-102. DOI: 10.1016/j.jhazmat.2018.08.062

26. Crognale S., Cocarta D.M., Streche C., D'Annibale A. Development of laboratory-scale sequential electrokinetic and biological treatment of chronically hydrocarbon-impacted soils. *New Biotechnology*. 2020. Vol. 58, p. 38-44. DOI: 10.1016/j.nbt.2020.04.002

27. Rada E.C., Istrate I.A., Ragazzi M. et al. Analysis of Electro-Oxidation Suitability for Landfill Leachate Treatment through an Experimental Study. *Sewage and Landfill Leachate. Assessment and Remediation of Environmental Hazards*. 2016, p. 149-172. DOI: 10.1201/b20005-13

28. Zhou W., Rajic L., Chen L. et al. Activated carbon as effective cathode material in iron-free Electro-Fenton process: Integrated H_2O_2 electrogeneration, activation, and pollutants adsorption. *Electrochimica Acta*. 2019. Vol. 296, p. 317-326. DOI: 10.1016/j.electacta.2018.11.052

29. Ganiyu S.O., Gamal El-Din M. Insight into in-situ radical and non-radical oxidative degradation of organic compounds in complex real matrix during electrooxidation with boron doped diamond electrode: A case study of oil sands process water treatment. *Applied Catalysis B: Environmental*. 2020. Vol. 279. N 119366. DOI: 10.1016/j.apcatb.2020.119366

30. Lawrence M.Z., Kenneth J.W., Pamukcu S. Case study: Electrochemical Geo-Oxidation (ECGO) treatment of Massachusetts New Bedford Harbor sediment PCBs. *Electrochimica Acta*. 2020. Vol. 354. N 136690. DOI: 10.1016/j.electacta.2020.136690

31. Vocciante M., Dovì V.G., Ferro S. Sustainability in ElectroKinetic Remediation Processes: A Critical Analysis. *Sustainability*. 2021. Vol. 13. Iss. 2. N 770. DOI: 10.3390/su13020770

32. Shabanov E.A., Prostov S.M., Gerasimov O.V. In vitro studies of electrochemical purification of foundation soil from oil products. *Journal of Construction and Architecture*. 2019. Vol. 21. N 4, p. 168-180. DOI: 10.31675/1607-1859-2019-21-4-168-180

33. Ganiyu S.O., Martínez-Huitle C.A., Rodrigo M.A. Renewable energies driven electrochemical wastewater/soil decontamination technologies: A critical review of fundamental concepts and applications. *Applied Catalysis B: Environmental*. 2020. Vol. 270. N 118857. DOI: 10.1016/j.apcatb.2020.118857

34. Gingine V., Shah R., Venkata Koteswara Rao P., Hari Krishna P. A review on study of Electrokinetic stabilization of Expansive soil. *International Journal of Earth Sciences and Engineering*. 2013. Vol. 6. N 2 (1), p. 176-181. DOI: 10.13140/2.1.2809.4086

35. Streche C., Cocârță D.M., Istrate I.A., Badea A.A. Decontamination of Petroleum-Contaminated Soils Using The Electrochemical Technique: Remediation Degree and Energy Consumption. *Scientific Reports*. 2018. Vol. 8. N 3272. DOI: 10.1038/s41598-018-21606-4

36. Shulaev N.S., Pryanichnikova V.V., Kadyrov R.R., Bykovsky N.A. The phytoremediation of oil-contaminated soil. *Butlerov Communications*. 2016. Vol. 47. N 8, p. 133-138.

37. Shulaev N.S., Meshalkin V.P., Pryanichnikova V.V. et al. Electrochemical Cleaning of Oil-Contaminated Soils, Taking into Account the Terrain. *Ecology and Industry of Russia*. 2022. Vol. 26. Iss. 2, p. 9-13 (in Russian). DOI: 10.18412/1816-0395-2022-2-9-13

38. Shulaev N.S., Pryanichnikova V.V., Kadyrov R.R. Regularities of electrochemical cleaning of oil-contaminated soils. *Journal of Mining Institute*. 2021. Vol. 252, p. 937-946. DOI: 10.31897/PMI.2021.6.15

39. Meshalkin V.P., Shulaev N.S., Chelnokov V.V. et al. Determination of electrical parameters for the electrochemical treatment of soils contaminated with oil. *IOP Conference Series: Materials Science and Engineering*. 2019. Vol. 537. N 062069 (in Russian). DOI: 10.1088/1757-899X/537/6/062069

40. Fahid M., Arslan M., Shabir G. et al. Phragmites australis in combination with hydrocarbons degrading bacteria is a suitable option for remediation of diesel-contaminated water in floating wetlands. *Chemosphere*. 2020. Vol. 240. N 124890. DOI: 10.1016/j.chemosphere.2019.124890

41. Shaikhiev I.G., Sverguzova S.V., Galimova R.Z., Grechina A.S. Using wastes of buckwheat processing as sorption materials for the removal of pollutants from aqueous media: a review. *IOP Conference Series: Materials Science and Engineering*. 2020. Vol. 945. N 012044. DOI: 10.1088/1757-899X/945/1/012044

Authors: **Nikolai S. Shulaev,** *Doctor of Engineering Sciences, Professor, https://orcid.org/0000-0002-3595-6948 (Ufa State Petroleum Technological University, Ufa, Russia),* **Ramil R. Kadyrov,** *Candidate of Engineering Sciences, Associate Professor, https://orcid.org/0000-0001-6665-9375 (Ufa State Petroleum Technological University, Ufa, Russia),* **Valeriya V. Pryanichnikova,** *Candidate of Engineering Sciences, Associate Professor, prvaleria@mail.ru, https://orcid.org/0000-0001-8997-5186 (Ufa State Petroleum Technological University, Ufa, Russia).*

The authors declare no conflict of interests.

ISSN 2411-3336; e-ISSN 2541-9404

JOURNAL OF MINING INSTITUTE

Zapiski Gornogo instituta

Journal homepage: pmi.spmi.ru

Research article

Mathematical modeling of the electric field of an in-line diagnostic probe of a cathode-polarized pipeline

Vladimir N. KRIZSKII[1], **Oleg V. KOSAREV**[1]✉, **Pavel N. ALEKSANDROV**[2], **Yana A. LUNTOVSKAYA**[1]

[1] *Empress Catherine II Saint Petersburg Mining University, Saint Petersburg, Russia*

[2] *Schmidt Institute of Physics of the Earth of the RAS, Moscow, Russia*

How to cite this article: Krizskii V.N., Kosarev O.V., Aleksandrov P.N., Luntovskaya Ya.A. Mathematical modeling of the electric field of an in-line diagnostic probe of a cathode-polarized pipeline. Journal of Mining Institute. 2024. Vol. 256, p. 156-164. EDN XRDQFW

Abstract. A mathematical model of the in-line control of the insulation resistance state for cathodically polarized main pipelines according to electrometry data is considered. The relevance of the work is caused by the opportunity to create in-line internal isolation defects indicators of the main pipelines for transported liquids that are good conductors and expand the functionality of monitoring and controlling cathodic protection systems of the main pipelines. Features of the mathematical model are: consideration of the electric conductivity of transported liquid influence on electric field distribution; consideration of the influence of external and internal insulating coating resistance; use of the electric field of an in-line diagnostic probe for quality control of internal insulation. Practical significance consists in the development of modeling methods for control subsystems of main pipeline protection against corrosion and the development of special mathematical and algorithmic support systems for monitoring and controlling the operating modes of the cathodic protection station of main pipelines.

Keywords: mathematical modeling of the electric field; main pipeline cathodic electrochemical protection; external and internal insulating coating; in-line diagnostics; corrosion; fictitious source method; electric field gradient; computational experiment; electric probing

Received: 10.07.2022 ***Accepted: 20.06.2023*** ***Online: 06.09.2023*** ***Published: 29.02.2024***

Introduction. Main pipelines (MP) are prone to corrosion, which is the main cause of pipeline failures and downtime [1, 2]. Corrosion occurs due to the influence of mechanical impurities [3-5], stray currents of different nature [6], pipeline and ground deformation [7-9], inner and outer insulation coating defects, etc. In practice, ultrasonic and magnetometric methods are widely used for pipeline diagnostics [10, 11]. Ultrasonic methods of nondestructive testing are developing both towards optimization of the number and spatial location of sensors [12] and towards more complex processing of reflected signals [13-15]. External insulation condition monitoring [16, 17] is usually performed manually using special equipment [18-20], but remote methods of nondestructive testing are also being intensively developed [21]. It is difficult to assess the quality of in-line insulation outside the pipe due to the properties of the pipe metal shielding the excited field. A solution in such cases is the use of in-line tools (probes) [22]. Magnetometric [23] and ultrasonic methods of pipe metal quality evaluation are used for in-line inspection. The use of an in-line source of direct electric current in highly conductive transported media (salt solutions, water, some products of multi-tonnage chemical productions, etc.) and water-oil media [24, 25] makes it possible to investigate the mutual influence of internal insulation quality and the gradient of electric field measured by the probe. Such a sufficiently

Journal of Mining Institute. 2024. Vol. 265. P. 156-164

operative estimation of the internal insulation quality contributes to the development of special mathematical and algorithmic support for the monitoring and control systems of cathodic protection stations (CPS) in MP.

The purpose of this work is to develop a mathematical model for in-line monitoring of the insulation resistance state of cathodically polarized MP using electrometric data. The relevance of the work is determined by the possibility of creating in-line indicators of internal insulation defects in MP and extending the functionality of monitoring and control systems of CPS of MP at the expense of this information. For this purpose, the following tasks have been solved: the constructed differential mathematical model of the electric field of the CPS and in-line electric probe by a method of fictitious sources has been reduced to a discrete model in the form of a system of linear algebraic equations (SLAE); influence of internal isolation failure on the gradient of the electric field of the in-line probe has been studied by means of a computational experiment.

Methods. Ensuring the required quality of corrosion protection for operating oil and gas equipment [26-28] includes maintaining the required level of protective cathodic potential on the metal surface. Modern computing technologies, including neural networks, are used to solve this problem [29]. A mathematical model of the cathodically polarized MP should describe the distribution of currents and potentials along the entire length of the section to be protected by the CPS. The realization of the model allows calculating the values of currents and voltages in the pipe and on the interfaces "pipe – ground" and "pipe – transported liquid" [30-32]. Initial data for the calculations are the electric properties of all current spreading media, auxiliary current strength CPS, geometrical characteristics of the MP, and also the spatial coordinates of the MP, anode earth electrode, and current drainage point. Note that due to the impossibility of exact determination in time and space of all physical quantities describing the real operation of a MP, an absolutely accurate description of such a system is fundamentally impossible [16]. Nevertheless, as the analysis of scientific research shows [17, 33], in calculations, such a model of MP medium as homogeneous isotropic half-space with averaged (and constant) specific ground conductivity is used. Therefore, in order to achieve the purpose of this work, it is necessary to develop a mathematical model adequate to the practice of the direct problem of electromagnetic field distribution of direct DC of MP cathode protection system in homogeneous medium of "ground – external insulation – metal – internal insulation – transported liquid – probe" type and conduct a computational experiment to study the influence of transient resistance of internal insulation on current distribution in the system.

Let a homogeneous space be given (Fig.1), divided by a flat boundary into two half-spaces – Ω_0 (air) with specific conductivity $\sigma_0 = 0$ S/m and Ω_g (ground) with a given constant specific conductivity of the filling substance σ_g = const S/m. Suppose that a rectilinear pipeline of length L_t is located in a half-space Ω_g. Inside the pipeline, in the transported liquid with specific conductivity σ_l there is a diagnostic probe ($A_{pr} - B_{pr}$) injecting a I_{pr} DC. The CPS provides a protective DC I_a, flowing through a point anode located at point $A(x_A, y_A, z_A)$ of the half space Ω_g. The protective current drains from the pipe metal at point B_t. The coordinates of points A and B_t in the Cartesian coordinate system are known. The origin of the coordinate system is chosen at the "air – ground" surface. The Ox axis is parallel to the pipe axis, and the Oz axis is downward.

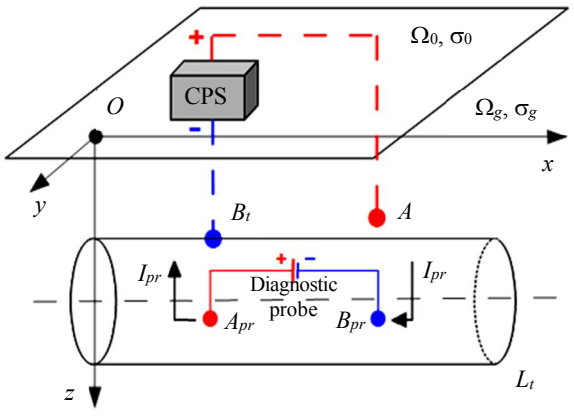

Fig.1. Inclusion of a diagnostic probe in the cathodic protection scheme of a MP in a homogeneous half-space

A mathematical model describing the distribution of the DC electric field potential in the system at an arbitrary point of space $P(x_P, y_P, z_P)$ is:

$$\Delta U_g(P) = -\frac{I_a}{\sigma_g}\delta(P-A); \quad (1)$$

$$\Delta U_m(P) = 0;\ \Delta U_l(P) = -I_{pr}\left(\delta(P-A_{pr}) - \delta(P-B_{pr})\right); \quad (2)$$

$$\left.\frac{\partial U_g(P)}{\partial z}\right|_{z=0} = 0;\ U_g(P) \to 0,\ P \to \infty; \quad (3)$$

$$\left.\frac{\partial U_m}{\partial x}\right|_{x=0;L_t} = 0;\ \left.\frac{\partial U_l}{\partial x}\right|_{x=0;L_t} = 0; \quad (4)$$

$$U_g(P) - C_{gm}(P)\sigma_g(P)\left.\frac{\partial U_g(P)}{\partial n}\right|_{S_{gm}} = U_m(P); \quad (5)$$

$$U_l(P) + C_{ml}(P)\sigma_l(P)\left.\frac{\partial U_l(P)}{\partial n}\right|_{S_{ml}} = U_m(P); \quad (6)$$

$$\left[\frac{\partial U_m(P)}{\partial x}\right]_{B_t} = \frac{I_a}{\sigma_m S_m}, \quad (7)$$

where $C_{gm}(P)$ – transient resistance reflecting the state of the external insulating coating of the pipe at point P, Ohm·m^2; S_{gm} – area of the external surface of the pipe, m^2; n – normal to the pipe surface; $C_{ml}(P)$ – transient resistance reflecting the state of the internal insulating coating at point P, Ohm·m^2; S_{ml} – area of the internal surface of the pipe, m^2; S_m – cross-sectional area of the metal, m^2; σ_m – specific electrical conductivity of the pipe metal, S/m; the indices used here are: g – ground; m – pipe metal; l – transported liquid; gm – "ground – metal" boundary; ml – "metal – liquid" boundary.

The equations in the mathematical model (1)-(7) describe the following processes: (1) – potential distribution U_g of the electric current in the ground; (2) – potential distribution U_m of the electric current in the pipe metal and the potential U_l in the transported liquid; (3) – the condition of no current flow through the "air – ground" boundary and the regularity of the solution at infinity; (4) – no current flow condition at the end faces for the pipe metal and the liquid to transported liquid; (5) – the condition of current flow across the "ground – metal" boundary; (6) – the condition of current flow across the "metal – liquid" interface; (7) – the condition of connection of cathode station to pipeline at drainage point.

To solve the problem, we apply the fictitious source method [17, 33]. Let us represent a MP as a sequence of M_t of segments of the same length (Fig.2). For each such segment i ($i = 1 \ldots M_t$) on the pipeline, consider the averaged values: U_g^i – potential in the ground at the "ground – metal" interface, V; U_m^i – potential in the pipe metal, V; U_l^i – potential in the liquid, V; I_{gm}^i – current flowing from the ground into the pipe metal through the lateral surface, A; I_m^i – longitudinal current in pipe metal, A; I_{ml}^i – current intensity at the "metal – liquid" interface, A; I_l^i – longitudinal current in liquid, A. The diagnostic probe is a source of DC I_{pr} between the electrodes located at points A_{pr} and B_{pr}.

Journal of Mining Institute. 2024. Vol. 265. P. 156-164

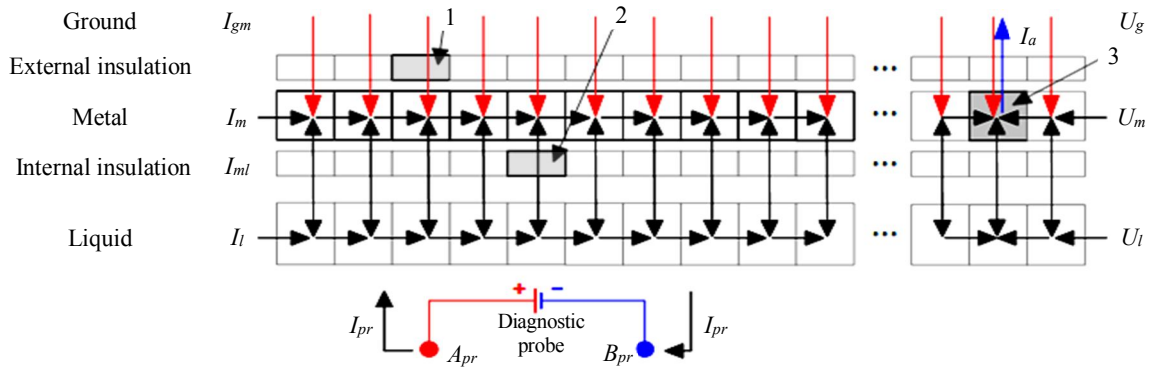

Fig.2. Fragment of a discrete pipeline model

1-2 – sections with broken insulation: 1 – external; 2 – internal; 3 – section with drain point B_t of protective current I_a

Each pipe segment forms fictitious point sources and (or) sinks of current. For each fictitious source and (or) sink, the outgoing and (or) incoming currents are described by Kirchhoff's laws:

$$I_{gm}^i + I_m^{i-1} - I_m^i - I_{ml}^i - I_a \delta\left(B_m^i, B_t\right) = 0; \tag{8}$$

$$i = \overline{1, M_t},\ I_m^0 = 0,\ I_m^{M_t} = 0;$$

$$I_{ml}^i + I_l^{i-1} - I_l^i + \delta\left(B_l^i, A_{pr}\right) I_{pr} - \delta\left(B_l^i, B_{pr}\right) I_{pr} = 0; \tag{9}$$

$$i = \overline{1, M_t},\ I_l^0 = 0,\ I_l^{M_t} = 0,$$

where B_m^i – coordinates of the middle point in the metal of the i-th segment; A_{pr} and B_{pr} current positions of electrodes of the diagnostic probe inside the transported liquid in the pipe, referred to the middle points of the segments in the liquid.

In equations (8) and (9) condition (4) of no current flow on end faces for pipe metal and transported liquid are considered.

Equations describe the discrete formulas of Ohm's law for the currents between pairs of neighboring segments:

$$U_m^{i+1} - U_m^i = -R_m I_m^i,\ \ i = \overline{1, M_t - 1},\ \ R_m = \frac{L_t}{M_t \sigma_m S_m}; \tag{10}$$

$$U_l^{i+1} - U_l^i = -R_l I_l^i,\ i = \overline{1, M_t - 1},\ \ R_l = \frac{L_t}{M_t \sigma_l S_l}, \tag{11}$$

where S_l – is the cross-sectional area of the transported liquid.

The discrete analogue of the formulas for boundary conditions of the third kind at the "ground – metal" and "metal – liquid" boundary is described by equations:

$$U_g^i - \frac{C_{gm}^i I_{gm}^i}{S_{gm}^i} = U_m^i,\ i = \overline{1, M_t}; \tag{12}$$

$$U_l^i + \frac{C_{ml}^i I_{ml}^i}{S_{ml}^i} = U_m^i,\ i = \overline{1, M_t}. \tag{13}$$

The electric current potential at any point of the homogeneous half-space containing the pipeline, according to the principle of superposition of fields, will be generated by the point anode source of the CPS A and M_t fictitious sources by the number of the formed pipeline segments. The potential is described by equation:

$$U_g(P) = I_a G(P, A) - \sum_{i=1}^{M_t} I_{gm}^i G\left(P, B_m^i\right), \tag{14}$$

where $G(P, Q)$ – is Green's function [30] of the enclosing homogeneous half-space, a function that calculates the value of electric current field potential at the point $P(x_P, y_P, z_P)$ of the half-space when the point source of electric current of unit intensity is found at the point $Q(x_Q, y_Q, z_Q)$.

The discrete model (8)-(14) by substituting in (14) the ground points $P = B_g^k, k = \overline{1, M_t}$ located near the ground-metal boundary, is a SLAE with the following unknowns: U_m, U_g, U_l, I_{gm}, I_m, I_l, I_{ml}. Here, each unknown is a vector of segment-averaged current or voltage values. The expanded SLAE matrix is of size $(7M_t - 2)\times(7M_t - 1)$. The solution of the SLAE gives the values of the desired current and voltage parameters for each discrete segment. Thus, the original differential mathematical model (1)-(7), describing the distribution of the DC field potential in the system is reduced to a SLAE equations (8)-(14) by the fictitious source method.

The computational experiment is based on the following methodology. The first step is to determine the probe electric field in the transported liquid when the internal and external insulation are undisturbed and the CPS current is zero $I_a = 0$ A. Call the resulting field the "normal" probe field.

At the second the "working" electric field was calculated – the probe field when the transient resistance of the internal and (or) external insulation on the pipe segment is broken and the CPS current is switched on. The "normal" field was then subtracted from the "working" field. The result of the step is the "abnormal" electric current field.

At steps 1 and 2, the movement of an in-line probe in the pipe was simulated. The size of the in-tube probe was set equal to the length of seven segments of the discrete pipeline model (7 m for the computational experiment below). Fifteen consecutive probe positions were calculated at which the middle of the probe was offset from the middle of the "defective" segment in the range of [–7; +7] segments.

At the third step, the field gradient between the fixed inner points of the probe, which simulates the position of its sensors, was calculated. The initial data of the computational experiment are given in the Table.

Computational experiment initial data

Parameter	Designation	Value
MP length, m	L_t	10000
Number of segments, psc	M_t	10000
Length of one model segment, m	l	1
MP depth, m	H_t	2.0
MP diameter, m	D_t	0.53
MP wall thickness, m	h_{tm}	0.008
Coordinates of point anode A, m	(x_A, y_A, z_A)	(5000; 350; 25)
Drainage point coordinates B_t, m	(x_{Bt}, y_{Bt}, z_{Bt})	(5000; 5.0; 2.265)
Drainage point segment number B_t	–	5001
Segment number with an external insulation defect	–	2501
Segment number with an internal insulation defect	–	2501
CPS DC current, A	I_a	1.0
Diagnostic probe, DC current, A	I_{pr}	1.0
MP metal specific conductivity, S/m	σ_m	$4.082\cdot10^6$
Ground specific electrical conductivity, S/m	σ_g	0.01
Liquid specific conductivity, S/m	σ_l	1.04
MP external insulation transient resistance, Ohm·m^2	C_{gt}	14000
MP internal insulation transient resistance, Ohm·m^2	C_{ml}	10000
MP external insulation transient resistance of defective segment N 2501, Ohm·m^2	C_{gt_2501}	1.4
MP internal insulation transient resistance of defective segment N 2501, Ohm·m^2	C_{ml_2501}	1.0

Journal of Mining Institute. 2024. Vol. 265. P. 156-164

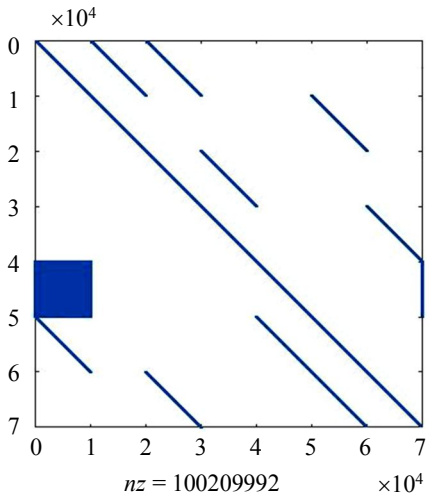

Fig.3. Structure of the extended SLAE matrix

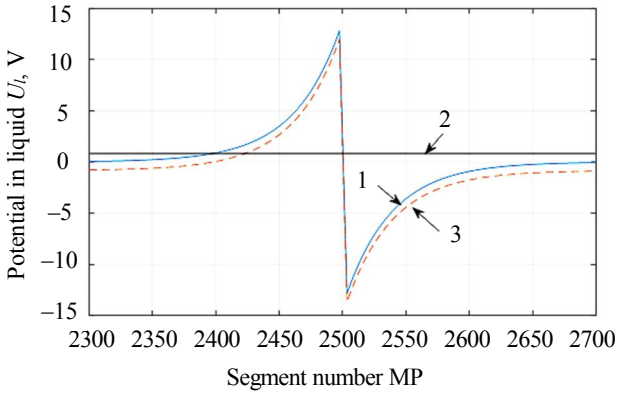

Fig.4. Potential distribution of electric current fields in the conveyed liquid at the zero probe position

1 – "normal"; 2 – "abnormal"; 3 – "working" field

The computational experiment was performed in the Matlab environment using the sparse matrix plug-in. To solve the SLAE left division operations were applied to the matrices. Figure 3 shows the structure of the expanded SLAE matrix for one of the probe positions in the pipe, where the blue dots represent the positions of non-zero elements of the system, with *nz* denoting the number of non-zero elements of the expanded matrix. The fill density of the expanded matrix is about 2 %.

A complete SLAE matrix for the number of segments $M_t = 10000$ in double data format has a size of about 36 GB. The problem was solved on a computer with a 10th generation Intel I5 processor and 12 GB of RAM in Matlab using the sparse matrix apparatus. The calculation of the SLAE for one probe position takes about 10-11 h.

The potential distribution of the "normal" probe field (Fig.4, curve 1) the superposition of the CPS fields aperture + probe fields for a "defective" insulated pipe (Fig.4, curve 2) and the "abnormal" (difference between the "working" and "normal" fields, Fig.4, line 3) in the transported liquid. Here, the segment including the segment with defective insulation (N 2501) is taken along the O*x*-axis. An insulation failure on the pipe segment results in redistribution of the probe's electric field due to leakage of part of the probe's current into the pipe metal.

For this case, the probe position in the pipe is fixed – the middle of the probe falls in the middle of the "defective" segment (zero probe position $dz = 0$). Figure 5 shows fragments of the "abnormal" field calculated at some offsets of the in-line probe. The range of probe center segment displacements is in the range of [–7; +7] pipe segments relative to the segment with defective insulation.

It is of practical interest to determine the number of the segment with defective insulation when the diagnostic probe moves inside the MP. The specific potential value in this case is secondary to the nature of the field change during the passage of the defective segment. Therefore, at the third step of the computational experiment, the field gradient between two segments of the diagnostic probe (two measuring probes) that are symmetrical with respect to the center was calculated. Figure 6 shows the "abnormal" field gradients based on the potential differences between the symmetrical probe segments, as the probe moves inside the pipeline. In the figure, the letters z_x denote the probe segments used to find the finite differences (x – is the segment displacement relative to the middle segment z_0. As can be seen in the figure, the gradient diagrams are symmetric with respect to the "defective" segment, and when the center of the probe coincides with the defective segment, they turn to zero. These gradient properties can be used as an indication of a defective pipe segment detection.

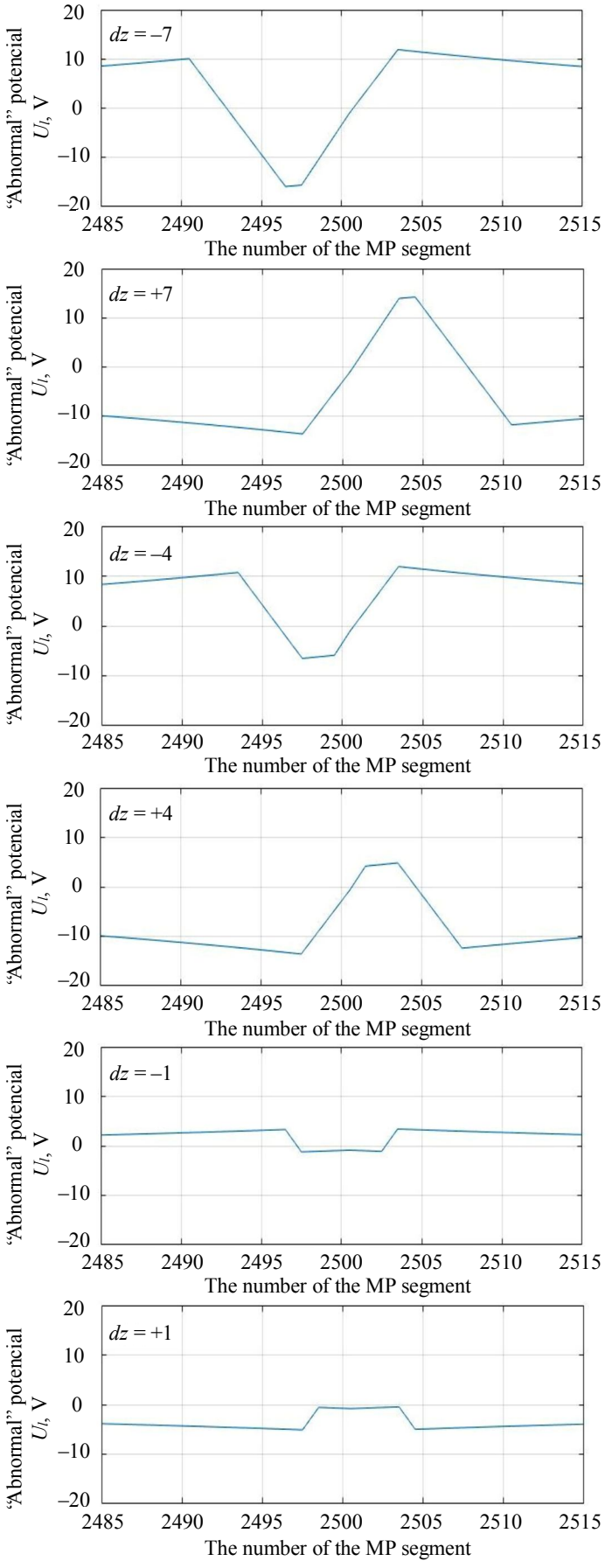

Fig.5. Plots of "abnormal" potential U_l in the transported liquid

Discussion of results. The DC field potential distribution model of an in-line cathodically polarized pipe probe proposed in this work allows detecting a breach of the internal insulation layer. The inclusion of a diagnostic probe in the model solves two problems. Firstly, the currents flowing inside the transported liquid and flowing from the liquid into the pipe metal can be increased by varying the probe current to values detectable by the instruments. Secondly, the simultaneous tracking of diagnostic probe position in MP and recording of potentials in liquid allow localizing the location of in-line insulation failure with an accuracy determined by the characteristics of the sensor for measuring current potentials (current gradient) in the liquid and the sensor for determining position sensor in the pipe. Locating the probe in a branched pipeline network [34, 35] is one of the important independent subtasks. The determination of the coordinates of a segment with disturbed insulation allows including the electric probing method into the intelligent analytical core of automated control systems for electrochemical protection of MP.

The inclusion of an in-line DC source in the model potentially expands the class of pipelines under investigation. This may also include pipelines operated without the use of cathodic protection systems.

The model proposed in the paper in the form of a SLAE (8)-(14) and the method of its solution make it possible to achieve discretization of a pipeline length of 1 m. This is by an order of magnitude greater than the discretization parameters achieved in the previous work of the authors [30] and the studies of other teams in this direction [33, 36].

Conclusion. The mathematical model proposed in this work describes the distribution of DC field potential in the electrochemical protection system of a MP. The results obtained as a result of modeling for a number of particular cases agree with those previously known [17, 30, 36].

Journal of Mining Institute. 2024. Vol. 265. P. 156-164

The distinctive features of the model are: taking into account the influence of the electric conductivity of transported liquid and the transient resistance of internal insulating coating on the distribution of electric fields; using the electric field of an in-tube diagnostic probe for quality control of internal insulation. Practical significance consists in the development of modeling methods for systems of electrochemical protection of MP against corrosion and the development of special mathematical and algorithmic support for subsystems of monitoring and control of CPS of MP. The length of one pipeline segment in the model is 1 m, which is an order of magnitude higher than the known solutions. Such an accuracy in coating defect localization makes it expedient to use autonomous robotic complexes for inspection of pipelines.

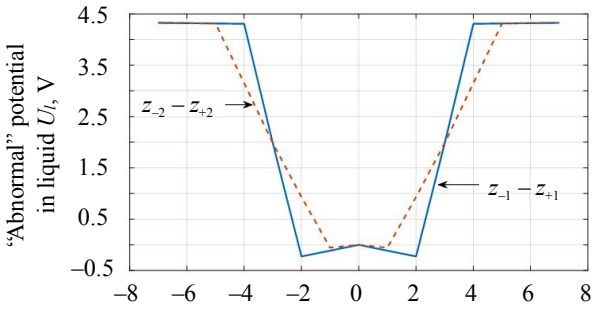

Fig.6. Field gradient distribution in the liquid as the probe moves

REFERENCES

1. Nishkevich Yu.A., Kozlov I.A. Corrosion: methods of corrosion control in the oil industry. Moscow: NITs INFRA-M, 2018, p. 88 (in Russian). DOI: 10.12737/monography_59a018d0867c99.11635048

2. Mustafin F.M., Chen' Tsyun', Mustafin O.F. et al. Passive protection of pipelines from corrosion. *Neftegaz.RU*. 2020. N 2, p. 86-90 (in Russian).

3. Burkov P.V., Burkov V.P., Fat'yanov D.S., Timofeev V.Yu. Studying the stress-strain state of oilfield pipelines exposed to rill corrosion. *Vestnik of Kuzbass State Technical University*. 2018. N 3, p. 5-12 (in Russian). DOI: 10.26730/1999-4125-2018-3-5-12

4. Ismaiylov G.G., Iskenderov E.Kh., Ismaiylova F.B. Problems of hydrodynamic corrosion in multiphase pipelines. *Fizikokhimiya poverkhnosti i zashchita materialov*. 2021. Vol. 57. N 1, p. 106-112 (in Russian). DOI: 10.31857/S0044185621010125

5. Bolobov V.I., Popov G.G. Methodology for testing pipeline steels for resistance to grooving corrosion. *Journal of Mining Institute*. 2021. Vol. 252, p. 854-860. DOI: 10.31897/PMI.2021.6.7

6. Aginei R.V., Isupova E.V., Guskov S.S., Musonov V.V. Theoretical estimation of the corrosion rate of main pipelines caused by the influence of a geomagnetic-induced stray current source. *Nauka i tekhnika v gazovoi promyshlennosti*. 2020. N 4, p. 62-73 (in Russian).

7. Baktizin R.N., Zaripov R.M., Korobkov G.E., Masalimov R.B. Assessment of internal pressure effect, causing additional bending of the pipeline. *Journal of Mining Institute*. 2020. Vol. 242, p. 160-168. DOI: 10.31897/PMI.2020.2.160

8. Shammazov I.A., Sidorkin D.I., Dzhemilev E.R. Research of the Dependence of the Pipeline Ends Displacement Value When Cutting Out Its Defective Section on the Elastic Stresses in the Pipe Body. *IOP Conference Series: Earth and Environmental Science*. 2022. Vol. 988. Iss. 2. N 022077. DOI: 10.1088/1755-1315/988/2/022077

9. Litvinenko V.S., Dvoynikov M.V., Trushko V.L. Elaboration of a conceptual solution for the development of the Arctic shelf from seasonally flooded coastal areas. *International Journal of Mining Science and Technology*. 2022. Vol. 32. Iss. 1, p. 113-119. DOI: 10.1016/j.ijmst.2021.09.010

10. Manko P.O., Kochergin A.V. Diagnostics of pipelines using in-tube defectoscopes. *Vestnik Lugansk Vladimir Dahl National University*. 2021. N 9 (51), p. 35-39 (in Russian).

11. Movchan I.B., Yakovleva A.A. Approach to automation of field diagnosis data interpretation for localization of pitting in the pipeline wall. *International Journal of Civil Engineering and Technology*. 2019. Vol. 10. N 2, p. 1571-1581.

12. Glinkin D.Y., Mezhuev A.V., Yudin M.I. Promising areas for developing ultrasonic inline inspection tools. *Science & Technologies: Oil and Oil Products Pipeline Transportation*. 2019. Vol. 9. N 4, p. 434-439 (in Russian). DOI: 10.28999/2541-9595-2019-9-4-434-439

13. Bazylev D.N., Romanovich V.A., Vedyakov A.A. Automated method of in-tube ultrasonic control using phased antenna array. *Journal of Instrument Engineering*. 2019. Vol. 62. N 9, p. 805-813 (in Russian). DOI: 10.17586/0021-3454-2019-62-9-805-813

14. Zhukov A.D., Grigoriev M.V., Danilov V.N. The research for an identification of crack – like corrosion – mechanical defect by acoustic in-line inspection tools. *Testing. Diagnostics*. 2020. N 2, p. 56-63 (in Russian). DOI: 10.14489/td.2020.02.pp.056-063

15. Potapov A.I., Kondratev A.V. Non-destructive testing of multilayer medium by the method of velocity of elastic waves hodograph. *Journal of Mining Institute*. 2020. Vol. 243, p. 348-356. DOI: 10.31897/PMI.2020.3.348

16. Mitolo M., Pettinger A. Interactions Between Cathodically Protected Pipelines and Grounding Systems. *IEEE Transactions on Industry Applications*. 2016. Vol. 52. Iss. 5, p. 3694-3698. DOI: 10.1109/tia.2016.2582795

17. Bolotnov A.M., Khisametdinov F.Z. Determining the state of pipe insulation protection according to the results of measurements of "soil-pipe" potential difference. *Bulletin of Bashkir University*. 2017. Vol. 22. N 1, p. 20-24 (in Russian).

18. Dzhala R., Verbenets B., Dzhala V. et al. Contactless testing of insulation damages distribution of the underground pipelines. *Procedia Structural Integrity*. 2022. Vol. 36, p. 17-23. DOI: 10.1016/j.prostr.2021.12.077

19. Bhadran V., Shukla A., Karki H. Non-contact flaw detection and condition monitoring of subsurface metallic pipelines using magnetometric method. *Materials Today: Proceedings*. 2020. Vol. 28. Part 2, p. 860-864. DOI: 10.1016/j.matpr.2019.12.313

20. Bobrov A., Kuten M. Intellectual Innovations in Acoustic Emission Control in the Safety System of Pipeline Transport. *Transportation Research Procedia*. 2021. Vol. 54, p. 340-345. DOI: 10.1016/j.trpro.2021.02.081

21. Asadzadeh S., de Oliveira W.J., de Souza Filho C.R. UAV-based remote sensing for the petroleum industry and environmental monitoring: State-of-the-art and perspectives. *Journal of Petroleum Science and Engineering*. 2022. Vol. 208. Part D. N 109633. DOI: 10.1016/j.petrol.2021.109633

22. Makhutov N.A., Neganov D.A., Studenov E.P., Zorin N.E. Development of status, strength and operating life diagnostics and monitoring methods for continuously operating oil trunk pipelines. *Procedia Structural Integrity*. 2022. Vol. 40, p. 283-295. DOI: 10.1016/j.prostr.2022.04.038

23. Grigorev G.S., Salishchev M.V., Senchina N.P. On the applicability of electromagnetic monitoring of hydraulic fracturing. *Journal of Mining Institute.* 2021. Vol. 250, p. 492-500. DOI: 10.31897/PMI.2021.4.2

24. Golubev I.A., Golubev A.V., Laptev A.B. Practice of using the magnetic treatment devices to intensify the processes of primary oil treating. *Journal of Mining Institute.* 2020. Vol. 245, p. 554-560. DOI: 10.31897/PMI.2020.5.7

25. Mayet A.M., Alizadeh S.M., Nurgalieva K.S. et al. Extraction of Time-Domain Characteristics and Selection of Effective Features Using Correlation Analysis to Increase the Accuracy of Petroleum Fluid Monitoring Systems. *Energies*. 2022. Vol. 15. Iss. 6. N 1986. DOI: 10.3390/en15061986

26. Samimi A., Zarinabadi S., Shahbazi Kootenaei A.H. et al. Corrosion classification of pipelines in hydrocracking units (ISOMAX) by data mining. *South African Journal of Chemical Engineering*. 2020. Vol. 3, p. 44-50. DOI: 10.1016/j.sajce.2019.11.006

27. Shafeek H., Soltan H.A., Abdel-Aziz M.H. Corrosion monitoring in pipelines with a computerized system. *Alexandria Engineering Journal*. 2021. Vol. 60. Iss. 6, p. 5771-5778. DOI: 10.1016/j.aej.2021.04.006

28. Syromyatnikova A., Bolshakov A., Ivanov A. et al. The corrosion damage mechanisms of the gas pipelines in the Republic of Sakha (Yakutia). *Procedia Structural Integrity*. 2019. Vol. 20, p. 259-264. DOI: 10.1016/j.prostr.2019.12.149

29. Lozovan V., Dzhala R., Skrynkovskyy R., Yuzevych V. Detection of specific features in the functioning of a system for the anti-corrosion protection of underground pipelines at oil and gas enterprises using neural networks. *Eastern-European Journal of Enterprise Technologies*. 2019. Vol. 1. Iss. 5 (97), p. 20-27. DOI: 10.15587/1729-4061.2019.154999

30. Krizsky V.N., Alexandrov P.N., Kovalskii A.A., Victorov S.V. Determination Transition Resistance of Cathode-Polarized Main Pipeline on Magnetometery Data. *International Journal of Mathematical, Engineering and Management Sciences*. 2021. Vol. 6. N 6, p. 1729-1740. DOI: 10.33889/ijmems.2021.6.6.102

31. Al-Gabalawy M.A., Mostafa M.A., Hamza A.S., Hussien S.A. Modeling of the KOH-Polarization cells for mitigating the induced AC voltage in the metallic pipelines. *Heliyon*. 2020. Vol. 6. Iss. 3. N e03417. DOI: 10.1016/j.heliyon.2020.e03417

32. Dzhala R., Dzhala V., Savula R. et al. Determination of components of transient resistance of underground pipeline. *Procedia Structural Integrity*. 2019. Vol. 16, p. 218-222. DOI: 10.1016/j.prostr.2019.07.044

33. Khisametdinov F.Z. Parameters of the electric field in cathodic protection of underground pipeline calculation and visualization. *Modern high technologies.* 2018. N 9, p. 126-130 (in Russian).

34. Lutonin A.S., Bogdanova K.A. Development of robotic platform for underground geomonitoring. *Izvestiya Tula State University. Technical sciences.* 2021. Iss. 12, p. 209-216 (in Russian). DOI: 10.24412/2071-6168-2021-12-209-217

35. Bogdanova K.A. Application of SLAM algorithms for three-dimensional modelling of mine workings. *Izvestiya Tula State University. Technical sciences.* 2021. Iss. 2, p. 134-140 (in Russian).

36. Zentsov V.N., Bolotnov A.M., Udalova E.A. et al. Optimization of parameters of electric field of gas product and oil pipes cathodic protection. *Bulletin of the Tomsk Polytechnic University. Geo Assets Engineering.* 2019. Vol. 330. N 5, p. 35-43 (in Russian). DOI: 10.18799/24131830/2019/5/255

***Authors*: Vladimir N. Krizskii,** *Doctor of Physics and Mathematics*, *Professor*, *https://orcid.org/0000-0002-4244-4692* (*Empress Catherine II Saint Petersburg Mining University*, *Saint Petersburg*, *Russia*), **Oleg V. Kosarev,** *Candidate of Engineering Sciences*, *Assistant Professor*, *kosarev_ov@pers.spmi.ru*, *https://orcid.org/0000-0003-3427-6593* (*Empress Catherine II Saint Petersburg Mining University*, *Saint Petersburg*, *Russia*), **Pavel N. Aleksandrov,** *Doctor of Physics and Mathematics, https://orcid.org/0000-0002-2101-0625* (*Schmidt Institute of Physics of the Earth of the RAS*, *Moscow*, *Russia*), **Yana A. Luntovskaya,** *Postgraduate Student, https://orcid.org/0000-0001-9694-4732* (*Empress Catherine II Saint Petersburg Mining University*, *Saint Petersburg*, *Russia*).

The authors declare no conflict of interests.